

## Research Statement: Michael C. Hillman, Ph.D.

### Biography

Dr. Hillman received his PhD in civil engineering from UCLA in 2013 and worked as a postdoctoral scholar at UC San Diego until joining Penn State in 2016. His research expertise is computational mechanics with an emphasis on meshfree methods. A persistent theme of his research has been to formulate these approaches such that obtaining practical solutions to complex problems is possible. External support for his research at Penn State has included both government and private industry. He has graduated an MS student and two PhD students, and he currently advises five PhD students. The attached CV provides relevant details.

### Current Areas and Goals

Since the advent of the finite element method (FEM), numerical analysis is now standard in science and engineering. Nevertheless, more novel approaches such as meshfree methods that can tackle non-trivial obstacles in FEM must carefully confront several issues to be effective. Dr. Hillman's current career goal is to solidify himself as one of the world's leading scholars in meshfree approaches that can effectively model computationally challenging phenomena including material damage, fracture, and separation; topological domain changes with evolving free surfaces; and extreme deformations and material flow. He has focused on fundamental advances in meshfree methods to this end including: (i) unifying frameworks for local and non-local meshfree methods; (ii) stabilized nodal integration; and (iii) the variational consistency of quadrature and boundary conditions.

### Hybrid Local-nonlocal Meshfree Methods and High-order Peridynamics

In recent work (attached), Hillman, Pasetto, and Zhou (2019) investigated the relationship between traditional meshfree approaches and peridynamic-based meshfree methods that have the potential to tackle the challenge of computational fracture mechanics. While a relationship had been established in ideal conditions, this work finally illuminated the precise connection between the two. Casting the approximations as a unified operator, both classical and peridynamic meshfree derivatives can be obtained. *This also generalized the concept of a peridynamic derivative allowing both high-order numerical differentiation and high-order accurate non-local approximations. When applied to boundary value problems, this provides arbitrary-order accurate (convergent) peridynamic solutions whereas the previously existing formulation provides no convergence in a general setting.* Exposing the link between classical and peridynamic meshfree methods led to Hillman's NSF CAREER award in 2020.

A broad new research direction for Hillman is leveraging the bridge between the two disparate numerical models to enable vast improvements to the more nascent peridynamic method. Here, Hillman targets modeling failure of structures and materials under extreme deformations and high rates, and accordingly, enhanced hybrid meshfree methods for fracture, shockwaves, and impact.

### Stabilized Nodal Integration

A nodally-integrated Galerkin equation is a central concept in meshfree methods: it preserves the nature of the approach on the discrete quadrature level and provides an efficient and straightforward implementation

when appropriately stabilized. Since 2016, Hillman has developed stabilized nodal integration methods for single-field, two-field, and self- and non-self-adjoint systems (Hillman and Chen 2016a, 2016b; Wei, Chen and Hillman 2016; Hillman and Lin 2021a, 2021b). Notably, Hillman and Chen (2016a) introduced naturally stabilized nodal integration (NSNI) *that provides a speedup of up to 20 times his and others' previous works*. In the attached two-part paper, Hillman and Lin (2021a, 2021b) develop this method to provide these speedups in thermomechanical meshfree methods for the first time. *Part II also presents a formulation that bypasses the prohibitive  $\mathcal{O}(h^2)$  explicit critical time step requirement (with  $h$  the nodal spacing) of the energy equation, with a formulation requiring only a uniform monolithic  $\mathcal{O}(h)$  time step of pure solid mechanics*. Meanwhile, this technique provides solutions indistinguishable from the classical theory. In the future, this approach will be extended to fluid-structure interaction problems under an immersed formulation recently proposed by his group and collaborators (preprint: Wang et al., 2021). Thermomechanical-fluid-structure interaction with fragmentation will then be targeted longer-term for explicit impact simulation of structures at high temperatures and high Mach numbers, the basis for a recently awarded STTR Phase II project. Other tangential future long-term thermo-mechanical applications include additive (e.g., fused deposition modeling, laser cladding), and subtractive (e.g., machining, cutting) manufacturing, targeting industry needs and sponsorship.

### **Consistent Weak Formulations**

Meshfree methods are unique in their capabilities, but also their properties concerning the Galerkin approach: these methods are non-interpolatory, so that imposing essential boundary conditions is not trivial as in FEM. Weak enforcement, and strong enforcement in conjunction with the traditional weak formulation, have addressed this issue. Yet, there remained an inconsistency in the latter more popular approach: most meshfree approximations cannot actually construct subspaces required in the standard weak formulation.

Hillman and Lin (2001c), attached, showed that this inconsistency results in an  $\mathcal{O}(h)$  error in the energy norm of the Galerkin solution to second-order PDEs independent of the approximation, placing a barrier on the order of solution accuracy to linear. This inconsistency was also shown to result in the loss of Galerkin orthogonality and the celebrated best approximation property. Hillman and Lin (2021c) then introduced consistent weak forms to rectify this, which permitted meshfree approximations. *This formulation restores orthogonality of the Galerkin solution and thus allows  $p$ -refinement,  $p$ th order optimal rates in  $h$ -refinement, and allows for a new concept called  $a$ -refinement*. Future work in this area includes the variational multiscale (VMS) method for consistent boundary condition enforcement. A longer-term goal is to use VMS to develop consistent and enhanced meshfree methods for problems involving stationary and evolving strong and weak discontinuities, and error indicators for adaptive node refinement.

### **Accelerated and High-order Accurate Galerkin Meshfree Methods**

While one can readily construct approximations with arbitrary-order accuracy, this does not guarantee the Galerkin formulation will achieve this order even in the setting of polynomial solutions, or so-called patch tests. Unlike FEM, this is challenging in meshfree methods due to the numerical integration of rational approximations with no intrinsic tie of their support to integration cells. Conventional techniques necessitate high-order quadrature rules to ensure accurate solutions, yet the associated computational cost makes this intractable. Low-order integration is much faster of course, but this cannot yield the accuracy of the former, presenting an impasse.

In the attached, Chen, Hillman and Rüter (2013) introduced the concept of variationally consistent (VC) integration, which set forth the requirements for arbitrary  $p$ th-order accuracy in the Galerkin equation. *This work finally showed an alternative path to high-order accuracy without using high-order*

quadrature. It also introduced an efficient correction where optimal convergence can be achieved with low-order integration, alleviating the efficiency bottleneck that plagued Galerkin meshfree methods since their inception. This framework has since served as the basis of new techniques developed by other research groups. When combined with NSNI (VC-NSNI) of Hillman and Chen (2016a) meshfree methods also provide the key desirable characteristics of numerical approaches: accuracy, stability, and efficiency. These two concepts have shown to be trivially combined, also providing ease of implementation. Hillman and Lin (2021a, 2021b), attached, extended VC integration to coupled problems, allowing arbitrary-order accuracy in the Galerkin meshfree solution of two-field problems for the first time.

While this approach can provide significant speedups, the relative remaining cost versus traditional FEM and low-order meshfree methods such as smoothed particle hydrodynamics (SPH) still makes these methods less attractive to analysts despite their benefits. In the future, Hillman will further accelerate computations by leveraging recent developments in peridynamic-based meshfree methods. Jafarzadeh et al. (2021) introduced a fast-Fourier transform technique without the traditional limitations that previously barred its use in most engineering applications, and provides speedups of several orders of magnitude (hours to minutes, days to hours). Dr. Hillman and the student author Jafarzadeh have agreed on a postdoctoral hire after graduation and will apply this work to Galerkin-based meshfree methods. Long-term, this approach will be extended to the various research areas in Hillman's group.

## Impact of Research Accomplishments

Dr. Hillman's contributions have addressed the previously existing bottlenecks in meshfree methods for extreme deformation and failure. *Naturally stabilized nodal integration* formulated under the framework of *variational consistency* (VC-NSNI) has enabled high accuracy, stability, and efficiency not previously possible in computationally challenging applications such as penetration/fragment-impact, blast-loaded structures, landslides, explosive welding, earth-moving, and 3D printing. His methods have also allowed numerical investigation of complex phenomena, including shock wave propagation in solids under blast and impact loadings, shear band formation in landslides, and failure mechanisms in man-made disasters. Dr. Hillman's VC-NSNI methods have been implemented into codes used by the DoD (US Army Corps of Engineers' NMAP and MEGA), DoE (Sandia National Laboratories' SIERRA), the commercial code LS-DYNA, as well as codes used in private industry (Case New Holland Industrial America LLC, and Karagozian & Case Inc.).

## Papers Attached

1. Hillman, M., Pasetto, M. and Zhou, G. (2019) 'Generalized reproducing kernel peridynamics: Unification of local and non-local meshfree methods, non-local derivative operations, and an arbitrary-order state-based peridynamic formulation', *Computational Particle Mechanics*, 7(2), pp. 435–469.
2. Hillman, M. and Lin, K. C. (2021a) 'Nodally integrated thermo-mechanical RKPM: Part I —Thermoelasticity', *Computational Mechanics*, in press.
3. Hillman, M. and Lin, K.-C. (2021b) 'Nodally integrated thermo-mechanical RKPM: Part II —Generalized thermoelasticity and hyperbolic finite-strain thermoplasticity', *Computational Mechanics*, in press.
4. Hillman, M. and Lin, K. C. (2021c) 'Consistent weak forms for meshfree methods: Full realization of  $h$ -refinement,  $p$ -refinement, and  $a$ -refinement in strong-type essential boundary condition enforcement', *Computer Methods in Applied Mechanics and Engineering*, 373, p. 113448.
5. Chen, J. S., Hillman, M. and Rüter, M. (2013) 'An arbitrary order variationally consistent integration for Galerkin meshfree methods', *International Journal for Numerical Methods in Engineering*, 95(5), pp. 387–418.

# Michael Hillman, Ph.D.

L. Robert and Mary L. Kimball Assistant Professor  
Department of Civil and Environmental Engineering  
The Pennsylvania State University

Tel: 814-863-0623 Email: mhillman@psu.edu Web: [mcharleshillman.com](http://mcharleshillman.com)

## Education

- 2013 Ph.D.**, Civil Engineering, University of California, Los Angeles  
Topic: An Arbitrary Order Variationally Consistent Integration Method for Galerkin Meshfree Methods  
Advisor: J. S. Chen  
Focus: Computational Mechanics
- 2009 M.S.**, Civil Engineering, University of California, Los Angeles  
Focus: Structural and geotechnical earthquake engineering
- 2008 B.S.**, Civil Engineering, California State University, Fullerton

## Appointments

- 2016–present Kimball Assistant Professor**, The Pennsylvania State University  
Department of Civil and Environmental Engineering
- 2014–2016 Postdoctoral Scholar, Instructor**, University of California, San Diego  
Department of Structural Engineering (Advisor: J. S. Chen)
- 2013 Postdoctoral Scholar, Instructor**, University of California, Los Angeles  
Department of Civil and Environmental Engineering (Advisor: J. S. Chen)
- 2009–2013 Graduate Student Researcher**, University of California, Los Angeles  
Department of Civil and Environmental Engineering
- 2011–2012 Teaching Assistant**, University of California, Los Angeles  
Department of Civil and Environmental Engineering

## Honors and Awards

1. CAREER Award, The National Science Foundation, 2020
2. L. Robert and Mary L. Kimball Early Career Development Endowed Professorship, The Pennsylvania State University, 2019–2022
3. L. Robert and Mary L. Kimball Early Career Development Endowed Professorship, The Pennsylvania State University, 2016–2019
4. Best Department Poster, Jacobs School of Engineering Research Expo, University of California, San Diego, 2014
5. Fellowship Award, Graduate Division, University of California, Los Angeles, 2013
6. Fellowship Award, Graduate Division, University of California, Los Angeles, 2011
7. Travel Award, United States Association for Computational Mechanics, 2010

## Research Interests

### Development of Advanced Computational Methods

- Accelerated Galerkin meshfree methods for extreme deformation analysis
- Variationally consistent domain integration for arbitrary-order Galerkin accuracy
- Stabilized nodal integration
- Unification of local and non-local meshfree methods
- High-order non-local meshfree methods
- Physics-based shock modeling

## Application of Computational Mechanics to Material Failure and Extreme Deformations

- Numerical investigation of damage processes and failure mechanisms of concrete walls and steel panels with varying thickness and impact velocities
- Numerical investigation of shock propagation in reinforced concrete members subjected to blast
- Numerical investigation of tillage and earth-moving operations
- Numerical simulation of three-dimensional deposition printing (concrete, thermoplastics)

## Supervised Students and Postdoctoral Scholars

### Ph.D. Dissertation Advisor

2020–present	Wang, Y.	"A cohesive reproducing kernel particle method for brittle fracture"
2020–present	Groeneveld, A.	"An immersed variational multiscale reproducing kernel particle method with application to fiber reinforcement in ultra-high performance concrete"
2020–present	Liu, F.	"Hybrid reproducing kernel peridynamic method for extreme event simulation"
2018–2021 (graduated)	Wang, J.	"Stabilized meshfree methods for material failure and composite analysis"
2017–2021 (expected)	Yang, S.	"Reproducing kernel finite volume methods for dynamic brittle fracture"
2016–2020 (graduated)	Lin, K. C.	"A nodally integrated thermo-mechanical meshfree formulation with application to fused deposition modeling"

### M.S. Dissertation Advisor

2017–2017 (graduated)	Chen, G. (co-advised)	"A numerical framework of viscoelastic modeling for 3D printable concrete simulation"
-----------------------	-----------------------	---

### Postdoctoral Advisor

2018–2020	Madra, A.	"Damage characterization and data-driven meshfree modeling of composite structures"
2017–2018	Zhou, G.	"Immersed meshfree methods for composite solid analysis and fluid-structure interaction"

### Undergraduate Research Advisor

2019–2020	Wang, Y.	"Linear system solver selection in meshfree methods"
-----------	----------	--

## Supervised Student and Postdoctoral Scholar Awards

### Students

1. Yang, S., Harry G. Miller Fellowship In Engineering, The Pennsylvania State University, 2020
2. Yang, S., USACM Thematic Conference on Meshfree and Particle Methods Travel Award, United States Association for Computational Mechanics, 2018
3. Lin, K. C., USACM Thematic Conference on Meshfree and Particle Methods Travel Award, United States Association for Computational Mechanics, 2018
4. Yang, S., IMECE2018 Travel Award, American Society of Mechanical Engineers, 2018
5. Yang, S., WCCM13 Travel Award, International Association for Computational Mechanics, 2018

### Postdoctoral Scholars

1. Madra, M., Second Place, Computation/Modeling, Materials Visualization Competition, The Pennsylvania State University, 2018

## Teaching Experience

§New course developed

### Penn State

<b>Fall 2020</b>	Graduate	The Finite Element Method (linear static and dynamic analysis)	9 students, one section
<b>Fall 2020</b>	Graduate	Meshfree Methods for Linear and Nonlinear Solid Mechanics <sup>§</sup>	11 students, one section
<b>Spring 2020</b>	Graduate	The Finite Element Method (linear static and dynamic analysis)	7 students, one section
<b>Fall 2019</b>	Undergraduate	Structural Analysis (determinate and indeterminate structures)	153 students, two sections
<b>Spring 2019</b>	Graduate	Meshfree Methods for Linear and Nonlinear Solid Mechanics <sup>§</sup>	4 students, one section
<b>Fall 2018</b>	Undergraduate	Structural Analysis (determinate and indeterminate structures)	155 students, two sections
<b>Spring 2018</b>	Graduate	The Finite Element Method (linear static and dynamic analysis)	9 students, one section
<b>Fall 2017</b>	Undergraduate	Structural Analysis (determinate and indeterminate structures)	60 students, one section
<b>Spring 2017</b>	Graduate	Meshfree Methods for Linear and Nonlinear Solid Mechanics <sup>§</sup>	6 students, one section
<b>Fall 2016</b>	Undergraduate	Structural Analysis (determinate and indeterminate structures)	82 students, one section

### UCSD

<b>Summer 2016</b>	Undergraduate	Structural Analysis (determinate and indeterminate structures)	30 students, one section
<b>Summer 2015</b>	Undergraduate	Algorithms and Programming for Structural Engineering	25 students, one section
<b>Summer 2014</b>	Undergraduate	Algorithms and Programming for Structural Engineering	24 students, one section

### UCLA

<b>Summer 2013</b>	Undergraduate	Introduction to Computing for Civil Engineers	11 students, one section
--------------------	---------------	---	--------------------------

## Publications

†Supervised student author

‡Supervised postdoctoral author

### Journal Publications

1. Hillman, M., Lin, K. C.<sup>†</sup>, Nodally integrated thermomechanical RKPM: Part I—Thermoelasticity, *Computational Mechanics*, In Press. [Download Preprint](#).
2. Hillman, M., Lin, K. C.<sup>†</sup>, Nodally integrated thermomechanical RKPM: Part II—Generalized thermoelasticity and hyperbolic finite-strain thermoplasticity, *Computational Mechanics*, In Press. [Download Preprint](#).
3. Tang, Y., Su, K., Man, R., Hillman, M., Du, J., Investigation of internal cracks in epoxy-alumina using in situ mechanical testing coupled with micro-CT, *JOM*, Available Online. Doi:10.1007/s11837-021-04714-x. [Download](#).

4. Baek, J., Chen, J. S., Zhou, G.<sup>‡</sup>, Arnett, K. P., Hillman, M., Hegemier, G., Hardesty, S., A semi-Lagrangian RKPM with node-based shock algorithm for explosive welding simulation, *Computational Mechanics*, Vol. 67, pp. 1601–1627, 2021. [Download](#).
5. Hillman, M., Lin, K. C.<sup>†</sup>, Consistent weak forms for meshfree methods: Full realization of  $h$ -refinement,  $p$ -refinement, and  $a$ -refinement in strong-type essential boundary condition enforcement, *Computer Methods in Applied Mechanics and Engineering*, Vol. 373, p. 113448, 2021. [Download](#).
6. Hillman, M., Pasetto, M., Zhou, G.<sup>‡</sup>, Generalized reproducing kernel peridynamics: Unification of local and non-local meshfree methods, non-local derivative operations, and an arbitrary-order state-based peridynamic formulation, *Computational Particle Mechanics*, Vol. 7, pp. 435–469, 2020. [Download](#).
7. Zhou, G.<sup>‡</sup>, Hillman, M., A Non-ordinary state-based Godunov peridynamics formulation for strong shocks in solids, *Computational Particle Mechanics*, Vol. 7, pp. 365–375, 2020. [Download](#).
8. Chen, J. S., Huang, T. H., Wei, H., Hillman, M., RKPM2D: An open-source implementation of nodally integrated reproducing kernel particle method for solving partial differential equations, *Computational Particle Mechanics*, Vol. 7, pp. 393–433, 2020. [Download](#).
9. Khaghani, M., Rajabipour, F., Gholizadeh-Vayghan, A., Hillman, M., Characterization of viscoelastic behavior of synthetic alkali–silica reaction gels, *Cement and Concrete Composites*, Vol. 104, p. 103359, 2019. [Download](#).
10. Liang, S., Chen, J. S., Li, J., Lin, S. P., Chi, S. W., Hillman, M., Roth, M. J., Heard, W., Numerical investigation of statistical variation of concrete damage between scales, *International Journal of Fracture*, Vol 208(1), pp. 97–113, 2017. [Download](#).
11. Bazilevs, Y., Moutsanidis, G., Bueno, J., Kamran, K., Kamensky, D., Hillman, M., Gomez, H., Chen, J.S., A new formulation for air-blast fluid structure interaction using an immersed approach. Part II—Coupling of IGA and meshfree discretizations, *Computational Mechanics*, Vol. 60, pp. 101–116, 2017. [Download](#).
12. Chen, J. S., Hillman, M., Chi, S. W., Meshfree methods: progress made after 20 years, *Journal of Engineering Mechanics*, Vol. 143(4), p. 04017001, 2017. [Download](#).
13. Hillman, M., Chen, J. S., An accelerated, convergent and stable nodal integration in Galerkin meshfree methods for linear and nonlinear mechanics, *International Journal for Numerical Methods in Engineering*, Vol. 107, pp. 603–630, 2016. [Download](#).
14. Hillman, M., Chen, J. S., Nodally integrated implicit gradient reproducing kernel particle method for convection dominated problems, *Computer Methods in Applied Mechanics and Engineering*, Vol. 299, pp. 381–400, 2016. [Download](#).
15. Haoyan W., Chen, J. S., Hillman, M., A stabilized nodally integrated meshfree formulation for fully coupled hydro-mechanical analysis of fluid-saturated porous media, *Computers and Fluids*, Vol. 141, pp. 105–115, 2016. [Download](#).
16. Sherburn, J., Roth, M. J., Chen, J. S., Hillman, M., Meshfree modeling of concrete slab perforation using a reproducing kernel particle impact and penetration formulation, *International Journal of Impact Engineering*, Vol. 86, pp. 96–110, 2015. [Download](#).
17. Hillman, M., Chen, J. S., Bazilevs, Y., Variationally consistent domain integration for isogeometric analysis, *Computer Methods in Applied Mechanics and Engineering*, Vol. 284, pp. 521–540, 2015. [Download](#).
18. Hillman, M., Chen, J. S., Stabilized and variationally consistent nodal integration for meshfree modeling of impact problems, *Computational Particle Mechanics*, Vol. 1, pp. 245–256, 2014. [Download](#).

19. Chen, J. S., Hillman, M., Rüter, M., An arbitrary order variationally consistent method for Galerkin meshfree methods, *International Journal for Numerical Methods in Engineering*, Vol. 95, pp. 387–418, 2013. [Download](#).

#### **Journal Publications Under Review**

1. Wang, J.<sup>†</sup>, Zhou, G.<sup>‡</sup>, Hillman, M., Madra, A.<sup>‡</sup>, Bazilevs, Y., Du, J., Su, K. Consistent immersed volumetric Nitsche methods for composite analysis, *Computer Methods in Applied Mechanics and Engineering*, Accepted pending revision. [Download Preprint](#).

#### **Book Chapters**

1. Hillman, M., Chen, J. S., Performance comparison of nodally Integrated Galerkin meshfree methods and nodally collocated strong form meshfree methods, In: *Advances in Computational Plasticity Vol. 46*, Eugenio Oñate, Djordje Peric, Eduardo de Souza Neto, and Michele Chiumenti (Eds.), pp. 145–164, Cham: Springer, 2018. [Download](#).
2. Chen, J. S., Liu, W. K., Hillman, M., Chi, S. W., Lian, Y., Bessa, M. A., Reproducing kernel particle method for solving partial differential equations, In: *Encyclopedia of Computational Mechanics Second Edition*, Erwin Stein, Renè de Borst and Tom Hughes (Eds.), Volume 2, Chapter 17, London: Wiley, 2018. [Download](#).
3. Hillman, M., Chen, J. S., An implicit gradient meshfree formulation for convection-dominated problems, In: *Advances in Computational Fluid-Structure Interaction and Flow Simulation*, Yuri Bazilevs and Kenji Takizawa (Eds.), pp. 25–37, Cham: Springer, 2016. [Download](#).
4. Rüter, M., Hillman, M., Chen, J. S., Corrected stabilized non-conforming nodal integration in meshfree methods, In: *Lecture Notes in Computational Science and Engineering VI*, Michael Griebel and Marc Alexander Schweitzer (Eds.), pp. 75–93, Cham: Springer, 2013. [Download](#).

#### **Articles**

1. Chen, J. S., Chi, S. W., Hillman, M., Preface: Meshfree and particle methods for modeling extreme loadings, in memory of Steve Attaway, *Computational Particle Mechanics*, Vol. 7, pp. 173–176, 2020. [Download](#).
2. Hillman, M., Chen, J. S., Roth, M. J., Advanced computational methods to understand & mitigate extreme events, *IACM Expressions*, Vol. 39, pp. 12–16, 2016. [Download](#).
3. Chen, J. S., Hillman, M., Rüter, M., Hu, H. Y., Chi, S. W., The role of quadrature in meshfree Methods: Variational consistency in Galerkin weak form and collocation in strong form, *IACM Expressions*, Vol. 34, pp. 11–17, 2014. [Download](#).

#### **Conference Papers**

1. Chen, J. S., Baek, J., Huang, T. H., Hillman, M., Accelerated and stabilized meshfree method for impact-blast modeling, proceedings, 2020 ASCE Structures Congress, St. Louis, Missouri, April 5–8, 2020. [Download](#).
2. Hillman, M., Lin, K. C.<sup>†</sup>, Madra, A.<sup>‡</sup>, The meshfree explicit Galerkin analysis (MEGA) code, proceedings, 14<sup>ème</sup> Colloque National en Calcul des Structures, Presqu'île de Giens, May 13–17, 2019. [Download](#).
3. Madra, A.<sup>‡</sup>, Su, K., Du, J., Hillman, M., Multi-scale reduced-order model of composite microstructure based on X-ray micro-CT imaging, proceedings, 14<sup>ème</sup> Colloque National en Calcul des Structures, Presqu'île de Giens, May 13–17, 2019. [Download](#).
4. Littlewood, D., Hillman, M., Yreux, E., Bishop, J., Chen, J.S., Implementation and verification of RKPM in the Sierra/SolidMechanics analysis code, proceedings, ASME 2015 International Mechanical Engineering Congress & Exposition, Houston, Texas, November 13–19, 2015. [Download](#).

## Research Grants

Hillman has been PI/Co-PI on ten externally funded research projects (PI on nine), with total external funding \$2.1M (Hillman's share: \$1.8M).

- 2021–2023**      **STTR phase II: Enhancing thermo-mechanically coupled computational models for high-temperature impact and fracture** (PI: M. Hillman)  
Funding Source: Karagozian and Case, Inc.; Prime: Missile Defense Agency  
Total awarded: \$358,228 (100% to Hillman)
- 2021–2022**      **Numerical modeling of 3D printable concrete** (PI: A. Radlinska, co-PI: M. Hillman)  
Funding Source: Penn State  
Total awarded: \$60,000 (50% to Hillman)
- 2020–2021**      **Enhanced reproducing kernel particle method for strong shock hydrodynamics** (PI: M. Hillman)  
Funding Source: Karagozian and Case, Inc.  
Total awarded: \$23,090 (100% to Hillman)
- 2020–2025**      **CAREER: A hybrid local-nonlocal peridynamics framework to model failure across deformations and strain rates** (PI: M. Hillman)  
Funding Source: The National Science Foundation  
Total awarded: \$580,845 (100% to Hillman)
- 2019–2020**      **STTR phase I: High temperature fracture mechanics** (PI: M. Hillman)  
Funding Source: Karagozian and Case, Inc.; Prime: Missile Defense Agency  
Total awarded: \$30,000 (100% to Hillman)
- 2019–2021**      **Prototype of an enhanced and validated discrete-continuum particle method for microstructural failure simulation in high-performance concrete** (PI: M. Hillman)  
Funding Source: U.S. Army Engineer Research and Development Center  
Total awarded: \$300,000 (100% to Hillman)
- 2019–2020**      **Enhanced reproducing kernel particle method: Variationally consistent naturally stabilized nodal integration** (PI: M. Hillman)  
Funding Source: Karagozian and Case, Inc.  
Total awarded: \$72,698 (100% to Hillman)
- 2018–2021**      **An integrated computational-experimental approach to three-dimensional fracture in polymer-ceramic composites** (PI: M. Hillman, Co-PI: J. Du)  
Funding Source: The National Science Foundation  
Total awarded: \$545,418 (47% to Hillman)
- 2019**              **Benchmarking the reproducing kernel particle method for geotechnical operations** (PI: M. Hillman)  
Funding Source: Case New Holland Industrial America LLC  
Total awarded: \$59,995 (100% to Hillman)
- 2019**              **Evaluation of concrete materials performance in aging structures** (PI: A. Siad, Co-PI: M. Hillman)  
Funding Source: The Johns Hopkins University Applied Physics Laboratory LLC  
Total awarded: \$34,900 (35% to Hillman)

- 2018–2019**     **A discrete continuum particle method for understanding micro-structural failure of concrete** (PI: M. Hillman)  
 Funding Source: U.S. Army Engineer Research and Development Center  
 Total awarded: \$103,995 (100% to Hillman)
- 2018–2019**     **Development and experimental validation of variational collocation meshfree simulation of fracture of nanoparticle toughened composite materials** (PI: M. Hillman, co-PI: C. Bakis)  
 Funding Source: Penn State  
 Total awarded: \$60,000 (96% to Hillman)

## Presentations and Posters

### Presenter

†Supervised student author

‡Supervised postdoctoral author

### Invited Talks

1. Hillman, M. "Meshfree methods for extreme deformations and material damage," Simulia Corp., Providence, Road Island, April 30, 2019.
2. Hillman, M. "Stable high-order meshfree formulations: Recent enhancements and emerging developments," Center for Extreme Events Research Summit, University of California, San Diego, San Diego, California, March 22, 2019.
3. Hillman, M. "Computational frameworks for damage assessment of structures subject to extreme loadings," Department of Mathematics and Statistics, University of New Mexico, Albuquerque, New Mexico, March 4, 2016.
4. Hillman, M. "Computational frameworks for damage assessment of structures subject to extreme loadings," Computer Science Research Institute, Sandia National Laboratories, Albuquerque, New Mexico, February 29, 2016.

### Keynote Talks

1. Hillman, M., Chen, J. S., "Stable and robust meshfree integration for extreme event simulations," Engineering Mechanics Institute Conference, San Diego, California, June 4–7, 2017.

### Conference Presentations

1. Wang, J.<sup>†</sup>, Hillman, M. "A hybrid Lagrangian/semi-Lagrangian meshfree formulation for efficient simulation of extreme deformation problems," 2021 Engineering Mechanics Institute Conference, Virtual, May 25–28, 2021.
2. Hillman, M., Wang, J.<sup>†</sup>, "The reproducing kernel finite volume method for elastodynamics," 2021 Engineering Mechanics Institute Conference, Virtual, May 25–28, 2021.
3. Hillman, M., "Instabilities in Petrov-Galerkin methods for elastodynamics," 14th World Congress in Computational Mechanics, Virtual, January 11–15, 2021.
4. Hillman, M., Yang, S.<sup>†</sup>, "A reproducing kernel finite volume method for elastodynamics," 14th World Congress in Computational Mechanics, Virtual, January 11–15, 2021.
5. Madra, A.<sup>‡</sup>, Hillman, M., "Reduced-order model of concrete microstructure based on X-ray microtomographic imaging," 14th World Congress in Computational Mechanics, Virtual, January 11–15, 2021.
6. Hillman, M., Wang, J.<sup>†</sup>, Zhou, G.<sup>‡</sup>, Madra, A.<sup>‡</sup>, "An immersed nolumetric Nitsche's approach for composites with application to direct numerical simulation of micro-CT Images," International Mechanical Engineering Congress and Exposition 2020, Virtual, November 16–19, 2020.
7. Yang, S.<sup>†</sup>, Hillman, M. "A cohesive reproducing kernel finite volume method for brittle fracture simulation," International Mechanical Engineering Congress and Exposition 2020, Virtual, November 16–19, 2020.

8. Wang, J.<sup>†</sup>, Hillman, M. "A smoothed Lagrangian naturally stabilized meshfree method for dynamic simulations," International Mechanical Engineering Congress and Exposition 2020, Virtual, November 16–19, 2020.
9. Wang, Y.<sup>†</sup>, Hillman, M. "Complexity and accuracy analysis of Galerkin and collocation meshfree methods," International Mechanical Engineering Congress and Exposition 2020, Virtual, November 16–19, 2020.
10. Gao, J., Man, R., Wang, Y., Tang, Y., Su, K., Hillman, M., Du, J. "Fracture mechanisms of epoxy-alumina composites," The Minerals, Metals & Materials Society Conference 2020, San Diego, California, February 23–27, 2020.
11. Hillman, M., Wang, J.<sup>†</sup>, Zhou, G.<sup>‡</sup>, Madra, A.<sup>‡</sup> "An immersed volumetric Nitsche's approach for composites with application to direct numerical simulation of micro-CT Images," International Mechanical Engineering Congress and Exposition 2019, Salt Lake City, UT, November 11–14, 2019.
12. Hillman, M., Pasetto, M., Zhou, G.<sup>‡</sup>, "Generalized reproducing kernel peridynamics," 15th International Conference on Computational Plasticity, Barcelona, Spain, September 3–5, 2019.
13. Bazilevs, Y., Moutsanidis, G., Kamensky, D., Hillman, M., Chen, J. S., "Recent advances in IGA-meshfree methods for extreme events," 15th International Conference on Computational Plasticity, Barcelona, Spain, September 3–5, 2019.
14. Yang, S.<sup>†</sup>, Hillman, M., "A reproducing kernel particle finite volume method for linear and non-linear mechanics," 15th US National Congress of Computational Mechanics, Austin, Texas, July 28 – August 1, 2019.
15. Hillman, M., Wang, J.<sup>†</sup>, Zhou, G.<sup>‡</sup>, "An immersed volumetric Nitsche's approach for meshfree analysis of composites," 15th US National Congress of Computational Mechanics, Austin, Texas, July 28 – August 1, 2019.
16. Lin, K. C.<sup>†</sup>, Hillman, M., "Naturally stabilized nodal integration for meshfree methods in thermoelasticity," 15th US National Congress of Computational Mechanics, Austin, Texas, July 28 – August 1, 2019.
17. Madra, A.<sup>‡</sup>, Hillman, M., Loeffler, C., Nie, X., Heard, W., Sherburn, J., "Semantically valid deep-learning classification of fracture morphology in high-strength concrete," 15th US National Congress of Computational Mechanics, Austin, Texas, July 28 – August 1, 2019.
18. Hillman, M., Zhou, G.<sup>‡</sup>, "An immersed volumetric Nitsche's approach for meshfree analysis of composites," 2019 Engineering Mechanics Institute Conference, Pasadena, California, June 18–21, 2019.
19. Madra, A.<sup>‡</sup>, Du, J., Hillman, M., "Multi-scale reduced-order model of composite microstructure based on X-ray micro-CT imaging," 14ème Colloque National en Calcul des Structures, Presqu'île de Giens, France, May 13–17, 2019.
20. Hillman, M., Lin, K. C.<sup>†</sup>, Madra, A.<sup>‡</sup>, "The meshfree explicit Galerkin analysis (MEGA) code," 14ème Colloque National en Calcul des Structures, Presqu'île de Giens, France, May 13–17, 2019.
21. Hillman, M., "A finite volume meshfree method: An elegant alternative to Galerkin implementations," Workshop on Meshfree Method and Advances in Computational Mechanics, Pleasanton, California March 10–12, 2019.
22. Yang, S.<sup>†</sup>, Hillman, M., "A conforming reproducing kernel finite volume method," 2018 International Mechanical Engineering Congress and Exposition, Pittsburgh, Pennsylvania, November 9–15, 2018.
23. Lin, K. C.<sup>†</sup>, Hillman, M., "Consistent strong enforcement of essential boundary conditions in meshfree methods," 2018 International Mechanical Engineering Congress and Exposition, Pittsburgh, Pennsylvania, November 9–15, 2018.

24. Hillman, M., "Generalized reproducing kernel peridynamics," 2018 International Mechanical Engineering Congress and Exposition, Pittsburgh, Pennsylvania, November 9–15, 2018.
25. Yang, S.<sup>†</sup>, Hillman, M., "A finite volume reproducing kernel particle method," USACM Thematic Workshop on Meshfree and Particle Methods: Application and Theory, Santa Fe, New Mexico, September 10–12, 2018.
26. Lin, K. C.<sup>†</sup>, Hillman, M., "Consistent strong enforcement of essential boundary conditions in meshfree methods," USACM Thematic Workshop on Meshfree and Particle Methods: Application and Theory, Santa Fe, New Mexico, September 10–12, 2018.
27. Baek, J., Zhou, G.<sup>‡</sup>, Chen, J. S., Hillman, M., "Coupled shock-plasticity-damage modeling of explosive welding by RKPM," USACM Thematic Workshop on Meshfree and Particle Methods: Application and Theory, Santa Fe, New Mexico, September 10–12, 2018.
28. Hillman, M., "Generalized reproducing kernel peridynamics," USACM Thematic Workshop on Meshfree and Particle Methods: Application and Theory, Santa Fe, New Mexico, September 10–12, 2018.
29. Chen, J. S., Hillman, M., Chi, S. W., "Implicit gradient for numerical solution of PDEs," USACM Thematic Workshop on Meshfree and Particle Methods: Application and Theory, Santa Fe, New Mexico, September 10–12, 2018.
30. Zhou, G.<sup>‡</sup>, Hillman, M., "A non-ordinary state-based Godunov-peridynamics formulation for shocks in solids," 13th World Congress in Computational Mechanics, New York, New York, July 22–27, 2018.
31. Yang, S.<sup>†</sup>, Hillman, M., "A reproducing kernel finite volume method," 13th World Congress in Computational Mechanics, New York, New York, July 22–27, 2018.
32. Lin, K. C.<sup>†</sup>, Hillman, M., "Consistent strong enforcement of essential boundary conditions in meshfree methods," 13th World Congress in Computational Mechanics, New York, New York, July 22–27, 2018.
33. Baek, J., Zhou, G.<sup>‡</sup>, Chen, J. S., Hillman, M., "Coupled shock-plasticity-damage modeling of explosive welding by RKPM," 13th World Congress in Computational Mechanics, New York, New York, July 22–27, 2018.
34. Hillman, M., Zhou, G.<sup>‡</sup>, "Generalized reproducing kernel peridynamics," 13th World Congress in Computational Mechanics, New York, New York, July 22–27, 2018.
35. Chen, J. S., Hillman, M., "Implicit gradient for numerical solution of PDEs," 13th World Congress in Computational Mechanics, New York, New York, July 22–27, 2018.
36. Chen, J. S., Hillman, M., "Performance comparison of nodally integrated Galerkin meshfree methods and nodally collocated strong form meshfree methods," 13th World Congress in Computational Mechanics, New York, New York, July 22–27, 2018.
37. Hillman, M., "A general framework for reproducing kernel peridynamics," 18th U.S. National Congress for Theoretical and Applied Mechanics, Chicago, Illinois, June 4–9, 2018.
38. Yang, S.<sup>†</sup>, Hillman, M., "A reproducing kernel finite volume method," 2018 Engineering Mechanics Institute Conference, Boston, Massachusetts, May 29 – June 1, 2018.
39. Lin, K. C.<sup>†</sup>, Hillman, M., "Consistent strong enforcement of essential boundary conditions in meshfree methods," 2018 Engineering Mechanics Institute Conference, Boston, Massachusetts, May 29 – June 1, 2018.
40. Hillman, M., Zhou, G.<sup>‡</sup>, "Generalized reproducing kernel peridynamics," 2018 Engineering Mechanics Institute Conference, Boston, Massachusetts, May 29 – June 1, 2018.
41. Chen, J. S., Hillman, M., Chi, S. W., "Meshfree methods: Progress made after 20 years and future directions," *Plenary Lecture*, 2018 Engineering Mechanics Institute Conference, Boston, Massachusetts, May 29 – June 1, 2018.

42. Hillman, M., Chen, J. S., "A smoothed implicit gradient reproducing kernel particle method for extreme event modelling," 14th International Conference on Computational Plasticity, Barcelona, Spain, September 5–7, 2017.
43. Chen, J. S., Hillman, M., "Recent advances in accelerated and stabilized meshfree method for modeling man-made and natural disasters," *Plenary Lecture*, 14th International Conference on Computational Plasticity, Barcelona, Spain, September 5–7, 2017.
44. Hillman, M., Chen, J. S., "Non-conforming naturally stabilized nodal integration," 14th US National Congress of Computational Mechanics, Montréal, Canada, July 16–20, 2017.
45. Chen, J. S., Zhou, G.<sup>‡</sup>, Hillman, M., "A reproducing kernel particle method framework for modeling failure of solids subjected to blast loadings," 14th US National Congress of Computational Mechanics, Montréal, Canada, July 16–20, 2017.
46. Chen, J. S., Hillman, M., "Multiscale mechanics and modeling of concrete," 2017 Engineering Mechanics Institute Conference, San Diego, California, June 4–7, 2017.
47. Zhou, G.<sup>‡</sup>, Chen, J. S., Hillman, M., "A Riemann-SNNI Galerkin meshfree method for solid and fluid dynamics," 2017 Engineering Mechanics Institute Conference, San Diego, California, June 4–7, 2017.
48. Beckwith, F., Hillman, M., Chen, J. S., "Fragment impact modeling of concrete structures," 2017 Engineering Mechanics Institute Conference, San Diego, California, June 4–7, 2017.
49. Wei, H., Chen, J. S., Hillman, M., "RKPM formulation for fully Coupled hydro-mechanical analysis of fluid-saturated porous media," Engineering Mechanics Institute Conference, San Diego, California, June 4–7, 2017.
50. Moutsanidis, G., Bueno, J., Kamran, K., Kamensky, D., Hillman, M., Chen, J.S., Bazilevs, Y., "A new formulation for air-blast fluid-structure interaction based on an immersed isogeometric-meshfree approach," Engineering Mechanics Institute Conference, San Diego, California, June 4–7, 2017.
51. Chen, J. S., Hillman, M., Chi, S. W., "Meshfree methods: Progress made after 20 years," *Plenary Lecture*, Chinese Conference on Computational Mechanics 2016, Hangzhou, China, October 16–20, 2016.
52. Hillman, M., Chen, J. S., "Accelerated meshfree methods under a smoothed implicit gradient framework," USACM Conference on Isogeometric Analysis and Meshfree Methods, La Jolla, California, October 10–12, 2016.
53. Zhou, G.<sup>‡</sup>, Chen, J.S., Hillman, M., "A Riemann-SNNI Galerkin meshfree method for solid and fluid dynamics," USACM Conference on Isogeometric Analysis and Meshfree Methods, La Jolla, California, October 10–12, 2016.
54. Bueno, J., Moutsanidis, G., Kamran, K., Hillman, M., Gomez, H., Chen, J.S., Bazilevs, Y., "A new immersed isogeometric-meshfree technique for fluid-structure interaction problems involving high Mach numbers, part I," USACM Conference on Isogeometric Analysis and Meshfree Methods, La Jolla, California, October 10–12, 2016.
55. Bueno, J., Moutsanidis, G., Kamran, K., Hillman, M., Gomez, H., Chen, J.S., Bazilevs, Y., "A new immersed isogeometric-meshfree technique for fluid-structure interaction problems involving high Mach numbers, Part II," USACM Conference on Isogeometric Analysis and Meshfree Methods, La Jolla, California, October 10–12, 2016.
56. Roth, J., Sherburn, J., Beckwith, F., Hillman, M., Chen, J.S., "Application of meshfree methods to penetration and blast effects modeling," USACM Conference on Isogeometric Analysis and Meshfree Methods, La Jolla, California, October 10–12, 2016.
57. Beckwith, F., Hillman, M., Chen, J.S., "Fragment-impact modeling of concrete structures," USACM Conference on Isogeometric Analysis and Meshfree Methods, La Jolla, California, October 10–12, 2016.

58. Wei, H., Chen, J.S., Hillman, M., “RKPM formulation for fully coupled hydro- mechanical analysis of fluid-saturated porous media,” USACM Conference on Isogeometric Analysis and Meshfree Methods, La Jolla, California, October 10–12, 2016.
59. Hillman, M., Chen, J. S., “Accelerated meshfree methods using variationally consistent naturally stabilized nodal integration,” 12th World Congress on Computational Mechanics, Seoul, Korea, July 24–29, 2016.
60. Chen, J. S., Hillman, M., Yreux, E., Zhou, G.<sup>‡</sup>, “Fracture to damage multiscale modeling and application to extreme events simulation,” *Plenary Lecture*, 12th World Congress on Computational Mechanics, Seoul, Korea, July 24–29, 2016.
61. Hillman, M., Roth, J., Slawson, T., Chen, J. S., “Modeling projectile penetration mechanics in a meshfree computational framework,” 2016 Engineering Mechanics Institute Conference, Nashville, Tennessee, May 22–25, 2016.
62. Chen, J. S., Hillman, M., Yreux, “Fracture to damage multiscale modeling,” *Plenary Lecture*, Association of Computational Mechanics Taiwan Conference, Taipei, Taiwan, October 22–23, 2015.
63. Hillman, M., Chen, J. S., “Stable and efficient variationally consistent nodal integration for mesh-free methods using Taylor expansion,” 13th US National Congress of Computational Mechanics, San Diego, California, July 26–30, 2015.
64. Roth, M., Sherburn, J., Slawson, T., Chen, J.S., Hillman, M., “Modeling projectile penetration mechanics in a mesh-free computational framework,” 13th US National Congress of Computational Mechanics, San Diego, California, July 26–30, 2015.
65. Chen, J. S., Yreux, E., Hillman, M., “A stabilized quasi-linear reproducing kernel particle method for modeling material damages under extreme events,” 13th US National Congress of Computational Mechanics, San Diego, California, July 26–30, 2015.
66. Hu, H.Y., Chen, J. S., Hillman, M., Rüter, M., “The role of quadrature in meshfree methods,” 3rd International Eurasian Conference on Mathematical Sciences and Applications, Vienna, Austria, August 25–28, 2014.
67. Hillman, M., Chen, J. S., Bazilevs, Y., “Variationally consistent integration for meshfree and isogeometric analysis,” 11th World Congress on Computational Mechanics, Barcelona, Spain, July 20–25, 2014.
68. Chen, J. S., and Hillman, M., “The role of quadrature In meshfree method: Variational consistency in Galerkin weak form and collocation in strong form,” Seventh International Workshop, Meshfree Methods for Partial Differential Equations, Bonn, Germany, September 9–11, 2013.
69. Chen, J. S., Hillman, M., Rüter, M., “An arbitrary order variationally consistent domain integration method for Galerkin meshfree methods,” 12th US National Congress of Computational Mechanics, Raleigh, North Carolina, July 22–25, 2013.
70. Hillman, M., Chen, J. S., “An arbitrary order variationally consistent integration method for Galerkin thin plate analysis,” 12th US National Congress of Computational Mechanics, Raleigh, North Carolina, July 22–25, 2013.
71. Chen, J. S., Hillman, M., Rüter, M., “A general framework of domain integration in meshfree methods,” Advances in Computational Mechanics, San Diego, California, February 24–28, 2013.
72. Chen, J. S., Chi, S. W., Hu, H. Y., Hillman, M., Rüter, M., Yang, J. P. “Stabilized Galerkin and collocation meshfree methods: convergence, stability, and applications,” European Congress on Computational Methods in Applied Sciences and Engineering, Vienna, Austria, September 10–14, 2012.
73. Chen, J. S., Hillman, M., Rüter, M., “A general framework of domain integration in meshfree methods,” 10th World Congress on Computational Mechanics, São Paulo, Brazil, July 8–13, 2012.

74. Chen, J. S., Hillman, M., "A general framework of domain integration in Galerkin meshfree methods," 48th Annual Conference of Society of Engineering Sciences, Northwestern University, October 12–14, 2011.
75. Chen, J. S., Hillman, M., "General framework of domain integration in Galerkin meshfree methods," 6th International Workshop on Meshfree Methods for Partial Differential Equations, Bonn, Germany, October 4–6, 2011.
76. Chen, J. S., Hillman, M., "Implicit upwind reproducing kernel particle method for convection dominated problems," 11th US National Congress on Computational Mechanics, Minneapolis, USA July 25–28 2011.
77. Chen, J. S., Hillman, M., "Fragment-impact modeling using RKPM Level set kernel contact algorithms," 9th World Congress on Computational Mechanics, Sydney, Australia, July 19–23, 2010.

### **Posters**

1. Zhou, G., Hillman, M., "Numerical methods for extreme events modeling," UCSD Jacobs School of Engineering Research Expo, San Diego, California, April 16, 2015.
2. Zhou, G., Hillman, M., Pasetto, M., Beckwith, F. "Recent advances in modeling extreme events and application to homeland security," UCSD Jacobs School of Engineering Research Expo, San Diego, California, April 16, 2015.
3. Yreux, E., Hillman, M., Zhou, G. "Meshfree methods for fragment-impact modeling and homeland security applications," UCSD Jacobs School of Engineering Research Expo, San Diego, California, April 16, 2015.
4. Yreux, E., Hillman, M. "Meshfree methods for fragment-impact modeling and homeland security applications," UCSD Jacobs School of Engineering Research Expo, San Diego, California, April 16, 2014.
5. Hillman, M., Roth, J., Chi, S. W. "Advances in meshfree methods for fragment-impact modeling and homeland security applications," UCLA Henry Samueli School of Engineering and Applied Science Tech Forum, Los Angeles, California, May 8, 2013.
6. Yreux, E., Hillman, M. "An arbitrary order variationally consistent domain integration method for galerkin thin plate analysis," 12th US National Congress of Computational Mechanics, Raleigh, North Carolina, July 22-25, 2013.
7. Hillman, M., "Implicit upwind reproducing kernel particle method for convection dominated problems," 11th US National Congress on Computational Mechanics, Minneapolis, Minnesota, July 25-28, 2011.
8. Hillman, M., Lin, S. P. "Computational mechanics for earth moving simulation," UCLA Henry Samueli School of Engineering and Applied Science Tech Forum, Los Angeles, California, March 1, 2011.

### **Professional Service**

#### **Conferences Committees**

1. Member, International Scientific Committee, 2021 Engineering Mechanics Institute Conference, Virtual, May 25–28, 2021
2. Member, Technical Committee, Workshop on Meshfree Method and Advances in Computational Mechanics, Pleasanton, California, March 10–12, 2019
3. Member, Scientific Committee, 18th United States Congress for Theoretical and Applied Mechanics, Chicago, Illinois, June 4–9, 2018
4. Member, International Scientific Committee, 2018 Engineering Mechanics Institute Conference, Cambridge, Massachusetts, May 29 – June 1, 2018

5. Member, Scientific Organizing Committee, Meshfree and Particle Methods: Applications and Theory, Santa Fe, New Mexico, September 10–12, 2018
6. Member, Scientific Committee, Computations Subcommittee, 18th U.S. National Congress for Theoretical and Applied Mechanics, Chicago, Illinois, June 4–9, 2018
7. Member, International Scientific Committee, 2017 Engineering Mechanics Institute Conference, La Jolla, California, June 4–7, 2017
8. Member, Scientific Committee, USACM Conference on Isogeometric Analysis and Meshfree Methods, La Jolla, California, October 10–12, 2016

### **Organizing Minisymposia**

1. Invited Session Organizer, "Extreme Events," Meshfree and Novel Finite Elements with Applications, Berkeley, California, September 25–27, 2022
2. Session Organizer, "Simulation-based Disaster Prediction and Mitigation," 15th World Congress in Computational Mechanics, Yokohama, Japan, July 31–August 5, 2022
3. Invited Topic Organizer, "Recent Advances and Applications in Meshfree and Particle Methods," 2021 International Mechanical Engineering Congress and Exposition, Virtual, November 1–5, 2021
4. Invited Session Organizer, "Meshfree, Peridynamics, and Particle Methods: Contemporary Methods and Applications," 16th International Conference on Computational Plasticity, Barcelona, Spain, September 7–10, 2021
5. Session Organizer, "Recent Advances and Applications in Meshfree and Particle Methods," 16th US National Congress of Computational Mechanics, Virtual, July 25–29, 2021
6. Session Organizer, "Meshfree, Peridynamic, and Particle Methods: Contemporary Methods and Applications," 2021 Engineering Mechanics Institute Conference, Virtual, May 25–28, 2021
7. Session Organizer, "Advances and Application of Meshfree and Particle Methods," 14th World Congress in Computational Mechanics, Virtual, January 11–15, 2021
8. Session Organizer, "Computational Modeling of Natural and Manmade Disasters," 14th World Congress in Computational Mechanics, Virtual, January 11–15, 2021
9. Invited Topic Organizer, "Recent Advances and Applications in Meshfree and Particle Methods," 2020 International Mechanical Engineering Congress and Exposition, Virtual, November 16–19, 2020
10. Topic Organizer, "Recent Advances and Applications in Meshfree and Particle Methods," 2019 International Mechanical Engineering Congress and Exposition, Salt Lake City, Utah, November 11–14, 2019
11. Session Organizer, "Meshfree, Particle, and Peridynamic Methods," 15th International Conference on Computational Plasticity, Barcelona, Spain, September 3–5, 2019
12. Session Organizer, "Advances and Applications in Meshfree and Particle Methods," 15th US National Congress of Computational Mechanics, Austin, Texas, July 28–August 1, 2019
13. Session Organizer, "Meshfree, Peridynamics, and Particle Methods: Contemporary Methods and Applications," 2019 Engineering Mechanics Institute Conference, Pasadena, California, June 18–21, 2019
14. Session Organizer, "Robust, Adaptive, High-Resolution Methods For Unsteady Flows," 20th International Conference on Fluid Flow Problems, Chicago, Illinois, March 31–April 3, 2019
15. Session Organizer, "Recent Advances and Applications in Meshfree and Particle Methods," 2018 International Mechanical Engineering Congress and Exposition, Pittsburgh, Pennsylvania, November 9–15, 2018
16. Session Organizer, "New Trends in Extreme Events Modeling," 13th World Congress in Computational Mechanics, New York, New York, July 22–27, 2018

17. Invited Focus Area Organizer, "Penetration and Perforation," Meshfree and Particle Methods: Applications and Theory, Santa Fe, New Mexico, September 10–12, 2018
18. Session Organizer, "Meshfree, Peridynamics, and Particle Methods: Contemporary Methods and Applications," 2018 Engineering Mechanics Institute Conference, Cambridge, Massachusetts, May 29–June 1, 2018
19. Session Organizer, "Simulation, Prediction, and Mitigation of Extreme Events," 2018 Engineering Mechanics Institute Conference, Cambridge, Massachusetts, May 29–June 1, 2018
20. Session Organizer, "Meshfree and Particle Methods: New Developments and Applications," 14th US National Congress of Computational Mechanics, Montréal, Québec, Canada, July 17–20, 2017
21. Session Organizer, "Extreme Event Modeling," 2017 Engineering Mechanics Institute Conference, La Jolla, California, June 4–7, 2017
22. Invited Session Organizer, "Quadrature and Stability Issues in IGA and Meshfree Methods," US-ACM Conference on Isogeometric Analysis and Meshfree Methods, La Jolla, California, October 10–12, 2016

### **Professional Committees**

1. Elected Member, United States Association for Computational Mechanics Technical Thrust Area on Novel Methods in Computational Engineering & Sciences (2019–present)
2. Elected Member, Engineering Mechanics Institute Computational Mechanics Technical Committee (2016–present)

### **Editorial Service**

1. Associate Editor, Computer Modeling in Engineering and Sciences (2020–present)
2. Editorial Board, Science Progress (2019–present)
3. Guest Editor, Computational Particle Mechanics, Thematic Issue, Meshfree and Particle Methods for Modeling Extreme Loadings (2019)
4. Editorial Board, Frontiers in Built Environment, Computational Methods in Structural Engineering Specialty Section (2018–present)

### **Peer Review of Manuscripts**

1. Reviewer, Computational Mechanics (10)
2. Reviewer, Computer Methods in Applied Mechanics and Engineering (5)
3. Reviewer, International Journal for Numerical Methods in Engineering (5)
4. Reviewer, Journal of Engineering Mechanics (3)
5. Reviewer, Finite Elements in Analysis and Design (1)
6. Reviewer, Computers and Geotechnics (1)

### **Peer Review of Grant Proposals**

1. Reviewer, The National Science Foundation (1 panel)
2. Reviewer, The Research Grants Council of Hong Kong (2 proposals)

### **Memberships**

1. American Society of Civil Engineers, Central Pennsylvania (2016–present)
2. Engineering Mechanics Institute (2016–present)
3. International Association of Computational Mechanics (2014–present)
4. United States Association of Computational Mechanics (2013–present)
5. American Society of Civil Engineers (2008–present)

## **University Service**

### **Department**

1. Member, Graduate Program Committee (2020–present)

2. Member, Civil and Environmental Engineering Seminar Series Committee (2019–2020)
3. Chair, Research Innovation Committee (2019–2020)
4. Chair, Civil and Environmental Engineering Seminar Series Committee (2017–2019)
5. Member, Faculty Search Committee (2016, 2017, 2019)
6. Chair, PhD Qualifying Exam Committee (2017–present)
7. Member, PhD Candidacy Exam Committee (2016)

#### **College**

1. Chair, College of Engineering Research Computing Committee (2018–2020)
2. Member, College of Engineering Research Computing Committee (2017–2018)

#### **University**

1. Member, Institute for Computational and Data Sciences 2020 Symposium Planning Committee (2019–2020)
2. Member, Research Computing and Cyberinfrastructure Advisory Council (2018–present)
3. Member, Institute for Computational and Data Sciences Coordinating Committee (2017–present)

#### **Memberships**

1. Associate Member, Institute for CyberScience (2017–present)
2. Member, Fluid Dynamics Research Consortium (2016–present)



# Generalized reproducing kernel peridynamics: unification of local and non-local meshfree methods, non-local derivative operations, and an arbitrary-order state-based peridynamic formulation

Michael Hillman<sup>1</sup> · Marco Pasetto<sup>2</sup> · Guohua Zhou<sup>3</sup>

Received: 3 June 2019 / Revised: 3 July 2019 / Accepted: 5 July 2019  
© The Author(s) 2019

## Abstract

State-based peridynamics is a non-local reformulation of solid mechanics that replaces the force density of the divergence of stress with an integral of the action of force states on bonds local to a given position, which precludes differentiation with the aim to model strong discontinuities effortlessly. A popular implementation is a meshfree formulation where the integral is discretized by quadrature points, which results in a series of unknowns at the points under the strong-form collocation framework. In this work, the meshfree discretization of state-based peridynamics under the correspondence principle is examined and compared to traditional meshfree methods based on the classical local formulation of solid mechanics. It is first shown that the way in which the peridynamic formulation approximates differentiation can be unified with the implicit gradient approximation, and this is termed the reproducing kernel peridynamic approximation. This allows the construction of non-local deformation gradients with arbitrary-order accuracy, as well as non-local approximations of higher-order derivatives. A high-order accurate non-local divergence of stress is then proposed to replace the force density in the original state-based peridynamics, in order to obtain global arbitrary-order accuracy in the numerical solution. These two operators used in conjunction with one another is termed the reproducing kernel peridynamic method. The strong-form collocation version of the method is tested against benchmark solutions to examine and verify the high-order accuracy and convergence properties of the method. The method is shown to exhibit superconvergent behavior in the nodal collocation setting.

**Keywords** Meshfree methods · Peridynamics · Reproducing kernel · Non-local derivatives · High-order

## 1 Introduction

Meshfree methods for continuum mechanics can generally be cast under two formulations: Galerkin meshfree methods and collocation meshfree methods [1]. Among these, the governing equations solved under these frameworks can also be different. On one branch, there are meshfree discretizations of the classical local model, namely the differential equation for linear momentum. Using the

Galerkin formulation with a meshfree discretization of this equation results in methods such as the diffuse element method [2], the element free Galerkin method [3], the reproducing kernel particle method [4, 5], and the many methods that ensued thereafter [6–13]. On the other hand, due to the global smoothness that can easily be attained with meshfree approximations, collocation of the strong form is straightforward, and several methods using this technique have been proposed starting with radial basis functions [14, 15], and later with the reproducing kernel and moving least squares approximations [16–18], among others.

Recently, a non-local reformulation of continuum mechanics has been proposed [19, 20] called peridynamics, in order to circumvent difficulties in treating discontinuities in the local models, first under a bond-based framework [19], and later under the so-called state-based framework

---

✉ Michael Hillman  
mhillman@psu.edu

<sup>1</sup> The Pennsylvania State University, University Park, PA, USA

<sup>2</sup> University of California, San Diego, La Jolla, CA, USA

<sup>3</sup> Optimal Inc., Plymouth, MI, USA

[20]. This theory replaces the differentiation in classical continuum mechanics, i.e., the force density of the divergence of stress, with an integral of the actions of bonds to a given position, and admits discontinuities by precluding derivatives in the governing equations. In addition, the action is considered over a finite distance, embedding a length scale in the governing equations, resulting in a formulation which is non-local in nature. While the peridynamic equations can be solved under the Galerkin formulation [21, 22], this approach requires evaluation of a double (six-dimensional) integral [23], which results in considerable computational expense. Therefore, for practical applications, the strong form version is often employed. Due to the simplicity of its implementation and relatively low-computational cost, the peridynamic strong form equations are generally solved by a node-based meshfree approach [24], which is based on nodal collocation and nodal discretization of the integral terms in the peridynamic equations. In this meshfree approach, the unknowns are therefore associated with the nodal points, which are both collocation and quadrature points, similar to smoothed particle hydrodynamics [25, 26]. In this paper, discussions are focused on the collocation meshfree implementation of the state-based version under the correspondence principle [20], which constructs a non-local deformation gradient to facilitate the use of classical constitutive models, and is most closely related to meshfree discretizations of local models as first shown in [27] for uniform discretizations and infinite domains. In particular, the main focus of this study is the accuracy and convergence properties of the state-based peridynamic method, and enhancement thereof.

Theoretical analysis of the accuracy and convergence of local meshfree methods is well established, for instance see [28–31] for Galerkin analysis, and [18, 32–35] for collocation analysis. Sufficiently smooth problems solved with monomial basis vectors exhibit algebraic convergence in both strong formulations [35], and weak formulations [29], while global approximations such as radial basis show exponential convergence [33]. In particular, Galerkin meshfree methods with  $n$ th monomial completeness exhibit a rate of  $n + 1$  in the displacement solution. On the other hand, meshfree collocation approaches exhibit a rate of  $n + 1$  for a least-squares formulation using more collocation points than source points (approximation functions) [18], while using an equal number of source and collocation points exhibits an *odd–even phenomenon* where the rate of  $n$  is obtained for even orders, and  $n - 1$  for odd orders [17, 36–38], which has also been observed in isogeometric collocation [39, 40]. A recently developed recursive gradient formulation [37] has been developed that exhibits *superconvergence*, that is, rates of  $n$  and  $n + 1$  for even and odd orders of approximations,

respectively. Notably this allows linear basis to converge in collocation analysis, in contrast to direct gradients [18]. Finally, it should be noted that the accuracy of numerical integration in the weak-form based versions can heavily influence theoretical rates [41], although several approaches are available to rectify this situation (the interested reader is referred to [1] and references therein for details).

For peridynamics, the concept of convergence can be understood in several ways; see [42, 43] for details: (1)  $N$ -convergence, when the non-locality of the continuous peridynamic problem is kept fixed while the discretization is refined (convergence to the non-local continuum solution); (2)  $\delta$ -convergence, when the nonlocality is reduced for a fixed discretization (convergence to the discrete local solution); or (3)  $N$ - $\delta$  convergence, when both discretization and nonlocality approach the vanishing limit simultaneously (convergence to the continuum local solution). In this work, the third type of convergence is studied. It has been noted that this type of convergence is linked to the concept of asymptotic compatibility, with discretizations being asymptotically compatible if they converge to the correct local model and solution associated with the nonlocal model [43, 44].

The accuracy and convergence properties of state-based peridynamics has been studied in several works. Material models play an important role in convergence study of peridynamics since the results using different models converge to different solutions [45]. In [45], three different material models were tested to attempt to reproduce the solution of static linear elasticity. Among these, only the deformation gradient-based model [20] gave a convergent solution to all problems tested, with a first-order convergence rate in the  $L_2$  error norm.

The effect of numerical integration in the non-local integrals has also been a focus in studies, as it may also have a strong effect on convergence in peridynamics [46–50]. In the first meshfree implementation of peridynamics [24], the peridynamic equation of motion was discretized by nodal integration with the full physical nodal volume as the integration weight, resulting in the so-called full volume (FV) integration. The FV integration shows erratic convergence behavior, both converging and diverging with refinement [46, 51]. Several studies suggest this issue is due to rough approximation of the integration weights near the edges of the integration domains in the peridynamic equations [46–49]. So-called partial volume (PV) integration schemes have been proposed, including approximate PV [47, 48] and analytical PV [49], to more accurately compute the partial volumes intersecting with neighborhoods that serve as integration weights for particles. Partial volume schemes have been shown to improve the accuracy and yield more consistent convergence rates compared with the FV integration [46]. Influence functions

that smoothly decay to zero at the boundary of the horizon have also been investigated under the FV integration framework, and it has been shown that this enhances the accuracy and can also give more consistent convergence behavior [46]. The idea behind smoothly decaying influence functions is to reduce the influence of the particles near the neighborhood boundary, mitigating the error due to numerical integration. These techniques exhibit first-order convergence in displacements [46]. The limitation of first-order convergence was attributed in [50] to the piecewise constant nature of the approximation employed, where the reproducing kernel approximation was introduced in the peridynamic displacement field to increase the convergence rate. However, high-order Gauss integration was employed to achieve the integration accuracy necessary to avoid the aforementioned oscillatory convergence behavior, resulting in an increased computational cost. A high-order non-local deformation gradient was proposed in [52] for stability reasons, but was limited to uniform discretizations, and meanwhile the convergence properties of this method were not tested.

Taking another point of view, the non-local deformation gradient and force density in state-based peridynamics under the correspondence principle can be viewed as mathematical operators with certain approximation properties. In [27, 53] it was shown that for uniform discretizations away from the boundary, the accuracy in the non-local deformation gradient is second-order. This is confirmed by other studies, where it has been further shown that near the boundary the accuracy will be first-order [52, 54].

The precise relationship between the meshfree peridynamic method and the classical meshfree methods discussed has not been made clear. So far, one effort [27] has attempted to examine the relationship between the peridynamic approximation of derivatives via the non-local deformation gradient and the traditional meshfree approximation of derivatives. There it was shown that the state-based peridynamic formulation based on correspondence is equivalent to employing a second-order accurate implicit gradient reproducing kernel approximation [55], for both the deformation gradient operation on displacement, and force density operation on the stress, but this equivalence was established only for uniform discretizations, away from a boundary. However, this relationship also implies that these operations are both second-order accurate, at least in uniform discretizations, and away from the influence of a boundary.

In this paper, the precise relationship between meshfree methods for local models and non-local peridynamic meshfree discretizations under the correspondence principle is introduced, for general non-uniform discretizations,

and finite domains. A generalized approximation which unifies these approaches is introduced termed *the reproducing kernel peridynamic approximation*, under both continuous (integral form) and discrete frameworks. It is shown that this approximation can yield four distinct cases: implicit gradients, the traditional non-local deformation gradient, as well as an arbitrary-order accurate non-local deformation gradient, and arbitrary-order accurate non-local higher-order derivatives. A formulation is then proposed called the reproducing kernel peridynamic (RKPD) method, consisting of the high-order accurate non-local deformation gradients, in conjunction with a high-order accurate force density, which results in an arbitrary-order accurate state-based peridynamic method. The formulation is tested under the node-based collocation framework, although a weak formulation is also possible. In contrast to the original formulation, the method is shown to exhibit convergent solutions with and without ghost boundary nodes, under both uniform and nonuniform discretizations, with superconvergent solutions for odd orders of accuracy.

The remainder of this paper is organized as follows. In Sect. 2, the governing equations for classical local methods and state-based peridynamics are briefly reviewed. The integral forms for the reproducing kernel and implicit gradient approximation are given in Sect. 3, and compared with the integral forms of the state-based peridynamic equations. In addition, the equivalence of implicit gradients and the peridynamic differential operator [56] is established. These formulations are then compared and contrasted, and the orders of accuracy are assessed. In Sect. 4, the continuous reproducing kernel peridynamic approximation is given, which unifies the two formulations, and provides arbitrary-order accurate non-local deformation gradients, and arbitrary-order accurate higher-order non-local derivative approximations. The discrete implicit gradient and peridynamic approximations are then discussed and compared in Sect. 5, with the order of accuracy in the discrete case assessed. Section 6 introduces the discrete reproducing kernel peridynamic approximation. The collocation implementation of the proposed formulation, the reproducing kernel peridynamic method, is then summarized in Sect. 7, and numerical examples are given in Sect. 8. Conclusions, and discussions on implications and possible future work are given in Sect. 9.

## 2 Governing equations

In this section, the governing equations for classical continuum mechanics and state-based peridynamics under the correspondence principle are briefly reviewed.

## 2.1 Classical continuum mechanics

The equation of motion for finite-strain continuum mechanics problems stated in the reference configuration  $\Omega$  at material position  $\mathbf{X}$  at time  $t$  is

$$\ddot{\mathbf{u}}(\mathbf{X}, t)\rho(\mathbf{X}) = \nabla \cdot \boldsymbol{\sigma}^T(\mathbf{X}, t) + \mathbf{b}(\mathbf{X}, t) \quad (1)$$

where  $\ddot{\mathbf{u}} \equiv D\mathbf{v}/Dt$  is the material time derivative of the velocity  $\mathbf{v}$ ,  $\rho$  is the material density in the undeformed configuration,  $\boldsymbol{\sigma}$  is the 1st Piola–Kirchhoff (PK) stress tensor ( $\boldsymbol{\sigma}^T$  is the nominal stress),  $\nabla$  denotes the del operator with respect to the undeformed configuration, and  $\mathbf{b}$  is the body force in the undeformed configuration. In this work a Lagrangian description is adopted, as state-based peridynamics under correspondence relates the 1st PK stress to the force density in the governing equations [20].

Given a strain energy density function  $W(\mathbf{F})$ , kinetic variables such as the first 1st PK stress  $\boldsymbol{\sigma}$  can be obtained as  $\boldsymbol{\sigma} = \partial W(\mathbf{F})/\partial \mathbf{F}$ . In state-based peridynamics, an analogous relationship exists between the kinematic and kinetic entities, as described in the next section.

## 2.2 State-based peridynamics

In order to deal with discontinuities, peridynamics [19, 20] has been introduced which precludes the differentiation involved in the governing equations for classical continuum mechanics (1). In state-based peridynamics, the force density of the divergence of nominal stress in (1) is replaced by an integral of force states  $\underline{\mathbf{T}}$  [20]:

$$\ddot{\mathbf{u}}(\mathbf{X}, t)\rho(\mathbf{X}) = \int_{\mathcal{H}_x} \underline{\mathbf{T}}[\mathbf{X}, t]\langle \mathbf{X}' - \mathbf{X} \rangle - \underline{\mathbf{T}}[\mathbf{X}', t]\langle \mathbf{X} - \mathbf{X}' \rangle d\mathbf{X}' + \mathbf{b}(\mathbf{X}, t) \quad (2)$$

where  $\mathcal{H}_x$  is the so-called neighborhood of the particle  $\mathbf{X}$ , which is often defined by a sphere encompassing the point

$\mathbf{X}$  with radius  $\delta$  called the *horizon*, as shown in Fig. 1. The notation employed for the mathematical entity of states is that angle brackets denote the operation on that variable, while square brackets denote the dependence on the variable.

A fundamental kinetic entity is the *force state*  $\underline{\mathbf{T}}(\cdot)$ , rather than for instance, the 1st PK stress in the Lagrangian formulation of classical solid mechanics. The quantity  $\mathbf{X}' - \mathbf{X}$  is said to be a “bond” of the points  $\mathbf{X}'$  and  $\mathbf{X}$ . Thus, it can be seen when comparing (1) to (2) that the force density of the divergence of stress is replaced by an integral of the action of states  $\underline{\mathbf{T}}$  on bonds local to  $\mathbf{X}$ .

A fundamental kinematic entity in peridynamics is the deformation state  $\underline{\mathbf{Y}}(\cdot)$  which maps (possibly nonlinearly and discontinuously) a bond in the undeformed configuration  $\mathbf{X}' - \mathbf{X}$ , to a bond in the current configuration  $\mathbf{x}' - \mathbf{x}$ , as shown in Fig. 1:

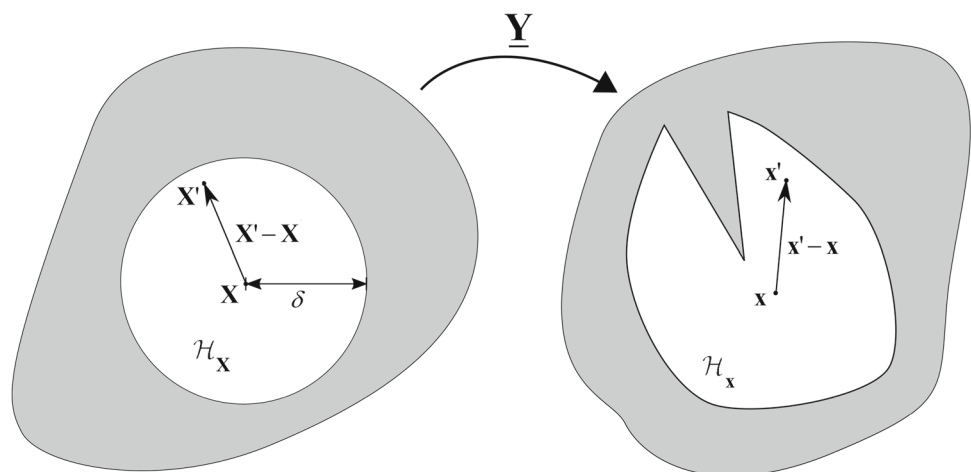
$$\underline{\mathbf{Y}}(\mathbf{X}' - \mathbf{X}) = \mathbf{x}' - \mathbf{x}. \quad (3)$$

Analogous to the dependence of stress measures on strain measures in classical mechanics, the force state  $\underline{\mathbf{T}}$  depends on the deformation state. On the other hand, in order to facilitate the use of constitutive models in the local theory, a non-local deformation gradient  $\mathcal{F}$  can be obtained through a principle called *reduction* [20], which is briefly reviewed in Sect. 3.5. The 1st PK stress can be obtained via  $\mathcal{F}$ , and can then be related to the force state  $\underline{\mathbf{T}}$  by means of energy principles.

## 3 Continuous reproducing kernel and peridynamic approximations

As will be demonstrated, the implicit gradient counterpart [36, 55, 57, 58] to the reproducing kernel (RK) approximation [4, 5] is most closely related to the non-local deformation gradient employed in peridynamics. In this section, the continuous (integral) form of the reproducing

**Fig. 1** Peridynamic continuum in undeformed (left) and deformed configuration (right)



kernel and peridynamic approximations are analyzed and compared. A brief review of both is given. The continuous versions must be discretized in practice; the discrete versions will be analyzed and compared in Sect. 5. Remarkably, if the quadrature and discretizations are consistent with one another, the main results of these analyses are the same, with minor exceptions.

### 3.1 Continuous reproducing kernel approximation

The continuous RK approximation of a function  $u(\mathbf{x})$  on a domain  $\Omega \subset \mathbb{R}^d$  is constructed by the product of a kernel function  $\Phi_a$  with compact support, and a correction function composed of a linear combination of basis functions in the following form [4, 5]:

$$\begin{aligned} u(\mathbf{x}) &\simeq \mathcal{R}_{[n]} \{u(\mathbf{x})\} \\ &= \int_{\Omega} \mathbf{H}^T(\mathbf{x}' - \mathbf{x}) \mathbf{b}(\mathbf{x}) \Phi_a(\mathbf{x}' - \mathbf{x}) u(\mathbf{x}') d\mathbf{x}' \end{aligned} \quad (4)$$

where  $\mathbf{H}(\mathbf{x})$  is a column vector of complete  $n$ th order monomials (although other bases could be employed), and  $\mathbf{b}(\mathbf{x})$  is a column vector of associated coefficients to be determined. The dependence of these vectors in the RK approximation on the free parameter  $n$  is to be understood herein for notational simplicity.

It should be noted that, in much of the literature, the shifted basis term  $\mathbf{x} - \mathbf{x}'$  is employed, while here the basis using  $\mathbf{x}' - \mathbf{x}$  is employed in order to unify the reproducing kernel approximation and peridynamic derivative approximation later in the text. The choice is arbitrary, and only results in sign differences in gradient reproducing conditions.

The kernel function  $\Phi_a$  has compact support with measure  $a$ , and the smoothness of the approximation is inherited from the kernel. For example, using  $C^2$  kernels yields  $C^2$  continuity of the approximation. In this work, the cubic B-spline kernel is employed for kernel functions and influence functions, which play the analogous role in peridynamics as discussed in Sect. 3.5. The one-dimensional cubic B-spline kernel shown in Fig. 2 is constructed as:

$$\Phi_a(z) = \begin{cases} \frac{2}{3} - 4z^2 + 4z^3 & \text{for } 0 \leq z \leq \frac{1}{2} \\ \frac{4}{3} - 4z + 4z^2 - \frac{4}{3}z^3 & \text{for } \frac{1}{2} \leq z \leq 1 \\ 0 & \text{otherwise} \end{cases} \quad (5)$$

$$z \equiv \frac{|x' - x|}{a}.$$

In multiple dimensions, one may construct a kernel by tensor product yielding a box or cuboid support:

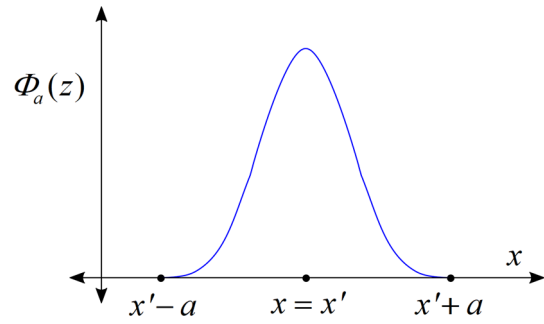


Fig. 2 Kernel function  $\Phi_a(z)$

$$\Phi_a(\mathbf{x}' - \mathbf{x}) = \prod_{i=1}^d \Phi_{a_i}(x'_i - x_i), \quad (6)$$

or by defining  $\Phi_a(\mathbf{x}' - \mathbf{x}) = \Phi_a(z)$  with  $z = |\mathbf{x}' - \mathbf{x}|/a$ , yielding a spherical support.

When monomials are employed for  $\mathbf{H}(\mathbf{x})$ , the coefficients  $\mathbf{b}(\mathbf{x})$  are determined by enforcing  $n$ th order accuracy of the approximation in (4). This can be achieved by directly enforcing the so-called reproducing conditions (discussed later), or by using a Taylor expansion. In this work, the latter approach is employed in order to fully illustrate the meaning and construction of an implicit gradient. The Taylor series expansion of  $u(\mathbf{x}')$  around  $\mathbf{x}$  truncated to order  $n$  is:

$$u(\mathbf{x}') \simeq \sum_{|\alpha|=0}^n \frac{1}{\alpha!} (\mathbf{x}' - \mathbf{x})^\alpha \partial^\alpha u(\mathbf{x}) \quad (7)$$

where  $\alpha = (\alpha_1, \dots, \alpha_d)$  is a multi-index in  $\mathbb{R}^d$  of non-negative integers equipped with the notation  $|\alpha| = \alpha_1 + \dots + \alpha_d$ ,  $\alpha! = \alpha_1! \dots \alpha_d!$ ,  $\mathbf{x}^\alpha = x_1^{\alpha_1} \dots x_d^{\alpha_d}$ , and  $\partial^\alpha = \partial^{\alpha_1} \dots \partial^{\alpha_d} / \partial x_1^{\alpha_1} \dots \partial x_d^{\alpha_d}$ .

In matrix form (7) can be expressed as:

$$u(\mathbf{x}') = \mathbf{D}(\mathbf{x}) \mathbf{J} \mathbf{H}(\mathbf{x}' - \mathbf{x}) \quad (8)$$

where  $\mathbf{D}(\mathbf{x})$  is a row vector of  $\{\partial^\beta u(\mathbf{x})\}_{|\beta|=0}^n$  and  $\mathbf{J}$  is a diagonal matrix with entries  $\{1/\beta!\}_{|\beta|=0}^n$ . Substituting (8) into (4) yields

$$\mathcal{R}_{[n]} \{u(\mathbf{x})\} = \mathbf{D}(\mathbf{x}) \mathbf{J} \int_{\Omega} \mathbf{H}(\mathbf{x}' - \mathbf{x}) \mathbf{H}^T(\mathbf{x}' - \mathbf{x}) \mathbf{b}(\mathbf{x}) \Phi_a(\mathbf{x}' - \mathbf{x}) d\mathbf{x}' \quad (9)$$

The  $n$ th order accuracy of the approximation requires that  $\mathcal{R}_{[n]} \{u(\mathbf{x})\} = u(\mathbf{x})$  in the above. Examining (9), this can be phrased as the following vanishing moment conditions:

$$\int_{\Omega} \mathbf{H}(\mathbf{x}' - \mathbf{x}) \mathbf{H}^T(\mathbf{x}' - \mathbf{x}) \mathbf{b}(\mathbf{x}) \Phi_a(\mathbf{x}' - \mathbf{x}) d\mathbf{x}' = \mathbf{H}(\mathbf{0}) \quad (10)$$

where the fact that  $\{1/\beta!\}_{|\beta|=0} = 1$  has been employed. Solving for  $\mathbf{b}(\mathbf{x})$  from (10), the continuous RK approximation is obtained as

$$\begin{aligned}\mathcal{R}_{[n]} \{u(\mathbf{x})\} &= \int_{\Omega} \mathbf{H}(\mathbf{0})^T \mathbf{M}^{-1}(\mathbf{x}) \mathbf{H}(\mathbf{x}' - \mathbf{x}) \Phi_a(\mathbf{x}' - \mathbf{x}) u(\mathbf{x}') d\mathbf{x}' \\ &\equiv \int_{\Omega} \Psi(\mathbf{x}; \mathbf{x}' - \mathbf{x}) u(\mathbf{x}') d\mathbf{x}'\end{aligned}\quad (11)$$

where  $\Psi(\mathbf{x}; \mathbf{x}' - \mathbf{x})$  is the  $n$ th order continuous reproducing kernel function with the dependency on  $a$  and  $n$  implied, and

$$\mathbf{M}(\mathbf{x}) = \int_{\Omega} \mathbf{H}(\mathbf{x}' - \mathbf{x}) \mathbf{H}^T(\mathbf{x}' - \mathbf{x}) \Phi_a(\mathbf{x}' - \mathbf{x}) d\mathbf{x}' \quad (12)$$

is the so-called *moment matrix*. In arriving at (11) the symmetry of  $\mathbf{M}$  was employed, although it is not necessary to construct the approximation.

In addition to  $n$ th order accuracy, the approximation can be shown to satisfy the following equivalent *reproducing conditions*:

$$\begin{aligned}\mathcal{R}_{[n]} \{\mathbf{H}(\mathbf{x})\} &= \mathbf{H}(\mathbf{x}) \\ \text{or} \\ \int_{\Omega} \Psi(\mathbf{x}; \mathbf{x}' - \mathbf{x}) \mathbf{H}(\mathbf{x}') d\mathbf{x}' &= \mathbf{H}(\mathbf{x})\end{aligned}\quad (13)$$

which is often employed as the condition (for better conditioning of the moment matrix):

$$\int_{\Omega} \Psi(\mathbf{x}; \mathbf{x}' - \mathbf{x}) \mathbf{H}(\mathbf{x}' - \mathbf{x}) d\mathbf{x}' = \mathbf{H}(\mathbf{0}). \quad (14)$$

As previously mentioned, it can be seen that the reproducing kernel approximation (11) can also be obtained by directly imposing the reproducing conditions (14) with the construction in (4).

### 3.2 Continuous implicit gradient

An implicit gradient directly approximates the derivative  $\partial^\alpha u(\mathbf{x})$  of a function  $u(\mathbf{x})$  for some fixed  $\alpha$  in the same form of the reproducing kernel [55, 57]:

$$\partial^\alpha u \simeq \mathcal{D}_{[n]}^{(\alpha)} \{u(\mathbf{x})\} = \int_{\Omega} \mathbf{H}^T(\mathbf{x}' - \mathbf{x}) \mathbf{b}^{(\alpha)}(\mathbf{x}) \Phi_a(\mathbf{x}' - \mathbf{x}) u(\mathbf{x}') d\mathbf{x}' \quad (15)$$

where the notation of multi-indices with parenthesis ( $\alpha$ ) is introduced to indicate evaluation with a fixed value of  $\alpha$  and to distinguish between terms of the form  $\mathbf{x}^\alpha$ . Substitution of the Taylor series expansion in (8) into (15) yields

$$\mathcal{D}_{[n]}^{(\alpha)} \{u(\mathbf{x})\} = \mathbf{D}(\mathbf{x}) \mathbf{J} \int_{\Omega} \mathbf{H}(\mathbf{x}' - \mathbf{x}) \mathbf{H}^T(\mathbf{x}' - \mathbf{x}) \mathbf{b}^{(\alpha)}(\mathbf{x}) \Phi_a(\mathbf{x}' - \mathbf{x}) d\mathbf{x}'. \quad (16)$$

The condition to reproduce the gradient  $\partial^\alpha u$  up to  $n$ th order accuracy can be expressed as all moments vanishing except the moment corresponding to  $\alpha$ , that is, requiring  $\mathcal{D}_{[n]}^{(\alpha)} \{u(\mathbf{x})\} = \partial^\alpha u(\mathbf{x})$  for some given  $\alpha$ , which can be expressed as:

$$\int_{\Omega} \mathbf{H}(\mathbf{x}' - \mathbf{x}) \mathbf{H}^T(\mathbf{x}' - \mathbf{x}) \mathbf{b}^{(\alpha)}(\mathbf{x}) \Phi_a(\mathbf{x}' - \mathbf{x}) d\mathbf{x}' = \mathbf{H}^{(\alpha)} \quad (17)$$

where  $\mathbf{H}^{(\alpha)}$  is a column vector of  $\{\alpha! \delta_{\alpha\beta}\}_{|\beta|=0}^n$  (emanating from  $\mathbf{J}^{-1}$ ):

$$\mathbf{H}^{(\alpha)} = [0, \dots, 0, \underset{\substack{\uparrow \\ \alpha \text{ position}}}{\alpha!}, 0, \dots, 0]^T. \quad (18)$$

To make the multi-index notation clear, consider  $\mathbf{H}(\mathbf{x})$  and  $\mathbf{H}^{(\alpha)}$  in the construction of  $\mathcal{D}_{[n]}^{(\alpha)} \{u(\mathbf{x})\}$  in two dimensions with  $n = 2$ , and  $\alpha = (1, 0)$ , that is, to approximate first order derivatives with respect to  $x_1$  with second-order accuracy:

$$\begin{aligned}\mathbf{H}(\mathbf{x}) &= [1, x_1, x_2, x_1^2, x_1 x_2, x_2^2]^T, \\ \mathbf{H}^{(1,0)} &= [0, 1, 0, 0, 0, 0]^T.\end{aligned}\quad (19)$$

Solving for  $\mathbf{b}^{(\alpha)}$  from (17), the continuous implicit gradient approximation for  $\partial^\alpha u(\mathbf{x})$  is obtained as

$$\begin{aligned}\mathcal{D}_{[n]}^{(\alpha)} \{u(\mathbf{x})\} &= \int_{\Omega} [\mathbf{H}^{(\alpha)}]^T \mathbf{M}^{-1}(\mathbf{x}) \mathbf{H}(\mathbf{x}' - \mathbf{x}) \Phi_a(\mathbf{x}' - \mathbf{x}) u(\mathbf{x}') d\mathbf{x}' \\ &\equiv \int_{\Omega} \Psi^{(\alpha)}(\mathbf{x}; \mathbf{x}' - \mathbf{x}) u(\mathbf{x}') d\mathbf{x}'\end{aligned}\quad (20)$$

where again the symmetry of  $\mathbf{M}$  has been employed. From the above, it can be seen that the RK approximation (11) can be considered a special case of (20) with  $|\alpha| = 0$ , i.e.,  $\Psi^{(0,0,0)} = \Psi$  which has been observed in the early history of meshfree methods [57, 59]. This also demonstrates that since a simple change of  $\mathbf{H}(\mathbf{0})$  to  $\mathbf{H}^{(\alpha)}$  can approximate derivatives, the matrix  $\mathbf{M}(\mathbf{x})$  contains information about derivatives as well as the function itself, and provides an efficient way to obtain derivative approximations rather than direct differentiation of (11), for which the cost is not trivial [35]. This fact has been leveraged for solving partial differential equations more efficiently than using direct differentiation [36, 60].

In addition, the implicit gradient approximation has been utilized for strain regularization to avoid ambiguous boundary conditions [55], avoid differentiation in stabilization for convection dominated problems [58], among other applications [60], and historically, the implicit gradient has in fact been widely used (in its discrete form) to solve partial differential equations: the generalized finite difference method [61], synchronized derivatives [57], as well as the pioneering work of the diffuse element method [2] all utilize approximations which are essentially coincident with the implicit gradient (for details, see [1]). Finally as will be discussed in Sect. 3.3, the so-called peridynamic differential operator [56] is also the implicit gradient approximation with the selection of the same bases and weighting functions.

Analogous to the RK approximation, the implicit gradient can be shown to satisfy the following *gradient reproducing conditions* [55]:

$$\int_{\Omega} \Psi^{(\alpha)}(\mathbf{x}; \mathbf{x}' - \mathbf{x}) \mathbf{H}(\mathbf{x}') d\mathbf{x}' = \partial^{\alpha} \mathbf{H}(\mathbf{x}). \tag{21}$$

Or equivalently,

$$\int_{\Omega} \Psi^{(\alpha)}(\mathbf{x}; \mathbf{x}' - \mathbf{x}) \mathbf{H}(\mathbf{x}' - \mathbf{x}) d\mathbf{x}' = \mathbf{H}^{(\alpha)}. \tag{22}$$

Similar to the reproducing kernel approximation, it can be seen that the implicit gradient approximation (20) can be also obtained by directly imposing (22) on the approximation (15).

### 3.3 Equivalence of the peridynamic differential operator and the implicit gradient

In this section, the implicit gradient approximation reviewed in Sect. 3.2, and the peridynamic differential operator introduced in [56] are compared.

Let us start by recasting the implicit gradient from (15) as:

$$\partial^{\alpha} u = \mathcal{D}_{[n]}^{(\alpha)} \{u(\mathbf{x})\} = \int_{H_a} \hat{\Phi}_a(\mathbf{x}; \mathbf{x}' - \mathbf{x}) u(\mathbf{x}') d\mathbf{x}', \tag{23}$$

where  $\hat{\Phi}_a$  represents the corrected kernel function:

$$\hat{\Phi}_a(\mathbf{x}; \mathbf{x}' - \mathbf{x}) = \hat{\mathbf{H}}^T(\mathbf{x}' - \mathbf{x}) \mathbf{b}^{(\alpha)}(\mathbf{x}) \Phi_a(\mathbf{x}' - \mathbf{x}) \tag{24}$$

and  $H_a$  is the kernel support, i.e., the portion of the domain where  $\Phi_a(\mathbf{x}' - \mathbf{x})$  is non-zero. Note that  $\hat{\mathbf{H}} = \mathbf{H}$  in (15), that is, monomial bases of order  $n$  are employed, while here  $\hat{\mathbf{H}}$  is used to indicate that a generic basis vector can be employed.

Directly imposing the condition of gradient reproduction (22) on (23) can be written as

$$\int_{H_a} \mathbf{H}(\mathbf{x}' - \mathbf{x}) \hat{\Phi}_a(\mathbf{x}; \mathbf{x}' - \mathbf{x}) d\mathbf{x}' = \mathbf{H}^{(\alpha)}, \tag{25}$$

which is, for  $0 \leq |\beta| \leq n$ ,

$$\int_{H_a} (\mathbf{x}' - \mathbf{x})^{\beta} \hat{\Phi}_a(\mathbf{x}; \mathbf{x}' - \mathbf{x}) d\mathbf{x}' = \alpha! \delta_{\alpha\beta}. \tag{26}$$

Also, from (26) we get the following system:

$$\left\{ \int_{H_a} \mathbf{H}(\mathbf{x}' - \mathbf{x}) \hat{\mathbf{H}}^T(\mathbf{x}' - \mathbf{x}) \Phi_a(\mathbf{x}' - \mathbf{x}) d\mathbf{x}' \right\} \mathbf{b}^{(\alpha)}(\mathbf{x}) = \mathbf{H}^{(\alpha)}, \tag{27}$$

or

$$\hat{\mathbf{M}}(\mathbf{x}) \mathbf{b}^{(\alpha)}(\mathbf{x}) = \mathbf{H}^{(\alpha)}, \tag{28}$$

where  $\hat{\mathbf{M}}(\mathbf{x}) = \int_{H_a} \mathbf{H}(\mathbf{x}' - \mathbf{x}) \hat{\mathbf{H}}^T(\mathbf{x}' - \mathbf{x}) \Phi_a(\mathbf{x}' - \mathbf{x}) d\mathbf{x}'$ , which, when we select the basis vector  $\hat{\mathbf{H}}$  to be  $\mathbf{H}$ , becomes the moment matrix employed in Sects. 3.1 and 3.2, and leads to the construction in (20).

Consider now the peridynamic differential operator introduced in [56]. A Taylor expansion of a function  $f(\mathbf{x})$  is first considered:

$$f(\mathbf{x} + \xi) = \sum_{n_1=0}^n \sum_{n_2=0}^{n-n_1} \dots \sum_{n_d=0}^{n-n_1-\dots-n_{d-1}} \frac{1}{n_1! n_2! \dots n_d!} \xi_1^{n_1} \xi_2^{n_2} \dots \xi_d^{n_d} \frac{\partial^{n_1+n_2+\dots+n_d} f(\mathbf{x})}{\partial x_1^{n_1} \partial x_2^{n_2} \dots \partial x_d^{n_d}} + R(n, \mathbf{x}), \tag{29}$$

where  $\xi = \mathbf{x}' - \mathbf{x}$  and the remainder  $R(n, \mathbf{x})$  is considered negligible.

The main idea of the peridynamic differential operator is to define orthogonal functions  $g_n^{p_1 p_2 \dots p_d}(\xi)$ , where  $p_i$ , is akin to  $\alpha_i$  (i.e.,  $p$  and  $\alpha$  are the same), and represents the order of differentiation with respect to  $x_i$ , with  $i = 1, \dots, d$ , such that the following gradient reproducing conditions are imposed:

$$\begin{aligned} \partial^p f &= \int_{H_x} f(\mathbf{x} + \xi) g_n^{p_1 p_2 \dots p_d}(\xi) dV \\ &= \int_{H_x} f(\mathbf{x}') g_n^{p_1 p_2 \dots p_d}(\mathbf{x}' - \mathbf{x}) d\mathbf{x}', \end{aligned} \tag{30}$$

where  $\partial^p f = \frac{\partial^{p_1 p_2 \dots p_d} f(\mathbf{x})}{\partial x_1^{p_1} \partial x_2^{p_2} \dots \partial x_d^{p_d}}$ , for some fixed  $p = (p_1, p_2, \dots, p_d)$ , and  $H_x$  is the peridynamic neighbourhood of  $\mathbf{x}$ .

By comparing (23) of the implicit gradient and (30) of the peridynamic differential operator we see that they both

aim at reproducing derivatives of a function of  $\mathbf{x}$  through a convolution by finding an appropriate kernel function. In fact:

- $H_{\mathbf{x}}$  in (30) is the same as  $H_a$  in (23), as long as the RK kernel support and peridynamic neighbourhood coincide
- $f(\mathbf{x})$  in (30) is  $u(\mathbf{x})$  in (23): they both represent a generic function of  $\mathbf{x}$
- $g_n^{p_1 p_2 \dots p_d}(\mathbf{x}' - \mathbf{x})$  in (30) plays the role of  $\hat{\Phi}_a(\mathbf{x}; \mathbf{x}' - \mathbf{x})$  in (23).

The functions  $g_n^{p_1 p_2 \dots p_d}(\xi)$  are found by imposing satisfaction of the following orthogonality property:

$$\frac{1}{n_1! n_2! \dots n_d!} \int_{H_{\mathbf{x}}} \xi_1^{n_1} \xi_2^{n_2} \dots \xi_d^{n_d} g_n^{p_1 p_2 \dots p_d}(\xi) dV \tag{31}$$

$$= \delta_{n_1 p_1} \delta_{n_2 p_2} \dots \delta_{n_{d-1} p_{d-1}} \delta_{n_d p_d},$$

that is, using the notation introduced in Sect. 3.2,

$$\int_{H_{\mathbf{x}}} (\mathbf{x}' - \mathbf{x})^{\tilde{n}} g_n^p(\mathbf{x}' - \mathbf{x}) d\mathbf{x}' = \tilde{n}! \delta_{\tilde{n} p}, \tag{32}$$

where  $\tilde{n} = (n_1, n_2, \dots, n_d)$ . This is the same condition that is imposed on the corrected kernel  $\hat{\Phi}_a(\mathbf{x}; \mathbf{x}' - \mathbf{x})$  of the RK implicit gradient (26). Therefore, if  $\hat{\Phi}_a(\mathbf{x}; \mathbf{x}' - \mathbf{x}) = g_n^{p_1 p_2 \dots p_d}(\mathbf{x}' - \mathbf{x})$  then the reproducing kernel implicit gradient and the peridynamic differential operator coincide. In [56]  $g_n^p(\mathbf{x}' - \mathbf{x})$  is defined as:

$$g_n^p(\mathbf{x}' - \mathbf{x}) = \sum_{q_1=0}^n \sum_{q_2=0}^{n-q_1} \dots \sum_{q_d=0}^{n-q_1 \dots -q_{d-1}} a_{q_1 q_2 \dots q_d}^{p_1 p_2 \dots p_d} w_{q_1 q_2 \dots q_d}(|\mathbf{x}' - \mathbf{x}|) (x'_1 - x_1)^{q_1} \dots (x'_d - x_d)^{q_d}, \tag{33}$$

which can be rewritten as:

$$g_n^p(\mathbf{x}' - \mathbf{x}) = \tilde{\mathbf{H}}^T(\mathbf{x}' - \mathbf{x}) \mathbf{a}^{(p)}, \tag{34}$$

where  $\tilde{\mathbf{H}}(\mathbf{x}' - \mathbf{x})$  is a column vector of  $\{w_q(\mathbf{x}' - \mathbf{x})^q\}_{|q|=0}^n$  and, for a given  $p$ ,  $\mathbf{a}^{(p)}$  is a column vector of unknown coefficients  $\{a_q^{(p)}\}_{|q|=0}^n$ . For example, in two dimensions ( $d = 2$ ):

$$\tilde{\mathbf{H}}^T(\mathbf{x}' - \mathbf{x}) = [w_{00}, w_{10}(x'_1 - x_1), w_{01}(x'_2 - x_2), \dots, w_{n0}(x'_1 - x_1)^n, w_{0n}(x'_2 - x_2)^n], \tag{35}$$

$$\mathbf{a}^{(p)} = [a_{00}^{p_1 p_2}, a_{10}^{p_1 p_2}, a_{01}^{p_1 p_2}, \dots, a_{n0}^{p_1 p_2}, a_{0n}^{p_1 p_2}]. \tag{36}$$

By comparing (34) and (24) we notice that the definitions of  $\hat{\Phi}_a(\mathbf{x}; \mathbf{x}' - \mathbf{x})$  and  $g_n^{p_1 p_2 \dots p_d}(\mathbf{x}' - \mathbf{x})$  are analogous:

both are the product of a weighted basis vector ( $\hat{\mathbf{H}}^T(\mathbf{x}' - \mathbf{x})\Phi_a(\mathbf{x}' - \mathbf{x})$  in (24) and  $\tilde{\mathbf{H}}^T(\mathbf{x}' - \mathbf{x})$  in (34), respectively) and unknown coefficients to be determined (i.e.,  $\mathbf{b}^{(\alpha)}(\mathbf{x})$  and  $\mathbf{a}^{(p)}$ ). It is therefore clear that, if the same weighted basis vectors are selected, the two are the same, meaning that the RK implicit gradient and the peridynamic differential operator are the same operator. For example, to select the same weighted basis vectors:

- Due to the arbitrariness of the choice of basis, one can select  $\hat{\mathbf{H}}^T(\mathbf{x}' - \mathbf{x})$  and  $\Phi_a(\mathbf{x}' - \mathbf{x})$  in the RK implicit gradient so that  $\hat{\mathbf{H}}^T(\mathbf{x}' - \mathbf{x})\Phi_a(\mathbf{x}' - \mathbf{x}) = \tilde{\mathbf{H}}^T(\mathbf{x}' - \mathbf{x})$
- If  $w_{q_1 q_2 \dots q_d}(|\mathbf{x}' - \mathbf{x}|)$  is chosen so that  $w_{q_1 q_2 \dots q_d}(|\mathbf{x}' - \mathbf{x}|) = w(|\mathbf{x}' - \mathbf{x}|)$  [56], then  $\tilde{\mathbf{H}}^T(\mathbf{x}' - \mathbf{x}) = w(|\mathbf{x}' - \mathbf{x}|)\mathbf{H}^T(\mathbf{x}' - \mathbf{x})$ . Therefore, by selecting  $\hat{\mathbf{H}}^T(\mathbf{x}' - \mathbf{x}) = \mathbf{H}^T(\mathbf{x}' - \mathbf{x})$  as in Sect. 3.2, and choosing  $\Phi_a(\mathbf{x}' - \mathbf{x}) = w(|\mathbf{x}' - \mathbf{x}|)$ , the same weighted basis vector is employed.

Now, the unknown coefficients of the peridynamic differential operator are found by substituting the definition of  $g_n^p(\mathbf{x}' - \mathbf{x})$  [see (34)] into (32):

$$\int_{H_{\mathbf{x}}} (\mathbf{x}' - \mathbf{x})^{\tilde{n}} \tilde{\mathbf{H}}^T(\mathbf{x}' - \mathbf{x}) \mathbf{a}^{(p)}(\mathbf{x}) d\mathbf{x}' = \tilde{n}! \delta_{\tilde{n} p}, \tag{37}$$

which, for some given  $p$  and for  $0 \leq |\tilde{n}| \leq n$ , leads to

$$\left\{ \int_{H_{\mathbf{x}}} \mathbf{H}(\mathbf{x}' - \mathbf{x}) \tilde{\mathbf{H}}^T(\mathbf{x}' - \mathbf{x}) d\mathbf{x}' \right\} \mathbf{a}^{(p)} = \tilde{\mathbf{b}}_n^p, \tag{38}$$

or

$$\mathbf{A} \mathbf{a}^{(p)} = \tilde{\mathbf{b}}_n^p, \tag{39}$$

where  $\tilde{\mathbf{b}}_n^p$  is a column vector  $\{\tilde{n}! \delta_{\tilde{n} p}\}_{|\tilde{n}|=0}^n$  and  $\mathbf{A} = \int_{H_{\mathbf{x}}} \mathbf{H}(\mathbf{x}' - \mathbf{x}) \tilde{\mathbf{H}}^T(\mathbf{x}' - \mathbf{x}) d\mathbf{x}'$  [56]. Again, we can see that for a given gradient to be reproduced, if the same weighted basis vector is chosen (i.e.,  $\hat{\mathbf{H}}^T(\mathbf{x}' - \mathbf{x})\Phi_a(\mathbf{x}' - \mathbf{x}) = \tilde{\mathbf{H}}^T(\mathbf{x}' - \mathbf{x})$ ), then (38) and (39), and (27) and (28) are the same, respectively, and this leads to  $\mathbf{b}^{(\alpha)}(\mathbf{x}) = \hat{\mathbf{M}}^{-1}(\mathbf{x})\mathbf{H}^{(\alpha)} = \mathbf{A}^{-1}\tilde{\mathbf{b}}_n^p = \mathbf{a}^{(p)}$  when  $\alpha = p$ . Now, (39) is for reproducing the gradient  $\partial^p f$  for a given  $p$ . Since  $\mathbf{A}$  is independent of  $p$ , the equations associated with reproducing gradients  $\partial^p f$  for  $0 \leq |p| \leq n$  can be combined [56]. For example, in the two-dimensional case we can write

$$\mathbf{A} \mathbf{a} = \tilde{\mathbf{b}}, \tag{40}$$

where

$$\mathbf{a} = [\mathbf{a}^{(00)}, \mathbf{a}^{(10)}, \mathbf{a}^{(01)}, \mathbf{a}^{(20)}, \dots, \mathbf{a}^{(0n)}], \tag{41}$$

and

$$\tilde{\mathbf{b}} = [\tilde{\mathbf{b}}^{(00)}, \tilde{\mathbf{b}}^{(10)}, \tilde{\mathbf{b}}^{(01)}, \tilde{\mathbf{b}}^{(20)}, \dots, \tilde{\mathbf{b}}^{(0n)}]. \tag{42}$$

In conclusion we have shown, even though the peridynamic differential operator represents arbitrary derivatives of functions through a convolution over the peridynamic neighbourhood, while the RK implicit gradient performs it over the RK kernel support, the two operators and the idea behind them, i.e., correcting a convolution operator using a weighted basis vector to obtain gradients, are the same.

### 3.4 Deformation gradient under continuous implicit gradients

We now return to the analysis and comparison of the implicit gradient and the way in which state-based peridynamics constructs the non-local deformation gradient. In the Lagrangian RK approximation [62], shape functions are constructed with reference to the material coordinate  $\mathbf{X}$ , and the approximation to displacement  $\mathbf{u}^h$  is constructed as:

$$\mathbf{u}^h(\mathbf{X}, t) \simeq \mathcal{R}_{[n]} \{ \mathbf{u}(\mathbf{X}, t) \} = \int_{\Omega} \Psi(\mathbf{X}; \mathbf{X}' - \mathbf{X}) \mathbf{u}(\mathbf{X}', t) d\mathbf{X}'. \tag{43}$$

For simplicity, the dependence of these constructions on  $t$  will be implied for other expressions. The deformation gradient  $\mathbf{F}$  is the gradient of the motion of the body  $\mathbf{x} = \varphi(\mathbf{x}, t)$  and is constructed as

$$F_{ij}(\mathbf{X}) = I_{ij} + \frac{\partial u_i^h(\mathbf{X})}{\partial X_j} \tag{44}$$

where  $\mathbf{I}$  is the identity tensor. If implicit gradients (20) are employed under the Lagrangian formulation, the deformation is approximated in the material coordinate as

$$F_{ij}(\mathbf{X}) = I_{ij} + \int_{\Omega} [\mathbf{H}_j^{\nabla}]^T \mathbf{M}^{-1}(\mathbf{X}) \mathbf{H}(\mathbf{X}' - \mathbf{X}) \Phi_a(\mathbf{X}' - \mathbf{X}) u_i(\mathbf{X}') d\mathbf{X}' \tag{45}$$

where  $\mathbf{H}_j^{\nabla} = [0, \delta_{1j}, \delta_{2j}, \delta_{3j}, 0, \dots, 0]$  corresponds to the case of  $\mathbf{H}^{(\alpha)}$  with  $|\alpha| = 1$ , for approximating first order derivatives with respect to  $X_j$ , i.e.:

$$\mathbf{H}_j^{\nabla} = [0, \dots, 0, \underset{\substack{\uparrow \\ (j+1)th \text{ position}}}{1}, \dots, 0]^T. \tag{46}$$

From the derivation by the Taylor expansion in Sect. 3.2, it can be inferred (or directly shown) that the deformation

gradient constructed by implicit gradients possess  $n$ th order accuracy (or  $n$ th order consistency) without additional analysis needed.

### 3.5 Deformation gradient under continuous peridynamics

To relate the theory of peridynamics to classical continuum mechanics and provide the ability to employ conventional constitutive models, a principle called *reduction* can be employed [20] to relate the kinematic entity of the state  $\underline{\mathbf{Y}}$  to a non-local version of a deformation gradient  $\mathcal{F}$ , which yields

$$\mathcal{F}(\underline{\mathbf{Y}}) = \mathbf{S} \cdot \mathbf{K}^{-1} \tag{47}$$

where  $\mathbf{K}$  is the *reference shape tensor*

$$\mathbf{K}(\mathbf{X}) = \int_{\mathcal{H}_x} w_{\delta}(\mathbf{X}' - \mathbf{X})(\mathbf{X}' - \mathbf{X}) \otimes (\mathbf{X}' - \mathbf{X}) d\mathbf{X}' \tag{48}$$

that describes the undeformed configuration around the point  $\mathbf{X}$ , and  $\mathbf{S}$  is the *deformed shape tensor*

$$\mathbf{S}(\mathbf{X}) = \int_{\mathcal{H}_x} w_{\delta}(\mathbf{X}' - \mathbf{X})(\mathbf{x}' - \mathbf{x}) \otimes (\mathbf{X}' - \mathbf{X}) d\mathbf{X}' \tag{49}$$

which describes the deformed configuration around the point  $\mathbf{X}$ . In the above, the function  $w_{\delta}(\mathbf{X}' - \mathbf{X})$  is called the *influence function*, which has compact support with measure  $\delta$ . Thus the influence function in the non-local deformation gradient plays a closely analogous role to the kernel function in the construction of the deformation gradient by the implicit gradient (45), since both control the locality of the approximation of deformation.

With  $\mathcal{F}$  in hand, the associated stress is calculated as in classical continuum mechanics, and is then related to the force state  $\underline{\mathbf{T}}$ , which will be discussed in Sect. 4.3.

### 3.6 Analysis of the continuous peridynamic deformation gradient

We next examine the properties of the nonlocal deformation gradient  $\mathcal{F}$ . First, considering that the displacement  $\mathbf{u} = \mathbf{x} - \mathbf{X}$ , using the definition of the deformation state  $\underline{\mathbf{Y}}(\mathbf{X}' - \mathbf{X}) = \mathbf{x}' - \mathbf{x}$  and the reference position state  $\underline{\mathbf{X}}(\mathbf{X}' - \mathbf{X}) = \mathbf{X}' - \mathbf{X}$ , the deformed shape tensor  $\mathbf{S}$  can be expressed as:

$$\begin{aligned} \mathbf{S}(\mathbf{X}) &= \int_{\mathcal{H}_x} w_{\delta}(\mathbf{X}' - \mathbf{X}) ((\mathbf{X}' + \mathbf{u}(\mathbf{X}')) - (\mathbf{X} + \mathbf{u}(\mathbf{X}))) \otimes (\mathbf{X}' - \mathbf{X}) d\mathbf{X}' \\ &= \mathbf{K}(\mathbf{X}) + \int_{\mathcal{H}_x} w_{\delta}(\mathbf{X}' - \mathbf{X}) (\mathbf{u}(\mathbf{X}') - \mathbf{u}(\mathbf{X})) \otimes (\mathbf{X}' - \mathbf{X}) d\mathbf{X}'. \end{aligned} \tag{50}$$

Using (50), the non-local deformation gradient (47) can then be expressed as

$$\begin{aligned} \mathbf{S}(\mathbf{X}) &= \int_{\mathcal{H}_X} w_\delta(\mathbf{X}' - \mathbf{X})((\mathbf{X}' + \mathbf{u}(\mathbf{X}')) - (\mathbf{X} + \mathbf{u}(\mathbf{X}))) \otimes (\mathbf{X}' - \mathbf{X}) d\mathbf{X}' \\ &= \mathbf{K}(\mathbf{X}) + \int_{\mathcal{H}_X} w_\delta(\mathbf{X}' - \mathbf{X})(\mathbf{u}(\mathbf{X}') - \mathbf{u}(\mathbf{X})) \otimes (\mathbf{X}' - \mathbf{X}) d\mathbf{X}'. \end{aligned} \tag{51}$$

In component form, the above is,

$$\mathcal{F}_{ij}(\mathbf{X}) = I_{ij} + \int_{\mathcal{H}_X} w_\delta(\mathbf{X}' - \mathbf{X})(u_i(\mathbf{X}') - u_i(\mathbf{X}))(X'_m - X_m)K_{mj}^{-1}(\mathbf{X}) d\mathbf{X}'. \tag{52}$$

A Taylor expansion on  $u_i(\mathbf{X}')$  gives, after some algebra,

$$\begin{aligned} \mathcal{F}_{ij}(\mathbf{X}) &= I_{ij} + \frac{\partial u_i(\mathbf{X})}{\partial X_j} \\ &+ \frac{\partial^2 u_i(\mathbf{X})}{\partial X_k \partial X_l} \frac{1}{2} \int_{\mathcal{H}_X} w_\delta(\mathbf{X}' - \mathbf{X})(X'_k - X_k)(X'_l - X_l) \\ &\times (X'_m - X_m)K_{mj}^{-1} d\mathbf{X}' \\ &+ \frac{\partial^3 u_i(\mathbf{X})}{\partial X_k \partial X_l \partial X_n} \frac{1}{6} \int_{\mathcal{H}_X} w_\delta(\mathbf{X}' - \mathbf{X})(X'_k - X_k) \\ &\times (X'_l - X_l)(X'_n - X_n)(X'_m - X_m)K_{mj}^{-1} d\mathbf{X}' \\ &+ O(\delta^3). \end{aligned} \tag{53}$$

Since the fourth term is an even function about  $\mathbf{X}$  for symmetric functions  $w_\delta$ , we have the following truncation error for the continuous non-local deformation gradient:

$$\begin{aligned} \mathcal{F}_{ij}(\mathbf{X}) &= I_{ij} + \frac{\partial u_i(\mathbf{X})}{\partial X_j} \\ &+ \frac{\partial^2 u_i(\mathbf{X})}{\partial X_k \partial X_l} \frac{1}{2} \int_{\mathcal{H}_X} w_\delta(\mathbf{X}' - \mathbf{X})(X'_k - X_k) \\ &\times (X'_l - X_l)(X'_m - X_m)K_{mj}^{-1} d\mathbf{X}' + O(\delta^2). \end{aligned} \tag{54}$$

When the neighborhood  $\mathcal{H}_X$  and influence function  $w_\delta(\mathbf{X}' - \mathbf{X})$  are centred around  $\mathbf{X}$  and symmetric about each axis (as in the case of spherically-shaped influence functions that are purely a function of  $|\mathbf{X}' - \mathbf{X}|$ ), away from the influence of the boundary of the domain (maintaining a perfectly spherical neighborhood) the third term on the right-hand-side vanishes when integrated, since it is then an odd function centred around  $\mathbf{X}$  and thus

$$\mathcal{F}_{ij}(\mathbf{X}) = I_{ij} + \frac{\partial u_i(\mathbf{X})}{\partial X_j} + O(\delta^2) \tag{55}$$

and the continuous form of the non-local deformation gradient in peridynamics is second-order accurate.

Near the boundary of the domain, or in the case that the shape of  $\mathcal{H}_X$  or the influence function  $w_\delta(\mathbf{X}' - \mathbf{X})$  is not symmetric about each axis, the third term does not vanish, and we have:

$$\mathcal{F}_{ij}(\mathbf{X}) = I_{ij} + \frac{\partial u_i(\mathbf{X})}{\partial X_j} + O(\delta) \tag{56}$$

and the continuous non-local deformation gradient is first-order accurate. Thus in finite domains where the neighborhood is not symmetric near the boundary, and in a general case of arbitrary influence functions and neighborhood definitions, the continuous non-local deformation gradient is globally first-order accurate.

### 3.7 Comparison between continuous implicit gradients and peridynamics

In [27], it was shown that in the interior of a domain (away from the boundary, or in an infinite domain) with uniformly discretized state-based peridynamics using the correspondence principle, the discretized non-local deformation gradient (47) is equivalent to employing a local deformation gradient by the discretized form of implicit gradients (45). However, it will be demonstrated that in the general case, this is not true for both the discretized form and continuous form.

In order to facilitate a more general comparison between the non-local deformation gradient by peridynamics and the RK approximation, we first express the shape tensors (49) in matrix form:

$$\mathbf{K}(\mathbf{X}) = \int_{\mathcal{H}_X} w_\delta(\mathbf{X}' - \mathbf{X})\mathbf{P}(\mathbf{X}' - \mathbf{X})\mathbf{P}^T(\mathbf{X}' - \mathbf{X}) d\mathbf{X}' \tag{57}$$

where  $\mathbf{P}(\mathbf{X}) \equiv [X_1 \ X_2 \ X_3]^T$  can be considered a type of “basis vector” consisting of monomials of order one. When the shape tensor is expressed this way, it is immediately apparent that it is coincident with the Lagrangian RK moment matrix with  $a = \delta$ ,  $\Phi_a(\mathbf{X} - \mathbf{X}') = w_\delta(\mathbf{X} - \mathbf{X}')$ , and linear basis, but omitting the unity term in the RK basis vector  $\mathbf{H}(\mathbf{X})$ . More discussion on this point will follow later in the text.

The deformed shape tensor can also be expressed in matrix form as

$$\mathbf{S}(\mathbf{X}) = \int_{\mathcal{H}_X} w_\delta(\mathbf{X}' - \mathbf{X})\mathbf{P}(\mathbf{x}(\mathbf{X}') - \mathbf{x}(\mathbf{X}))\mathbf{P}^T(\mathbf{X}' - \mathbf{X}) d\mathbf{X}'. \tag{58}$$

Noting that  $\mathbf{P}(\mathbf{x}(\mathbf{X}') - \mathbf{x}(\mathbf{X})) = \mathbf{P}(\mathbf{X}' - \mathbf{X}) + (\mathbf{u}(\mathbf{X}') - \mathbf{u}(\mathbf{X}))$  we have

$$\begin{aligned} \mathbf{S}(\mathbf{X}) &= \mathbf{K}(\mathbf{X}) \\ &+ \int_{\mathcal{H}_X} w_\delta(\mathbf{X}-\mathbf{X}')(\mathbf{u}(\mathbf{X}') - \mathbf{u}(\mathbf{X}))\mathbf{P}^T(\mathbf{X}' - \mathbf{X})d\mathbf{X}' \end{aligned} \quad (59)$$

so that

$$\begin{aligned} \mathcal{F}(\mathbf{X}) &= \mathbf{S}(\mathbf{X})\mathbf{K}^{-1}(\mathbf{X}) \\ &= \left( \mathbf{K}(\mathbf{X}) + \int_{\mathcal{H}_X} w_\delta(\mathbf{X}' - \mathbf{X})(\mathbf{u}(\mathbf{X}') - \mathbf{u}(\mathbf{X}))\mathbf{P}^T(\mathbf{X}' - \mathbf{X})d\mathbf{X}' \right) \mathbf{K}^{-1}(\mathbf{X}) \\ &= \mathbf{I} + \int_{\mathcal{H}_X} w_\delta(\mathbf{X}' - \mathbf{X})(\mathbf{u}(\mathbf{X}') - \mathbf{u}(\mathbf{X}))\mathbf{P}^T(\mathbf{X}' - \mathbf{X})\mathbf{K}^{-1}(\mathbf{X})d\mathbf{X}'. \end{aligned} \quad (60)$$

Introducing a vector  $\mathbf{P}_j^\nabla = [\delta_{1j}, \delta_{2j}, \delta_{3j}]$  and using the symmetry of  $\mathbf{K}$ , the expression (60) can be recast in indicial notation as:

$$\begin{aligned} \mathcal{F}_{ij}(\mathbf{X}) &= I_{ij} + \int_{\mathcal{H}_X} \left( \mathbf{P}_j^\nabla \right)^T \mathbf{K}^{-1}(\mathbf{X})\mathbf{P}(\mathbf{X}' - \mathbf{X})w_\delta(\mathbf{X}' - \mathbf{X}) \\ &\quad \times (u_i(\mathbf{X}') - u_i(\mathbf{X}))d\mathbf{X}'. \end{aligned} \quad (61)$$

For comparison, the local deformation gradient  $F_{ij}$  calculated by implicit gradients (45) with  $a = \delta$ , and  $\Phi_a(\mathbf{X} - \mathbf{X}') = w_\delta(\mathbf{X} - \mathbf{X}')$  can be expressed as:

$$F_{ij}(\mathbf{X}) = I_{ij} + \int_{\mathcal{H}_X} \left( \mathbf{H}_j^\nabla \right)^T \mathbf{M}^{-1}(\mathbf{X})\mathbf{H}(\mathbf{X}' - \mathbf{X})w_\delta(\mathbf{X}' - \mathbf{X})u_i(\mathbf{X}')d\mathbf{X}'. \quad (62)$$

Thus, the implicit gradient can be viewed as a type of non-local operation with length-scale  $a$ , which is not surprising since it approximates differentiation by integration, just like the non-local deformation gradient in peridynamics (see [27] for additional discussions). Two key differences can be observed however. One is that the “basis” in peridynamics  $\mathbf{P}(\mathbf{X})$  omits the unity term in  $\mathbf{H}(\mathbf{X})$ . If  $\mathbf{P}(\mathbf{X})$  were to be employed in the implicit gradient approximation (20), partition of nullity [the completeness condition for 0th order accuracy in (13)] would not be able to be satisfied. This fact however seems to be “compensated for” in the peridynamic gradient by the convolution with  $u_i(\mathbf{X}') - u_i(\mathbf{X})$  rather than  $u_i(\mathbf{X}')$  alone. That is, if  $\mathbf{u} = \text{constant}$  then the non-local deformation gradient (61) yields the correct result of  $\mathcal{F}_{ij} = I_{ij}$  (0th order accuracy). Thus it can be seen that the form (61) is inherently first-order accurate, and in special cases, as has been demonstrated, is second-order accurate.

Another interesting point is that in examining (61), the non-local peridynamic calculation of a gradient uses values of  $\mathbf{u}$  near  $\mathbf{X}$ , except the actual value at  $\mathbf{X}$ , while the implicit gradient still uses the value of  $\mathbf{u}$  at  $\mathbf{X}$ . Thus one could

interpret the peridynamic operation “more non-local” versus the implicit gradient approximation. Indeed, when  $\mathbf{X}' = \mathbf{X}$  in (61), the peridynamic “kernel” in the convolution also vanishes since  $\mathbf{P}$  only contains first-order monomials.

Finally, it should be emphasised that the deformation gradient by implicit gradients, and the non-local deformation gradient by peridynamics, are clearly not the same. In [27] however, an equivalence was established in the special case of a uniform discretization, and away from the influence of the boundary.

## 4 Continuous reproducing kernel peridynamic approximation

In this section, the continuous reproducing kernel peridynamic approximation is presented, which unifies the way in which state-based peridynamics under correspondence approximates gradients, and the implicit gradient approximation. The unification also provides two other distinct cases which will be discussed.

### 4.1 Continuous reproducing kernel peridynamic approximation

The convolution operations for the approximation of the gradient of a function in (61) and (62) can be unified as follows. First, consider a kernel estimate of the type (15) with a basis of monomials from order  $m$  to  $n$  to estimate gradients of a scalar field  $u(\mathbf{X})$ , with the convolution of  $u(\mathbf{X}') - u(\mathbf{X})$  rather than  $u(\mathbf{X}')$  as in (15), and a general weighting function  $\omega_l$  with measure  $l$ :

$$\begin{aligned} \bar{\mathcal{D}}_{[n]}^{(x)}\{u(\mathbf{X})\} &= \int_{\Omega} \mathbf{Q}_{[m,n]}^T(\mathbf{X}' - \mathbf{X})\bar{\mathbf{b}}^{(x)}(\mathbf{X})\omega_l(\mathbf{X}' - \mathbf{X})(u(\mathbf{X}') - u(\mathbf{X}))d\mathbf{X}' \\ &\equiv \int_{\Omega} \bar{\Psi}_{[m,n]}^{(x)}(\mathbf{X};\mathbf{X}' - \mathbf{X})(u(\mathbf{X}') - u(\mathbf{X}))d\mathbf{X}' \end{aligned} \quad (63)$$

where  $\mathbf{Q}_{[m,n]}(\mathbf{X})$  is a column vector of the set of monomials  $\{\mathbf{X}^\beta\}_{|\beta|=m}^n$ , and the dependency of the operator on  $m$  and  $l$  is implied for notational simplicity. To facilitate  $n$ th order accuracy in this approximation, taking the Taylor expansion on  $u(\mathbf{X}')$  in (7) yields:

$$\begin{aligned} \bar{\mathcal{D}}_{[n]}^{(x)}\{u(\mathbf{X})\} &= \bar{\mathbf{D}}(\mathbf{X})\bar{\mathbf{J}} \int_{\Omega} \mathbf{Q}_{[1,n]}(\mathbf{X}' - \mathbf{X}) \\ &\quad \times \mathbf{Q}_{[m,n]}^T(\mathbf{X}' - \mathbf{X})\bar{\mathbf{b}}^{(x)}(\mathbf{X})\omega_l(\mathbf{X}' - \mathbf{X})d\mathbf{X}' \end{aligned} \quad (64)$$

where  $\bar{\mathbf{D}}(\mathbf{X})$  is a row vector of  $\{\partial^\beta u(\mathbf{X})\}_{|\beta|=1}^n$  and  $\bar{\mathbf{J}}$  is a diagonal matrix with entries  $\{1/\beta!\}_{|\beta|=1}^n$ . Examining (64), it

is apparent that in order to reproduce gradients  $\bar{\mathcal{D}}_{[n]}^{(\alpha)}\{u(\mathbf{X})\} = \partial^\alpha u(\mathbf{X})$  up to  $n$ th order accuracy, we have the following vanishing moment conditions:

$$\int_{\Omega} \mathbf{Q}_{[1,n]}(\mathbf{X}' - \mathbf{X}) \mathbf{Q}_{[m,n]}^T(\mathbf{X}' - \mathbf{X}) \bar{\mathbf{b}}^{(\alpha)}(\mathbf{X}) \omega_l(\mathbf{X}' - \mathbf{X}) d\mathbf{X}' = \mathbf{Q}_{[1,n]}^{(\alpha)} \quad (65)$$

where  $\mathbf{Q}_{[m,n]}^{(\alpha)}$  is a column vector of  $\{\alpha! \delta_{\alpha\beta}\}_{|\beta|=m}^n$ :

$$\mathbf{Q}_{[m,n]}^{(\alpha)} = \begin{bmatrix} 0, & \dots, & 0, & \alpha!, & 0, & \dots, & 0 \end{bmatrix}^T. \quad (66)$$

$\uparrow$   
 $\alpha$  position

If  $m = 1$ , then the system in (65) has a unique solution. Alternatively, if  $m = 0$  and  $n > 0$  the system is underdetermined and an additional condition is required for determining  $\bar{\mathbf{b}}^{(\alpha)}$ .

Consider also imposing the partition of nullity on (63) in the case of  $m = 0$  and  $n > 0$ , that is, in addition to (65), the following is imposed:

$$\int_{\Omega} \bar{\Psi}_{[m,n]}^{(\alpha)}(\mathbf{X}; \mathbf{X}' - \mathbf{X}) d\mathbf{X}' = 0, \quad m = 0, \quad n > 0. \quad (67)$$

The system (65) can then be recast with (67) in hand to yield a determined system for all free variables:

$$\bar{\mathbf{M}}_{[m,n]}(\mathbf{X}) \bar{\mathbf{b}}^{(\alpha)}(\mathbf{X}) = \mathbf{Q}_{[m,n]}^{(\alpha)} \quad (68)$$

where

$$\bar{\mathbf{M}}_{[m,n]}(\mathbf{X}) = \int_{\Omega} \mathbf{Q}_{[m,n]}(\mathbf{X}' - \mathbf{X}) \mathbf{Q}_{[m,n]}^T(\mathbf{X}' - \mathbf{X}) \omega_l(\mathbf{X}' - \mathbf{X}) d\mathbf{X}'. \quad (69)$$

A unified approximation is finally obtained by solving for  $\bar{\mathbf{b}}^{(\alpha)}$  from (68) and substituting into (63):

$$\bar{\mathcal{D}}_{[n]}^{(\alpha)}\{u(\mathbf{X})\} = \int_{\Omega} \left( \mathbf{Q}_{[m,n]}^{(\alpha)} \right)^T \bar{\mathbf{M}}_{[m,n]}^{-1}(\mathbf{X}) \mathbf{Q}_{[m,n]}(\mathbf{X}' - \mathbf{X}) \times \omega_l(\mathbf{X}' - \mathbf{X}) (u(\mathbf{X}') - u(\mathbf{X})) d\mathbf{X}'. \quad (70)$$

The approximation in (70) for derivatives is termed the *continuous reproducing kernel peridynamic approximation* herein. The selection of possible values of  $\omega_l$ ,  $|\alpha|$ ,  $n$  and  $m$ , yield the implicit gradient approximation, as well as the manner in which the deformation gradient is approximated by peridynamics. In addition, two more approximations can be obtained which are termed the *continuous  $n$ th order non-local deformation gradient*, and *continuous  $n$ th order non-local higher-order derivatives*, enumerated as follows:

1. When  $|\alpha| > 0$ ,  $m = 0$ ,  $\omega_l = \Phi_a$  and  $n$  is a free variable, (70) yields the implicit gradient approximation (20), since  $\mathbf{Q}_{[0,n]}(\mathbf{X}) = \mathbf{H}(\mathbf{X})$  and  $\mathbf{Q}_{[0,n]}^{(\alpha)}(\mathbf{X}) = \mathbf{H}^{(\alpha)}$ , and further if  $m = 0$ , then partition of nullity is satisfied by the imposition of (67) in (68), and the approximation (70) yields:

$$\begin{aligned} \bar{\mathcal{D}}_{[n]}^{(\alpha)}\{u(\mathbf{X})\} &= \int_{\Omega} \bar{\Psi}_{[0,n]}^{(\alpha)}(\mathbf{X}; \mathbf{X}' - \mathbf{X}) (u(\mathbf{X}') - u(\mathbf{X})) d\mathbf{X}' \\ &= \int_{\Omega} \bar{\Psi}_{[0,n]}^{(\alpha)}(\mathbf{X}; \mathbf{X}' - \mathbf{X}) u(\mathbf{X}') d\mathbf{X}' \\ &\quad - u(\mathbf{X}) \underbrace{\int_{\Omega} \bar{\Psi}_{[0,n]}^{(\alpha)}(\mathbf{X}; \mathbf{X}' - \mathbf{X}) d\mathbf{X}'}_0 \\ &= \int_{\Omega} \bar{\Psi}_{[0,n]}^{(\alpha)}(\mathbf{X}; \mathbf{X}' - \mathbf{X}) u(\mathbf{X}') d\mathbf{X}' \\ &= \mathcal{D}_{[n]}^{(\alpha)}\{u(\mathbf{X})\} \end{aligned} \quad (71)$$

2. When  $m = 1$ ,  $n = 1$ , and  $|\alpha| = 1$  (approximating first order derivatives only), and choosing  $\omega_l = w_\delta$ , (70) yields the peridynamic deformation gradient (61) when approximating the derivative of  $u_i$ , since in this case  $\mathbf{Q}_{[1,1]}(\mathbf{X}) = \mathbf{P}(\mathbf{X})$ ,  $\bar{\mathbf{M}}_{[1,1]}(\mathbf{X}) = \mathbf{K}(\mathbf{X})$ , and when taking the derivative with respect to  $X_j$  we have  $\mathbf{Q}_{[m,n]}^{(\alpha)} = \mathbf{Q}_{[1,1]}^{(\delta_{j1}, \delta_{j2}, \delta_{j3})} = \mathbf{P}_j^\nabla$ , and

$$\begin{aligned} \frac{\partial u_i}{\partial X_j} &\simeq I_{ij} + \bar{\mathcal{D}}_{[1]}^{(\delta_{j1}, \delta_{j2}, \delta_{j3})}\{u_i(\mathbf{X})\} = I_{ij} \\ &\quad + \int_{\mathcal{H}_x} \left( \mathbf{P}_j^\nabla \right)^T \mathbf{K}^{-1}(\mathbf{X}) \mathbf{P}(\mathbf{X}' - \mathbf{X}) \\ &\quad \times w_\delta(\mathbf{X}' - \mathbf{X}) (u_i(\mathbf{X}') - u_i(\mathbf{X})) d\mathbf{X}' = \mathcal{F}_{ij}(\mathbf{X}) \end{aligned} \quad (72)$$

3. When  $m = 1$ ,  $|\alpha| = 1$ ,  $\omega_l = w_\delta$ , and  $n > 1$  is a free parameter, when taking the gradient of the displacement  $u_i$  with respect to  $X_j$ , (70) yields a  *$n$ th order accurate non-local deformation gradient* which is denoted  $\mathcal{F}_{[n]}$  herein:

$$\frac{\partial u_i}{\partial X_j} \simeq (\mathcal{F}_{[n]})_{ij}(\mathbf{X}) = I_{ij} + \bar{\mathcal{D}}_{[n]}^{(\delta_{j1}, \delta_{j2}, \delta_{j3})}\{u_i(\mathbf{X})\} \quad (73)$$

where

$$\begin{aligned} \bar{\mathcal{D}}_{[n]}^{(\delta_{j1}, \delta_{j2}, \delta_{j3})}\{u(\mathbf{X})\} &= \int_{\mathcal{H}_x} \left( \mathbf{Q}_j^\nabla \right)^T \bar{\mathbf{M}}_{[1,n]}^{-1}(\mathbf{X}) \mathbf{Q}_{[1,n]}(\mathbf{X}' - \mathbf{X}) w_\delta(\mathbf{X}' - \mathbf{X}) \\ &\quad \times (u(\mathbf{X}') - u(\mathbf{X})) d\mathbf{X}' \end{aligned} \quad (74)$$

and

$$\mathbf{Q}_j^\nabla \equiv \mathbf{Q}_{[1,n]}^{(\delta_{j1}, \delta_{j2}, \delta_{j3})} = [0, \dots, 0, \underset{\substack{\uparrow \\ \text{jth entry}}}{1}, 0, \dots, 0]^\top. \quad (75)$$

In the above,  $\bar{\mathbf{M}}_{[1,n]}$  can be interpreted as a high-order reference shape tensor, while  $\mathbf{Q}_{[1,n]}$  can also be understood in the context of states. The arbitrarily high-order versions of non-local deformation gradients can also be understood in terms of reduction and expansion of states to tensors, and tensors to states, respectively. Details are given in ‘‘Appendix A’’.

4. When  $m = 1$ ,  $|\alpha| > 1$ , and  $n$  is a free variable, choosing  $\omega_l = w_\delta$  in (70) yields *nth order accurate non-local higher order derivatives*:

$$\begin{aligned} \bar{\mathcal{D}}_{[n]}^{(\alpha)}\{u(\mathbf{X})\} &= \int_{\mathcal{H}_x} \left(\mathbf{Q}_{[1,n]}^{(\alpha)}\right)^\top \bar{\mathbf{M}}_{[1,n]}^{-1}(\mathbf{X}) \mathbf{Q}_{[1,n]}(\mathbf{X}' - \mathbf{X}) \\ &\times w_\delta(\mathbf{X}' - \mathbf{X})(u(\mathbf{X}') - u(\mathbf{X}))d\mathbf{X}', \quad |\alpha| > 1 \end{aligned} \quad (76)$$

The terminology adopted herein is that when  $m = 1$  and  $\omega_l = w_\delta$ , the derivative approximations are termed *non-local* or *peridynamic* since they approximate derivatives in the same manner as the non-local deformation gradient, they embed the non-local length scale  $\delta$ , and also perform differentiation by integration. The generalization occurs with  $|\alpha| > 1$  and/or  $n > 1$ . That is, the original non-local deformation gradient is recovered in the non-local derivatives when  $|\alpha| = 1$  and  $n = 1$ . Thus the general expression for *nth order accurate non-local derivatives* in the continuous case is

$$\begin{aligned} \bar{\mathcal{D}}_{[n]}^{(\alpha)}\{u(\mathbf{X})\} &= \int_{\mathcal{H}_x} \left(\mathbf{Q}_{[1,n]}^{(\alpha)}\right)^\top \bar{\mathbf{M}}_{[1,n]}^{-1}(\mathbf{X}) \mathbf{Q}_{[1,n]}(\mathbf{X}' - \mathbf{X}) \\ &\times w_\delta(\mathbf{X}' - \mathbf{X})(u(\mathbf{X}') - u(\mathbf{X}))d\mathbf{X}'. \end{aligned} \quad (77)$$

Therefore, *the present formulation can be regarded as a generalization of the way in which state-based peridynamics approximates derivatives using the non-local technique*.

## 4.2 Continuous nth order non-local gradient and divergence operations

High-order non-local gradient and divergence operations can be derived from the general formulation (70) with  $m = 1$ ,  $\omega_l = w_\delta$  as in (77). Examining (70) with  $|\alpha| = 1$  (for first order derivatives) and casting it as an operator to approximate a non-local derivative of a function  $u$  with respect to  $X_j$ , one obtains:

$$\begin{aligned} (\nabla u(\mathbf{X}))_j &\simeq \left(\mathcal{D}_{[n]}^\nabla\{u(\mathbf{X})\}\right)_j \\ &= \int_{\mathcal{H}_x} \left(\mathbf{Q}_j^\nabla\right)^\top \bar{\mathbf{M}}_{[1,n]}^{-1}(\mathbf{X}) \mathbf{Q}_{[1,n]}(\mathbf{X}' - \mathbf{X}) w_\delta(\mathbf{X}' - \mathbf{X}) \\ &\times (u(\mathbf{X}') - u(\mathbf{X}))d\mathbf{X}' \end{aligned} \quad (78)$$

where  $\mathbf{Q}_j^\nabla$  is the same vector in (75).

In vector form, (78) can be cast as

$$\begin{aligned} \nabla u(\mathbf{X}) &\simeq \mathcal{D}_{[n]}^\nabla\{u(\mathbf{X})\} \\ &= \int_{\mathcal{H}_x} \left(\tilde{\mathbf{Q}}^\nabla\right)^\top \bar{\mathbf{M}}_{[1,n]}^{-1}(\mathbf{X}) \mathbf{Q}_{[1,n]}(\mathbf{X}' - \mathbf{X}) \\ &\times w_\delta(\mathbf{X}' - \mathbf{X})[u(\mathbf{X}') - u(\mathbf{X})]d\mathbf{X}' \end{aligned} \quad (79)$$

where

$$\tilde{\mathbf{Q}}^\nabla = [\mathbf{Q}_1^\nabla, \mathbf{Q}_2^\nabla, \mathbf{Q}_3^\nabla] \quad (80)$$

and here  $\nabla u$  is a column vector. Thus the *nth order non-local gradient operation* on a vector field  $\mathbf{f}$  can be expressed as:

$$\begin{aligned} \nabla \otimes \mathbf{f}(\mathbf{X}) &\simeq \mathcal{D}_{[n]}^\nabla \otimes \mathbf{f}(\mathbf{X}) \\ &= \int_{\mathcal{H}_x} \left(\tilde{\mathbf{Q}}^\nabla\right)^\top \bar{\mathbf{M}}_{[1,n]}^{-1}(\mathbf{X}) \mathbf{Q}_{[1,n]}(\mathbf{X}' - \mathbf{X}) w_\delta(\mathbf{X}' - \mathbf{X}) \\ &\times (\mathbf{f}(\mathbf{X}') - \mathbf{f}(\mathbf{X}))^\top d\mathbf{X}' \end{aligned} \quad (81)$$

where on the right hand side,  $\mathbf{f}$  is represented as a column vector. Likewise, the *nth order non-local divergence* on a vector field  $\mathbf{f}$  can be expressed as:

$$\begin{aligned} \nabla \cdot \mathbf{f}(\mathbf{X}) &\simeq \mathcal{D}_{[n]}^\nabla \cdot \mathbf{f}(\mathbf{X}) \\ &= \int_{\mathcal{H}_x} (\mathbf{f}(\mathbf{X}') - \mathbf{f}(\mathbf{X}))^\top \left(\tilde{\mathbf{Q}}^\nabla\right)^\top \bar{\mathbf{M}}_{[1,n]}^{-1}(\mathbf{X}) \\ &\times \mathbf{Q}_{[1,n]}(\mathbf{X}' - \mathbf{X}) w_\delta(\mathbf{X}' - \mathbf{X})d\mathbf{X}' \end{aligned} \quad (82)$$

## 4.3 High-order force density via non-local divergence of stress: continuous case

According to the correspondence principle [20], the force state  $\underline{\mathbf{T}}$  can be calculated from the 1st PK stress  $\boldsymbol{\sigma}$  as a function of the non-local deformation gradient (61) for state-based peridynamics as:

$$\underline{\mathbf{T}}[\mathbf{X}, t](\mathbf{X}' - \mathbf{X}) = \boldsymbol{\sigma}(\mathbf{X})\mathbf{K}^{-1}(\mathbf{X})\mathbf{P}(\mathbf{X}' - \mathbf{X})w_\delta(\mathbf{X}' - \mathbf{X}). \quad (83)$$

In the above, and in the following text,  $\boldsymbol{\sigma}$  denotes the matrix form of the 1st PK stress according to the context.

Comparing (1), (2) and (83), the integration of the force state as a function of stress can be interpreted as a type of non-local divergence operation on the nominal stress  $\boldsymbol{\sigma}^T$  as:

$$\begin{aligned} \nabla \cdot \boldsymbol{\sigma}^T(\mathbf{X}) \rightarrow \int_{\mathcal{H}_x} \{ & \boldsymbol{\sigma}(\mathbf{X})\mathbf{K}^{-1}(\mathbf{X})\mathbf{P}(\mathbf{X}' - \mathbf{X}) \\ & - \boldsymbol{\sigma}(\mathbf{X}')\mathbf{K}^{-1}(\mathbf{X}')\mathbf{P}(\mathbf{X} - \mathbf{X}') \} w_\delta(\mathbf{X}' - \mathbf{X}) d\mathbf{X}' \end{aligned} \quad (84)$$

where the fact that  $w_\delta = w_\delta(|\mathbf{X} - \mathbf{X}'|)$  was employed. A force state consistent with the high order non-local deformation gradient (73) can be obtained using the same correspondence principle as (see ‘‘Appendix B’’ for the derivation):

$$\underline{\mathbf{T}}[\mathbf{X}, t](\mathbf{X}' - \mathbf{X}) = \boldsymbol{\sigma}(\mathbf{X}) \left( \tilde{\mathbf{Q}}^\nabla \right)^T \bar{\mathbf{M}}_{[1,n]}^{-1}(\mathbf{X}) \mathbf{Q}_{[1,n]}(\mathbf{X}' - \mathbf{X}) w_\delta(\mathbf{X}' - \mathbf{X}). \quad (85)$$

The corresponding non-local divergence operation that results from this force state can be expressed as:

$$\begin{aligned} \nabla \cdot \boldsymbol{\sigma}^T(\mathbf{X}) \rightarrow \int_{\mathcal{H}_x} \left\{ & \boldsymbol{\sigma}(\mathbf{X}) \left( \tilde{\mathbf{Q}}^\nabla \right)^T \bar{\mathbf{M}}_{[1,n]}^{-1}(\mathbf{X}) \mathbf{Q}_{[1,n]}(\mathbf{X}' - \mathbf{X}) \right. \\ & \left. - \boldsymbol{\sigma}(\mathbf{X}') \left( \tilde{\mathbf{Q}}^\nabla \right)^T \bar{\mathbf{M}}_{[1,n]}^{-1}(\mathbf{X}') \mathbf{Q}_{[1,n]}(\mathbf{X} - \mathbf{X}') \right\} w_\delta(\mathbf{X}' - \mathbf{X}) d\mathbf{X}'. \end{aligned} \quad (86)$$

However, despite being derived from the high-order accurate deformation gradient, numerical testing shows that the discretized form of the force density (86) viewed as a mathematical operator on  $\boldsymbol{\sigma}^T$  does not guarantee even 0th order accuracy in the general case. That is, when the nominal stress  $\boldsymbol{\sigma}^T$  is constant, the total force density contribution to a point  $\mathbf{X}$  may be non-zero. Notably, this is also true of (84), where under a constant state of stress, the corresponding force-density could be non-zero, and the original formulation using (84) also does not possess even 0th order accuracy in the general case. Thus, despite whatever the accuracy the non-local deformation gradient possesses (using the original formulation (47), with linear accuracy, or the high-order formulation (73), with  $n$ th order accuracy), the final solution computed using either (84) or (86) may not even have 0th accuracy because of the operation of computing the force density. This assertion is verified numerically in Sect. 6.5.

Accordingly, a non-local divergence of the nominal stress  $\boldsymbol{\sigma}^T$  is proposed, which can be computed from the generalization of (82) from vectors to tensors as

$$\begin{aligned} \mathcal{D}_{[n]}^\nabla \cdot \boldsymbol{\sigma}^T(\mathbf{X}) = \int_{\mathcal{H}_x} (\boldsymbol{\sigma}(\mathbf{X}') - \boldsymbol{\sigma}(\mathbf{X}))^T \left( \tilde{\mathbf{Q}}^\nabla \right)^T \\ \times \bar{\mathbf{M}}_{[1,n]}^{-1}(\mathbf{X}) \mathbf{Q}_{[1,n]}(\mathbf{X}' - \mathbf{X}) w_\delta(\mathbf{X}' - \mathbf{X}) d\mathbf{X}'. \end{aligned} \quad (87)$$

For the linear case ( $n = 1$ ), the force density computed by the proposed non-local divergence can be expressed as:

$$\begin{aligned} \mathcal{D}_{[1]}^\nabla \cdot \boldsymbol{\sigma}^T(\mathbf{X}) = \int_{\mathcal{H}_x} (\boldsymbol{\sigma}(\mathbf{X}') + \boldsymbol{\sigma}(\mathbf{X}))^T \mathbf{K}^{-1}(\mathbf{X}) \mathbf{P}(\mathbf{X}' - \mathbf{X}) \\ \times w_\delta(\mathbf{X}' - \mathbf{X}) d\mathbf{X}' \end{aligned} \quad (88)$$

where the fact that  $\mathbf{P}(\mathbf{X}' - \mathbf{X}) = -\mathbf{P}(\mathbf{X} - \mathbf{X}')$  was employed. Comparing to the standard force density by peridynamics (84), which can also be simplified as

$$\begin{aligned} \nabla \cdot \boldsymbol{\sigma}^T(\mathbf{X}) \rightarrow \int_{\mathcal{H}_x} \{ \boldsymbol{\sigma}(\mathbf{X})\mathbf{K}^{-1}(\mathbf{X}) + \boldsymbol{\sigma}(\mathbf{X}')\mathbf{K}^{-1}(\mathbf{X}') \} \\ \times \mathbf{P}(\mathbf{X}' - \mathbf{X}) w_\delta(\mathbf{X}' - \mathbf{X}) d\mathbf{X}', \end{aligned} \quad (89)$$

it can be seen that constant and linear accuracy can be introduced easily into state-based peridynamics via a small modification of (89) to (88). In Sect. 6.5, it will be demonstrated that any order of accuracy desired is maintained in the discrete case.

## 5 Discrete reproducing kernel approximation and peridynamic deformation gradient

In this section, the discretized versions of the continuous approximations discussed in Sect. 3 are analysed and compared.

### 5.1 Discrete reproducing kernel approximation

A discrete version of the reproducing kernel approximation (4) can be obtained by performing numerical integration on both (11) and (12) at a set of  $NP$  nodes  $\{\mathbf{x}_J | \mathbf{x}_J \in \Omega\}_{J=1}^{NP}$  that discretize a domain  $\Omega$ :

$$\begin{aligned} \mathcal{R}_{[n]}^h \{u(\mathbf{x})\} &= \sum_{J=1}^{NP} \mathbf{H}(\mathbf{0})^T \mathbf{M}^{-1}(\mathbf{x}) \mathbf{H}(\mathbf{x}_J - \mathbf{x}) \Phi_a(\mathbf{x}_J - \mathbf{x}) V_J u_J \\ &\equiv \sum_{J=1}^{NP} \Psi_J(\mathbf{x}) u_J \end{aligned} \quad (90)$$

$$\mathbf{M}(\mathbf{x}) = \sum_{J=1}^{NP} \mathbf{H}(\mathbf{x}_J - \mathbf{x}) \mathbf{H}^T(\mathbf{x}_J - \mathbf{x}) \Phi_a(\mathbf{x}_J - \mathbf{x}) V_J \quad (91)$$

where  $u_J \equiv u(\mathbf{x}_J)$  are nodal coefficients,  $\Psi_J(\mathbf{x})$  is the reproducing kernel shape function,  $V_J$  is the nodal quadrature weight for point  $\mathbf{x}_J$ , and  $\mathbf{M}(\mathbf{x})$  is the discrete moment matrix. For notational simplicity, it should be understood that  $\mathbf{M}(\mathbf{x})$  and other quantities denote the discrete or continuous counterparts depending on the context in which they are employed.

Unlike the continuous case, the moment matrix (91) is conditionally invertible, which requires  $(n + d)!/(n!d!)$  nodal kernels covering  $\mathbf{x}$  which are non-colinear (in 2D) or non-coplanar (in 3D) [29]. The selection of a kernel value of  $a = h(n + 1)$  with  $h$  the nodal spacing generally suffices as a rule of thumb.

It is important to note that when the quadrature in (90) is the same as in (91),  $n$ th order accuracy is maintained [5]. The construction in (90)–(91) can also be derived by using the Taylor expansion procedure in Sect. 3 (the derivation is omitted here), or can be derived by enforcing the reproducing conditions directly on  $\Psi_J$ , both of which can also demonstrate that the discretized form possesses  $n$ th order accuracy. The interested reader is referred to the literature for these procedures, e.g., [1], and for discussions on quadrature, see [5].

The set of shape functions  $\Psi_J(\mathbf{x})$  satisfy the so-called  $n$ th order reproducing conditions, i.e., possess  $n$ th order completeness:

$$\sum_{J=1}^{NP} \Psi_J(\mathbf{x})\mathbf{H}(\mathbf{x}_J) = \mathbf{H}(\mathbf{x}) \tag{92}$$

or equivalently, as it is often expressed and employed for better conditioning of the moment matrix:

$$\sum_{J=1}^{NP} \Psi_J(\mathbf{x})\mathbf{H}(\mathbf{x}_J - \mathbf{x}) = \mathbf{H}(\mathbf{0}). \tag{93}$$

Alternative to the construction in (90)–(91), determination of quadrature weights may be avoided by constructing the so-called discrete RK approximation [62], which directly imposes (92) on a corrected kernel function.

### 5.2 Discrete implicit gradient approximation

Analogous to the case of the discrete RK approximation (90), a discrete implicit gradient approximation can be obtained by employing quadrature on (20) at nodal locations:

$$\begin{aligned} \left[ \mathcal{D}_{[n]}^h \right]^{(\alpha)} \{u(\mathbf{x})\} &= \sum_{J=1}^{NP} \mathbf{H}^{(\alpha)} \mathbf{M}(\mathbf{x})^{-1} \mathbf{H}(\mathbf{x}_J - \mathbf{x}) \Phi_a(\mathbf{x}_J - \mathbf{x}) V_J u_J \\ &\equiv \sum_{J=1}^{NP} \Psi_J^{(\alpha)}(\mathbf{x}) u_J \end{aligned} \tag{94}$$

where  $\mathbf{M}(\mathbf{x})$  is the same discrete moment matrix in (91). It is apparent that as in the continuous case, as a special case of (94) with  $|\alpha| = 0$  we obtain (90), that is  $\Psi_J^{(0,0,0)}(\mathbf{x}) = \Psi_J(\mathbf{x})$ .

So long as the moment matrix is discretized with the same quadrature in (94), the gradients also enjoy  $n$ th order accuracy, which can be confirmed by deriving (94) from a Taylor expansion point of view (again the derivation is omitted here), as in the RK approximation, or by directly enforcing gradient reproducing conditions on  $\Psi_J^{(\alpha)}$ .

It can be shown that the derivative approximations (94) enjoy gradient completeness [55]:

$$\sum_{J=1}^{NP} \mathbf{H}(\mathbf{x}_J) \Psi_J^{(\alpha)}(\mathbf{x}) = \partial^\alpha \mathbf{H}(\mathbf{x}). \tag{95}$$

Or again, analogous to (22),

$$\sum_{J=1}^{NP} \mathbf{H}(\mathbf{x}_J - \mathbf{x}) \Psi_J^{(\alpha)}(\mathbf{x}) = \mathbf{H}^{(\alpha)}. \tag{96}$$

If desired, quadrature weights in implicit gradients may also be avoided by employing a discrete implicit gradient approximation [55], which directly imposes (95) on a corrected kernel.

One final point to note which will be revisited, is that given a discrete set of scattered data  $\{u_J\}_{J=1}^{NP}$ , an approximation to derivatives  $\partial^\alpha u$  can be obtained at any given point  $\mathbf{x}$  of interest using the implicit gradient approximation, providing a smooth field of derivative estimates in the entire domain.

### 5.3 Deformation gradient under discrete implicit gradient approximation

The discretization of the deformation gradient under the implicit gradient approximation (45) is calculated in the Lagrangian coordinates in a similar fashion as the continuous case:

$$\begin{aligned} F_{ij}(\mathbf{X}) &= I_{ij} \\ &+ \sum_{J=1}^{NP} \left[ \mathbf{H}_J^\nabla \right]^T \mathbf{M}^{-1}(\mathbf{X}) \mathbf{H}(\mathbf{X}_J - \mathbf{X}) \Phi_a(\mathbf{X}_J - \mathbf{X}) V_J u_{Ji} \end{aligned} \tag{97}$$

where  $\mathbf{H}_J^\nabla$  is the same vector in (46).

Since the deformation gradient is constructed by discrete implicit gradients with  $n$ th order accuracy (or  $n$ th order consistency), it can again be directly inferred that the discrete deformation gradient (97) possesses  $n$ th order accuracy without additional analysis needed.

#### 5.4 The discrete deformation gradient under peridynamics

To discretize (47)–(49), nodal quadrature at  $NP$  nodes is employed in the meshfree implementation [24], similar to the discrete RK approximation and discrete implicit gradient approximation:

$$\begin{aligned}\mathbf{K}(\mathbf{X}) &= \sum_{J=1}^{NP} w_{\delta}(\mathbf{X}_J - \mathbf{X})(\mathbf{X}_J - \mathbf{X}) \otimes (\mathbf{X}_J - \mathbf{X}) V_J, \\ \mathbf{S}(\mathbf{X}) &= \sum_{J=1}^{NP} w_{\delta}(\mathbf{X}_J - \mathbf{X})(\mathbf{x}_J - \mathbf{x}) \otimes (\mathbf{X}_J - \mathbf{X}) V_J.\end{aligned}\quad (98)$$

The discretized non-local deformation gradient is calculated from the above quantities as

$$\mathcal{F}(\mathbf{X}) = \mathbf{S}(\mathbf{X}) \cdot \mathbf{K}^{-1}(\mathbf{X}). \quad (99)$$

Again, for notational simplicity, depending on the context it should be understood whether  $\mathbf{K}$ ,  $\mathbf{S}$  or  $\mathcal{F}$  is the continuous or discrete form.

#### 5.5 Analysis of the discrete deformation gradient under peridynamics

Following the procedures in the continuous case in Sect. 3.6, a Taylor expansion on the displacement in (98)–(99) obtained from  $\mathbf{x}(\mathbf{X}) = \mathbf{X} + \mathbf{u}(\mathbf{X})$  yields the discrete expression:

$$\begin{aligned}\mathcal{F}_{ij}(\mathbf{X}) &= I_{ij} + \frac{\partial u_i(\mathbf{X})}{\partial X_j} \\ &+ \frac{\partial^2 u_i(\mathbf{X})}{\partial X_k \partial X_l} \frac{1}{2} \sum_{J=1}^{NP} w_a(\mathbf{X}_J - \mathbf{X})(X_{kJ} - X_k) \\ &\times (X_{lJ} - X_l)(X_{mJ} - X_m) K_{mj}^{-1}(\mathbf{X}) V_J \\ &+ \frac{\partial^3 u_i(\mathbf{X})}{\partial X_k \partial X_l \partial X_n} \frac{1}{6} \sum_{J=1}^{NP} w_a(\mathbf{X}_J - \mathbf{X})(X_{kJ} - X_k) \\ &\times (X_{lJ} - X_l)(X_{nJ} - X_n)(X_{mJ} - X_m) K_{mj}^{-1}(\mathbf{X}) V_J \\ &+ \mathcal{O}(\delta^3).\end{aligned}\quad (100)$$

In order to interpret the implications of (100), first consider the case of a uniform discretization, away from the boundary, with symmetric influence functions. The fourth term on the right hand side is an even function (centred around  $\mathbf{X}$ ) and will be non-zero due to the symmetry and

constant nodal weights. Under these conditions, the following is obtained:

$$\begin{aligned}\mathcal{F}_{ij}(\mathbf{X}) &= I_{ij} + \frac{\partial u_i(\mathbf{X})}{\partial X_j} \\ &+ \frac{\partial^2 u_i(\mathbf{X})}{\partial X_p \partial X_q} \frac{1}{2} \sum_{J=1}^{NP} w_a(\mathbf{X}_J - \mathbf{X})(X_{pJ} - X_p)(X_{qJ} - X_q) \\ &\times (X_{mJ} - X_m) K_{mj}^{-1}(\mathbf{X}) V_J + \mathcal{O}(\delta^2).\end{aligned}\quad (101)$$

In the same situation, the third term disappears, but this time only at nodal locations due to the discrete quadrature, as the terms being summed will only cancel when they are “anti-symmetric” (which only occurs at nodal locations):

$$\mathcal{F}_{ij}(\mathbf{X}) = \delta_{ij} + \frac{\partial u_i(\mathbf{X})}{\partial X_j} + \mathcal{O}(\delta^2) \text{ when } \mathbf{X} \text{ is a nodal location} \quad (102)$$

This also indicates that in the general case, it will be non-zero unless a careful selection of the combination of influence functions, nodal quadrature weights, and so on, are selected, as was performed in [52], but is difficult to generalize to non-uniform discretizations.

Finally, in the case of a non-uniform discretizations, or even in a uniform discretization near the boundary, and also away from nodal locations, the third term in (100) will not disappear and the expression reduces to

$$\mathcal{F}_{ij}(\mathbf{X}) = \frac{\partial x_i(\mathbf{X})}{\partial X_j} + \mathcal{O}(\delta). \quad (103)$$

Thus the discrete form and the continuous form share the similar order of accuracy and behavior in accuracy; in the best-case they are both second order accurate, and in the general case, they are first-order accurate.

In summary, the same order of accuracy is attained for both continuous and discrete versions of implicit gradients, yet the continuous and discrete versions of the non-local deformation gradient in peridynamics slightly differ. That is, the accuracy is second-order in the best case (away from the boundary, uniform discretizations, symmetric influence functions), but in the discrete case second-order accuracy can only be obtained at the nodes in this situation. In the general case, the constructions are first-order accurate, for both integral and discrete forms. These situations can be rectified with the proposed generalized discrete formulation given in Sect. 6.1.

#### 5.6 Comparison between discrete implicit gradients and peridynamics

In order to facilitate a comparison between the discrete non-local deformation gradient by peridynamics and the

discrete RK approximation, we first express the discrete shape tensors (98) in matrix form:

$$\begin{aligned}\mathbf{K}(\mathbf{X}) &= \sum_{J=1}^{NP} w_{\delta}(\mathbf{X}_J - \mathbf{X}) \mathbf{P}(\mathbf{X}_J - \mathbf{X}) \mathbf{P}^T(\mathbf{X}_J - \mathbf{X}) V_J, \\ \mathbf{S}(\mathbf{X}) &= \sum_{J=1}^{NP} w_{\delta}(\mathbf{X}_J - \mathbf{X}) \mathbf{P}(\mathbf{x}(\mathbf{X}_J) - \mathbf{x}(\mathbf{X})) \mathbf{P}^T(\mathbf{X}_J - \mathbf{X}) V_J.\end{aligned}\quad (104)$$

As before, the undeformed shape tensor is coincident with the Lagrangian RK discrete moment matrix (91) with  $a = \delta$ ,  $\Phi_a = w_{\delta}$ , and linear basis, but omitting the unity term in the vector  $\mathbf{H}(\mathbf{X})$ .

Following the procedures in Sect. 3.7, the discrete non-local deformation gradient can be rearranged and expressed as:

$$\begin{aligned}\mathcal{F}_{ij}(\mathbf{X}) &= I_{ij} + \sum_{J=1}^{NP} \left[ \mathbf{P}_j^{\nabla} \right]^T \mathbf{K}^{-1}(\mathbf{X}) \mathbf{P}(\mathbf{X}_J - \mathbf{X}) \\ &\quad \times w_{\delta}(\mathbf{X}_J - \mathbf{X}) [u_i(\mathbf{X}_J) - u_i(\mathbf{X})] V_J.\end{aligned}\quad (105)$$

For comparison, the local deformation gradient  $F_{ij}$  calculated by discrete implicit gradients (94) with  $a = \delta$ , and  $\Phi_a = w_{\delta}$  can be expressed as:

$$\begin{aligned}F_{ij}(\mathbf{X}) &= I_{ij} + \sum_{J=1}^{NP} \left[ \mathbf{H}_j^{\nabla} \right]^T \mathbf{M}^{-1}(\mathbf{X}) \mathbf{H}(\mathbf{X}_J - \mathbf{X}) \\ &\quad \times w_{\delta}(\mathbf{X}_J - \mathbf{X}) [u_i(\mathbf{X}_J)] V_J.\end{aligned}\quad (106)$$

It can be seen that in the discrete case, if  $\mathbf{P}(\mathbf{X})$  were to be employed in the implicit gradient approximation, partition of nullity would also not be able to be satisfied. This fact is again “compensated for” in the discrete peridynamic gradient by the summation with  $[u_i(\mathbf{X}_J) - u_i(\mathbf{X})]$  rather than  $u_i(\mathbf{X}_J)$  alone. That is, if  $\mathbf{u} = \text{constant}$  then the discrete non-local deformation gradient still yields the correct result of  $\mathcal{F}_{ij} = I_{ij}$ .

Another interesting point is that the gradient approximation (105) does not allow a continuous gradient field representation from a discrete set of nodal data, since in computing the quantity away from the discrete points with known solutions (e.g., from scattered data or a PDE)  $u_i(\mathbf{X}_J)$ , the quantity  $u_i(\mathbf{X})$  is unknown. This places a serious drawback on the approximation, as it can only yield gradient estimations at the scattered data points themselves, but does not provide for an interpolation function for the data. Thus formally, the peridynamic approximation cannot provide a smooth field at all points  $\mathbf{X}$  in the domain given a finite set of nodal coefficients  $\{u_J\}_{J=1}^{NP}$ . It can however, given a function  $u(\mathbf{X})$  defined in the entire domain, provide an estimate of derivatives. Finally, it can be noted that it would be possible to interpolate the

derivative estimates at nodes, although this yields some additional complexity.

## 6 Reproducing kernel peridynamic approximation

In this section, the discrete form of the reproducing kernel peridynamic approximation is given. High-order non-local discrete deformation gradients and non-local divergence operations are derived, as well as several other discrete approximations. The order of accuracy of these operators is also verified numerically.

### 6.1 Reproducing kernel peridynamic approximation

Similar to the continuous case, the operations for the discrete approximation of the gradient by peridynamics and implicit gradients can be unified as follows. First, consider a discrete approximation of the type (94) with a basis of monomials from order  $m$  to  $n$  to estimate gradients of a scalar field  $u(\mathbf{X})$ , with use of  $u(\mathbf{X}_J) - u(\mathbf{X})$  rather than  $u(\mathbf{X}_J)$  as in (105):

$$\begin{aligned}\left[ \bar{\mathcal{D}}_{[n]}^h \right]^{(\alpha)} \{u(\mathbf{X})\} &= \sum_{J=1}^{NP} \mathbf{Q}_{[m,n]}^T(\mathbf{X}_J - \mathbf{X}) \\ &\quad \times \bar{\mathbf{b}}^{(\alpha)}(\mathbf{X}) \omega_l(\mathbf{X}_J - \mathbf{X}) [u(\mathbf{X}_J) - u(\mathbf{X})] V_J \\ &\equiv \sum_{J=1}^{NP} \bar{\Psi}_{[m,n]J}^{(\alpha)}(\mathbf{X}) [u(\mathbf{X}_J) - u(\mathbf{X})]\end{aligned}\quad (107)$$

where  $\mathbf{Q}_{[m,n]}(\mathbf{X})$  is the same column vector of the set of monomials  $\{\mathbf{X}^{\beta}\}_{|\beta|=m}^n$  as the continuous case. To facilitate  $n$ th order accuracy in this approximation, taking the Taylor expansion on  $u(\mathbf{X}_J)$  in (7) yields:

$$\begin{aligned}\left[ \bar{\mathcal{D}}_{[n]}^h \right]^{(\alpha)} \{u(\mathbf{X})\} &= \bar{\mathbf{D}}(\mathbf{X}) \bar{\mathbf{J}} \sum_{J=1}^{NP} \mathbf{Q}_{[1,n]}(\mathbf{X}_J - \mathbf{X}) \\ &\quad \times \mathbf{Q}_{[m,n]}^T(\mathbf{X}_J - \mathbf{X}) \bar{\mathbf{b}}^{(\alpha)}(\mathbf{X}) \omega_l(\mathbf{X}_J - \mathbf{X}) V_J\end{aligned}\quad (108)$$

where  $\bar{\mathbf{D}}(\mathbf{X})$  and  $\bar{\mathbf{J}}$  are the same vectors and matrices in the continuous case (64). Examining (108), it is apparent that in order to reproduce gradients up to  $n$ th order accuracy, we have the following discrete vanishing moment conditions:

$$\begin{aligned} & \sum_{J=1}^{NP} \mathbf{Q}_{[1,n]}(\mathbf{X}_J - \mathbf{X}) \mathbf{Q}_{[m,n]}^T(\mathbf{X}_J - \mathbf{X}) \bar{\mathbf{b}}^{(\alpha)}(\mathbf{X}) \omega_l(\mathbf{X}_J - \mathbf{X}) V_J \\ & = \mathbf{Q}_{[1,n]}^{(\alpha)} \end{aligned} \quad (109)$$

where  $\mathbf{Q}_{[m,n]}^{(\alpha)}$  is again a column vector of  $\{\alpha! \delta_{\alpha\beta}\}_{|\beta|=m}^n$ . As before, when  $m = 0$  and  $n > 0$  the system is underdetermined and an additional condition is required for determining  $\bar{\mathbf{b}}^{(\alpha)}$ . Imposing the partition of nullity on (107) in the case of  $m = 0$  and  $n > 0$ :

$$\sum_{J=1}^{NP} \bar{\Psi}_{[m,n]J}^{(\alpha)}(\mathbf{X}) = 0, m = 0, n > 0 \quad (110)$$

the system (109) can then be recast with (110) in hand to yield a determined system for all free variables:

$$\bar{\mathbf{M}}_{[m,n]}(\mathbf{X}) \bar{\mathbf{b}}^{(\alpha)}(\mathbf{X}) = \mathbf{Q}_{[m,n]}^{(\alpha)} \quad (111)$$

where

$$\bar{\mathbf{M}}_{[m,n]}(\mathbf{X}) = \sum_{J=1}^{NP} \mathbf{Q}_{[m,n]}(\mathbf{X}_J - \mathbf{X}) \mathbf{Q}_{[m,n]}^T(\mathbf{X}_J - \mathbf{X}) \omega_l(\mathbf{X}_J - \mathbf{X}) V_J. \quad (112)$$

A unified discrete approximation is obtained by solving for  $\bar{\mathbf{b}}^{(\alpha)}$  from (111) and substituting into (107):

$$\begin{aligned} & \left[ \bar{\mathcal{D}}_{[n]}^h \right]^{(\alpha)} \{u(\mathbf{X})\} = \sum_{J=1}^{NP} \left[ \mathbf{Q}_{[m,n]}^{(\alpha)} \right]^T \bar{\mathbf{M}}_{[m,n]}^{-1}(\mathbf{X}) \\ & \times \mathbf{Q}_{[m,n]}(\mathbf{X}_J - \mathbf{X}) \omega_l(\mathbf{X}_J - \mathbf{X}) [u(\mathbf{X}_J) - u(\mathbf{X})] V_J. \end{aligned} \quad (113)$$

The approximation in (113) for derivatives is termed the *reproducing kernel peridynamic approximation* herein. The selection of possible values of  $\omega_l$ ,  $|\alpha|$ ,  $n$  and  $m$ , yield both the discrete implicit gradient approximation, as well as the manner in which the deformation gradient is approximated by the discretized version of peridynamics, and as before, two additional approximations can be obtained which are termed the  *$n$ th order non-local deformation gradient*, and  *$n$ th order non-local higher order derivatives* herein:

1. When  $|\alpha| > 0$ ,  $m = 0$ ,  $\omega_l = \Phi_a$ , and  $n$  is a free variable, (113) yields the discrete implicit gradient approximation (94), since  $\mathbf{Q}_{[0,n]}(\mathbf{x}) = \mathbf{H}(\mathbf{x})$  and  $\mathbf{Q}_{[0,n]}^{(\alpha)}(\mathbf{x}) = \mathbf{H}^{(\alpha)}$ , and further if  $m = 0$ , then the discrete partition of nullity is satisfied by the imposition of (110), and the approximation yields:

$$\begin{aligned} & \left[ \bar{\mathcal{D}}_{[n]}^h \right]^{(\alpha)} \{u(\mathbf{X})\} = \sum_{J=1}^{NP} \bar{\Psi}_{[0,n]J}^{(\alpha)}(\mathbf{x}) [u(\mathbf{X}_J) - u(\mathbf{X})] \\ & = \sum_{J=1}^{NP} \bar{\Psi}_{[0,n]J}^{(\alpha)}(\mathbf{x}) u(\mathbf{X}_J) - u(\mathbf{X}) \underbrace{\sum_{J=1}^{NP} \bar{\Psi}_{[0,n]J}^{(\alpha)}(\mathbf{x})}_0 \\ & = \sum_{J=1}^{NP} \bar{\Psi}_{[0,n]J}^{(\alpha)}(\mathbf{x}) u(\mathbf{X}_J) \\ & = \left[ \bar{\mathcal{D}}_{[n]}^h \right]^{(\alpha)} \{u(\mathbf{x})\} \end{aligned} \quad (114)$$

2. When  $m = 1$ ,  $n = 1$ ,  $\omega_l = w_\delta$ , and  $|\alpha| = 1$  (approximating first order derivatives only), (113) yields the discrete peridynamic deformation gradient (105) when approximating the derivative of  $u_i$ , since  $\mathbf{Q}_{[1,1]}(\mathbf{X}) = \mathbf{P}(\mathbf{X})$ ,  $\bar{\mathbf{M}}_{[1,1]}(\mathbf{X}) = \mathbf{K}(\mathbf{X})$ , and when taking the derivative with respect to  $X_j$  we have  $\mathbf{Q}_{[1,1]}^{(\delta_{j1}, \delta_{j2}, \delta_{j3})} = \mathbf{P}_j^\nabla$  and thus

$$\begin{aligned} & F_{ij}(\mathbf{X}) \simeq I_{ij} + \left[ \bar{\mathcal{D}}_{[1]}^h \right]^{(\delta_{j1}, \delta_{j2}, \delta_{j3})} \{u_i(\mathbf{X})\} \\ & = I_{ij} + \sum_{J=1}^{NP} \left[ \mathbf{P}_j^\nabla \right]^T \mathbf{K}^{-1}(\mathbf{X}) \mathbf{P}(\mathbf{X}_J - \mathbf{X}) \\ & \times w_\delta(\mathbf{X}_J - \mathbf{X}) [u_i(\mathbf{X}_J) - u_i(\mathbf{X})] V_J = \mathcal{F}_{ij}(\mathbf{X}) \end{aligned} \quad (115)$$

3. When  $m = 1$ ,  $|\alpha| = 1$ ,  $\omega_l = w_\delta$ , and  $n > 1$  is a free parameter, when taking the gradient of the displacement  $u_i$ , (113) yields a  *$n$ th order accurate non-local deformation gradient* denoted  $\mathcal{F}_{[n]}$  herein:

$$\left[ \mathcal{F}_{[n]} \right]_{ij}(\mathbf{X}) = I_{ij} + \left[ \bar{\mathcal{D}}_{[n]}^h \right]^{(\delta_{j1}, \delta_{j2}, \delta_{j3})} \{u_i(\mathbf{X})\} \quad (116)$$

where

$$\begin{aligned} & \left[ \bar{\mathcal{D}}_{[n]}^h \right]^{(\delta_{j1}, \delta_{j2}, \delta_{j3})} = \sum_{J=1}^{NP} \left[ \mathbf{Q}_J^\nabla \right]^T \bar{\mathbf{M}}_{[1,n]}^{-1}(\mathbf{X}) \\ & \times \mathbf{Q}_{[1,n]}(\mathbf{X}_J - \mathbf{X}) w_\delta(\mathbf{X}_J - \mathbf{X}) [u(\mathbf{X}_J) - u(\mathbf{X})] V_J \end{aligned} \quad (117)$$

and  $\mathbf{Q}_J^\nabla$  is the vector in (75).

4. When  $m = 1$ ,  $|\alpha| > 1$ , and  $n$  is a free variable, choosing  $\omega_l = w_\delta$ , (113) yields  *$n$ th order accurate non-local higher order derivatives*:

$$\begin{aligned} & \left[ \bar{\mathcal{D}}_{[n]}^h \right]^{(\alpha)} \{u(\mathbf{X})\} = \sum_{J=1}^{NP} \left( \mathbf{Q}_{[1,n]}^{(\alpha)} \right)^T \bar{\mathbf{M}}_{[1,n]}^{-1}(\mathbf{X}) \\ & \times \mathbf{Q}_{[1,n]}(\mathbf{X}_J - \mathbf{X}) w_\delta(\mathbf{X}_J - \mathbf{X}) [u(\mathbf{X}_J) - u(\mathbf{X})] V_J, \quad |\alpha| > 1 \end{aligned} \quad (118)$$

As before, a general expression for discrete  $n$ th order accurate non-local derivatives can be found by setting  $m = 1$  and  $\omega_l = w_\delta$  in (113):

$$\begin{aligned} \left[ \widehat{\mathcal{D}}_{[n]}^h \right]^{(\alpha)} \{u(\mathbf{X})\} &= \sum_{J=1}^{NP} \left( \mathbf{Q}_{[1,n]}^{(\alpha)} \right)^T \widehat{\mathbf{M}}_{[1,n]}^{-1}(\mathbf{X}) \\ &\times \mathbf{Q}_{[1,n]}(\mathbf{X}_J - \mathbf{X}) w_\delta (\mathbf{X}_J - \mathbf{X}) [u(\mathbf{X}_J) - u(\mathbf{X})] V_J. \end{aligned} \tag{119}$$

It should be noted that similar to the discrete deformation gradient in (99), this approximation cannot yield a continuous field of derivative estimates from a set of data  $\{u_J\}_{J=1}^{NP}$ , since  $u(\mathbf{X})$  would be required at other points aside from the nodal positions. This again places a limitation on the approximation. However derivative approximations can be obtained at the nodal positions  $\mathbf{X}_J$  themselves as:

$$\begin{aligned} \left[ \widehat{\mathcal{D}}_{[n]}^h \right]^{(\alpha)} \{u(\mathbf{X})\} \Big|_{\mathbf{X}=\mathbf{X}_I} &= \sum_{J=1}^{NP} \left( \mathbf{Q}_{[1,n]}^{(\alpha)} \right)^T \widehat{\mathbf{M}}_{[1,n]}^{-1}(\mathbf{X}_I) \\ &\times \mathbf{Q}_{[1,n]}(\mathbf{X}_J - \mathbf{X}_I) w_\delta (\mathbf{X}_J - \mathbf{X}_I) [u_J - u_I] V_J \end{aligned} \tag{120}$$

with  $u_J \equiv u(\mathbf{X}_J)$ .

In contrast, the implicit gradient approximation (94), as well as the direct derivative of the RK approximation (90) can yield an approximation to derivatives of a field at every point, constructed from a set of scattered nodal data  $\{u_J\}_{J=1}^{NP}$ . For the construction in (119), a form of post-processing or reinterpolation would be involved.

Finally, it is notable that a discrete version of (113) can be employed that omits quadrature weights entirely. Following the procedures common in the RK literature [1], the following expression for the discrete reproducing kernel peridynamic approximation without quadrature can be shown to maintain  $n$ th order accuracy:

$$\begin{aligned} \left[ \widehat{\mathcal{D}}_{[n]}^h \right]^{(\alpha)} \{u(\mathbf{X})\} &= \sum_{J=1}^{NP} \left[ \mathbf{Q}_{[m,n]}^{(\alpha)} \right]^T \widehat{\mathbf{M}}_{[m,n]}^{-1}(\mathbf{X}) \mathbf{Q}_{[m,n]}(\mathbf{X}_J - \mathbf{X}) \omega_l (\mathbf{X}_J - \mathbf{X}) \\ &\times [u(\mathbf{X}_J) - u(\mathbf{X})] \end{aligned} \tag{121}$$

where

$$\widehat{\mathbf{M}}_{[m,n]}(\mathbf{X}) = \sum_{J=1}^{NP} \mathbf{Q}_{[m,n]}(\mathbf{X}_J - \mathbf{X}) \mathbf{Q}_{[m,n]}^T(\mathbf{X}_J - \mathbf{X}) \omega_l (\mathbf{X}_J - \mathbf{X}). \tag{122}$$

### 6.2 Deformation gradient test

Here the accuracy of the non-local deformation gradient by the standard technique (99) and the proposed high-order technique (116) is assessed and verified. The following displacement fields are considered, with each component ( $i = 1, 2$ , two dimensions) prescribed the same value:

1. First order:  $u_i^{(1)} = 2x + 3y$ ,  $\mathbf{F}^{\text{exact}} = \mathbf{I} + \begin{bmatrix} 2 & 3 \\ 2 & 3 \end{bmatrix}$
2. Second order:  $u_i^{(2)} = 2x + 3y + 2x^2 + 4xy + 3y^2$ ,  $\mathbf{F}^{\text{exact}} = \mathbf{I} + \begin{bmatrix} 2 + 4x + 4y & 3 + 6y + 4x \\ 2 + 4x + 4y & 3 + 6y + 4x \end{bmatrix}$
3. Third order:  $u_i^{(3)} = 2x + 3y + 2x^2 + 4xy + 3y^2 + x^3 + 2x^2y + 3xy^2 + 4y^3$ ,  $\mathbf{F}^{\text{exact}} = \mathbf{I} + \begin{bmatrix} 2 + 4x + 4y + 3x^2 + 4xy + 3y^2 & 3 + 6y + 4x + 2x^2 + 6xy + 12y^2 \\ 2 + 4x + 4y + 3x^2 + 4xy + 3y^2 & 3 + 6y + 4x + 2x^2 + 6xy + 12y^2 \end{bmatrix}$

The error in  $F_{11}$  and  $F_{12}$  are assessed since each component of the displacement is the same. Two cases are chosen: uniform and non-uniform discretizations of a domain  $[-1, 1] \times [-1, 1]$  with nodal spacing of 0.2, as shown in Fig. 3. Two points are chosen as indicated in the figure, to verify the analysis in Sect. 5.5, for points away from the influence of the boundary, and points near the boundary. Fixed horizon to nodal spacing ratios are chosen as 1.75, 2.5, and 3.5 for the linear, quadratic, and cubic formulations, respectively, and cubic B-spline influence functions in (5) are employed.

Tables 1 and 2 show the absolute values of the errors for the different orders of the solution for the uniform and non-uniform discretizations, respectively. Here,  $\mathcal{F}_{ij}^{PD}$  denotes the standard technique to compute the deformation gradient (99), while  $\mathcal{F}_{ij}^{HOPD}$  denotes the deformation gradient computed with the high-order technique (116), with the order of accuracy chosen as the solution order. Note that for order 1, the formulations are co-incident.

Here it can be seen that in uniform discretizations, the original non-local deformation gradient has second-order accuracy away from the boundary, but only first order accuracy in the presence of the influence of the boundary. For the non-uniform discretization, the deformation gradient is first-order in all cases. This confirms the analysis and discussions in Sect. 5.5. In contrast, the proposed high-order formulation yields the desired order of accuracy in all cases, in both uniform and non-uniform discretizations, as well as in the presence of a boundary, and verifies the ability of the formulation to provide arbitrary-order accuracy in the discrete case.

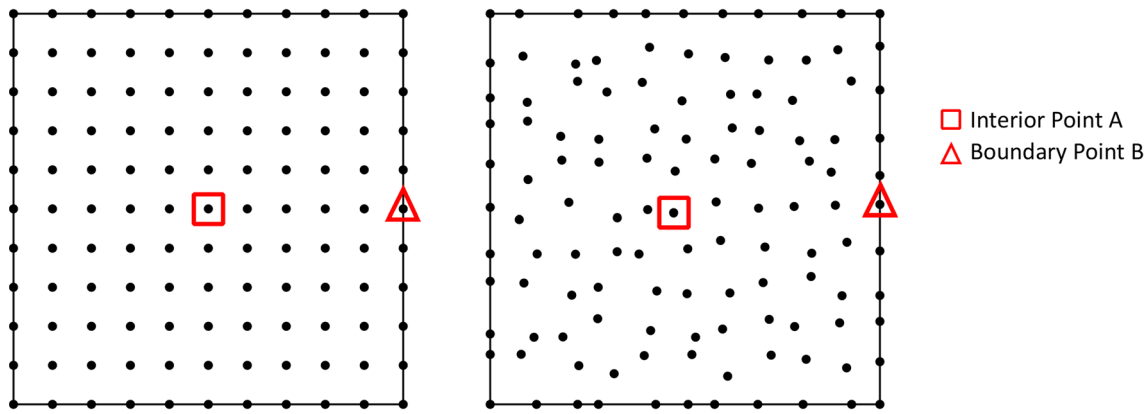


**Fig. 3** Nodal discretizations for deformation gradient and force density tests. Left: uniform discretization. Right: non-uniform discretization

**Table 1** Absolute values of errors in deformation gradients in the uniform node distribution

Solution order	Location	$\mathcal{F}_{11}^{PD}$	$\mathcal{F}_{12}^{PD}$	$\mathcal{F}_{11}^{HOPD}$	$\mathcal{F}_{12}^{HOPD}$
1	Interior point A	8.882e-16	8.882e-16	–	–
	Boundary point B	4.441e-16	8.882e-16	–	–
2	Interior point A	8.882e-16	8.882e-16	2.220e-16	1.776e-15
	Boundary point B	0.5437	0.1916	8.882e-15	8.882e-16
3	Interior point A	0.0687	0.1792	4.885e-15	3.553e-15
	Boundary point B	1.2186	0.2040	5.151e-14	1.421e-14

**Table 2** Absolute values of errors in deformation gradients in the non-uniform point distribution

Solution order	Location	$\mathcal{F}_{11}^{PD}$	$\mathcal{F}_{12}^{PD}$	$\mathcal{F}_{11}^{HOPD}$	$\mathcal{F}_{12}^{HOPD}$
1	Interior point A	8.882e-16	8.882e-16	–	–
	Boundary point B	1.332e-15	8.882e-16	–	–
2	Interior point A	0.0420	0.0407	2.220e-16	8.882e-16
	Boundary point B	0.6975	0.1695	6.306e-14	8.882e-16
3	Interior point A	0.1037	0.2168	1.332e-15	1.332e-15
	Boundary point B	1.5561	0.1768	9.237e-13	5.507e-14

### 6.3 nth order non-local gradient and divergence operations

High-order non-local gradient and divergence operations can be derived from (113) analogous to the continuous case. Setting  $m = 1$ ,  $|\alpha| = 1$  and  $\omega_l = w_\delta$  in (113) and casting it as an operator for the non-local first order derivative with respect to  $X_j$ , one obtains:

$$\begin{aligned}
 [\nabla u(\mathbf{X})]_j &\simeq \left[ \mathcal{D}_{[n]}^\nabla \{u(\mathbf{X})\} \right]_j = \sum_{J=1}^{NP} \left[ \mathbf{Q}_j^\nabla \right]^T \bar{\mathbf{M}}_{[1,n]}^{-1}(\mathbf{X}) \\
 &\quad \times \mathbf{Q}_{[1,n]}(\mathbf{X}_J - \mathbf{X}) w_\delta(\mathbf{X}_J - \mathbf{X}) [u(\mathbf{X}_J) - u(\mathbf{X})] V_J
 \end{aligned} \quad (123)$$

where  $\mathbf{Q}_j^\nabla$  is the same vector in (75). In column vector form, (123) can be expressed as

$$\begin{aligned}
 \nabla u(\mathbf{X}) &\simeq \mathcal{D}_{[n]}^\nabla \{u(\mathbf{X})\} = \sum_{J=1}^{NP} \left[ \hat{\mathbf{Q}}^\nabla \right]^T \bar{\mathbf{M}}_{[1,n]}^{-1}(\mathbf{X}) \\
 &\quad \times \mathbf{Q}_{[1,n]}(\mathbf{X}_J - \mathbf{X}) w_\delta(\mathbf{X}_J - \mathbf{X}) [u(\mathbf{X}_J) - u(\mathbf{X})] V_J
 \end{aligned} \quad (124)$$

where  $\hat{\mathbf{Q}}^\nabla$  is the same matrix in (80).

The discrete non-local gradient operation on a vector field  $\mathbf{f}$  can then be expressed as:

$$\begin{aligned} \nabla \otimes \mathbf{f}(\mathbf{X}) &\simeq \mathcal{D}_{[n]}^{\nabla} \otimes \mathbf{f}(\mathbf{X}) = \sum_{J=1}^{NP} \left[ \tilde{\mathbf{Q}}^{\nabla} \right]^T \bar{\mathbf{M}}_{[1,n]}^{-1}(\mathbf{X}) \\ &\times \mathbf{Q}_{[1,n]}(\mathbf{X}_J - \mathbf{X}) w_{\delta}(\mathbf{X}_J - \mathbf{X}) [\mathbf{f}(\mathbf{X}_J) - \mathbf{f}(\mathbf{X})]^T V_J. \end{aligned} \quad (125)$$

Likewise, the discrete non-local divergence on a vector field  $\mathbf{f}$  can be expressed as:

$$\begin{aligned} \nabla \cdot \mathbf{f}(\mathbf{X}) &\simeq \mathcal{D}_{[n]}^{\nabla} \cdot \mathbf{f}(\mathbf{X}) = \sum_{J=1}^{NP} [\mathbf{f}(\mathbf{X}_J) - \mathbf{f}(\mathbf{X})]^T \left[ \tilde{\mathbf{Q}}^{\nabla} \right]^T \\ &\times \bar{\mathbf{M}}_{[1,n]}^{-1}(\mathbf{X}) \mathbf{Q}_{[1,n]}(\mathbf{X}_J - \mathbf{X}) w_{\delta}(\mathbf{X}_J - \mathbf{X}) V_J. \end{aligned} \quad (126)$$

#### 6.4 High-order force density via non-local divergence of stress: discrete case

As discussed previously, in the original state-based peridynamic formulation under correspondence, the integral of the action of force states in terms of the nominal stress  $\boldsymbol{\sigma}^T$  can be interpreted as an operator yielding a non-local divergence operation. In the discrete case, this can be expressed as:

$$\begin{aligned} \nabla \cdot \boldsymbol{\sigma}^T(\mathbf{X}) &\rightarrow \sum_{J=1}^{NP} \left\{ \boldsymbol{\sigma}(\mathbf{X}) \mathbf{K}^{-1}(\mathbf{X}) \mathbf{P}(\mathbf{X}_J - \mathbf{X}) \right. \\ &\left. - \boldsymbol{\sigma}(\mathbf{X}_J) \mathbf{K}^{-1}(\mathbf{X}_J) \mathbf{P}(\mathbf{X} - \mathbf{X}_J) \right\} w_{\delta}(\mathbf{X}_J - \mathbf{X}) V_J. \end{aligned} \quad (127)$$

The discrete non-local divergence operation that results from the force state consistent with the high order non-local deformation gradient can be obtained using the same correspondence principle, as discussed in Sect. 4.3, and can be found by discretizing (86):

$$\begin{aligned} \nabla \cdot \boldsymbol{\sigma}^T(\mathbf{X}) &\rightarrow \sum_{J=1}^{NP} \left\{ \boldsymbol{\sigma}(\mathbf{X}) \left( \tilde{\mathbf{Q}}^{\nabla} \right)^T \bar{\mathbf{M}}_{[1,n]}^{-1}(\mathbf{X}) \mathbf{Q}_{[1,n]}(\mathbf{X}_J - \mathbf{X}) \right. \\ &\left. - \boldsymbol{\sigma}(\mathbf{X}_J) \left( \tilde{\mathbf{Q}}^{\nabla} \right)^T \bar{\mathbf{M}}_{[1,n]}^{-1}(\mathbf{X}_J) \mathbf{Q}_{[1,n]}(\mathbf{X} - \mathbf{X}_J) \right\} w_{\delta}(\mathbf{X}_J - \mathbf{X}) V_J. \end{aligned} \quad (128)$$

As discussed in Sect. 4.3, when (128) is viewed as a mathematical operator on  $\boldsymbol{\sigma}^T$ , it does not possess even 0th order accuracy in the general case. That is, when the nominal stress  $\boldsymbol{\sigma}^T$  is constant, the total force density contribution to a point  $\mathbf{X}$  may be non-zero. Again, this is also true of (127), where under a constant state of stress, the corresponding force-density could be non-zero, and the original formulation using (127) cannot guarantee even 0th order accuracy. Thus, again, despite whatever the accuracy the discrete non-local deformation gradient possesses

(using the original formulation (99) with linear accuracy, or the high-order formulation (116) with  $n$ th order accuracy), the final solution computed using either (127) or (128) may not even have 0th accuracy because of the operation of computing the force density. This assertion will be confirmed in Sect. 6.5, and in the numerical examples in Sect. 8.

Because of this, a discrete non-local divergence of the nominal stress  $\boldsymbol{\sigma}^T$  is proposed to replace both (127) and (128), which can be computed from the generalization of (126) from vectors to tensors as

$$\begin{aligned} \mathcal{D}_{[n]}^{\nabla} \cdot \boldsymbol{\sigma}^T(\mathbf{X}) &= \sum_{J=1}^{NP} (\boldsymbol{\sigma}(\mathbf{X}_J) - \boldsymbol{\sigma}(\mathbf{X}))^T \left( \tilde{\mathbf{Q}}^{\nabla} \right)^T \bar{\mathbf{M}}_{[1,n]}^{-1}(\mathbf{X}) \\ &\times \mathbf{Q}_{[1,n]}(\mathbf{X}_J - \mathbf{X}) w_{\delta}(\mathbf{X}_J - \mathbf{X}) V_J. \end{aligned} \quad (129)$$

For the linear case, the force density computed by the proposed non-local divergence can be expressed as:

$$\begin{aligned} \mathcal{D}_{[1]}^{\nabla} \cdot \boldsymbol{\sigma}^T(\mathbf{X}) &= \sum_{J=1}^{NP} (\boldsymbol{\sigma}(\mathbf{X}_J) + \boldsymbol{\sigma}(\mathbf{X}))^T \mathbf{K}^{-1}(\mathbf{X}) \\ &\times \mathbf{P}(\mathbf{X}_J - \mathbf{X}) w_{\delta}(\mathbf{X}_J - \mathbf{X}) V_J. \end{aligned} \quad (130)$$

Comparing to the standard discrete force density by peridynamics (127), which can also be simplified as

$$\begin{aligned} \nabla \cdot \boldsymbol{\sigma}^T(\mathbf{X}) &\rightarrow \sum_{J=1}^{NP} \left\{ \boldsymbol{\sigma}(\mathbf{X}) \mathbf{K}^{-1}(\mathbf{X}) + \boldsymbol{\sigma}(\mathbf{X}_J) \mathbf{K}^{-1}(\mathbf{X}_J) \right\} \\ &\times \mathbf{P}(\mathbf{X}_J - \mathbf{X}) w_{\delta}(\mathbf{X}_J - \mathbf{X}) V_J \end{aligned} \quad (131)$$

it can be seen that constant and linear accuracy (confirmed in the discrete case now, since the proposed operator is inherently  $n$ th order in the discrete case as well) can be introduced easily into the existing peridynamics formulation via a small modification.

#### 6.5 Force density test

Consider again the discretizations used in Sect. 6.2, with the uniform and non-uniform node distributions shown in Fig. 3. The interior and boundary points are again considered for testing the discrete force density by peridynamics (127) and the proposed non-local divergence of stress (129). Stresses are computed from the displacements fields listed in Sect. 6.2, yielding one order lower polynomial in the stress solution. The Lamé constants for this computation are chosen as Young's modulus  $E = 100$  and Poisson's ratio  $\nu = 0.3$ . The force density computed from the standard peridynamic technique is denoted  $\hat{T}_i^{\text{PD}}$ , while the force density from the high-order non-local divergence

**Table 3** Absolute values of errors in force density in the uniform node distribution

Stress order	Location	$\hat{T}_1^{PD}$	$\hat{T}_2^{PD}$	$\hat{T}_1^{HOPD}$	$\hat{T}_2^{HOPD}$
0	Interior point A	1.705e-13	5.684e-14	1.251e-13	1.051e-13
	Boundary point B	3.846e+3	1.602e+3	6.485e-13	5.004e-13
1	Interior point A	4.547e-13	6.821e-13	3.411e-13	2.274e-13
	Boundary point B	8.439e+3	4.187e+3	1.387e-11	9.095e-13
2	Interior point A	0.000e+0	2.273e-13	3.411e-13	1.137e-12
	Boundary point B	1.176e+4	5.990e+3	8.049e-11	3.638e-12

**Table 4** Absolute values of errors in force density in the nonuniform node distribution

Stress order	Location	$\hat{T}_1^{PD}$	$\hat{T}_2^{PD}$	$\hat{T}_1^{HOPD}$	$\hat{T}_2^{HOPD}$
0	Interior point A	937.1	657.7	2.012e-13	3.878e-13
	Boundary point B	3.204e+3	152.9	1.105e-12	6.027e-13
1	Interior point A	922.4	819.4	3.411e-13	4.548e-13
	Boundary point B	6.792e+3	1042.4	4.082e-11	2.956e-12
2	Interior point A	920.5	831.5	3.183e-12	3.411e-13
	Boundary point B	9.537e+3	1.921e+3	7.906e-10	5.275e-11

operation is denoted  $\hat{T}_i^{HOPD}$ . The order chosen in the higher-order accurate formulation is chosen to be one order higher than the stress, corresponding to the case that the same order of accuracy is used in both the deformation gradient and the force density calculation.

Tables 3 and 4 show the absolute error in the solution at the two points of interest, computed using these two methods for various orders of solutions, both for uniform and non-uniform discretizations, respectively. It can be seen that in uniform discretizations, the traditional technique can compute the correct solution in the interior of the domain for stress fields up to second-order. On the other hand, near the boundary, this method does not produce even 0th order accuracy. That is, when the stress is constant, the force density will be non-zero. For non-uniform discretizations, the traditional approach does not ever yield 0th order accuracy.

In contrast, the proposed formulation can compute the exact force density for constant, linear, and quadratic stress fields, regardless of the nodal arrangement (uniform, non-uniform), and also in the presence of a boundary. These numerical tests verify the necessity of the introduction of the non-local divergence operation introduced in Sect. 6.4. The numerical examples in Sect. 8 further demonstrate the consequences of the choice of formulation.

## 7 The reproducing kernel peridynamic method

In this section, a short summary of the proposed reproducing kernel peridynamic method is given. First, the discrete high-order deformation gradient is given in compact form, with some examples of implementation. The high-order non-local divergence of stress is then introduced, and finally, the node-based collocation formulation is given.

### 7.1 High-order non-local deformation gradient

The high-order accurate non-local deformation gradient in (116) can be expressed succinctly at a node  $\mathbf{X}_I$  as:

$$\mathcal{F}_{ij}(\mathbf{X}_I) = I_{ij} + \sum_{J=1}^{NP} \Phi_j^{IJ} [u_{Ji} - u_{Ii}] \tag{132}$$

where

$$\Phi_j^{IJ} = [\mathbf{Q}_j^{\nabla}]^T \bar{\mathbf{M}}_{[1,n]}^{-1}(\mathbf{X}_I) \mathbf{Q}_{[1,n]}(\mathbf{X}_J - \mathbf{X}_I) w_{\delta}(\mathbf{X}_J - \mathbf{X}_I) V_J. \tag{133}$$

Or, in matrix form, (132) can be expressed as:

$$\mathcal{F}(\mathbf{X}_I) = \mathbf{I} + \sum_{J=1}^{NP} \Phi^{IJ} [\mathbf{u}_J - \mathbf{u}_I]^T \quad (134)$$

with

$$\Phi^{IJ} = \left[ \tilde{\mathbf{Q}}^\nabla \right]^T \bar{\mathbf{M}}_{[1,n]}^{-1}(\mathbf{X}_I) \mathbf{Q}_{[1,n]}(\mathbf{X}_J - \mathbf{X}_I) w_\delta(\mathbf{X}_J - \mathbf{X}_I) V_J. \quad (135)$$

To take an example of the terms involved, selecting  $n = 2$ , one obtains the following:

$$\mathbf{Q}_{[1,2]}(\mathbf{X}) = [X_1, X_2, X_3, X_1^2, X_2^2, X_3^2, X_2X_3, X_1X_3, X_1X_2]^T \quad (136)$$

$$\begin{aligned} \mathbf{Q}_1^\nabla &= [1, 0, 0, 0, 0, 0, 0, 0, 0]^T \\ \mathbf{Q}_2^\nabla &= [0, 1, 0, 0, 0, 0, 0, 0, 0]^T \\ \mathbf{Q}_3^\nabla &= [0, 0, 1, 0, 0, 0, 0, 0, 0]^T \end{aligned} \quad (137)$$

$$\bar{\mathbf{M}}_{[1,2]} = \sum_{J=1}^{NP} \mathbf{Q}_{[1,2]}(\mathbf{X}_J - \mathbf{X}_I) \mathbf{Q}_{[1,2]}^T(\mathbf{X}_J - \mathbf{X}_I) w_\delta(\mathbf{X}_J - \mathbf{X}_I) V_J \quad (138)$$

where we recall here for convince  $\tilde{\mathbf{Q}}^\nabla = [\mathbf{Q}_1^\nabla, \mathbf{Q}_2^\nabla, \mathbf{Q}_3^\nabla]$ .

## 7.2 High-order non-local divergence of stress

With (132) in hand, classical techniques can be employed to compute the 1st PK stress  $\boldsymbol{\sigma}$  at each node. The non-local divergence of the nominal stress ( $\boldsymbol{\sigma}^T$ ) can then be computed at node  $\mathbf{X}_I$  as:

$$\begin{aligned} \mathcal{D}_{[n]}^\nabla \cdot \boldsymbol{\sigma}^T(\mathbf{X}_I) &= \sum_{J=1}^{NP} (\boldsymbol{\sigma}(\mathbf{X}_J) - \boldsymbol{\sigma}(\mathbf{X}_I))^T \left( \tilde{\mathbf{Q}}^\nabla \right)^T \\ &\times \bar{\mathbf{M}}_{[1,n]}^{-1}(\mathbf{X}_I) \mathbf{Q}_{[1,n]}(\mathbf{X}_J - \mathbf{X}_I) w_\delta(\mathbf{X}_J - \mathbf{X}_I) V_J \end{aligned} \quad (139)$$

or, simply,

$$\mathcal{D}_{[n]}^\nabla \cdot \boldsymbol{\sigma}^T(\mathbf{X}_I) = \sum_{J=1}^{NP} (\boldsymbol{\sigma}(\mathbf{X}_J) - \boldsymbol{\sigma}(\mathbf{X}_I))^T \Phi^{IJ} \quad (140)$$

where  $\Phi^{IJ}$  is the same term in (135). Finally, the non-local equation of motion is solved for the proposed formation under the nodal collocation framework, for all nodes  $\mathbf{X}_I$  which are not boundary nodes:

$$\ddot{\mathbf{u}}(\mathbf{X}_I, t) \rho(\mathbf{X}_I) = \mathcal{D}_{[n]}^\nabla \cdot \boldsymbol{\sigma}^T(\mathbf{X}_I, t) + \mathbf{b}(\mathbf{X}_I, t). \quad (141)$$

Procedures for construction of an elastic stiffness matrix based on peridynamic-type approximations (134) and (140) can be found in [63]. For dynamic problems, standard time integration techniques can be employed to solve the semi-discrete Eq. (141).

## 8 Numerical examples

In this section, the order of solution exactness of the collocation method using (134) and (140), described in Sect. 7, and the existing peridynamic method using (99) and (127) are tested, along with their associated convergence rates, with the resulting formulations denoted as PD for standard state-based peridynamics, and RKPD for the reproducing kernel peridynamic method, respectively. Permutations of their operators are also tested to examine the effect. Nodal quadrature is employed in all approximations of integrals.

In order to enforce essential boundary conditions, a ghost boundary layer is considered in the examples, along with direct enforcement on boundary nodes without a ghost layer to examine the effect. For ghost nodes, a layer of uniform ghost nodes is generated with thickness based on the horizon, sufficient to eliminate effects of a finite boundary. All boundary conditions are pure Dirichlet, to set aside any complications with enforcing natural boundary conditions. Finally, in addition to other nodes, ghost nodes are also employed as collocation points.

As discussed previously, convergence in peridynamics can be interpreted in a few ways [48]. For one, a non-local solution can be obtained with  $\delta$  fixed, and one may examine the error as the nodal spacing goes to zero. The numerical solution in this case converges to the non-local solution [46, 48]. On the other hand, as the non-local length scale in peridynamics goes to zero concurrently with the nodal spacing in the discretization, the numerical solution converges to the local solution [48]. In the following examples, the latter is chosen to be tested. Accordingly, horizon sizes with a fixed ratio to nodal spacing are chosen as 1.75, 2.5, and 3.5 for the linear, quadratic, and cubic order formulations, respectively. All problems are solved with influence functions chosen as the cubic B-spline in (5).

### 8.1 Patch tests

In the following set of patch tests, “PD” denotes the state-based peridynamic force density and deformation gradient, while “RKPD” indicates the proposed high-order peridynamic formulation for force density and deformation gradient. Permutations of these two formulations are tested in order to assess and verify the order of accuracy of the operators involved.

Consider a two-dimensional linear patch test, which requires recovering the exact solution by a numerical method when the solution to a boundary value problem is linear. Zero body force is prescribed with the following Dirichlet boundary conditions:

**Fig. 4** Nodal discretizations for patch tests: **a** uniform, **b** uniform with ghost nodes with two layers (used for the quadratic case), **c** nonuniform; and **d** nonuniform with ghost nodes with two layers (used for the quadratic case)

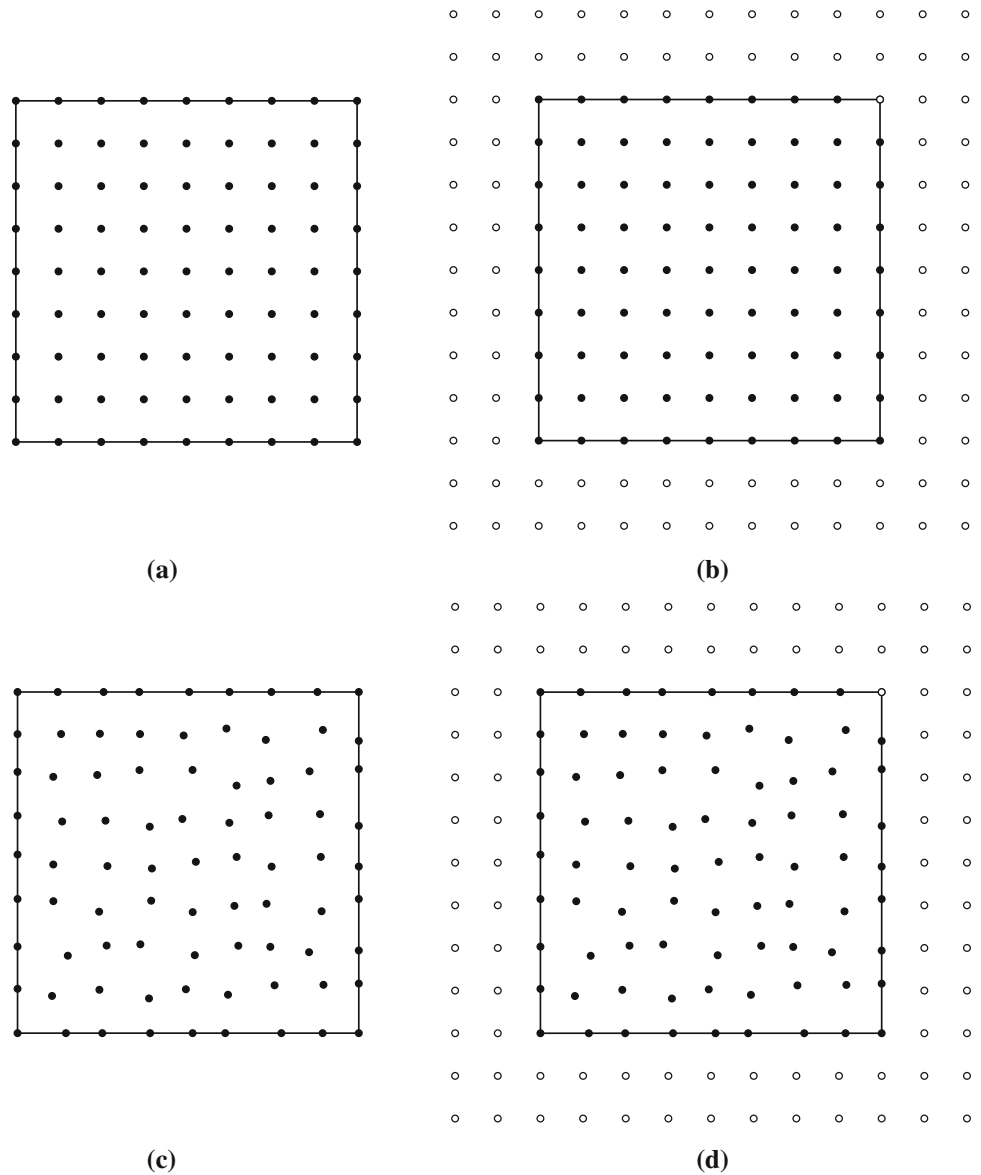


**Table 5** Linear patch test results for peridynamics and RKPD

Deformation Gradient	Force density	Discretization	Ghost boundary layer	L <sub>2</sub> error norm
Linear (standard)	PD	Uniform	No	0.072
<b>Linear (standard)</b>	<b>PD</b>	<b>Uniform</b>	<b>Yes</b>	<b>2.923e-16</b>
<b>Linear (standard)</b>	<b>RKPD</b>	<b>Uniform</b>	<b>No</b>	<b>3.043e-16</b>
Linear (standard)	PD	Non-uniform	No	0.239
Linear (standard)	PD	Non-uniform	Yes	0.358
<b>Linear (standard)</b>	<b>RKPD</b>	<b>Non-uniform</b>	<b>No</b>	<b>1.112e-15</b>

Rows of text in boldface indicates the method passes the patch test

$$\begin{aligned}
 u_1 &= 0.1x + 0.3y \quad \text{on } \Gamma_{g_1}, \\
 u_2 &= 0.2x + 0.4y \quad \text{on } \Gamma_{g_2}.
 \end{aligned}
 \tag{142}$$

With zero body force and the prescribed displacement in (142), the solution is the same linear displacement (142). Both the uniform and non-uniform discretizations shown in Fig. 4 are examined, in order to test the effect of non-

uniformity of node distributions. Here, the case with two layers of ghost nodes necessary to eliminate the boundary effect for the quadratic test is depicted for illustration. For the non-uniform case, the nodes in the uniform discretization are perturbed away from their original position in a random fashion, as shown in Fig. 4.

Table 5 shows the results for the linear patch test under various conditions. Note that the deformation gradient with linear accuracy under RKPD is coincident with the standard peridynamic deformation gradient, although the force density is not. First, it can be seen that the original formulation can only pass the linear patch test under a uniform discretization with ghost boundary nodes. On the other hand, RKPD is able to pass the patch test without ghost nodes, and in both uniform and non-uniform discretizations.

The deformation gradient analysis and tests show that the standard peridynamic deformation gradient exhibits at least linear accuracy in all situations: for a linear displacement field, such as the one in this problem, the associated constant deformation gradient is calculated exactly. Thus in this problem, the peridynamic force density is operating on a constant stress field. In the case of a non-uniform discretization and/or without ghost nodes, the standard peridynamic method fails the patch test, indicating that the peridynamic force density, considered as a mathematical operator on the stress, does not possess 0th order accuracy in non-uniform discretizations or near the boundary of the domain, which is confirmed also by the tests made in Sect. 6.5. On the other hand, these results confirm that the force density is at least 0th order accurate in uniform discretizations and away from the boundary, since in this problem it operates on a constant stress, and the patch test is passed in a uniform discretization with ghost nodes.

Now consider a quadratic patch test with the exact solution:

$$\begin{aligned} u_1 &= 0.12x + 0.14y + 0.16x^2 + 0.18xy + 0.2y^2, \\ u_2 &= 0.11x + 0.13y + 0.15x^2 + 0.1xy + 0.21y^2. \end{aligned} \quad (143)$$

The procedure to design such a higher-order patch test (boundary conditions and other prescribed data) has been described in various references (cf. [41]).

Table 6 shows the results using both linear accuracy in the deformation gradient (PD, RKPD coincident) and quadratic accuracy using RKPD, under various conditions. Once again the standard peridynamic method exhibits quadratic exactness in uniform discretizations with ghost nodes, which agrees with the analysis and other numerical tests herein. However when one or more of these

conditions is violated, the method fails to pass the patch test. The implications are discussed as follows.

Peridynamics in a uniform discretization with ghost nodes will calculate the exact linear deformation gradient for quadratic displacements; thus the peridynamic force density in this problem operates on a linear stress. And since the quadratic patch test is passed with peridynamics only in uniform discretizations with ghost nodes, this indicates that the peridynamic force density operation on the stress is at least first-order accurate in uniform discretizations, away from a boundary. And otherwise, the operator is again not even 0th order accurate, as in these cases the method fails the patch test.

Finally, the proposed formulation with second-order deformation gradient and second-order non-local divergence of stress can pass the quadratic patch test under both uniform and non-uniform discretizations, and does not need ghost nodes.

Next, a cubic patch test is considered. The boundary conditions and body force are prescribed according to the exact displacement solution:

$$\begin{aligned} u_1 &= 0.12x + 0.14y + 0.16x^2 + 0.18xy + 0.2y^2 \\ &\quad + 0.02x^3 + 0.04x^2y + 0.06xy^2 + 0.08y^3, \\ u_2 &= 0.11x + 0.13y + 0.15x^2 + 0.1xy \\ &\quad + 0.21y^2 + 0.11x^3 + 0.09x^2y + 0.07xy^2 + 0.1y^3. \end{aligned} \quad (144)$$

The results under the various conditions and permutations of formulations are shown in Table 7. With cubic accuracy in the deformation gradient, the exact quadratic deformation gradient is obtained under RKPD. Thus the standard peridynamic force density in this problem operates in some cases on a quadratic stress, and from the results in the patch test, the correct result can be obtained with uniform discretization and using a boundary layer. With this test, it is apparent that the original deformation gradient and the original force density can both yield quadratic accuracy in a uniform discretization away from the boundary, but in the general case, the force density operator does not possess even 0th order accuracy.

On the other hand, RKPD is seen to pass the patch test when both the deformation gradient and force density are calculated using the proposed formulation with cubic accuracy. Ghost nodes are not necessary, and it can pass the cubic patch test in a non-uniform discretization.

One final interesting note, is that formulations using two operators with quadratic accuracy can pass the cubic patch test in uniform discretizations with ghost nodes (i.e., the standard technique in uniform discretizations with ghost nodes, and RKPD). That is, when two operators of a certain order are used in conjunction with one another (such as a

**Table 6** Quadratic patch test results for peridynamics and RKPD

Deformation gradient	Force density	Discretization	Ghost boundary layer	$L_2$ error norm
Linear (standard)	Standard	Uniform	No	0.122
<b>Linear (standard)</b>	<b>Standard</b>	<b>Uniform</b>	<b>Yes</b>	<b>2.13E-16</b>
Linear (standard)	RKPD	Uniform	No	0.037
<b>Linear (standard)</b>	<b>RKPD</b>	<b>Uniform</b>	<b>Yes</b>	<b>2.15E-16</b>
Linear (standard)	Standard	Non-uniform	No	0.254
Linear (standard)	Standard	Non-uniform	Yes	0.388
Linear (standard)	RKPD	Non-uniform	No	0.019
Linear (standard)	RKPD	Non-uniform	Yes	0.019
Quadratic (RKPD)	Standard	Uniform	No	4.847
Quadratic (RKPD)	Standard	Uniform	Yes	0.487
<b>Quadratic (RKPD)</b>	<b>RKPD</b>	<b>Uniform</b>	<b>No</b>	<b>8.89E-15</b>
Quadratic (RKPD)	Standard	Non-uniform	No	19.63
Quadratic (RKPD)	Standard	Non-uniform	Yes	0.729
<b>Quadratic (RKPD)</b>	<b>RKPD</b>	<b>Non-uniform</b>	<b>No</b>	<b>1.37E-14</b>

Rows of text in boldface indicates the method passes the patch test

**Table 7** Cubic patch test results for peridynamics and RKPD

Deformation gradient	Force density	Discretization	Ghost boundary layer	$L_2$ error norm
Linear (standard)	Standard	Uniform	No	0.1472
<b>Linear (standard)</b>	<b>Standard</b>	<b>Uniform</b>	<b>Yes</b>	<b>3.19E-15</b>
Linear (standard)	RKPD	Uniform	No	0.0458
<b>Linear (standard)</b>	<b>RKPD</b>	<b>Uniform</b>	<b>Yes</b>	<b>2.58E-15</b>
Linear (standard)	Standard	Non-uniform	No	0.2839
Linear (standard)	Standard	Non-uniform	Yes	0.4576
Linear (standard)	RKPD	Non-uniform	No	0.0534
Linear (standard)	RKPD	Non-uniform	Yes	0.0201
Quadratic (RKPD)	Standard	Uniform	No	7.6464
<b>Quadratic (RKPD)</b>	<b>Standard</b>	<b>Uniform</b>	<b>Yes</b>	<b>1.20E-14</b>
Quadratic (RKPD)	RKPD	Uniform	No	0.0051
<b>Quadratic (RKPD)</b>	<b>RKPD</b>	<b>Uniform</b>	<b>Yes</b>	<b>1.24E-14</b>
Quadratic (RKPD)	Standard	Non-uniform	No	36.2528
Quadratic (RKPD)	Standard	Non-uniform	Yes	0.6386
Quadratic (RKPD)	RKPD	Non-uniform	No	0.0102
Quadratic (RKPD)	RKPD	Non-uniform	Yes	0.0059
Cubic (RKPD)	Standard	Uniform	No	5.3107
<b>Cubic (RKPD)</b>	<b>Standard</b>	<b>Uniform</b>	<b>Yes</b>	<b>2.02E-14</b>
<b>Cubic (RKPD)</b>	<b>RKPD</b>	<b>Uniform</b>	<b>No</b>	<b>1.40E-13</b>
Cubic (RKPD)	Standard	Non-uniform	No	4.3538
Cubic (RKPD)	Standard	Non-uniform	Yes	0.5503
<b>Cubic (RKPD)</b>	<b>RKPD</b>	<b>Non-uniform</b>	<b>No</b>	<b>7.40E-14</b>

Rows of text in boldface indicates the method passes the patch test

deformation gradient paired with the force density here), the combined formulation possesses one order of accuracy higher, at least in uniform discretizations, away from the

boundary. This observation is consistent with the results of the recursive gradient technique of using two combined operators [37].

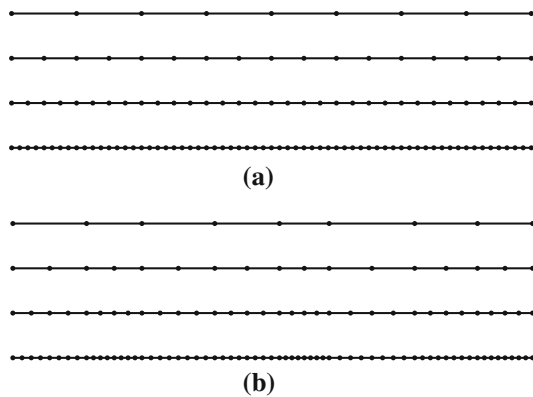


**Fig. 5** One-dimensional nodal discretizations and refinements for convergence test: **a** uniform; and **b** nonuniform

## 8.2 One-dimensional convergence in a manufactured solution

Consider the following one-dimensional equation:

$$\frac{d^2 u}{dx^2} = e^x \quad (145)$$

over the domain  $[-1, 1]$ , with boundary conditions:

$$\begin{aligned} u(-1) &= e^{-1} \\ u(1) &= e \end{aligned} \quad (146)$$

This problem can be considered a one-dimensional elastic bar with unit Young's modulus, with a high-order body force term. The solution to this problem is  $u = e^x$ .

Two cases are considered of uniform and non-uniform discretizations. The uniform case is discretized with nodal spacing  $h = [1/4, 1/8, 1/16, 1/32]$ , as shown in Fig. 5a. For the non-uniform case, shown in Fig. 5b, the first refinement of the uniform case is perturbed, with each

subsequent refinement adding nodes at the halfway point between two nodes.

The first case tested is the standard peridynamic formulation (PD) and higher-order peridynamics (RKPD) with linear accuracy. In this case, the deformation gradient calculations are the same, but the force densities differ. The convergence of the solutions in the  $L_2$  norm for uniform, non-uniform, ghost nodes, and no ghost nodes are shown in Fig. 6. Here it can be seen that the only case in which the standard peridynamic formulation converges is in the uniform case with ghost nodes. This could be attributed to the fact that in non-uniform discretizations, or in the presence of a finite boundary, the force density operation on the stress does not possess 0th order consistency. On the other hand, the proposed RKPD formulation converges at the rate of two ( $n + 1$ ) for both uniform and non-uniform discretizations, with and without ghost nodes. These results confirm the necessity of a high-order non-local divergence for a high-order numerical solution, that is, a high-order non-local deformation gradient alone is insufficient for high-order accuracy.

Finally, it should be noted that the rate of  $n + 1$  for this odd-order approximation indicates *superconvergence* of the solution. That is, in nodal collocation approaches, the rate of  $n - 1$  is observed for odd orders of accuracy [17, 36, 37, 40], with the further implication that linear completeness does not yield convergence. Meanwhile, the present formulation can converge with linear accuracy. This could be attributed to the fact that in essence, the combination of the two linear operators here produce something akin to higher-order differentiation, which is similar to the recursive gradient technique recently introduced [37], where linear basis was shown to be sufficient

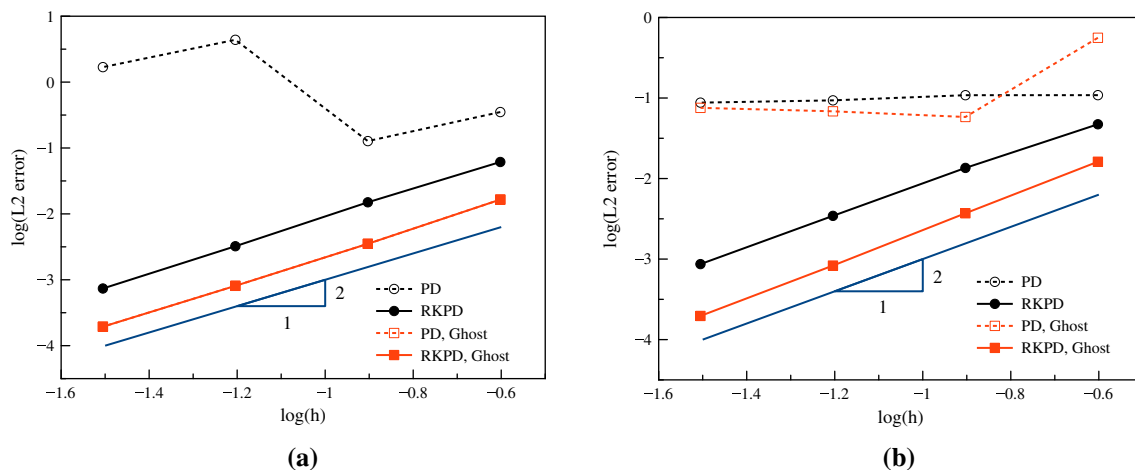


**Fig. 6** One-dimensional convergence test for PD and linear RKPD: **a** uniform discretization, **b** non-uniform discretization. In the uniform case (a), the case of PD with ghosts gives nearly identical results as RKPD with ghosts. Slope of  $n + 1$  is indicated

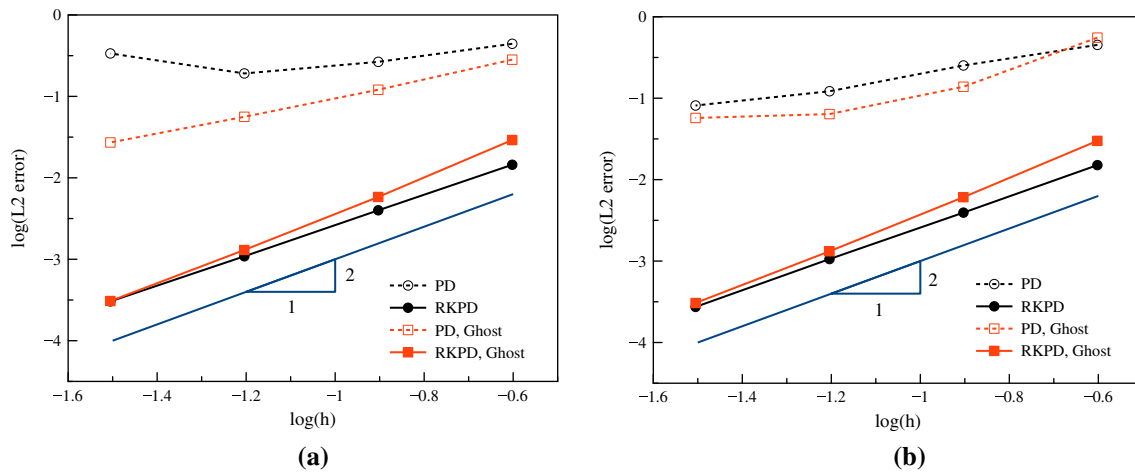


**Fig. 7** One-dimensional convergence test for PD and quadratic RKPd: **a** Uniform discretization, **b** non-uniform discretization. Slope of  $n$  is indicated

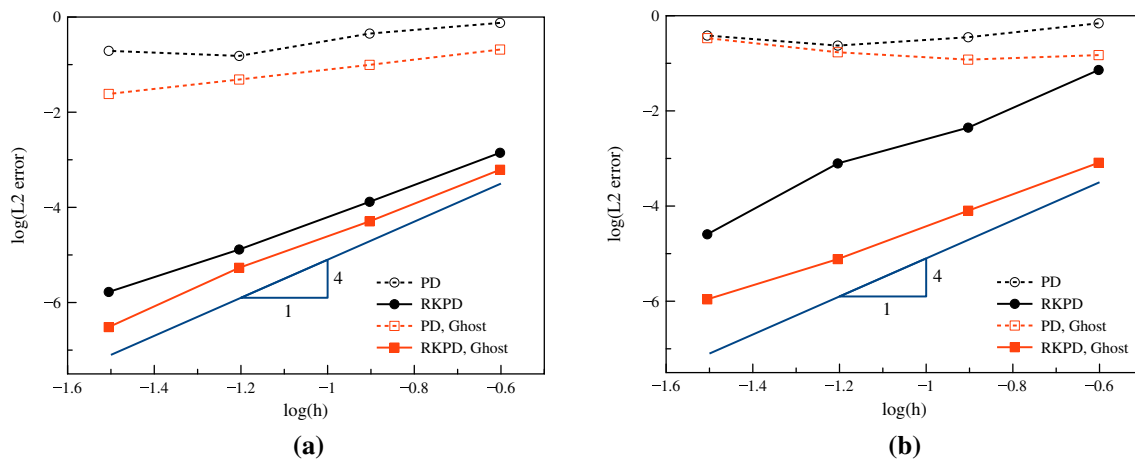


**Fig. 8** One-dimensional convergence test for PD and cubic RKPd: **a** uniform discretization, **b** non-uniform discretization. Slope of  $n + 1$  is indicated

for convergence in strong form collocation, while also exhibiting the superconvergence phenomenon.

The second case considered is a quadratic-order deformation gradient paired with the standard force density, denoted “PD” and the high-order force density, denoted “RKPd”, respectively, in order to test the effect of the different permutations, as well as the proposed RKPd formulation. Figure 7 shows the convergence plots for the cases tested. Here it can again be seen that using both the high-order deformation gradient and the high-order force density yields consistently convergent results. In addition, the proposed RKPd formulation can provide much lower errors than PD, and yields convergent solutions in both uniform and non-uniform cases tests, as well as with and without ghost nodes. On the other hand, the other cases either slowly converge, or do not converge at all. A slope of two ( $n$ ) is indicated in the figures, where it can be seen

that RKPd obtains rates consistent with nodal collocation of the strong form [17, 36–38]. That is, for even orders of accuracy, a rate of  $n$  is expected, and is obtained with the current formulation.

Finally, the cubic RKPd deformation gradient is tested, paired with the traditional force density, denoted “PD”, and the high-order force density, denoted “RKPd”. Figure 8 shows that the proposed formulation converges at the rate of  $n + 1$ , while PD does not converge at all. This again indicates superconvergence for odd orders of approximation (two orders higher than  $n - 1$  for standard nodal collocation formulations). In addition, the high-order accuracy can be obtained in uniform and non-uniform discretizations, with and without ghost nodes.

**Fig. 9** Two-dimensional nodal discretizations and refinements for convergence test: **a** uniform; and **b** nonuniform

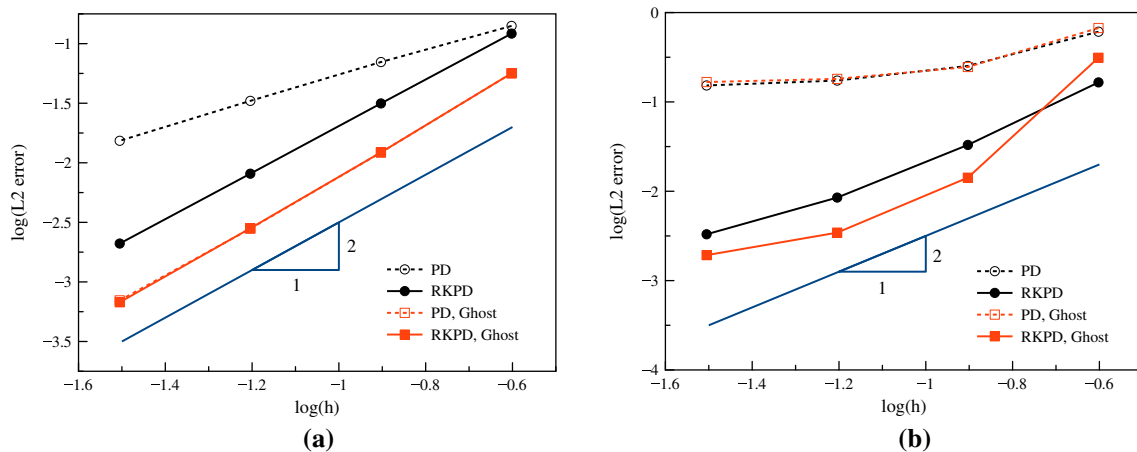
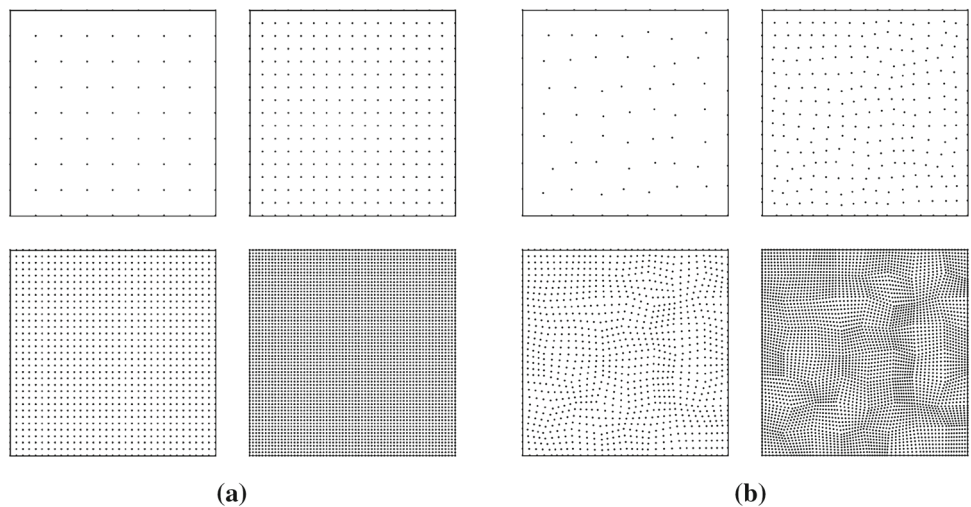


**Fig. 10** Two-dimensional convergence test for PD and linear RKP: **a** uniform discretization, **b** non-uniform discretization. In the uniform case (a), the case of PD with ghosts gives nearly identical/overlapping results as RKP with ghosts. Slope of  $n + 1$  is indicated

### 8.3 Convergence in a manufactured 2-D solution

A two dimensional manufactured plain-strain elasticity problem is considered over a domain  $[-1, 1] \times [-1, 1]$  with the following exact solution:

$$\begin{aligned} u_1 &= \sin\left(\frac{\pi x}{2}\right)\cos\left(\frac{\pi y}{2}\right), \\ u_2 &= \cos\left(\frac{\pi x}{2}\right)\sin\left(\frac{\pi y}{2}\right). \end{aligned} \tag{147}$$

Accordingly, the body force density components associated with this solution, given in components are

$$\begin{aligned} b_1 &= -\frac{E(1-\nu)\pi^2}{2(2\nu^2+\nu-1)}\sin\left(\frac{\pi x}{2}\right)\cos\left(\frac{\pi y}{2}\right), \\ b_2 &= -\frac{E(1-\nu)\pi^2}{2(2\nu^2+\nu-1)}\cos\left(\frac{\pi x}{2}\right)\sin\left(\frac{\pi y}{2}\right). \end{aligned} \tag{148}$$

where  $E$  is Young’s modulus, with  $E = 100,000$  and  $\nu$  is Poisson’s ratio, with  $\nu = 0.3$  in this example. The essential boundary conditions on all four edges of the domain are given by the displacement in (147).

As before, uniform and non-uniform discretizations are considered, shown in Fig. 9, with and without ghost boundary nodes, resulting in four test cases. The ghost nodes are uniform and the thickness of the ghost layer is selected to be sufficient to eliminate any effect of the boundary on the approximations, as in the previous examples.

First, linear accuracy in the deformation gradient (PD, RKP coincident) paired with both the standard force density (denoted PD) and the proposed high-order force density (denoted RKP) is considered. Figure 10 shows the convergence of the solution for both uniform and non-uniform discretizations. PD without ghost nodes converges

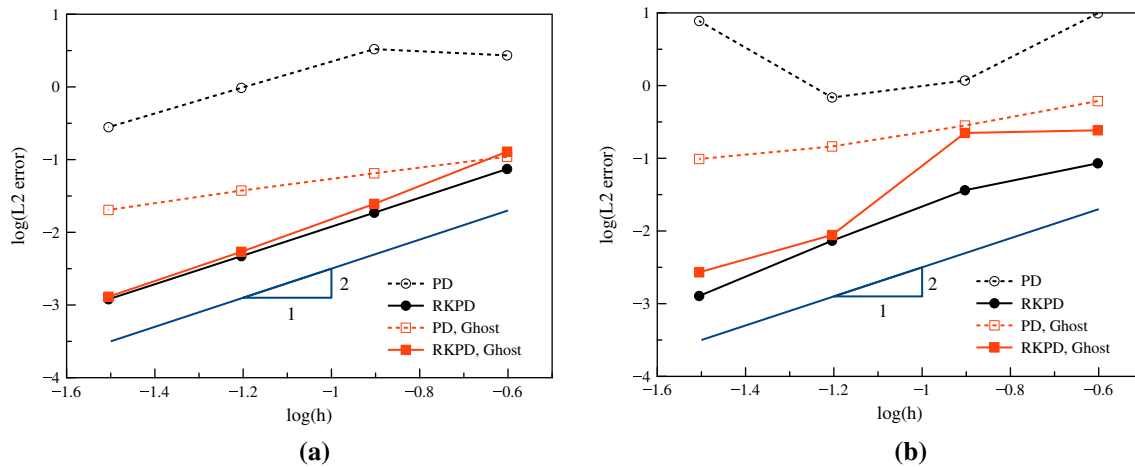


**Fig. 11** Two-dimensional convergence test for PD and quadratic RKPd: **a** uniform discretization, **b** non-uniform discretization. Slope of  $n$  indicated

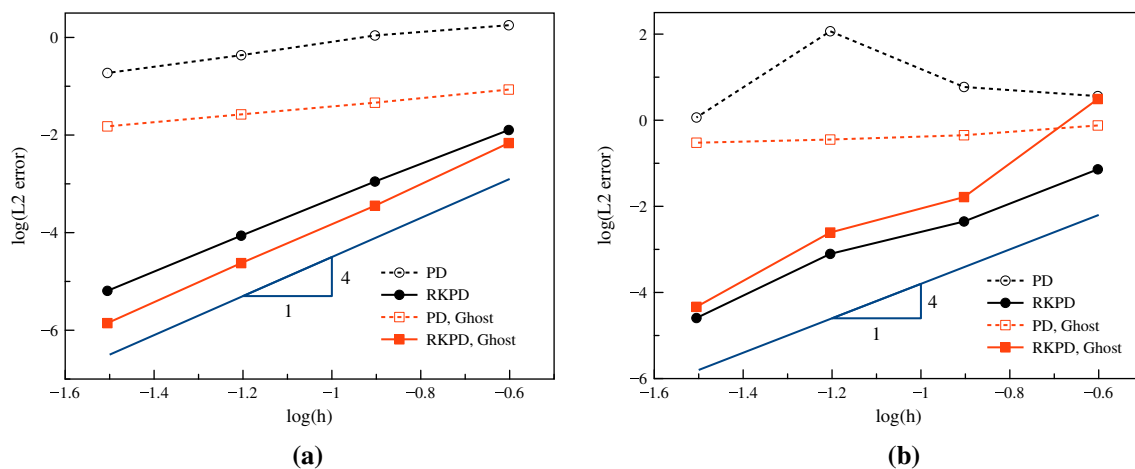


**Fig. 12** Two-dimensional convergence test for PD and cubic RKPd: **a** uniform discretization, **b** non-uniform discretization. Slope of  $n + 1$  indicated

at a rate of approximately one in the uniform case without ghost nodes, and approximately two in the case of a uniform discretization with ghost nodes. PD is seen to essentially not converge at all in the non-uniform case, likely due to the lack of consistency in the operation on stress to produce the force density in the standard formulation.

Finally, it is again seen that the proposed formulation can consistently give convergent results across all types of discretizations, with the superconvergent rate of  $n + 1$ , rather than  $n - 1$  in standard direct nodal collocation techniques.

A second-order case is considered next, with RKPd denoting second-order accurate operators, and PD denoting the second-order accurate deformation gradient paired with the standard force density. Figure 11 shows the

convergence behaviour of the various permutations in discretizations and solution techniques. The trend is similar to the one-dimensional case. Here, it is seen that second-order convergence is obtained (order  $n$ ), which is consistent with nodal collocation approaches with even-order accuracy. For the PD formulation, the solution is again seen to converge slowly or not at all, and in the case of PD without ghost nodes, the solution is seen to diverge in non-uniform discretizations.

Finally, the cubic case is considered. RKPd again denotes the pairing of the high-order deformation gradient and non-local divergence, while PD denotes the high-order deformation gradient paired with the standard force density. Figure 12 shows that the proposed RKPd formulation converges in all situations with the superconvergent rate of  $n + 1$  (rather than  $n - 1$ ), both with or without ghost

nodes, and in uniform and non-uniform discretizations. Similar to other cases, the PD approach either converges incrementally, or not at all.

## 9 Conclusion

A unification of local and non-local meshfree approximations is presented and is termed the reproducing kernel peridynamic approximation. The continuous, or integral form is presented, as well as the discrete form. With the selection of free parameters, the generalized approximation can yield both the implicit gradient approximation, and the way in which state-based peridynamics under the correspondence principle approximates derivatives via the non-local deformation gradient. Perhaps just as important, the generalization yields the ability to obtain arbitrary-order accurate non-local gradient and divergence operations, as well as higher-order non-local derivatives, with arbitrary accuracy as well. Thus, the formulation generalizes and formalizes the concept of non-local derivatives beyond first-order.

The framework also demonstrates that the non-local deformation gradient is not in fact equivalent to the implicit gradient approach, which has been speculated previously. In addition, it has been shown that the peridynamic differential operator is equivalent to the implicit gradient approximation, which by analogy is not equivalent to the generalization of the non-local approximation of derivatives.

The analysis presented demonstrates that the continuous form of the non-local deformation gradient is at best second-order accurate, but in the general case near the influence of a boundary, is first-order. In the discrete case, this deformation gradient is also at best second-order accurate, in the case of uniform nodal distributions, away from the influence of the boundary, but only at nodal locations. In all other situations, it is first-order accurate. Several numerical examples are provided to confirm this analysis.

The force density in terms of the stress, obtained via the standard peridynamic formulation is also found to be at best, second-order accurate, and at worst, without any order of consistency, which has been confirmed numerically using several tests. This work proposes a high-order accurate non-local divergence operation on the stress to replace this force density, in order to obtain globally high-order accurate numerical solutions. The pairing of the high-order non-local deformation gradient, along with the high-order non-local divergence of stress is termed the reproducing kernel peridynamic (RKPD) method. The method is tested under the collocation framework, although weak formulations are also certainly possible. It is suspected however, that in addition to the computational expense of

double integrals, numerical integration may play a key role on the convergence of the method, as in local Galerkin meshfree methods [1].

The numerical examples demonstrate that the existing peridynamic formulation can pass the linear, quadratic, and cubic patch tests, but only in uniform discretizations, with ghost nodes. In all other situations, the method fails to pass any patch test. On the other hand, the proposed formulation is able to pass arbitrary-order patch tests in both uniform and nonuniform discretizations, with and without ghost nodes.

The examples further show that the existing peridynamic formulation can generally converge at rates of two and one for uniform discretizations, with and without ghost nodes, respectively. The examples further demonstrate that in non-uniform discretizations, the standard deformation-gradient based peridynamic formulation essentially does not converge at all. This situation can be rectified by the proposed formulation, which shows consistent convergence behavior in both uniform and non-uniform discretizations, with and without ghost nodes. One noteworthy aspect of this approach is that linear accuracy will still yield convergent results, in contrast to the standard collocation approach. In addition, the proposed formulation exhibits superconvergence: a rate of  $n$  is obtained for even orders of accuracy, and  $n + 1$  for odd orders. This is in contrast to typical nodal collocation approaches, where the rates observed are  $n$  and  $n - 1$  for even and odd orders, respectively.

So far, the convergence behavior has been tested with respect to local solutions. Quadrature weights were also employed in the approximation, which are not necessary to obtain  $n$ th order accuracy. In addition, all problems tested were with pure Dirichlet boundary conditions. Finally, the performance against some existing similar methods, such as collocation with implicit gradients, or collocation with explicit gradients, was not tested, although the present generalized formulation can encapsulate these methods. Future work could examine the convergence to non-local solutions, natural boundary conditions, the approximation accuracy of the non-local approximation with and without quadrature weights, comparisons with similar numerical formulations, as well as formulation of the RKPD method under the Galerkin framework.

Other future work could possibly leverage the unification presented for techniques that have been extensively developed for local methods over the past several decades, such as the use of enrichment functions. Finally, the higher order non-local derivatives that can be obtained by the formulation have not been investigated for any particular use yet. Two possibilities would be to employ the non-local derivatives to directly discretize partial differential equations, or employ them for strain regularization in order to

avoid ambiguous boundary conditions. The direct discretization of derivatives however, is suspected to yield the typical collocation convergence rates, rather than the superconvergent rates of the present formulation.

One last point, the importance of which was emphasized by feedback from a talk on this method by the late Steve Attaway, is that under this unification, state-based peridynamic codes can be converted to use local meshfree approximation methods, while local meshfree codes can be converted to use non-local peridynamic approximations.

**Acknowledgements** Michael Hillman and Guohua Zhou greatly acknowledge the support of this work by Penn State.

## Compliance with ethical standards

**Conflict of interest** On behalf of all authors, the corresponding author states that there is no conflict of interest.

**Open Access** This article is distributed under the terms of the Creative Commons Attribution 4.0 International License (<http://creativecommons.org/licenses/by/4.0/>), which permits unrestricted use, distribution, and reproduction in any medium, provided you give appropriate credit to the original author(s) and the source, provide a link to the Creative Commons license, and indicate if changes were made.

## Appendix A: Higher order reductions and expansions

One may cast the generalization of peridynamics to  $n$ th order accuracy in terms of the entities of states given forth in [20]. We briefly recall some basic definitions and operations given and proceed to generalize them (for further details and definitions, the reader is referred to [20]).

First, the expansion of a tensor  $\mathbf{A}$  to a state  $\underline{\mathbf{A}}$  is defined as

$$\underline{\mathbf{A}} = \mathfrak{C}(\mathbf{A})\langle \mathbf{X} \rangle = \mathbf{A} \cdot \mathbf{X} \quad (149)$$

for all vectors  $\mathbf{X}$ . To relate a state to a tensor, a principle called *reduction* can be employed. First, define the reference shape tensor by the “\*” operation for states, with  $\underline{\mathbf{X}}$  by itself:

$$\begin{aligned} \mathbf{K}(\mathbf{X}) &= \underline{\mathbf{X}} * \underline{\mathbf{X}} \\ &\equiv \int_{\mathcal{H}_{\mathbf{X}}} w_{\delta}(\mathbf{X}' - \mathbf{X}) \underline{\mathbf{X}}\langle \mathbf{X}' - \mathbf{X} \rangle \otimes \underline{\mathbf{X}}\langle \mathbf{X}' - \mathbf{X} \rangle d\mathbf{X}' \end{aligned} \quad (150)$$

where  $\underline{\mathbf{X}}$  is the *reference position vector state* defined by  $\underline{\mathbf{X}}\langle \mathbf{X}' - \mathbf{X} \rangle = \mathbf{X}' - \mathbf{X}$ . The shape tensor  $\mathbf{K}(\mathbf{X})$  describes the undeformed configuration around the point  $\mathbf{X}$ . Then the reduction of a state  $\underline{\mathbf{A}}$  to a tensor  $\mathbf{A}$  is defined as

$$\mathbf{A} = \mathfrak{R}(\underline{\mathbf{A}}) = (\underline{\mathbf{A}} * \underline{\mathbf{X}}) \cdot \mathbf{K}^{-1} \quad (151)$$

It can be shown [20] that the reduction of a state obtained by the expansion of a tensor  $\mathbf{A}$  is the same tensor  $\mathbf{A}$ , that is,  $\mathfrak{R}(\mathfrak{C}(\mathbf{A})) = \mathbf{A}$ .

To relate the deformation state  $\underline{\mathbf{Y}}\langle \mathbf{X}' - \mathbf{X} \rangle = \mathbf{x}' - \mathbf{x}$  to a non-local deformation gradient  $\mathcal{F}$ , the reduction in (151) can be applied to  $\underline{\mathbf{Y}}$ :

$$\mathcal{F}(\underline{\mathbf{Y}}) = \mathfrak{R}(\underline{\mathbf{Y}}) = (\underline{\mathbf{Y}} * \underline{\mathbf{X}}) \cdot \mathbf{K}^{-1} \quad (152)$$

The above is often expressed as

$$\mathcal{F}(\underline{\mathbf{Y}}) = \mathbf{S} \cdot \mathbf{K}^{-1} \quad (153)$$

where

$$\begin{aligned} \mathbf{S}(\mathbf{X}) &= \underline{\mathbf{Y}} * \underline{\mathbf{X}} \\ &= \int_{\mathcal{H}_{\mathbf{X}}} w_{\delta}(\mathbf{X}' - \mathbf{X}) \underline{\mathbf{Y}}\langle \mathbf{X}' - \mathbf{X} \rangle \otimes \underline{\mathbf{X}}\langle \mathbf{X}' - \mathbf{X} \rangle d\mathbf{X}' \end{aligned} \quad (154)$$

is the deformed shape tensor which describes the deformed configuration around the point  $\mathbf{X}$ .

In order to generalize the concept of reduction, first define a state  $\underline{\zeta}$  which maps a vector  $\mathbf{X} \subset \mathbb{R}^d$  onto a vector  $\zeta \subset \mathbb{R}^q$  containing the complete  $n$ th order monomials greater than order zero, where  $q = (n + d)! / (n!d!) - 1$  is the total number of monomials and:

$$\underline{\zeta}\langle \mathbf{X} \rangle = \zeta = [X_1, X_2, X_3, X_1^2, \dots, X_3^n]. \quad (155)$$

We then define the  $n$ th order reference shape tensor:

$$\begin{aligned} \mathbf{K}_{[n]}(\mathbf{X}) &= \underline{\zeta} * \underline{\zeta} \\ &= \int_{\mathcal{H}_{\mathbf{X}}} w_{\delta}(\mathbf{X}' - \mathbf{X}) \underline{\zeta}\langle \mathbf{X}' - \mathbf{X} \rangle \otimes \underline{\zeta}\langle \mathbf{X}' - \mathbf{X} \rangle d\mathbf{X}' \end{aligned} \quad (156)$$

One can then define the  $n$ th order reduction of a state  $\underline{\mathbf{A}}$  to a second-order tensor  $\mathbf{A} \subset \mathbb{R}^d$

$$\mathfrak{R}_{[n]}(\underline{\mathbf{A}}) = (\underline{\mathbf{A}} * \underline{\zeta}) (\mathbf{K}_{[n]})^{-1} \cdot \hat{\mathbf{Q}} \quad (157)$$

where  $\hat{\mathbf{Q}} = \sum_{i=1}^3 \hat{\delta}^{[i]} \otimes \delta^{[i]}$ ;  $\hat{\delta}^{[i]}$  and  $\delta^{[i]}$  are identity-type vectors  $\hat{\delta}^{[i]} = [\delta_{1i} \ \delta_{2i} \ \delta_{3i} \ 0 \ \dots \ 0]$  and  $\delta^{[i]} = [\delta_{1i} \ \delta_{2i} \ \delta_{3i}]$ , of length  $q$  and three, respectively. It can be seen that the reduction (151) is the case of (157) with  $n = 1$ .

We may also define the  $n$ th order expansion, analogous to (149):

$$\mathfrak{C}_{[n]}(\mathbf{A})\langle \zeta \rangle = \mathbf{A} \cdot \zeta \quad \forall \zeta \quad (158)$$

If a state  $\underline{\mathbf{A}}$  is expanded from a second-order tensor  $\mathbf{A}$ , i.e.,  $\underline{\mathbf{A}}\langle \cdot \rangle = \mathfrak{C}_{[n]}(\mathbf{A})\langle \cdot \rangle$ , then the reduction (157) of the expansion (158) gives  $\mathbf{A}$ :

$$\begin{aligned}
 \mathfrak{R}_{[n]}(\underline{\mathbf{A}}) &= (\underline{\mathbf{A}} * \underline{\boldsymbol{\zeta}}) \cdot (\mathbf{K}_{[n]})^{-1} \cdot \hat{\mathbf{Q}} \\
 &= \left( \int_{\mathcal{H}_x} w_\delta(\mathbf{X}' - \mathbf{X}) \underline{\mathbf{A}} \cdot \underline{\boldsymbol{\zeta}} \otimes \underline{\boldsymbol{\zeta}} d\mathbf{X}' \right) \cdot (\mathbf{K}_{[n]})^{-1} \cdot \hat{\mathbf{Q}} \\
 &= \underline{\mathbf{A}} \cdot \mathbf{K}_{[n]} \cdot (\mathbf{K}_{[n]})^{-1} \cdot \hat{\mathbf{Q}} \\
 &= \underline{\mathbf{A}}
 \end{aligned} \tag{159}$$

The  $n$ th order reduction of the deformation state  $\underline{\mathbf{Y}}$  yields an  $n$ th order non-local deformation gradient tensor  $\mathcal{F}_{[n]}$ :

$$\mathcal{F}_{[n]} = \mathfrak{R}_{[n]}(\underline{\mathbf{Y}}) = \mathbf{S}_{[n]} \cdot (\mathbf{K}_{[n]})^{-1} \cdot \hat{\mathbf{Q}} \tag{160}$$

where  $\mathbf{S}_{[n]}(\mathbf{X})$  is a high-order deformed shape tensor and  $\mathbf{K}_{[n]}(\mathbf{X})$  is the high order reference shape tensor in (156)

$$\begin{aligned}
 \mathbf{S}_{[n]}(\mathbf{X}) &= \int_{\mathcal{H}_x} w_\delta(\mathbf{X}' - \mathbf{X}) \underline{\mathbf{Y}} \langle \mathbf{X}' - \mathbf{X} \rangle \otimes \underline{\boldsymbol{\zeta}} \langle \mathbf{X}' - \mathbf{X} \rangle d\mathbf{X}' \\
 \mathbf{K}_{[n]}(\mathbf{X}) &= \int_{\mathcal{H}_x} w_\delta(\mathbf{X}' - \mathbf{X}) \underline{\boldsymbol{\zeta}} \langle \mathbf{X}' - \mathbf{X} \rangle \otimes \underline{\boldsymbol{\zeta}} \langle \mathbf{X}' - \mathbf{X} \rangle d\mathbf{X}'
 \end{aligned} \tag{161}$$

The high-order non-local deformation gradient (160) is identical to the one expressed in (73).

## Appendix B: A force state for high-order non-local deformation gradients

A force state corresponding to the high-order deformation gradient can be obtained via energy principles [20]:

$$\begin{aligned}
 \Delta W &= \frac{\partial \Omega}{\partial \mathcal{F}_{ij}} \Delta \mathcal{F}_{ij} \\
 &= \frac{\partial \Omega}{\partial \mathcal{F}_{ij}} \Delta \mathcal{F}_{ijk} \cdot \Delta \underline{\mathbf{Y}}_k \\
 &= \sigma_{ij} \Delta \mathcal{F}_{ijk} \cdot \Delta \underline{\mathbf{Y}}_k
 \end{aligned} \tag{162}$$

where  $\sigma_{ij}$  is the first Piola–Kirchhoff stress tensor, and the dot product “ $\cdot$ ” for states is defined as

$$\underline{\mathbf{A}} \cdot \underline{\mathbf{B}} = \int_{\mathcal{H}_x} w_\delta(\mathbf{X}' - \mathbf{X}) \underline{\mathbf{A}} \langle \mathbf{X}' - \mathbf{X} \rangle \cdot \underline{\mathbf{B}} \langle \mathbf{X}' - \mathbf{X} \rangle d\mathbf{X}' \tag{163}$$

Using (160) and (161) we have the explicit expression

$$\begin{aligned}
 \mathcal{F}_{[n]}(\underline{\mathbf{Y}}) &= \int_{\mathcal{H}_x} w_\delta(\mathbf{X}' - \mathbf{X}) \underline{\mathbf{Y}} \langle \mathbf{X}' - \mathbf{X} \rangle \otimes \underline{\boldsymbol{\zeta}} \langle \mathbf{X}' - \mathbf{X} \rangle \\
 &\quad \cdot (\mathbf{K}_{[n]})^{-1} \cdot \hat{\mathbf{Q}} d\mathbf{X}'
 \end{aligned} \tag{164}$$

so that

$$\begin{aligned}
 \mathcal{F}_{[n]}(\underline{\mathbf{Y}} + \Delta \underline{\mathbf{Y}}) &= \mathcal{F}_{[n]}(\underline{\mathbf{Y}}) + \int_{\mathcal{H}_x} w_\delta(\mathbf{X}' - \mathbf{X}) \Delta \underline{\mathbf{Y}} \langle \mathbf{X}' - \mathbf{X} \rangle \\
 &\quad \otimes \underline{\boldsymbol{\zeta}} \langle \mathbf{X}' - \mathbf{X} \rangle \cdot (\mathbf{K}_{[n]})^{-1} \cdot \hat{\mathbf{Q}} d\mathbf{X}'
 \end{aligned} \tag{165}$$

Writing in component form,

$$\begin{aligned}
 [\mathcal{F}_{[n]}]_{ij}(\underline{\mathbf{Y}} + \Delta \underline{\mathbf{Y}}) &= [\mathcal{F}_{[n]}]_{ij}(\underline{\mathbf{Y}}) \\
 &\quad + \int_{\mathcal{H}_x} w_\delta(\mathbf{X}' - \mathbf{X}) \Delta \underline{Y}_i \langle \mathbf{X}' - \mathbf{X} \rangle \underline{\zeta}_p \langle \mathbf{X}' - \mathbf{X} \rangle (\mathbf{K}_{[n]})_{pr}^{-1} \hat{Q}_{rj} d\mathbf{X}'
 \end{aligned} \tag{166}$$

we have, rearranging (166),

$$\begin{aligned}
 [\mathcal{F}_{[n]}]_{ij}(\underline{\mathbf{Y}} + \Delta \underline{\mathbf{Y}}) &= [\mathcal{F}_{[n]}]_{ij}(\underline{\mathbf{Y}}) \\
 &\quad + \int_{\mathcal{H}_x} w_\delta(\mathbf{X}' - \mathbf{X}) \delta_{ki} \Delta \underline{Y}_k \langle \mathbf{X}' - \mathbf{X} \rangle \underline{\zeta}_p \langle \mathbf{X}' - \mathbf{X} \rangle (\mathbf{K}_{[n]})_{pr}^{-1} \hat{Q}_{rj} d\mathbf{X}' \\
 &= [\mathcal{F}_{[n]}]_{ij}(\underline{\mathbf{Y}}) + \Delta \underline{Y}_k \cdot [\Delta \mathcal{F}_{[n]}]_{ijk}
 \end{aligned} \tag{167}$$

where

$$[\Delta \mathcal{F}_{[n]}]_{ijk} = w_\delta(\mathbf{X}' - \mathbf{X}) \delta_{ki} \underline{\zeta}_p \langle \mathbf{X}' - \mathbf{X} \rangle (\mathbf{K}_{[n]})_{pr}^{-1} \hat{Q}_{rj} \tag{168}$$

Then using (162) we have

$$\begin{aligned}
 \Delta W &= \sigma_{ij} [\Delta \mathcal{F}_{[n]}]_{ijk} \cdot \Delta \underline{\mathbf{Y}}_k \\
 &= \sigma_{ij} w_\delta(\mathbf{X}' - \mathbf{X}) \delta_{ki} \underline{\zeta}_p \langle \mathbf{X}' - \mathbf{X} \rangle (\mathbf{K}_{[n]})_{pr}^{-1} \hat{Q}_{rj} \cdot \Delta \underline{\mathbf{Y}}_k \\
 &= \sigma_{kj} w_\delta(\mathbf{X}' - \mathbf{X}) \underline{\zeta}_p \langle \mathbf{X}' - \mathbf{X} \rangle (\mathbf{K}_{[n]})_{pr}^{-1} \hat{Q}_{rj} \cdot \Delta \underline{\mathbf{Y}}_k \\
 &= \sigma_{kj} w_\delta(\mathbf{X}' - \mathbf{X}) \hat{Q}_{rj} (\mathbf{K}_{[n]})_{pr}^{-1} \underline{\zeta}_p \langle \mathbf{X}' - \mathbf{X} \rangle \cdot \Delta \underline{\mathbf{Y}}_k
 \end{aligned} \tag{169}$$

For an elastic peridynamic continuum [20],  $\underline{\mathbf{T}} = \Delta W(\underline{\mathbf{Y}})$  and thus we have

$$\underline{T}_i = w_\delta(\mathbf{X}' - \mathbf{X}) \sigma_{ij} \hat{Q}_{rj} (\mathbf{K}_{[n]})_{rp}^{-1} \underline{\zeta}_p \langle \mathbf{X}' - \mathbf{X} \rangle \tag{170}$$

Finally, using the Piola transformation for the first PK stress  $\sigma_{ij} = J \tau_{ik} \mathcal{F}_{jk}^{-1}$  where  $J = \det(\mathcal{F})$  and  $\boldsymbol{\tau}$  is the Cauchy stress, it can be shown that the definition of the force state (170) satisfies angular momentum according to the requirements put forth in [20]:

$$\begin{aligned}
 & \left( \int_{\mathcal{H}_{\mathbf{x}}} \mathbf{Y}(\mathbf{X}' - \mathbf{X}) \times \mathbf{T}(\mathbf{X}' - \mathbf{X}) d\mathbf{X}' \right)_i \\
 &= e_{ijk} \left( \int_{\mathcal{H}_{\mathbf{x}}} \underline{Y}_j(\mathbf{X}' - \mathbf{X}) w_\delta(\mathbf{X}' - \mathbf{X}) (J\tau_{ks} \mathcal{F}_{qs}^{-1}) \hat{Q}_{pq}(\mathbf{K}_{[n]})_{pr}^{-1} \zeta_r(\mathbf{X}' - \mathbf{X}) d\mathbf{X}' \right) \\
 &= e_{ijk} (J\tau_{ks} \mathcal{F}_{qs}^{-1}) \hat{Q}_{pq}(\mathbf{K}_{[n]})_{pr}^{-1} \left( \int_{\mathcal{H}_{\mathbf{x}}} \underline{Y}_j(\mathbf{X}' - \mathbf{X}) w_\delta(\mathbf{X}' - \mathbf{X}) \zeta_r(\mathbf{X}' - \mathbf{X}) d\mathbf{X}' \right) \\
 &= e_{ijk} (J\tau_{ks} \mathcal{F}_{qs}^{-1}) \hat{Q}_{pq}(\mathbf{K}_{[n]})_{pr}^{-1} (\mathbf{S}_{[n]})_{jr} \\
 &= e_{ijk} (J\tau_{ks} \mathcal{F}_{qs}^{-1}) \mathcal{F}_{jq} \\
 &= e_{ijk} J\tau_{ks} \delta_{js} \\
 &= e_{ijk} J\tau_{kj} \\
 &= 0
 \end{aligned} \tag{171}$$

where  $e_{ijk}$  is the Levi-Civita symbol.

## References

- Chen J-S, Hillman M, Chi S-W (2017) Meshfree methods: progress made after 20 years. *J Eng Mech* 143(4):04017001
- Nayroles B, Touzot G, Villon P (1992) Generalizing the finite element method: diffuse approximation and diffuse elements. *Comput Mech* 10(5):307–318
- Belytschko T, Lu YY, Gu L (1994) Element-free Galerkin methods. *Int J Numer Methods Eng* 37:229–256
- Liu WK, Jun S, Zhang YF (1995) Reproducing kernel particle methods. *Int J Numer Methods Fluids* 20(8–9):1081–1106
- Chen J-S, Pan C, Wu C-T, Liu WK (1996) Reproducing kernel particle methods for large deformation analysis of non-linear structures. *Comput Methods Appl Mech Eng* 139(1–4):195–227
- Strouboulis T, Copps K, Babuška I (2001) The generalized finite element method. *Comput Methods Appl Mech Eng* 190(32–33):4081–4193
- Melenk JM, Babuška I (1996) The partition of unity finite element method: basic theory and applications. *Comput Methods Appl Mech Eng* 139(1–4):289–314
- Babuška I, Melenk JM (1997) The partition of unity method. *Int J Numer Methods Eng* 40(4):727–758
- Duarte CAM, Oden JT (1996) An h-p adaptive method using clouds. *Comput Methods Appl Mech Eng* 139(1–4):237–262
- Duarte CAM, Oden JT (1996) H-p clouds—an h-p meshless method. *Numer Methods Partial Differ Equ* 12(6):673–705
- Atluri SN, Zhu TL (1998) A new meshless local Petrov–Galerkin (MLPG) approach in computational mechanics. *Comput Mech* 22(2):117–127
- Sukumar N, Belytschko T (1998) The natural element method in solid mechanics. *Int J Numer Methods Eng* 43(5):839–887
- Griebel M, Schweitzer MA (2000) A particle-partition of unity method for the solution of elliptic, parabolic, and hyperbolic PDEs. *SIAM J Sci Comput* 22(3):853–890
- Kansa EJ (1990) Multiquadrics—a scattered data approximation scheme with applications to computational fluid-dynamics—I surface approximations and partial derivative estimates. *Comput Math Appl* 19(8–9):127–145
- Kansa EJ (1990) Multiquadrics—a scattered data approximation scheme with applications to computational fluid-dynamics—II solutions to parabolic, hyperbolic and elliptic partial differential equations. *Comput Math Appl* 19(8–9):147–161
- Oñate E, Idelsohn SR, Zienkiewicz OC, Taylor RL (1996) A finite point method in computational mechanics. Applications to convective transport and fluid flow. *Int J Numer Methods Eng* 39:3839–3866
- Aluru NR (2000) A point collocation method based on reproducing kernel approximations. *Int J Numer Methods Eng* 47(6):1083–1121
- Hu H-Y, Chen J-S, Hu W (2011) Error analysis of collocation method based on reproducing kernel approximation. *Numer Methods Partial Differ Equ* 27(3):554–580
- Silling SA (2000) Reformulation of elasticity theory for discontinuities and long-range forces. *J Mech Phys Solids* 48(1):175–209
- Silling SA, Epton MA, Weckner O, Xu J, Askari E (2007) Peridynamic states and constitutive modeling. *J Elast* 88(2):151–184
- Chen X, Gunzburger M (2011) Continuous and discontinuous finite element methods for a peridynamics model of mechanics. *Comput Methods Appl Mech Eng* 200(9–12):1237–1250
- Madenci E, Dorduncu M, Barut A, Phan N (2018) Weak form of peridynamics for nonlocal essential and natural boundary conditions. *Comput Methods Appl Mech Eng* 337:598–631
- Littlewood DJ (2016) Roadmap for peridynamic software implementation. In: Bobaru F, Foster JT, Geubelle PH, Silling SA (eds) *Handbook of peridynamic modeling*. CRC Press, Boca Raton
- Silling SA, Askari E (2005) A meshfree method based on the peridynamic model of solid mechanics. *Comput Struct* 83(17–18):1526–1535
- Gingold RA, Monaghan JJ (1977) Smoothed particle hydrodynamics—theory and application to non-spherical stars. *Mon Not R Astron Soc* 181:375–389
- Lucy LB (1977) A numerical approach to the testing of the fission hypothesis. *Astron J* 82:1013–1024
- Bessa MA, Foster JT, Belytschko T, Liu WK (2014) A meshfree unification: reproducing kernel peridynamics. *Comput Mech* 53(6):1251–1264
- Liu WK, Chen Y, Chang CT, Belytschko T (1996) Advances in multiple scale kernel particle methods. *Comput Mech* 18(2):73–111
- Liu WK, Li S, Belytschko T (1997) Moving least-square reproducing kernel methods (I) methodology and convergence. *Comput Methods Appl Mech Eng* 143(1–2):113–154
- Han W, Meng X (2001) Error analysis of the reproducing kernel particle method. *Comput Methods Appl Mech Eng* 190(46–47):6157–6181
- Chen J-S, Han W, You Y, Meng X (2003) A reproducing kernel method with nodal interpolation property. *Int J Numer Methods Eng* 56(7):935–960
- Madych WR, Nelson SA (1990) Multivariate interpolation and conditionally positive definite functions II. *Math Comput* 54(189):211–230
- Madych WR (1992) Miscellaneous error bounds for multiquadric and related interpolators. *Comput Math Appl* 24(12):121–138
- Hu H-Y, Chen J-S, Hu W (2007) Weighted radial basis collocation method for boundary value problems. *Int J Numer Methods Eng* 69(13):2736–2757
- Hu H-Y, Lai C-K, Chen J-S (2009) A study on convergence and complexity of reproducing kernel collocation method. *Interact Multiscale Mech* 2(3):295–319
- Chi S-W, Chen J-S, Hu H-Y, Yang JP (2013) A gradient reproducing kernel collocation method for boundary value problems. *Int J Numer Methods Eng* 93(13):1381–1402

37. Wang D, Wang J, Wu J (2018) Superconvergent gradient smoothing meshfree collocation method. *Comput Methods Appl Mech Eng* 340:728–766
38. Qi D, Wang D, Deng L, Xu X, Wu C-T (2019) Reproducing kernel mesh-free collocation analysis of structural vibrations. *Eng Comput* 36:736–764
39. Auricchio F, Da Veiga LB, Hughes TJR, Reali A, Sangalli G (2010) Isogeometric collocation methods. *Math Model Methods Appl Sci* 20(11):2075–2107
40. Schilling D, Evans JA, Reali A, Scott MA, Hughes TJR (2013) Isogeometric collocation: cost comparison with Galerkin methods and extension to adaptive hierarchical NURBS discretizations. *Comput Methods Appl Mech Eng* 267:170–232
41. Chen J-S, Hillman M, Rüter M (2013) An arbitrary order variationally consistent integration for Galerkin meshfree methods. *Int J Numer Methods Eng* 95(5):387–418
42. Bobaru F, Yang M, Alves LF, Silling SA, Askari E, Xu J (2009) Convergence, adaptive refinement, and scaling in 1D peridynamics. *Int J Numer Methods Eng* 77(6):852–877
43. Du Q (2016) Local limits and asymptotically compatible discretizations. In: Bobaru F, Foster JT, Geubelle PH, Silling SA (eds) *Handbook of peridynamic modeling*. CRC Press, Boca Raton
44. Du Q (2014) Asymptotically compatible schemes for peridynamics based on numerical quadratures. In: *ASME 2014 international mechanical engineering congress and exposition*. American Society of Mechanical Engineers
45. Queiruga AFF, Moridis G (2017) Numerical experiments on the convergence properties of state-based peridynamic laws and influence functions in two-dimensional problems. *Comput Methods Appl Mech Eng* 322:97–122
46. Seleson P, Littlewood DJ (2016) Convergence studies in mesh-free peridynamic simulations. *Comput Math Appl* 71(11):2432–2448
47. Parks ML, Lehoucq RB, Plimpton SJ, Silling SA (2008) Implementing peridynamics within a molecular dynamics code. *Comput Phys Commun* 179(11):777–783
48. Bobaru F, Ha YD (2011) Adaptive refinement and multiscale modeling in 2D peridynamics. *Int J Multiscale Comput Eng* 9(6):635–660
49. Seleson P (2014) Improved one-point quadrature algorithms for two-dimensional peridynamic models based on analytical calculations. *Comput Methods Appl Mech Eng* 282:184–217
50. Pasetto M, Leng Y, Chen J-S, Foster JT, Seleson P (2018) A reproducing kernel enhanced approach for peridynamic solutions. *Comput Methods Appl Mech Eng* 340:1044–1078
51. Freimanis A, Paeglitis A (2017) Mesh sensitivity in peridynamic quasi-static simulations. *Proc Eng* 172:284–291
52. Yaghoobi A, Chorzepa MG (2017) Higher-order approximation to suppress the zero-energy mode in non-ordinary state-based peridynamics. *Comput Struct* 188:63–79
53. Bažant ZP, Luo W, Chau VT, Bessa MA (2016) Wave dispersion and basic concepts of peridynamics compared to classical non-local damage models. *J Appl Mech* 83(11):111004
54. Ren B, Fan H, Bergel GL, Regueiro RA, Lai X, Li S (2014) A peridynamics–SPH coupling approach to simulate soil fragmentation induced by shock waves. *Comput Mech* 55(2):287–302
55. Chen J-S, Zhang X, Belytschko T (2004) An implicit gradient model by a reproducing kernel strain regularization in strain localization problems. *Comput Methods Appl Mech Eng* 193(27–29):2827–2844
56. Madenci E, Barut A, Futch M (2016) Peridynamic differential operator and its applications. *Comput Methods Appl Mech Eng* 304:408–451
57. Li S, Liu WK (1998) Synchronized reproducing kernel interpolant via multiple wavelet expansion. *Comput Mech* 21:28–47
58. Hillman M, Chen J-S (2016) Nodally integrated implicit gradient reproducing kernel particle method for convection dominated problems. *Comput Methods Appl Mech Eng* 299:381–400
59. Li S, Liu WK (1999) Reproducing kernel hierarchical partition of unity, part I—formulation and theory. *Int J Numer Methods Eng* 288:251–288
60. Li S, Liu WK (1999) Reproducing kernel hierarchical partition of unity, part II—applications. *Int J Numer Methods Eng* 45(3):289–317
61. Liszka TJ, Orkisz J (1980) The finite difference method at arbitrary irregular grids and its application in applied mechanics. *Comput Struct* 11(1–2):83–95
62. Chen J-S, Pan C, Roque CMOL, Wang H-P (1998) A Lagrangian reproducing kernel particle method for metal forming analysis. *Comput Mech* 22(3):289–307
63. Breitenfeld MS, Geubelle PH, Weckner O, Silling SA (2014) Non-ordinary state-based peridynamic analysis of stationary crack problems. *Comput Methods Appl Mech Eng* 272:233–250

**Publisher's Note** Springer Nature remains neutral with regard to jurisdictional claims in published maps and institutional affiliations.

# Nodally integrated thermomechanical RKPM: Part I — Thermoelasticity

Michael Hillman<sup>\*†</sup> and Kuan-Chung Lin<sup>‡</sup>

This is a post-peer-review, pre-copyedit version of an article [to be] published in Computational Mechanics. The final authenticated version is [will be] available online at: <http://dx.doi.org/10.1007/s00466-021-02047-9>.

## Abstract

In this two-part paper, a stable and efficient nodally-integrated reproducing kernel particle method (RKPM) is introduced for solving the governing equations of generalized thermomechanical theories. Part I investigates quadrature in the weak form using coupled and uncoupled classical thermoelasticity as model problems. It is first shown that nodal integration of these equations results in spurious oscillations in the solution many orders of magnitude greater than pure elasticity. A naturally stabilized nodal integration is then proposed for the coupled equations. The variational consistency conditions for  $n$ th order exactness and convergence in the two-field problem are then derived, and a uniform correction on the test function approximations is proposed to achieve these conditions. Several benchmark problems are solved to demonstrate the effectiveness of the proposed method. In the sequel, these methods are developed for generalized thermoelasticity and generalized finite-strain thermoplasticity theories of the hyperbolic type that are amenable to efficient explicit time integration.

**keywords** Meshfree, thermoelasticity, nodal integration, naturally stabilized nodal integration, variationally consistent integration, coupled problems

## 1 Introduction

The interaction between temperature, stress, and deformation is an important consideration in many engineering problems. The need for solving these partially- or fully-coupled systems may arise due to the presence of fracture, bending, contact, and friction, among other phenomena. Certain sub-classes of these problems such as additive and subtractive manufacturing also involve a large degree of material deformation, flow, and failure, with associated topological changes in the domain. Here, the use of mesh-based methods for analysis is obviously non-trivial. On the other hand, meshfree methods are adept at handling these phenomena, yet an effective solution technique requires careful treatment of quadrature, which is essentially an open-problem for meshfree thermomechanical analysis. In addition, the time step restriction for the associated classical parabolic type of energy equation is too restrictive

---

<sup>\*</sup>Kimball Assistant Professor, Department of Civil and Environmental Engineering, The Pennsylvania State University, University Park, PA 16802, USA.

<sup>†</sup>Corresponding author; email: [mhillman@psu.edu](mailto:mhillman@psu.edu); postal address: 224A Sackett Building, The Pennsylvania State University, University Park, PA 16802, USA.

<sup>‡</sup>Assistant Professor, Department of Civil Engineering, National Cheng Kung University, Tainan 70101, Taiwan, ROC.

for explicit analysis, which is often used for meshfree methods in extreme-deformation problems. The subject of this two-part paper is to address these issues and propose a stable and efficient meshfree technique for thermomechanical problems under the reproducing kernel particle method (RKPM) framework [39, 12, 40], which possesses  $n$ th-order accuracy and associated optimal convergence rates in smooth problems [40].

In this first part, efficient and stable quadrature of the Galerkin weak form for thermomechanical analysis is developed using classical thermoelasticity as a model problem. In the sequel, these approaches are extended to generalized thermoelasticity and generalized finite-strain plasticity theories of the hyperbolic type.

Due to the limitations of closed-form solutions to the classical thermoelastic equations e.g., [18, 19, 56, 5], numerical techniques are of course desired for more complex geometries and boundary conditions, in other words, applications. Numerical approaches to the classical theory have been developed over the past several decades, including finite element-based approaches [33, 6, 7, 48, 32] and boundary element methods [55, 8, 57, 29].

Meshfree methods [10] have also been developed for both coupled and uncoupled thermoelasticity. The element-free Galerkin method (EFG) has been used to solve the problem of shape optimization in linear thermoelastic solids [4]. The meshless local Petrov-Galerkin method (MLPG) has been employed for problems with orthotropic material properties [54], using various trial approximations [17, 50, 67]. Later, direct MLPG [23] was developed for thermoelasticity.

In these approaches, EFG uses quadrature points based on background cells which necessitates very high order (and thus expensive) quadrature for acceptable accuracy [20, 14, 11, 66]. For MLPG, integration is performed over local meshfree nodal domains, employing several quadrature points per cell, which is also expensive [24]. In addition, as recently shown in [66], even high-order quadrature is not variationally consistent (VC) [11], and it is theoretically impossible to converge at optimal rates and achieve the level of accuracy offered by the trial functions employed in the Galerkin solution with traditional quadrature. In [66], this analytical result was unequivocally demonstrated, offering new insight into the importance of alternative integration approaches in meshfree methods.

In contrast to classical approaches, nodal integration methods generally employ one quadrature point per node, and can greatly accelerate meshfree computations. They are also favored due to their relative simplicity, and their ability to preserve the mesh-free characteristics of the method on the quadrature level. Yet pure nodal integration, known as direct nodal integration (DNI) in the literature, exhibits poor solution accuracy and spatial instability in the form of oscillations [24]. The instability arises due to a zero gradient at nodal points for modes with a wavelength of twice the nodal spacing [2, 3, 14], severely under-sampling the strain energy density. Thus small-wavelength modes are admitted in the solution with little to no resistance, and can hence either severally pollute the solution or grow unbounded.

To circumvent this issue, several stabilized nodal integration methods have been proposed. In [2] a residual-based method was developed that supplements the Galerkin formulation with second-order gradient terms, which are non-zero at nodes. This method however necessitates the computation of high-order meshfree gradients which

are expensive, and it is not clear how to straightforwardly generalize a residual approach to non-linear solid mechanics. Stress points [51, 22] can eliminate the instability by sampling the internal energy at locations away from the nodes, but this can significantly increase the computational cost. A highly efficient stabilized conforming nodal integration (SCNI) has been proposed [14], which stabilizes the solution by employing strain-smoothing, and further provides first-order variational consistency (Galerkin exactness). A modified SCNI (MSCNI) has been developed [9, 49] to alleviate some remaining instabilities in SCNI when the discretization is sufficiently fine or the surface to volume ratio is small. Additional integration points are added in the nodal subdomain to sample the solution away from the nodes, similar to stress points. Taylor series expansions on strains [45, 38, 24, 44] (which originates from the finite element method [41]) and related methods [64, 63] can also stabilize the solution, and avoid the expense of sampling/stress points. In order to reduce the computational cost of meshfree gradients of strain in this method, a naturally stabilized nodal integration (NSNI) has been proposed [24] which employs implicit gradients (originating from synchronized derivatives [35] and the reproducing kernel hierarchical partition of unity method [36, 37]). This approach has been shown to accelerate computations by an order of magnitude over sampling point-type methods [24].

In order to correct the accuracy of nodal integration methods, several additional/combined approaches have been developed. In [14] it was shown that a condition exists on the numerical integration and test function in order to obtain first-order Galerkin exactness. This can be achieved using the SCNI technique via conforming strain smoothing. Later, the condition was generalized to the concept of variational consistency [11], or the conditions for arbitrary  $n$ th order exactness, where a correction was proposed to uniformly correct any choice of quadrature including nodal integration. The corrected integration methods using this approach are herein given a prefix as "VC-", e.g., VC-NSNI. SCNI has been extended under various frameworks to achieve higher-order variational consistency, such as quadratically consistent integration [21], and reproducing kernel gradient smoothing [60].

So far, only the strain-gradient methods in [64, 63] have been applied to thermo-mechanical analysis [65]. Staggered time integration was employed to overcome the time step restriction in the energy equation, and momentum smoothing was used for stabilization, both of which complicate the overall solution algorithm. In addition, the nodal integration employed violates the critical condition of variational consistency. The only other related methods are for the tangential problem of porous media. In [62], MSCNI was developed for poromechanics. To avoid the limitation of conforming cells in extreme deformation problems, a non-conforming version was proposed in [53, 42], but the relaxation of the conforming condition in strain-smoothing results in a loss of variational consistency and thus convergence [11]. To greatly reduce the computational cost of MSCNI, and circumvent the limitations of non-conforming methods, VC-NSNI was recently proposed for porous media simulation [61]. There the VC conditions for first order exactness were derived, yet an approximate lower-order condition was instead corrected for.

In this work, a nodally-integrated RKPM is developed for thermomechanical analysis. In Part I of this series, the VC conditions for arbitrary-order accuracy in the

Galerkin solution of the coupled problem of thermoelasticity are derived. It is shown that the conditions here require additional restrictions on the test functions compared to pure elasticity. A variationally consistent correction is then proposed to exactly satisfy the constraints up to  $n$ th order. To stabilize the meshfree solution, a naturally stabilized nodal integration is further proposed. Here it is shown that for thermoelastic problems, the solution instability in DNI results in oscillations *many orders of magnitude greater than in pure elasticity*, yielding meaningless results. The combined method VC-NSNI is then applied to several quasi-static and dynamic thermoelastic benchmark problems where stability and high accuracy in RKPM are achieved using the proposed nodal integration. Part II of this work extends these methods to generalized thermoelasticity theories and generalized finite-strain thermoplasticity, both of the hyperbolic type, in order to facilitate accelerated computations in explicit dynamics and a uniform time integration on displacement and temperature variables.

The remainder of this paper is organized as follows. The equations of thermoelasticity are given in Section 2. In Section 3 the reproducing kernel approximation is reviewed. Section 4 explores the challenges and instabilities in direct nodal integration for thermoelasticity. In Sections 5-7 NSNI, variationally consistent integration (VCI), and VC-NSNI are introduced for thermoelasticity. Numerical implementation details are given in Section 8, with the matrix forms and Newmark algorithm for the thermoelastic equations. Several static, quasi-static, and dynamic benchmark problems are solved in Section 9, with the proposed thermomechanical RKPM results compared with analytical solutions, and solutions by other numerical methods. Concluding remarks are then given in Section 10.

## 2 Governing equations and weak formulation

### 2.1 Strong form of thermoelasticity

#### 2.1.1 Equations of motion and energy conservation

Consider a domain  $\Omega \times ]0, t_f[$  with boundary  $\partial\Omega \times ]0, t_f[$ . The governing equations for linear thermoelasticity on the domain are [47]:

$$\nabla \cdot \boldsymbol{\sigma} + \mathbf{b} = \rho \ddot{\mathbf{u}} \quad (1)$$

$$-\nabla \cdot \mathbf{q} - \rho c_p \dot{\theta} + Q - \beta T_0 \nabla \cdot \dot{\mathbf{u}} = 0 \quad (2)$$

where  $\nabla$  is the Del operator,  $\boldsymbol{\sigma}$  is the Cauchy stress tensor,  $\mathbf{b}$  is a prescribed body force,  $\rho$  is the density,  $\ddot{\mathbf{u}} \equiv \partial^2 \mathbf{u} / \partial t^2$  is the acceleration;  $\mathbf{u}$  is the displacement field and herein is treated as a primary unknown,  $\mathbf{q}$  is the heat flux,  $c_p$  is the heat capacity,  $\theta \equiv T - T_0$  is the temperature difference and is treated as a primary unknown;  $T$  is the absolute temperature,  $T_0$  is the reference temperature and  $\dot{\theta} \equiv \partial \theta / \partial t$ ;  $Q$  is a prescribed heat source,  $\beta = \bar{\alpha}(3\lambda + 2\mu)$  is the thermal stress modulus;  $\bar{\alpha}$  is the thermal expansion coefficient,  $\lambda$  and  $\mu$  are Lamé's first and second constants; and  $\dot{\mathbf{u}} \equiv \partial \mathbf{u} / \partial t$  is the velocity.

Equation (1) is the conservation of linear momentum and (2) is the energy equation, or first law of thermodynamics (under specific assumptions). The nature of

coupling between the two primary fields of displacement  $\mathbf{u}$  and temperature difference  $\theta$  is dictated by the prescribed constitutive laws for  $\boldsymbol{\sigma}$  and  $\mathbf{q}$ .

Note that for the linear thermoelasticity, a small increment of the temperature difference compared with the reference temperature is assumed [47], that is

$$\frac{|\theta|}{T_0} \ll 1. \quad (3)$$

The boundary conditions associated with (1) and (2) are

$$\mathbf{u} = \mathbf{g} \quad \text{on } \partial\Omega_{\mathbf{g}} \times ]0, t_f[ \quad (4a)$$

$$\boldsymbol{\sigma} \cdot \mathbf{n} = \mathbf{h} \quad \text{on } \partial\Omega_{\mathbf{h}} \times ]0, t_f[ \quad (4b)$$

$$\theta = \bar{\theta} \quad \text{on } \partial\Omega_T \times ]0, t_f[ \quad (4c)$$

$$\mathbf{q} \cdot \mathbf{n} = \bar{q} \quad \text{on } \partial\Omega_q \times ]0, t_f[ \quad (4d)$$

where  $\mathbf{g}$ ,  $\mathbf{n}$ ,  $\mathbf{h}$ ,  $\bar{\theta}$ , and  $\bar{q}$  denote the prescribed displacement, outward unit normal to the boundary, prescribed traction, prescribed temperature difference, and prescribed heat flux, respectively, with  $\overline{\partial\Omega_{\mathbf{g}} \cup \partial\Omega_{\mathbf{h}}} = \overline{\partial\Omega_T \cup \partial\Omega_q} = \partial\Omega$  and  $\partial\Omega_{\mathbf{g}} \cap \partial\Omega_{\mathbf{h}} = \partial\Omega_T \cap \partial\Omega_q = \emptyset$ .

The complete problem in time is specified with the initial conditions at time  $t = 0$  for  $\mathbf{u}(\mathbf{x}, t)$  and  $\theta(\mathbf{x}, t)$ . Here we consider:

$$\mathbf{u}(\mathbf{x}, 0) = \mathbf{u}_0(\mathbf{x}), \quad \dot{\mathbf{u}}(\mathbf{x}, 0) = \mathbf{v}_0(\mathbf{x}), \quad \theta(\mathbf{x}, 0) = \theta_0(\mathbf{x}). \quad (5)$$

To complete the problem in space, the constitutive laws need to be prescribed. Without loss of generality, we consider a homogeneous isotropic media.

Classical isotropic thermoelasticity considers the Duhamel-Neumann law, which yields the relation between stress, strain, and temperature change. Herein, we consider the law with no prestrain:

$$\boldsymbol{\sigma} = \mathbb{C} : \boldsymbol{\varepsilon}(\mathbf{u}) - \beta\theta\mathbb{I} \quad (6)$$

where  $\boldsymbol{\varepsilon}(\mathbf{u}) \equiv \frac{1}{2}(\nabla\mathbf{u} + (\nabla\mathbf{u})^\top)$  is the strain tensor,  $\mathbb{C}$  denotes the isotropic fourth-order elasticity tensor, and  $\mathbb{I}$  denotes the second-order identity tensor.

For the heat flux, the classical Fourier law is employed with isotropic heat conduction:

$$\mathbf{q} = -k\nabla\theta \quad (7)$$

where  $k$  is the thermal conductivity. The reason for the specificity of these definitions will be clear in the sequel, where alternative relations are employed.

Employing (6) and (7), the governing equations (1) and (2) can be expressed directly in terms of the displacement  $\mathbf{u}$  and temperature change  $\theta$ :

$$\nabla \cdot (\mathbb{C} : \boldsymbol{\varepsilon}(\mathbf{u}) - \beta\theta\mathbb{I}) + \mathbf{b} = \rho\ddot{\mathbf{u}}, \quad (8a)$$

$$\nabla \cdot k\nabla\theta - \rho c_p \dot{\theta} + Q - \beta T_0 \nabla \cdot \dot{\mathbf{u}} = 0. \quad (8b)$$

## 2.2 Coupling parameter and dimensionless variables

### 2.2.1 Coupling parameter

To distinguish between a fully coupled and a partially coupled (also called uncoupled) problem, the following thermoelastic parameter is introduced for convenience:

$$\delta = \frac{\beta^2 T_0}{\rho c_p (\lambda + 2\mu)}. \quad (9)$$

When  $\delta = 0$  the system is uncoupled. On the other hand, if  $\delta$  is a non-zero value, it is the fully coupled case. Here the case where a fully coupled thermomechanical analysis should be considered is clear: only when the material constants yield  $\delta \approx 0$ , an uncoupled system can be used. This is often the case with metals.

In this paper, the coupled and uncoupled thermoelastic equations are studied; we use  $\delta = 1$  and  $\delta = 0$ , respectively, with all parameters given except  $T_0$ , which is calculated using (9):

$$T_0 = \frac{\delta \rho c_p (\lambda + 2\mu)}{\beta^2}. \quad (10)$$

### 2.2.2 Dimensionless variables

The solutions in this manuscript are interpreted in terms of the following dimensionless variables:

$$\bar{y} = \frac{y}{a}, \quad \bar{\theta} = \frac{\theta}{T_0}, \quad \bar{t} = \frac{\kappa}{a^2} t, \quad \bar{\sigma} = \frac{\sigma}{\beta T_0}, \quad \bar{u} = \frac{(\lambda + 2\mu)}{a \beta T_0} u, \quad (11)$$

where  $a = \kappa / (c_s \rho c_p)$ ;  $\kappa = k / (\rho c_p)$ , and  $c_s = \sqrt{(\lambda + 2\mu) / \rho}$ .

## 2.3 Weak form of thermoelasticity

Galerkin meshfree methods such as RKPM employ weak forms of the governing equations (8). Starting from the weighted residual approach, applying integration-by-parts and the divergence theorem these can be derived as: find  $\mathbf{u} \in U_g$ , and  $\theta \in \Theta_T$ , such that for all  $\mathbf{v} \in U_0$ , and  $S \in \Theta_0$ , the following equations hold:

$$\int_{\Omega} \rho \mathbf{v} \cdot \dot{\mathbf{u}} d\Omega + \int_{\Omega} \boldsymbol{\varepsilon}(\mathbf{v}) : \mathbb{C} : \boldsymbol{\varepsilon}(\mathbf{u}) d\Omega - \int_{\Omega} \beta \nabla \cdot \mathbf{v} \theta d\Omega = \int_{\Omega} \mathbf{v} \cdot \mathbf{b} d\Omega + \int_{\partial\Omega_h} \mathbf{v} \cdot \mathbf{h} d\Gamma, \quad (12a)$$

$$\int_{\Omega} k \nabla S \cdot \nabla \theta d\Omega + \int_{\Omega} \rho c_p S \dot{\theta} d\Omega - \int_{\Omega} \beta T_0 S \nabla \cdot \dot{\mathbf{u}} d\Omega = \int_{\Omega} S Q d\Omega + \int_{\partial\Omega_q} S \bar{q} d\Gamma, \quad (12b)$$

with

$$U_g = \{\mathbf{u} \mid \mathbf{u} \in H^1, \mathbf{u} = \mathbf{g} \text{ on } \partial\Omega_g \times ]0, t_f[ \}, \quad (13a)$$

$$U_0 = \{\mathbf{v} \mid \mathbf{v} \in H^1, \mathbf{v} = \mathbf{0} \text{ on } \partial\Omega_g \times ]0, t_f[ \}, \quad (13b)$$

$$\Theta_T = \{\theta \mid \theta \in H^1, \theta = \bar{\theta} \text{ on } \partial\Omega_T \times ]0, t_f[ \}, \quad (13c)$$

$$\Theta_0 = \{S \mid S \in H^1, S = 0 \text{ on } \partial\Omega_T \times ]0, t_f[ \}. \quad (13d)$$

In (12), both bilinear "stiffness" integrals contain gradients of the primary unknown,  $\nabla \mathbf{u}$  and  $\nabla \theta$ , in (12a) and (12b), respectively. Thus, when discretized by meshfree shape functions, it is easy to show that an oscillatory mode in both the displacement and temperature with a wavelength of twice the nodal spacing will not contribute to these terms away from the boundary, and this mode can potentially grow unrestricted [27].

Note that meshfree approximations generally do not meet the requirements (13) and need special techniques to impose essential boundary conditions. Here we employ the transformation method [13] with consistent weak forms [28] to attain Galerkin exactness in VC methods. The details are omitted for clarity of presentation of the proposed formulation; for details see [13, 28].

## 2.4 Galerkin form of thermoelasticity

The Galerkin statement of the problem (12) is: find  $\mathbf{u}^h \in U_g^h$ , and  $\theta^h \in \Theta_T^h$ , such that for all  $\mathbf{v}^h \in U_0^h$ , and  $S^h \in \Theta_0^h$ , the following equations hold:

$$\int_{\Omega} \rho \mathbf{v}^h \cdot \ddot{\mathbf{u}}^h d\Omega + \int_{\Omega} \boldsymbol{\varepsilon}(\mathbf{v}^h) : \mathbb{C} : \boldsymbol{\varepsilon}(\mathbf{u}^h) d\Omega - \int_{\Omega} \beta \nabla \cdot \mathbf{v}^h \theta^h d\Omega = \int_{\Omega} \mathbf{v}^h \cdot \mathbf{b} d\Omega + \int_{\partial\Omega_h} \mathbf{v}^h \cdot \mathbf{h} d\Gamma, \quad (14a)$$

$$\int_{\Omega} k \nabla S^h \cdot \nabla \theta^h d\Omega + \int_{\Omega} \rho c_p S^h \dot{\theta}^h d\Omega - \int_{\Omega} \beta T_0 S^h \nabla \cdot \dot{\mathbf{u}}^h d\Omega = \int_{\Omega} S Q d\Omega + \int_{\partial\Omega_q} S^h \bar{q} d\Gamma, \quad (14b)$$

with  $U_g^h \subset U_g$ ,  $\Theta_T^h \subset \Theta_T$ ,  $U_0^h \subset U_0$ , and  $\Theta_0^h \subset \Theta_0$ . The above necessitates quadrature, which motivates the current work. Gaussian integration sufficient for acceptable accuracy is prohibitively expensive, whereas nodal integration is extremely unstable, as will be seen.

## 3 Meshfree approximation

In this section, the reproducing kernel approximation is briefly reviewed. An overview of the implicit gradient is further given, which significantly lowers the computational cost of computing gradient terms in the stabilized formulation.

### 3.1 Reproducing Kernel approximation

Let a domain  $\bar{\Omega} = \Omega \cup \partial\Omega$  be discretized by a set of  $NP$  nodes  $\mathcal{S} = \{\mathbf{x}_I | \mathbf{x}_I \in \bar{\Omega}\}_{I=1}^{NP}$  with set of node numbers  $\mathcal{N} = \{I | \mathbf{x}_I \in \mathcal{S}\}$ . The  $n$ th order reproducing kernel (RK) approximation  $u^h(\mathbf{x})$  of a function  $u(\mathbf{x})$  is [39, 12, 40]:

$$u^h(\mathbf{x}) = \sum_{I \in \mathcal{N}} \Psi_I(\mathbf{x}) u_I \quad (15)$$

where  $\{\Psi_I(\mathbf{x})\}_{I \in \mathcal{N}}$  is the set of RK shape functions, and  $\{u_I\}_{I \in \mathcal{N}}$  are the associated coefficients. Note that the summation in (15) is only carried out over non-zero shape functions local to  $\mathbf{x}$  in practice, naturally defining connectivity.

The shape functions in (15) are constructed by the product of a kernel function  $\Phi_a(\mathbf{x} - \mathbf{x}_I)$  with normalized support  $a$  and a correction function  $C(\mathbf{x}; \mathbf{x} - \mathbf{x}_I)$ :

$$\Psi_I(\mathbf{x}) = \Phi_a(\mathbf{x} - \mathbf{x}_I)C(\mathbf{x}; \mathbf{x} - \mathbf{x}_I). \quad (16)$$

The correction function here is composed of a linear combination of  $n$ th order complete monomials, which allows the exact reproduction of these monomials. In matrix form the correction can be expressed as:

$$C(\mathbf{x}; \mathbf{x} - \mathbf{x}_I) = \mathbf{H}(\mathbf{x} - \mathbf{x}_I)^\top \mathbf{b}(\mathbf{x}). \quad (17)$$

where  $\mathbf{H}(\mathbf{x} - \mathbf{x}_I)$  is a column vector of the monomials:

$$\mathbf{H}(\mathbf{x} - \mathbf{x}_I) = [1, x_1 - x_{1I}, x_2 - x_{2I}, x_3 - x_{3I}, (x_1 - x_{1I})^2, \dots, (x_3 - x_{3I})^n]^\top \quad (18)$$

and  $\mathbf{b}(\mathbf{x})$  is a column vector of coefficients to be determined from the following  $n$ th order discrete reproducing conditions:

$$\sum_{I \in \mathcal{N}} \Psi_I(\mathbf{x}) \mathbf{H}(\mathbf{x}_I) = \mathbf{H}(\mathbf{x}) \quad \text{or} \quad \sum_{I \in \mathcal{N}} \Psi_I(\mathbf{x}) \mathbf{H}(\mathbf{x} - \mathbf{x}_I) = \mathbf{H}(\mathbf{0}) \quad (19)$$

which leads to  $\mathbf{b}(\mathbf{x})$  of the following form:

$$\mathbf{b}(\mathbf{x}) = \mathbf{M}(\mathbf{x})^{-1} \mathbf{H}(\mathbf{0}) \quad (20)$$

where the moment matrix  $\mathbf{M}$  is defined as follows:

$$\mathbf{M}(\mathbf{x}) = \sum_{I \in \mathcal{N}} \mathbf{H}(\mathbf{x} - \mathbf{x}_I) \mathbf{H}(\mathbf{x} - \mathbf{x}_I)^\top \Phi_a(\mathbf{x} - \mathbf{x}_I). \quad (21)$$

Employing (20), the RK shape functions are constructed as:

$$\Psi_I(\mathbf{x}) = \mathbf{H}(\mathbf{0})^\top \mathbf{M}(\mathbf{x})^{-1} \mathbf{H}(\mathbf{x} - \mathbf{x}_I) \Phi_a(\mathbf{x} - \mathbf{x}_I). \quad (22)$$

The shape function gradient necessary in the weak form can be computed straightforwardly based on the product rule:

$$\begin{aligned} \nabla \Psi_I(\mathbf{x}) &= \mathbf{H}(\mathbf{0})^\top \nabla (\mathbf{M}(\mathbf{x})^{-1}) \mathbf{H}(\mathbf{x} - \mathbf{x}_I) \Phi_a(\mathbf{x} - \mathbf{x}_I) \\ &\quad + \mathbf{H}(\mathbf{0})^\top \mathbf{M}(\mathbf{x})^{-1} \nabla \mathbf{H}(\mathbf{x} - \mathbf{x}_I) \Phi_a(\mathbf{x} - \mathbf{x}_I) \\ &\quad + \mathbf{H}(\mathbf{0}) \mathbf{M}(\mathbf{x})^{-1} \mathbf{H}(\mathbf{x} - \mathbf{x}_I) \nabla \Phi_a(\mathbf{x} - \mathbf{x}_I) \end{aligned} \quad (23)$$

where

$$\nabla (\mathbf{M}(\mathbf{x})^{-1}) = -\mathbf{M}(\mathbf{x})^{-1} \nabla \mathbf{M}(\mathbf{x}) \mathbf{M}(\mathbf{x})^{-1}. \quad (24)$$

However, the computational cost of computing this gradient is non-trivial (cf. [30]). Therefore a so-called *implicit* gradient (which originated from the synchronized derivative [35]) has been developed [16, 43] to save computational cost. This approximation preserves the essential properties of the explicit gradient, that is, the gradient reproducing properties of (23) (see (19) for reference)

$$\sum_{I=1}^{NP} \nabla \Psi_I(\mathbf{x}) \mathbf{H}(\mathbf{x}_I) = \nabla \mathbf{H}(\mathbf{x}) \quad (25)$$

are satisfied by the implicit gradient reproducing kernel shape function.

Starting from the analogy of (16), the implicit gradient shape function is constructed as [16, 35]

$$\Psi_{Ii}^\nabla(\mathbf{x}) = \Phi_a(\mathbf{x} - \mathbf{x}_I)C_i^\nabla(\mathbf{x}; \mathbf{x} - \mathbf{x}_I), \quad (26)$$

where  $i = 1, \dots, d$  where  $d$  is the dimension of the problem. A correction function is introduced composed of a linear combination of monomials:

$$C_i^\nabla(\mathbf{x}; \mathbf{x} - \mathbf{x}_I) = \mathbf{H}(\mathbf{x} - \mathbf{x}_I)^\top \mathbf{b}_i^\nabla(\mathbf{x}). \quad (27)$$

The implicit gradient is then obtained by enforcing the gradient reproducing conditions (25) on (26) and solving for  $\mathbf{b}_i^\nabla(\mathbf{x})$ :

$$\Psi_{Ii}^\nabla(\mathbf{x}) = [\mathbf{H}_i^\nabla]^\top \mathbf{M}(\mathbf{x})^{-1} \mathbf{H}(\mathbf{x} - \mathbf{x}_I) \Phi_a(\mathbf{x} - \mathbf{x}_I) \quad (28)$$

where  $\mathbf{M}(\mathbf{x})$  is the same moment matrix in (21), and  $\mathbf{H}_i^\nabla$  is a column vector of the form:

$$\mathbf{H}_i^\nabla = [0, \dots, 0, -1, 0, \dots, 0]^\top \quad (29)$$

where  $-1$  is  $(i + 1)^{th}$  entry. Compared to (23) it is easily seen that the implicit gradient (28) is much more computationally efficient. In fact, comparing (28) to (22), it costs virtually nothing since most of the terms already need to be computed in (22) — the last three terms are the exact same. Meanwhile, both possess the key property of satisfying the gradient reproducing conditions. Depending on the dimension of the problem  $d$ , the implicit gradient can reduce cost by a factor on the order of  $2d + 1$  over the explicit gradient in the shape function construction [24]. In the later sections, the implicit gradient will be utilized to reduce the computational cost of the proposed nodal integration technique.

## 4 Instability in nodal integration

In meshfree methods, direct nodal integration (or DNI) is well known to provide unstable results in solid mechanics [2, 14, 15, 24, 64]. Here, we examine the stability of DNI in thermomechanical analysis using quasi-static classical thermoelasticity (neglecting inertial terms in (12)) as a model problem.

Consider a linear elastic half-space  $y \geq 0$  subjected to a sudden temperature change and free traction on its boundary. This can be treated as a one-dimensional problem, either coupled or uncoupled depending on the constants. The material properties employed in this study are shown in Table 1.

	$k$	$\rho$	$c_p$	$\beta$	$\lambda + 2\mu$
value	$1.7 \times 10^3$	$7.82 \times 10^{-3}$	$4.61 \times 10^6$	$3.34 \times 10^4$	$1.99 \times 10^9$
unit	$\text{kg} \times \text{cm}/\text{K}/\text{s}^3$	$\text{kg}/\text{cm}^3$	$\text{cm}^2/\text{K}/\text{s}^3$	$\text{kg}/\text{cm}/\text{K}/\text{s}^2$	$\text{kg}/\text{cm}/\text{s}^2$

Table 1: Parameters for stability study.

For constructing the RK shape function, linear basis, cubic B-spline kernel, uniform node distribution with spacing  $\Delta x = 0.001$ , and a normalized support size of 2 are used. The analytical solution for this problem can be found in [7]. The implicit

and unconditionally stable backward difference method [48] with the time step  $\Delta t = 0.001$ s is used to discretize the time domain in this example.

Figure 1 shows the dimensionless results along the  $y$ -axis at time  $\bar{t} = 2$  for the coupled ( $\delta = 1$ ) and uncoupled ( $\delta = 0$ ) cases. It can be seen that DNI yields highly unstable temperature and displacement responses. It should be emphasized that these oscillations are many orders of magnitude (more than 30 here) worse than those observed in pure elasticity (see [2, 22, 64] for a few examples, these instabilities in elasticity typically result in oscillations with amplitude on the order of the solution itself, or less). Hence here, stabilization is absolutely necessary to obtain any meaningful solution at all. It can also be seen that this severe instability occurs in both the coupled and uncoupled cases.

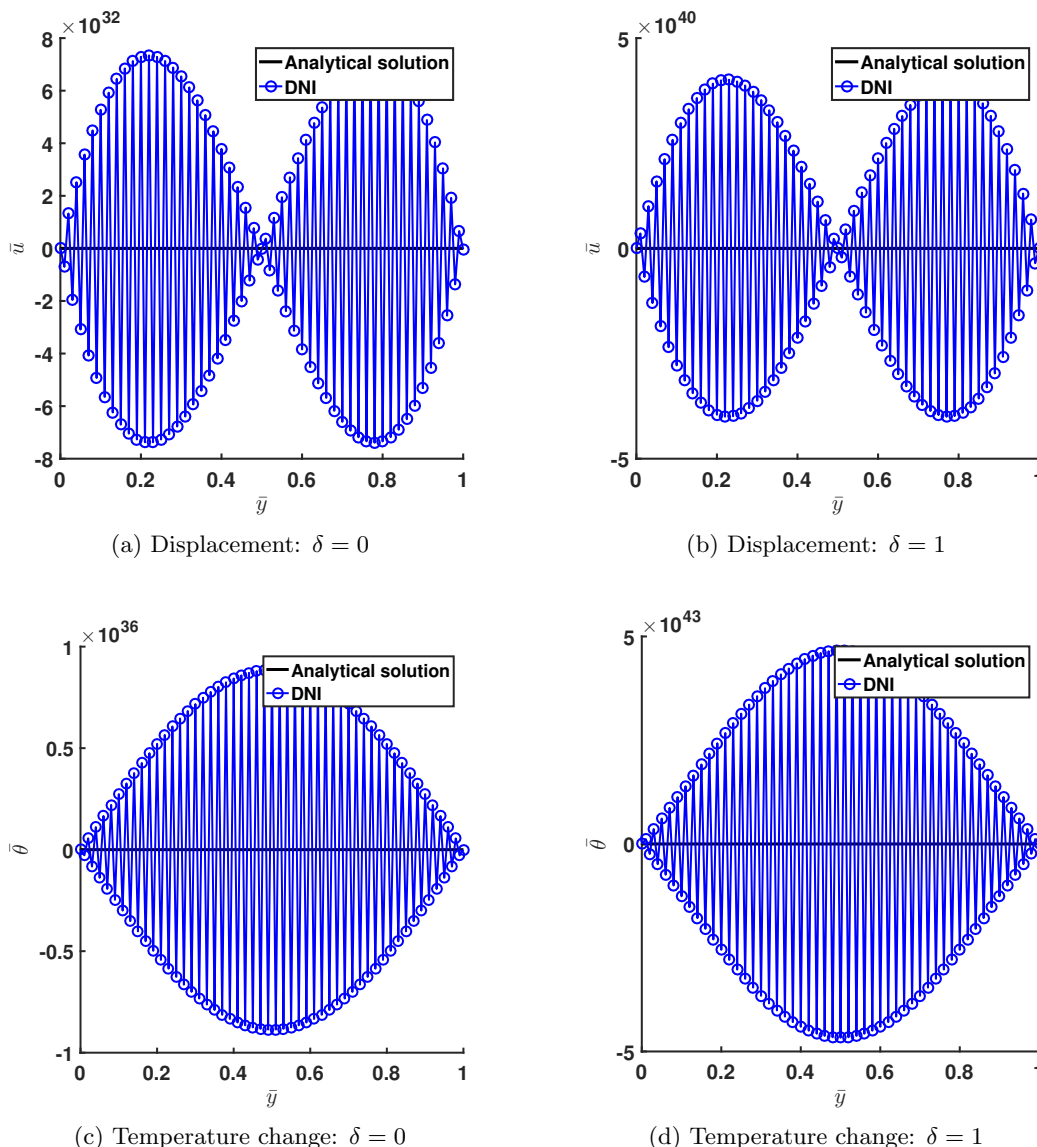


Figure 1: Coupled and uncoupled results along  $\bar{y}$  at  $\bar{t} = 2$  for the quasi-static DNI test.

The time histories at  $\bar{y} = 1$  shown in Figure 2 depict the evolution of displacement

and temperature difference over time. Here it can be seen that this instability is "explosive" in nature: the results appear to grow exponentially, which again is not the case in pure elasticity. As before, this occurs for both the coupled and uncoupled cases.

As explained in the introduction, DNI also provides poor accuracy. However, without stability, it is difficult to evaluate how the poor accuracy might manifest in this class of problems. Later, this issue will be revisited, where it is shown that stabilization alone (e.g., NSNI introduced in the next section) is insufficient to ensure acceptable accuracy, which motivates the introduction of variationally consistent NSNI (VC-NSNI), to attain both stability and accuracy in the solution of thermomechanical problems.

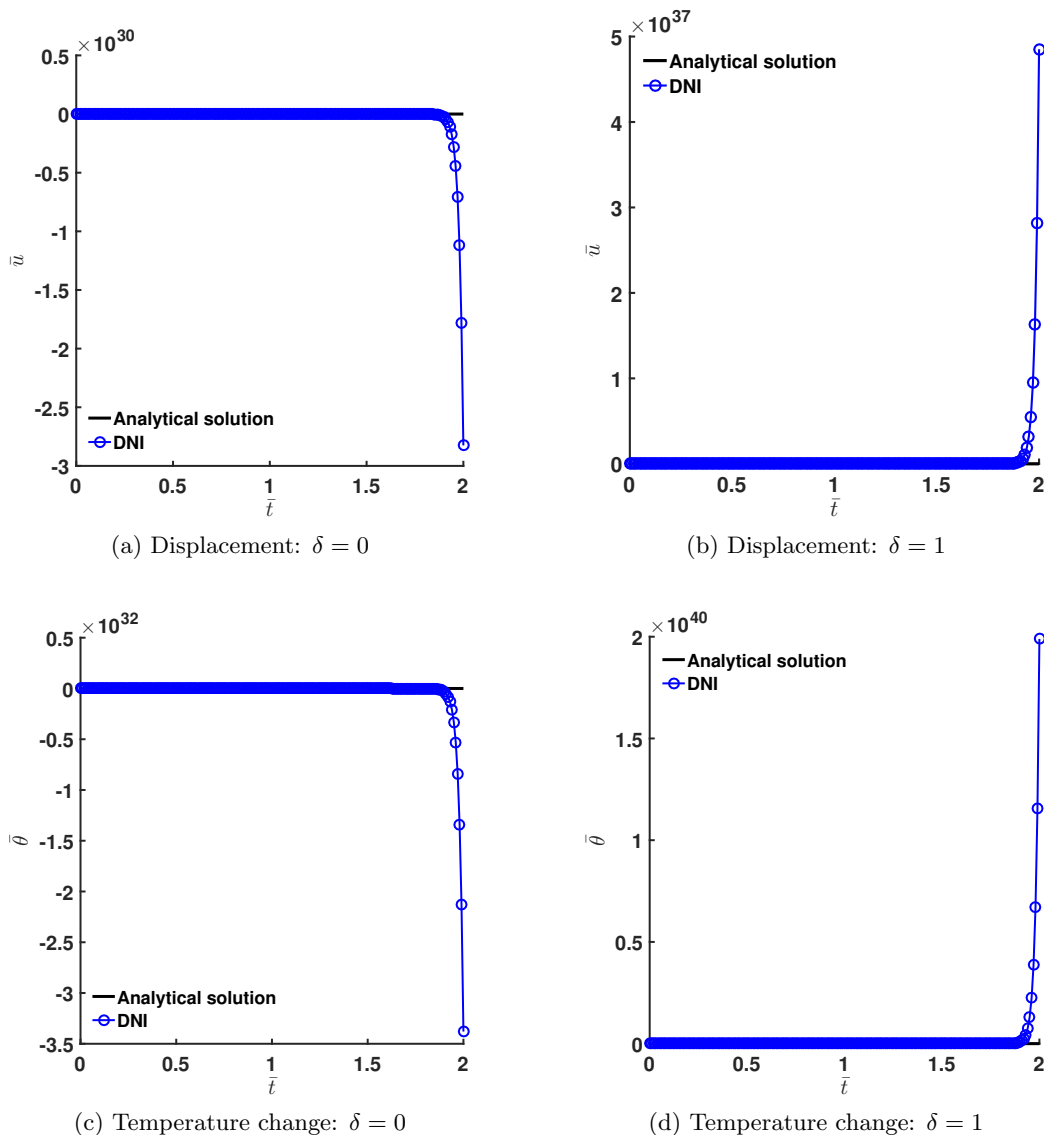


Figure 2: Coupled and uncoupled time history of results at  $\bar{y} = 1$  for the quasi-static DNI test.

## 5 Naturally stabilized nodal integration

As shown in the previous section, the DNI quadrature scheme can lead to severe numerical instabilities and does not appear to be a viable scheme for thermomechanical problems whatsoever. To eliminate the spurious oscillatory modes of direct nodal integration, naturally stabilized nodal integration (NSNI) [24] has been introduced. However, this technique has not been developed for thermomechanical problems. Without loss of generality, two-dimensional formulations are presented in the following sections which can be easily extended or contracted to 3-d or 1-d.

### 5.1 Stabilization of the displacement field

To start, the strains in nodal domains  $\Omega_L$  are expanded about the nodal position  $\mathbf{x}_L$  using a Taylor series expansion truncated to first order [24]:

$$\boldsymbol{\varepsilon}(\mathbf{u}^h) \approx \boldsymbol{\varepsilon}_L(\mathbf{u}^h) + \sum_{i=1}^2 \{(x_i - x_{Li})\boldsymbol{\varepsilon}_L(\mathbf{u}^h)_{,i}\} \quad (30)$$

where  $\boldsymbol{\varepsilon}_L(\mathbf{u}^h) \equiv \boldsymbol{\varepsilon}(\mathbf{u}^h(\mathbf{x}_L))$ . The strain of the test function is also defined the same as (30), that is

$$\boldsymbol{\varepsilon}(\mathbf{v}^h) \approx \boldsymbol{\varepsilon}_L(\mathbf{v}^h) + \sum_{i=1}^2 \{(x_i - x_{Li})\boldsymbol{\varepsilon}_L(\mathbf{v}^h)_{,i}\}. \quad (31)$$

Here, we have considered the linear ( $n = 1$ ) case and only retain first-order terms. Higher order cases of NSNI can be obtained straightforwardly following [44].

Substituting (30) and (31) into (14a) for each of the strains in the nodal domains and employing the implicit gradient approximation (28), the following naturally stabilized nodal quadrature version of the elastic bilinear form is obtained as:

$$a_{DN} \langle \mathbf{v}^h, \mathbf{u}^h \rangle = a_D \langle \mathbf{v}^h, \mathbf{u}^h \rangle + a_N \langle \mathbf{v}^h, \mathbf{u}^h \rangle \quad (32)$$

where  $a_D \langle \cdot, \cdot \rangle$  is the DNI quadrature version of the bilinear form:

$$a_D \langle \mathbf{v}^h, \mathbf{u}^h \rangle = \sum_{L=1}^{NP} \boldsymbol{\varepsilon}_L(\mathbf{v}^h) : \mathbb{C} : \boldsymbol{\varepsilon}_L(\mathbf{u}^h) W_L \quad (33)$$

where  $W_L$  is the integration weight associated with node  $L$  (the representative nodal area in 2-d), and the stabilization term  $a_N \langle \cdot, \cdot \rangle$  is

$$a_N \langle \mathbf{v}^h, \mathbf{u}^h \rangle = \sum_{L=1}^{NP} \sum_{i=1}^2 \hat{\boldsymbol{\varepsilon}}_{Li}(\mathbf{v}^h) : \mathbb{C} : \hat{\boldsymbol{\varepsilon}}_{Li}(\mathbf{u}^h) M_{Li} \quad (34)$$

where  $\hat{\boldsymbol{\varepsilon}}_{Li}(\cdot)$  is the implicit gradient approximation of  $\boldsymbol{\varepsilon}_L(\cdot)_{,i}$ , and

$$M_{Li} = \int_{\Omega_L} (x_i - x_{Li})^2 d\Omega, \quad (35)$$

which are the second moments of inertia of each integration zone. Note that the following (in 2-D, see [24] for more details on this assumption) has been utilized to obtain (34):

$$\int_{\Omega_L} (x_1 - x_{L1}) dx_1 = 0, \quad \text{or} \quad \int_{\Omega_L} (x_2 - x_{L2}) dx_2 = 0. \quad (36)$$

The assumption (36) is satisfied when the node is located at the centroid of the quadrature domain  $\Omega_L$  in at least one of the two Cartesian coordinates.

Using Voigt notation (for such terms throughout the manuscript), the standard nodal strain terms in (33) are constructed as:

$$\boldsymbol{\varepsilon}_L(\mathbf{u}^h) = \sum_{I=1}^{NP} \mathbf{B}_I^u(\mathbf{x}_L) \mathbf{u}_I, \quad \boldsymbol{\varepsilon}_L(\mathbf{v}^h) = \sum_{I=1}^{NP} \mathbf{B}_I^v(\mathbf{x}_L) \mathbf{v}_I, \quad (37)$$

with

$$\mathbf{B}_I^u(\mathbf{x}) = \begin{bmatrix} \Psi_{I,1}(\mathbf{x}) & 0 \\ 0 & \Psi_{I,2}(\mathbf{x}) \\ \Psi_{I,2}(\mathbf{x}) & \Psi_{I,1}(\mathbf{x}) \end{bmatrix}. \quad (38)$$

and the additional terms the containing derivatives of strains are approximated by implicit gradients (28) as

$$\begin{aligned} \hat{\boldsymbol{\varepsilon}}_{Li}(\mathbf{u}^h) &= \sum_{I=1}^{NP} \mathbf{B}_{Li}^{u\nabla}(\mathbf{x}_L) \mathbf{u}_I \equiv \mathbf{B}_i^{u\nabla}(\mathbf{x}_L) \mathbf{u}, & \hat{\boldsymbol{\varepsilon}}_{Li}(\mathbf{v}^h) &= \sum_{I=1}^{NP} \mathbf{B}_{Li}^{v\nabla}(\mathbf{x}_L) \mathbf{v}_I \equiv \mathbf{B}_i^{v\nabla}(\mathbf{x}_L) \mathbf{v}, \\ \mathbf{B}_{Li}^{u\nabla}(\mathbf{x}) &= \begin{bmatrix} \Psi_{Li1}^{\nabla}(\mathbf{x}) & 0 \\ 0 & \Psi_{Li2}^{\nabla}(\mathbf{x}) \\ \Psi_{Li2}^{\nabla}(\mathbf{x}) & \Psi_{Li1}^{\nabla}(\mathbf{x}) \end{bmatrix} \end{aligned} \quad (39)$$

where  $\Psi_{Lij}^{\nabla} = \frac{1}{2} \{ \Psi_{Li,j}^{\nabla} + \Psi_{Lj,i}^{\nabla} \}$  since  $\Psi_{Li,j}^{\nabla} \neq \Psi_{Lj,i}^{\nabla}$ .

## 5.2 Stabilization of temperature field

Following the stabilization of the displacement field, expanding the temperature gradient in nodal domains  $\Omega_L$  about  $\mathbf{x}_L$  is proposed in this work to achieve stabilization of the temperature field:

$$\nabla \theta^h(\mathbf{x}) \approx \nabla \theta_L^h + \sum_{i=1}^2 \{ (x_i - x_{Li}) (\nabla \theta_L^h)_{,i} \} \quad (40)$$

where  $\nabla \theta_L^h \equiv \nabla \theta^h(\mathbf{x}_L)$ . The test function gradient follows the same form:

$$\nabla S^h(\mathbf{x}) \approx \nabla S_L^h + \sum_{i=1}^2 \{ (x_i - x_{Li}) (\nabla S_L^h)_{,i} \} \quad (41)$$

where  $\nabla S_L^h \equiv \nabla S^h(\mathbf{x}_L)$ . Note that for the temperature field, stabilization also entails second-order derivatives, which are expensive to compute in meshfree approximations.

Here, implicit gradients will again be introduced to approximate the derivatives of the temperature gradients.

Taking equations (35) and (36) into consideration, and employing (40) and (41) in (14b), the following stabilized bilinear form is obtained for the temperature field:

$$\bar{a}_{DN} \langle S^h, \theta^h \rangle = \bar{a}_D \langle S^h, \theta^h \rangle + \bar{a}_N \langle S^h, \theta^h \rangle \quad (42)$$

where  $\bar{a}_D \langle \cdot, \cdot \rangle$  is the DNI quadrature version of the bilinear form:

$$\bar{a}_N \langle S^h, \theta^h \rangle = \sum_{L=1}^{NP} k(\nabla S_L^h) \cdot (\nabla \theta_L^h) W_L \quad (43)$$

and the stabilization term for temperature  $\bar{a}_N \langle \cdot, \cdot \rangle$  is computed as

$$\bar{a}_N \langle S^h, \theta^h \rangle = \sum_{L=1}^{NP} \sum_{i=1}^2 k(\hat{\nabla} S_{Li}^h) \cdot (\hat{\nabla} \theta_{Li}^h) M_{Li}. \quad (44)$$

where  $\hat{\nabla} S_{Li}^h$  and  $\hat{\nabla} \theta_{Li}^h$  denote the implicit derivative in the  $i^{th}$  direction of  $\nabla S_L^h$  and  $\nabla \theta_L^h$ , respectively.

For the nodal gradients in the DNI term, we have:

$$\nabla \theta_L^h = \sum_{I=1}^{NP} \mathbf{B}_I^\theta(\mathbf{x}_L) \theta_I, \quad \nabla S_L^h = \sum_{I=1}^{NP} \mathbf{B}_I^\theta(\mathbf{x}_L) S_I, \quad (45)$$

where

$$\mathbf{B}_I^\theta(\mathbf{x}) = [\Psi_{I,1}(\mathbf{x}) \quad \Psi_{I,2}(\mathbf{x})]^\top. \quad (46)$$

For the stabilization terms in (44), implicit gradients are utilized as follows:

$$\hat{\nabla} \theta_{Li}^h = \sum_{I=1}^{NP} \mathbf{B}_{Ii}^{\theta \nabla}(\mathbf{x}_L) \theta_I \equiv \mathbf{B}_i^{\theta \nabla}(\mathbf{x}_L) \boldsymbol{\theta}, \quad \hat{\nabla} S_{Li}^h = \sum_{I=1}^{NP} \mathbf{B}_{Ii}^{\theta \nabla}(\mathbf{x}_L) S_I \equiv \mathbf{B}_i^{\theta \nabla}(\mathbf{x}_L) \mathbf{S}, \quad (47)$$

$$\mathbf{B}_{Ii}^{\theta \nabla}(\mathbf{x}) = [\Psi_{Ii1}^{\nabla}(\mathbf{x}) \quad \Psi_{Ii2}^{\nabla}(\mathbf{x})]^\top.$$

Note that the weights  $W_L$  and second moments of inertia  $M_{Li}$  are the same as in Section 5.1.

## 6 Variational consistency conditions

In this section, the variational consistency conditions are derived for thermoelasticity. The key difference between the original derivation in [11] is the presence of two fields.

Following the concept in [11], consider a static thermoelasticity problem where the displacement solution is a linear combination of complete monomials up to order  $n$ :

$$\mathbf{u} = \sum_{|\alpha| \leq n} \mathbf{c}_\alpha \mathbf{x}^\alpha \equiv \mathbf{u}^{[n]} \quad (48)$$

where  $\alpha$  is a multi-index equipped with standard notation.

In [11], the conditions to obtain this type of solution was purely a function of the single field. Here we note that, unlike the pure elastic case, the associated boundary conditions now also need to consider the temperature change since, e.g., the prescribed traction will need to depend on  $\boldsymbol{\sigma} = \mathbb{C} : \boldsymbol{\varepsilon}(\mathbf{u}) - \beta\theta\mathbb{I}$ . In addition, the temperature change needs to be considered an independent variable. As such, an  $m$ th order temperature solution is assumed:

$$\theta = \sum_{|\gamma| \leq m} d_\gamma x^\gamma \equiv \theta^{[m]} \quad (49)$$

where  $\gamma$  is also a multi-index. With (48) and (49) in hand, the manufactured source term and boundary conditions consistent with these two fields can now be obtained as:

$$\mathbf{b} = -\nabla \cdot \boldsymbol{\sigma}^{[nm]} \quad \text{in } \Omega \quad (50a)$$

$$\mathbf{h} = \boldsymbol{\sigma}^{[nm]} \cdot \mathbf{n} \quad \text{on } \partial\Omega_{\mathbf{h}} \quad (50b)$$

$$\mathbf{g} = \mathbf{u}^{[n]} \quad \text{on } \partial\Omega_{\mathbf{g}} \quad (50c)$$

$$Q = -\nabla \cdot k\nabla\theta^{[m]} \quad \text{in } \Omega \quad (50d)$$

$$\bar{q} = k\nabla\theta^{[m]} \cdot \mathbf{n} \quad \text{on } \partial\Omega_q \quad (50e)$$

$$\bar{\theta} = \theta^{[m]} \quad \text{on } \partial\Omega_T. \quad (50f)$$

where

$$\boldsymbol{\sigma}^{[nm]} = \mathbb{C} : \boldsymbol{\varepsilon}(\mathbf{u}^{[n]}) - \beta\theta^{[m]}\mathbb{I} \quad (51)$$

is the stress associated with both fields.

For the Galerkin form, approximations for both solid displacement and temperature fields are as follows

$$\mathbf{u}^h = \sum_{I=1}^{NP} \mathbf{N}_I^u \mathbf{u}_I, \quad \theta^h = \sum_{I=1}^{NP} \bar{\Psi}_I \theta_I \quad (52)$$

where

$$\mathbf{N}_I^u = \begin{bmatrix} \Psi_I & 0 \\ 0 & \Psi_I \end{bmatrix}, \quad (53)$$

and the test functions are

$$\mathbf{v}^h = \sum_{I=1}^{NP} \hat{\mathbf{N}}_I^u \mathbf{v}_I, \quad S^h = \sum_{I=1}^{NP} \tilde{\Psi}_I S_I \quad (54)$$

where

$$\hat{\mathbf{N}}_I^u = \begin{bmatrix} \hat{\Psi}_I & 0 \\ 0 & \hat{\Psi}_I \end{bmatrix}, \quad (55)$$

in which  $\Psi$ ,  $\bar{\Psi}$ ,  $\hat{\Psi}$ , and  $\tilde{\Psi}$  are the RK shape functions for solid displacement and temperature fields, respectively, and  $\mathbf{u}_I$ ,  $\theta_I$ ,  $\mathbf{v}_I$ , and  $S_I$  are the nodal coefficients.

Now, in order to obtain Galerkin exactness (passing the patch test and obtaining the exact solutions (48) and (49)), the integration constraints should be satisfied. The meaning of integration constraints is that the numerical integration has to be consistent with the test functions in order to obtain exactness in the Galerkin approximation. Therefore here, the possibility that approximations to the test and trial functions differ is considered. Note that the integration constraints are tightly tied with Galerkin orthogonality [52], and are necessary for obtaining the standard error estimate for smooth problems [66].

In order to arrive at the integration constraints, weak forms employed in the Galerkin equation must attest to the strong forms [11]. A few options are the Lagrange multiplier method, Nitsche's method, or the newly proposed *consistent weak forms* [28]. Here we consider the consistent weak forms of (12) — the details are omitted here for clarity. The derivation follows the appendices of [28] straightforwardly.

Since the test functions are arbitrary, one governing equation can be considered at a time. Therefore, one should expect two independent constraints for each test function approximation.

First, consider the equation of motion. Following [11], the approximations (52) and (54) are substituted into the consistent versions of (14a) and (14b). Then, using the notation  $\mathbf{x}_I^\alpha \equiv x_{I1}^{\alpha_1} \cdot x_{I2}^{\alpha_2} \cdot \dots \cdot x_{Id}^{\alpha_d}$ , the exact nodal solutions  $\mathbf{u}_I^{[n]}$  and  $\theta_I^{[m]}$  are then employed along with the consistency conditions (19) yielding  $\mathbf{u}^h = \mathbf{u}^{[n]}$  and  $\theta^h = \theta^{[m]}$ . Using the prescribed conditions in (50), and employing numerical integration, the following integration constraints on the test function for the displacement field are obtained:

$$\left\langle \nabla \hat{\Psi}_I \cdot \boldsymbol{\sigma}^{[\alpha\gamma]} \right\rangle_\Omega = - \left\langle \hat{\Psi}_I \nabla \cdot \boldsymbol{\sigma}^{[\alpha\gamma]} \right\rangle_\Omega + \left\langle \hat{\Psi}_I \boldsymbol{\sigma}^{[\alpha\gamma]} \cdot \mathbf{n} \right\rangle_{\partial\Omega} \quad \forall I, |\alpha| = 0, 1, \dots, n, \quad |\gamma| = 0, 1, \dots, m \quad (56)$$

where  $\langle \cdot \rangle_\Omega$  and  $\langle \cdot \rangle_{\partial\Omega}$  denote the quadrature forms of the domain integral and the boundary integral, respectively, and  $\boldsymbol{\sigma}^{[\alpha\gamma]} = \mathbb{C} : \boldsymbol{\varepsilon}(\mathbf{u}^\alpha) - \beta\theta^\gamma \mathbb{I}$ . In the above, it can be seen that the integration constraint is the same as pure elasticity in terms of stress [11]. However here, the stress is a function of both displacement and temperature. Therefore the definition of  $\boldsymbol{\sigma}^{[\alpha\gamma]}$  must be used to further elucidate the constraints:

$$\left\langle \nabla^s \hat{\Psi}_I : \mathbb{C} : \nabla^s \mathbf{x}^\alpha \right\rangle_\Omega = - \left\langle \hat{\Psi}_I \nabla \cdot \mathbb{C} : \nabla^s \mathbf{x}^\alpha \right\rangle_\Omega + \left\langle \hat{\Psi}_I \mathbb{C} : \nabla^s \mathbf{x}^\alpha \cdot \mathbf{n} \right\rangle_{\partial\Omega} \quad \forall I, |\alpha| = 0, 1, \dots, n \quad (57a)$$

$$\left\langle \nabla^s \hat{\Psi}_I \cdot \beta x^\gamma \mathbb{I} \right\rangle_\Omega = - \left\langle \hat{\Psi}_I \nabla \cdot \beta x^\gamma \mathbb{I} \right\rangle_\Omega + \left\langle \hat{\Psi}_I \beta x^\gamma \mathbb{I} \cdot \mathbf{n} \right\rangle_{\partial\Omega} \quad \forall I, |\gamma| = 0, 1, \dots, m \quad (57b)$$

where  $\nabla^s(\cdot) = \frac{1}{2}(\nabla \otimes (\cdot) + (\cdot) \otimes \nabla)$ .

**Remark 1** The above convey a relation between the displacement test functions, quadrature, and both orders of monomials of the solution  $n$  and  $m$ . This is due to the fact that the stress in the momentum equation contains both the displacement and the temperature difference.

Now, if  $\mathbb{C}$  and  $\beta$  are constant, the constraint can be simplified as:

$$\left\langle \nabla^s \hat{\Psi}_I \cdot \nabla^s \mathbf{x}^\alpha \right\rangle_\Omega = - \left\langle \hat{\Psi}_I \nabla \cdot \nabla^s \mathbf{x}^\alpha \right\rangle_\Omega + \left\langle \hat{\Psi}_I \nabla^s \mathbf{x}^\alpha \cdot \mathbf{n} \right\rangle_{\partial\Omega} \quad \forall I, |\alpha| = 0, 1, \dots, n \quad (58a)$$

$$\left\langle \nabla^s \hat{\Psi}_I \cdot x^\gamma \mathbb{I} \right\rangle_\Omega = - \left\langle \hat{\Psi}_I \nabla \cdot x^\gamma \mathbb{I} \right\rangle_\Omega + \left\langle \hat{\Psi}_I x^\gamma \mathbb{I} \cdot \mathbf{n} \right\rangle_{\partial\Omega} \quad \forall I, |\gamma| = 0, 1, \dots, m. \quad (58b)$$

Now considering the static energy equation, the integration constraints on the test function of the temperature field can be obtained following the previous procedure and assuming constant  $k$ :

$$\left\langle \nabla \tilde{\Psi}_I \cdot \nabla x^\gamma \right\rangle_\Omega = - \left\langle \tilde{\Psi}_I \nabla^2 x^\gamma \right\rangle_\Omega + \left\langle \tilde{\Psi}_I \nabla x^\gamma \cdot \mathbf{n} \right\rangle_{\partial\Omega} \quad \forall I, |\gamma| = 0, 1, \dots, m \quad (59)$$

where  $\nabla^2 \equiv \nabla \cdot \nabla$ .

**Remark 2** Here it can be seen that this integration constraint only depends on the variable  $m$ , rather than a dependence on both  $n$  and  $m$  in the displacement constraint (57). This is due to the independence of  $\mathbf{u}$  and  $\theta$  in the energy equation in the static case.

To take an example of the specific constraints, consider linear fields of both temperature and displacement with  $n = m = 1$ . The following conditions on the displacement test function  $\hat{\Psi}_I$  can be straightforwardly obtained by taking the various cases of  $\alpha$  and  $\gamma$  up to length one in (57). In two dimensions, this yields:

$$\left\langle \hat{\Psi}_{I,j} \right\rangle_\Omega = \left\langle \hat{\Psi}_I n_j \right\rangle_{\partial\Omega}, \quad j = 1, 2 \quad \forall I \quad (60a)$$

$$\left\langle \hat{\Psi}_{I,2x_1} \right\rangle_\Omega = \left\langle \hat{\Psi}_I x_1 n_2 \right\rangle_{\partial\Omega} \quad \forall I \quad (60b)$$

$$\left\langle \hat{\Psi}_{I,1x_2} \right\rangle_\Omega = \left\langle \hat{\Psi}_I x_2 n_1 \right\rangle_{\partial\Omega} \quad \forall I \quad (60c)$$

$$\left\langle \hat{\Psi}_{I,1x_1} \right\rangle_\Omega = - \left\langle \hat{\Psi}_I \right\rangle_\Omega + \left\langle \hat{\Psi}_I x_1 n_1 \right\rangle_{\partial\Omega} \quad \forall I \quad (60d)$$

$$\left\langle \hat{\Psi}_{I,2x_2} \right\rangle_\Omega = - \left\langle \hat{\Psi}_I \right\rangle_\Omega + \left\langle \hat{\Psi}_I x_2 n_2 \right\rangle_{\partial\Omega} \quad \forall I. \quad (60e)$$

And in three dimensions, one obtains:

$$\left\langle \hat{\Psi}_{I,j} \right\rangle_{\Omega} = \left\langle \hat{\Psi}_I n_j \right\rangle_{\partial\Omega} \quad , \quad j = 1, 2, 3 \quad \forall I \quad (61a)$$

$$\left\langle \hat{\Psi}_{I,j} x_1 \right\rangle_{\Omega} = \left\langle \hat{\Psi}_I x_1 n_j \right\rangle_{\partial\Omega} \quad , \quad j = 2, 3 \quad \forall I \quad (61b)$$

$$\left\langle \hat{\Psi}_{I,j} x_2 \right\rangle_{\Omega} = \left\langle \hat{\Psi}_I x_2 n_j \right\rangle_{\partial\Omega} \quad , \quad j = 1, 3 \quad \forall I \quad (61c)$$

$$\left\langle \hat{\Psi}_{I,j} x_3 \right\rangle_{\Omega} = \left\langle \hat{\Psi}_I x_3 n_j \right\rangle_{\partial\Omega} \quad , \quad j = 1, 2 \quad \forall I \quad (61d)$$

$$\left\langle \hat{\Psi}_{I,1} x_1 \right\rangle_{\Omega} = - \left\langle \hat{\Psi}_I \right\rangle_{\Omega} + \left\langle \hat{\Psi}_I x_1 n_1 \right\rangle_{\partial\Omega} \quad \forall I \quad (61e)$$

$$\left\langle \hat{\Psi}_{I,2} x_2 \right\rangle_{\Omega} = - \left\langle \hat{\Psi}_I \right\rangle_{\Omega} + \left\langle \hat{\Psi}_I x_2 n_2 \right\rangle_{\partial\Omega} \quad \forall I \quad (61f)$$

$$\left\langle \hat{\Psi}_{I,3} x_3 \right\rangle_{\Omega} = - \left\langle \hat{\Psi}_I \right\rangle_{\Omega} + \left\langle \hat{\Psi}_I x_3 n_3 \right\rangle_{\partial\Omega} \quad \forall I. \quad (61g)$$

For the energy equation, the constraint on the test function for temperature change  $\tilde{\Psi}_I$  can be shown to have the following form using  $|\gamma| = 0, 1$ :

$$\left\langle \nabla \tilde{\Psi}_I \right\rangle_{\Omega} = \left\langle \tilde{\Psi}_I \mathbf{n} \right\rangle_{\partial\Omega} \quad \forall I. \quad (62)$$

**Remark 3** Satisfaction of the constraints associated with the displacement test function implies (62) as seen in (60a) and (61a). Therefore, if a single test function is used for both fields, then the displacement constraint can be employed for satisfaction of variational consistency uniformly up to order  $m = n$ .

**Remark 4** In thermoelasticity, the linear constraints are less trivial than in elasticity. However as will be seen, the corrections can still be constructed in a simple manner.

**Remark 5** It can be shown that the use of naturally stabilized nodal integration results in the same constraints as derived herein for the linear case. Therefore, the techniques in the following section can be straightforwardly applied for  $n = 1$ . The derivation follows [24] — if a linear field is assumed in (48) and (49), gradients are constant, and the derivative of gradients in NSNI stabilization terms are zero and drop out of the variational consistency conditions.

**Remark 6** Here, as in all other works based on variationally consistent integration, we have only considered a monomial distribution of a solution distributed in space, constant in time. Therefore dynamic terms are not considered. Nevertheless, as shown in [27], it was clearly demonstrated via numerical examples that satisfaction of these static conditions significantly improves the response in a dynamic setting. In addition, it was shown in [52, 66] that this condition is necessary in order to obtain the standard error estimates (optimal rates for smooth problems) and restore Galerkin orthogonality.

## 7 Variationally consistent integration for thermoelasticity

Satisfaction of (60) and (62) can be achieved by modifying the shape function gradient of the test function in the following from [25]:

$$\nabla \Psi_I^c(\mathbf{x}) = \nabla \Psi_I(\mathbf{x}) + R_I(\mathbf{x}) \begin{Bmatrix} \zeta_{I1} \\ \zeta_{I2} \end{Bmatrix} + R_I(\mathbf{x}) \cdot (x_1 - x_{1I}) \begin{Bmatrix} \zeta_{I3} \\ \zeta_{I4} \end{Bmatrix} + R_I(\mathbf{x}) \cdot (x_2 - x_{2I}) \begin{Bmatrix} \zeta_{I5} \\ \zeta_{I6} \end{Bmatrix} \quad (63)$$

where

$$R_I(\mathbf{x}) = \begin{cases} 1, & \text{if } \mathbf{x} \in \text{supp}(\Psi_I) \\ 0, & \text{if } \mathbf{x} \notin \text{supp}(\Psi_I) \end{cases} \quad (64)$$

where  $\text{supp}(\Psi_I)$  denotes the support of  $\Psi_I$ . Substitution of (63) into (60) results in two systems of equations:

$$\mathbf{A}_I \boldsymbol{\zeta}_I^{c1} = \mathbf{r}_I^{c1} \quad (65a)$$

$$\mathbf{A}_I \boldsymbol{\zeta}_I^{c2} = \mathbf{r}_I^{c2} \quad (65b)$$

where

$$\mathbf{A}_I = \langle \mathbf{P}(\mathbf{x} - \mathbf{x}_I) \mathbf{P}^\top(\mathbf{x} - \mathbf{x}_I) R_I(\mathbf{x}) \rangle_\Omega \quad (66a)$$

$$\mathbf{P}(\mathbf{x}) = \{1, x_1, x_2\}^\top \quad (66b)$$

$$\boldsymbol{\zeta}_I^{c1} = \{\zeta_{I1}, \zeta_{I3}, \zeta_{I5}\}^\top \quad (66c)$$

$$\boldsymbol{\zeta}_I^{c2} = \{\zeta_{I2}, \zeta_{I4}, \zeta_{I6}\}^\top \quad (66d)$$

$$\mathbf{r}_I^{c1} = \{r_{I1}^1, r_{I1}^2, r_{I1}^3\}^\top \quad (66e)$$

$$\mathbf{r}_I^{c2} = \{r_{I2}^1, r_{I2}^2, r_{I2}^3\}^\top \quad (66f)$$

and

$$r_{I1}^1 = \langle \Psi_I n_1 \rangle_{\partial\Omega} - \langle \Psi_{I,1} \rangle_\Omega \quad (67a)$$

$$r_{I2}^1 = \langle \Psi_I n_2 \rangle_{\partial\Omega} - \langle \Psi_{I,2} \rangle_\Omega \quad (67b)$$

$$r_{I1}^2 = \langle \Psi_I n_1 (x_1 - x_{1I}) \rangle_{\partial\Omega} - \langle \Psi_I \rangle_\Omega - \langle \Psi_{I,1} (x_1 - x_{1I}) \rangle_\Omega \quad (67c)$$

$$r_{I2}^2 = \langle \Psi_I n_2 (x_1 - x_{1I}) \rangle_{\partial\Omega} - \langle \Psi_{I,2} (x_1 - x_{1I}) \rangle_\Omega \quad (67d)$$

$$r_{I1}^3 = \langle \Psi_I n_1 (x_2 - x_{2I}) \rangle_{\partial\Omega} - \langle \Psi_{I,1} (x_2 - x_{2I}) \rangle_\Omega \quad (67e)$$

$$r_{I2}^3 = \langle \Psi_I n_2 (x_2 - x_{2I}) \rangle_{\partial\Omega} - \langle \Psi_I \rangle_\Omega - \langle \Psi_{I,2} (x_2 - x_{2I}) \rangle_\Omega. \quad (67f)$$

Due to the locality of  $R_I(\mathbf{x})$ , and dependence on the nodal index  $I$ , the residuals (67) and correction terms (66) are relatively computationally inexpensive. In [24, 26] it was shown that the VC correction of nodal integration only slightly increases computational cost, and is far more effective than several other types of nodal integration in terms of CPU time for a given level of error achieved, and vice versa.

## 8 Space discretization and time integration scheme

### 8.1 Approximations

As previously mentioned, the VC scheme can be uniformly applied to both sets of test functions. Here, we also use the same set of trial functions for both fields. As a result, the approximation of displacement and temperature change are constructed as:

$$\mathbf{u}^h(\mathbf{x}) = \sum_{I=1}^{NP} \mathbf{N}_I(\mathbf{x}) \mathbf{u}_I \equiv \mathbf{N}(\mathbf{x}) \mathbf{u}, \quad \theta^h(\mathbf{x}) = \sum_{I=1}^{NP} \Psi_I(\mathbf{x}) \theta_I \equiv \Psi(\mathbf{x}) \boldsymbol{\theta} \quad (68)$$

where

$$\mathbf{N}_I(\mathbf{x}) = \begin{bmatrix} \Psi_I(\mathbf{x}) & 0 \\ 0 & \Psi_I(\mathbf{x}) \end{bmatrix}, \quad (69)$$

and the test functions are approximated as

$$\mathbf{v}^h(\mathbf{x}) = \sum_{I=1}^{NP} \mathbf{N}_I(\mathbf{x}) \mathbf{v}_I \equiv \mathbf{N}(\mathbf{x}) \mathbf{v}, \quad S^h(\mathbf{x}) = \sum_{I=1}^{NP} \Psi_I(\mathbf{x}) S_I \equiv \Psi(\mathbf{x}) \mathbf{S} \quad (70)$$

where  $\{\Psi_I\}_{I=1}^{NP}$  are the RK shape functions (22), and  $\mathbf{u}_I$ ,  $\theta_I$ ,  $\mathbf{v}_I$ , and  $S_I$  are the nodal coefficients in the Galerkin equation. Note that all approximations and assembly operations are carried out local to any integration point  $\mathbf{x}$ , that is, only over indices which are associated with non-zero shape functions at the location.

For the gradients, the assumed strain-type approach is adopted herein following [11], where the trial function terms are computed in a straightforward manner:

$$\boldsymbol{\varepsilon}(\mathbf{u}^h(\mathbf{x})) = \sum_{I=1}^{NP} \mathbf{B}_I^u(\mathbf{x}) \mathbf{u}_I \equiv \mathbf{B}^u(\mathbf{x}) \mathbf{u}, \quad \nabla \theta^h(\mathbf{x}) = \sum_{I=1}^{NP} \mathbf{B}_I^\theta(\mathbf{x}) \theta_I \equiv \mathbf{B}^\theta(\mathbf{x}) \boldsymbol{\theta} \quad (71)$$

where

$$\mathbf{B}_I^u(\mathbf{x}) = \begin{bmatrix} \Psi_{I,1}(\mathbf{x}) & 0 \\ 0 & \Psi_{I,2}(\mathbf{x}) \\ \Psi_{I,2}(\mathbf{x}) & \Psi_{I,1}(\mathbf{x}) \end{bmatrix}, \quad (72)$$

$$\mathbf{B}_I^\theta(\mathbf{x}) = [\Psi_{I,1}(\mathbf{x}), \Psi_{I,2}(\mathbf{x})]^\top.$$

and the test function terms are corrected using (63):

$$\boldsymbol{\varepsilon}(\mathbf{v}^h(\mathbf{x})) = \sum_{I=1}^{NP} \mathbf{B}_I^{uc}(\mathbf{x}) \mathbf{v}_I \equiv \mathbf{B}^{uc}(\mathbf{x}) \mathbf{v}, \quad \nabla S^h(\mathbf{x}) = \sum_{I=1}^{NP} \mathbf{B}_I^{\theta c}(\mathbf{x}) S_I \equiv \mathbf{B}^{\theta c}(\mathbf{x}) \mathbf{S} \quad (73)$$

where

$$\mathbf{B}_I^{uc}(\mathbf{x}) = \begin{bmatrix} \Psi_{I,1}^c(\mathbf{x}) & 0 \\ 0 & \Psi_{I,2}^c(\mathbf{x}) \\ \Psi_{I,2}^c(\mathbf{x}) & \Psi_{I,1}^c(\mathbf{x}) \end{bmatrix}, \quad (74)$$

$$\mathbf{B}_I^{\theta c}(\mathbf{x}) = [\Psi_{I,1}^c(\mathbf{x}), \Psi_{I,2}^c(\mathbf{x})]^\top.$$

**Remark 7** Since the the VC conditions (57) and (59) do not include natural boundary conditions, and the test function gradient correction (63)-(67) does not appear in the weak Galerkin enforcement of boundary conditions (14), the approach is easily applicable to complex engineering problems without special considerations. Similarly, NSNI methods expand gradient terms only in bilinear forms. Therefore, NSNI also need not be considered in any boundary conditions. For examples of the use of these approaches in more complex applications, see [1] or [61].

## 8.2 Semi-discrete matrix form

For the matrix forms, let the following subscript notation be adopted:  $u$  denotes the mechanical field, and  $\theta$  denotes the thermal field. Introducing (68), (70), (71), and (73) into the Galerkin equation (14), and employing the naturally stabilized nodal integration technique introduced in Section 5, the matrix system in 2D is obtained as:

$$\begin{bmatrix} \mathbf{M}_{uu} & \mathbf{0} \\ \mathbf{0} & \mathbf{0} \end{bmatrix} \begin{bmatrix} \ddot{\mathbf{u}} \\ \ddot{\boldsymbol{\theta}} \end{bmatrix} + \begin{bmatrix} \mathbf{0} & \mathbf{0} \\ \mathbf{C}_{\theta u} & \mathbf{C}_{\theta\theta} \end{bmatrix} \begin{Bmatrix} \dot{\mathbf{u}} \\ \dot{\boldsymbol{\theta}} \end{Bmatrix} + \begin{bmatrix} \mathbf{K}_{uu} & \mathbf{K}_{u\theta} \\ \mathbf{0} & \mathbf{K}_{\theta\theta} \end{bmatrix} \begin{Bmatrix} \mathbf{u} \\ \boldsymbol{\theta} \end{Bmatrix} = \begin{Bmatrix} \mathbf{F}^{\text{ext}} \\ \mathbf{Q}^{\text{ext}} \end{Bmatrix} \quad (75)$$

where  $\mathbf{u}$  and  $\boldsymbol{\theta}$  are the row vectors of  $\{\mathbf{u}_I\}_{I=1}^{NP}$  and  $\{\boldsymbol{\theta}_I\}_{I=1}^{NP}$ , respectively, and for a homogeneous media as presented in the examples:

$$\mathbf{M}_{uu} = \sum_{L=1}^{NP} \rho \mathbf{N}(\mathbf{x}_L)^\top \mathbf{N}(\mathbf{x}_L) W_L \quad (76a)$$

$$\mathbf{C}_{\theta u} = -T_0 \mathbf{K}_{u\theta}^\top \quad (76b)$$

$$\mathbf{C}_{\theta\theta} = \sum_{L=1}^{NP} \rho c_p \boldsymbol{\Psi}(\mathbf{x}_L)^\top \boldsymbol{\Psi}(\mathbf{x}_L) W_L \quad (76c)$$

$$\mathbf{K}_{uu} = \sum_{L=1}^{NP} (\mathbf{B}^{uc}(\mathbf{x}_L))^\top \mathbf{D} \mathbf{B}^u(\mathbf{x}_L) W_L + \sum_{L=1}^{NP} \sum_{i=1}^2 (\mathbf{B}_i^{u\nabla}(\mathbf{x}_L))^\top \mathbf{D} \mathbf{B}_i^{u\nabla}(\mathbf{x}_L) M_{Li} \quad (76d)$$

$$\mathbf{K}_{u\theta} = - \sum_{L=1}^{NP} \beta (\mathbf{B}^{uc}(\mathbf{x}_L))^\top \mathbf{I} \boldsymbol{\Psi}(\mathbf{x}_L) W_L \quad (76e)$$

$$\mathbf{K}_{\theta\theta} = \sum_{L=1}^{NP} k (\mathbf{B}^{\theta c}(\mathbf{x}_L))^\top \mathbf{B}^\theta(\mathbf{x}_L) W_L + \sum_{L=1}^{NP} \sum_{i=1}^2 k (\mathbf{B}_i^{\theta\nabla}(\mathbf{x}_L))^\top \mathbf{B}_i^{\theta\nabla}(\mathbf{x}_L) M_{Li} \quad (76f)$$

$$\mathbf{F}^{\text{ext}} = \sum_{L=1}^{NP} \mathbf{N}(\mathbf{x}_L)^\top \mathbf{b} W_L + \sum_{K=1}^{NBPu} \mathbf{N}(\mathbf{x}_K)^\top \mathbf{h} L_K^u \quad (76g)$$

$$\mathbf{Q}^{\text{ext}} = \sum_{L=1}^{NP} \boldsymbol{\Psi}(\mathbf{x}_L)^\top \mathbf{Q} W_L + \sum_{K=1}^{NBP\theta} \boldsymbol{\Psi}(\mathbf{x}_K)^\top \bar{q} L_K^\theta \quad (76h)$$

where  $\mathbf{I} = [1 \ 1 \ 0 \ 0]^\top$ ,  $\mathbf{D}$  is the matrix corresponding to the tensor  $\mathbb{C}$ ,  $\mathbf{b}$  and  $\mathbf{h}$  are the matrix forms of  $\mathbf{b}$  and  $\mathbf{h}$ , respectively,  $L_K^u$  and  $L_K^\theta$  denote the  $K$ th weight of one of the  $NBPu$  and  $NBP\theta$  integration points on the natural boundaries for the

displacement and temperature change, respectively, and  $\mathbf{B}_i^{u\nabla}$  and  $\mathbf{B}_i^{\theta\nabla}$  are the global matrices in (39) and (47), respectively.

The final semi-discrete linear time-dependent system (75) can be written in compact form as

$$\mathbf{M}\ddot{\mathbf{d}}(t) + \mathbf{C}\dot{\mathbf{d}}(t) + \mathbf{K}\mathbf{d}(t) = \mathbf{F}(t) \quad (77)$$

where

$$\mathbf{M} = \begin{bmatrix} \mathbf{M}_{uu} & \mathbf{0} \\ \mathbf{0} & \mathbf{0} \end{bmatrix}, \quad \mathbf{C} = \begin{bmatrix} \mathbf{0} & \mathbf{0} \\ \mathbf{C}_{\theta u} & \mathbf{C}_{\theta\theta} \end{bmatrix}, \quad \mathbf{K} = \begin{bmatrix} \mathbf{K}_{uu} & \mathbf{K}_{u\theta} \\ \mathbf{0} & \mathbf{K}_{\theta\theta} \end{bmatrix} \quad (78)$$

and

$$\mathbf{d} = \begin{bmatrix} \mathbf{u} \\ \boldsymbol{\theta} \end{bmatrix}, \quad \mathbf{F} = \begin{bmatrix} \mathbf{F}^{\text{ext}} \\ \mathbf{Q}^{\text{ext}} \end{bmatrix}. \quad (79)$$

### 8.3 Time integration

In this research, the semi-discrete equations are advanced in time using the Newmark method, which consists of the following equations [31]:

$$\mathbf{M}\mathbf{a}_{n+1} + \mathbf{C}\mathbf{v}_{n+1} + \mathbf{K}\mathbf{d}_{n+1} = \mathbf{F}_{n+1} \quad (80a)$$

$$\mathbf{d}_{n+1} = \mathbf{d}_n + \Delta t \mathbf{v}_n + \frac{\Delta t^2}{2} [(1 - 2\bar{\beta})\mathbf{a}_n + 2\bar{\beta}\mathbf{a}_{n+1}] \quad (80b)$$

$$\mathbf{v}_{n+1} = \mathbf{v}_n + \Delta t [(1 - \gamma)\mathbf{a}_n + \gamma\mathbf{a}_{n+1}] \quad (80c)$$

where  $\mathbf{d}_n$ ,  $\mathbf{v}_n$ , and  $\mathbf{a}_n$  are the approximations of  $\mathbf{d}(t_n)$ ,  $\dot{\mathbf{d}}(t_n)$ , and  $\ddot{\mathbf{d}}(t_n)$ , respectively, and  $\bar{\beta}$  and  $\gamma$  are the Newmark parameters.

## 9 Numerical examples

In this section numerical examples are presented to demonstrate the accuracy and stability of the proposed method. The following five numerical integration methods are tested for comparison:

1. Direct nodal integration (denoted DNI)
2. Variationally consistent integration with direct nodal integration (denoted VC-DNI)
3. Naturally stabilized nodal integration (denoted NSNI)
4. Variationally consistent integration with naturally stabilized nodal integration (denoted VC-NSNI)
5. Gaussian integration (denoted GI) with high order rules

Thermoelastic benchmarks are solved, and the solution by these approaches are compared with exact solutions and results from numerical methods in the literature.

Unless otherwise stated, for the RK approximation, linear basis with cubic B-spline kernels with a normalized support size of 2 are employed in all problems, using a uniform node distribution with a nodal spacing of  $\Delta x = 0.001$ . The five point

Gaussian quadrature rule is used for GI with cell boundaries coincident with the nodal positions. The implicit and unconditionally stable backward difference method [48] is employed with a time step of  $\Delta t = 0.001$  to discretize the time domain in all examples. The transformation method [12] is used for the imposition of essential boundary conditions. The solutions are presented in terms of the dimensionless variables given in (11), and unless otherwise stated the material properties used are given in Table 1.

Aside from the patch test, we will consider a linear elastic half-space  $y \geq 0$  subjected to either a time-dependent temperature change or heat flux on its boundary plane, free of traction. The following initial boundary value problems based on these conditions can be obtained: (a) the first Danilovskaya problem [18], (b) the second Danilovskaya problem [19], and (c) the Sternberg and Chakravorty problem [56]. These problems can be treated as one-dimensional, and can yield either coupled or uncoupled thermoelasticity.

### 9.1 Patch test for thermoelasticity

In this example, a one-dimensional patch test is performed to verify the exactness of the proposed VCI approach. The steady equations of energy and equilibrium on a domain  $\Omega = ]0, 1[$  can be cast as

$$\left( \frac{E}{1 - \nu^2} \right) \frac{\partial^2 u}{\partial x^2} - \beta \frac{\partial \theta}{\partial x} + b = 0 \quad \text{in } \Omega, \quad (81a)$$

$$k \frac{\partial^2 \theta}{\partial x^2} + Q = 0 \quad \text{in } \Omega. \quad (81b)$$

The boundary conditions considered here are

$$u(0) = 0, \quad u(1) = g, \quad (82a)$$

$$\theta(0) = 0, \quad \theta(1) = g. \quad (82b)$$

Linear solutions in both fields can be obtained using the following prescribed values:

$$b = \beta, \quad Q = 0, \quad g = 1, \quad (83)$$

which yields the exact solution of this problem for the two fields as

$$u = x, \quad \theta = x. \quad (84)$$

The discretized steady equations (81) yield the following matrix form:

$$\begin{bmatrix} \mathbf{K}_{uu} & \mathbf{K}_{u\theta} \\ \mathbf{0} & \mathbf{K}_{\theta\theta} \end{bmatrix} \begin{Bmatrix} \mathbf{u} \\ \theta \end{Bmatrix} = \begin{Bmatrix} \mathbf{F}^{\text{ext}} \\ \mathbf{Q}^{\text{ext}} \end{Bmatrix}. \quad (85)$$

It is important to note that for uniform discretizations, good accuracy or even exact solutions can be obtained by various integration methods, but in non-uniform discretizations, most methods fail the patch test. Therefore, the non-uniform discretization of the one dimensional domain shown in Figure 3 is employed in the study.



Figure 3: Non-uniform node distribution in one dimension

The dimensionless parameters  $E = 1$ ,  $\nu = 0.3$ , and  $\beta = 0.05$  are used in the patch test. As shown in Table 2, VC-DNI and the VC-NSNI pass the patch test (with machine precision) as expected. It can be seen that VC-DNI yields acceptable results for static thermoelasticity, but as will be seen in the next section, not for quasi-static and dynamic thermoelasticity. It is also notable that NSNI can drastically reduce the error without VC corrections. However, it will also be seen later that these treatments are still necessary to obtain good accuracy across all problems tested.

	DNI	VC-DNI	NSNI	VC-NSNI
u	0.2174	1.4418E-14	0.0035	1.6187E-13
$\theta$	0.2113	1.2204E-14	0.0035	5.6947E-15

Table 2:  $L_2$  norm of error for various methods in a 1-D static thermoelastic patch test

## 9.2 Quasi-static benchmarks: the first Danilovskaya problem

In this subsection, we study the quasi-static case of the first Danilovskaya problem under various discretizations and quadrature schemes. The first Danilovskaya problem [18] concerns a linear elastic half-space subjected to a uniform sudden temperature change on its boundary, with free traction. The boundary conditions in this problem are given as

$$\theta(0, t) = \theta_0, \quad (86a)$$

$$\sigma(0, t) = 0. \quad (86b)$$

The quasi-static problem neglects inertial effects, and the semi-discretized equations are

$$\mathbf{C}\dot{\mathbf{d}}(t) + \mathbf{K}\mathbf{d}(t) = \mathbf{F}(t). \quad (87)$$

### 9.2.1 Stability study

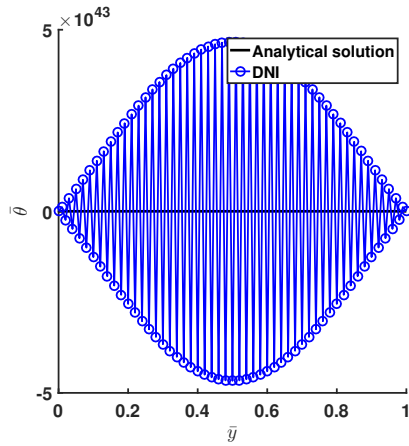
First, the stability of the proposed methods is studied. Uniform discretizations are employed, where spatial stability is more problematic in nodal integration [49, 24].

The spatial distributions of temperature change and displacement at  $\bar{t} = 2$  are presented in Figures 4 and 5, respectively. It can be seen that DNI provides wildly unstable results, as before, for both the coupled and uncoupled cases. The node-to-node oscillations are typical of instability in nodal integration, yet here it is again seen these are orders of magnitude higher than pure elasticity.

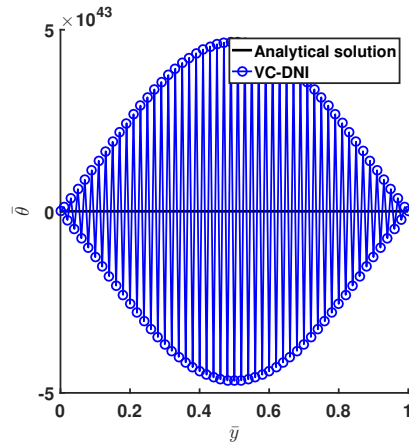
The VC test function correction of DNI fails to provide any additional stability to the solution. This can be explained easily. The source of the instability is the calculation of meshfree gradients of the trial functions, not the test functions [24]. Therefore, the stability of the solution will not be affected by the selection of the test

function. In [27] it was shown that while VC corrections can provide additional stability in non-uniform discretizations, they fail to provide it in uniform discretizations. Therefore additional stability must be provided by other means for the solution to be stable across all types of discretizations. Taking another point of view, in uniform discretizations the residuals of the integration constraints are generally very low [14, 11, 66]. Meanwhile, the VC corrections are driven by the residual, so little to no modification to the overall numerical method is made in this case.

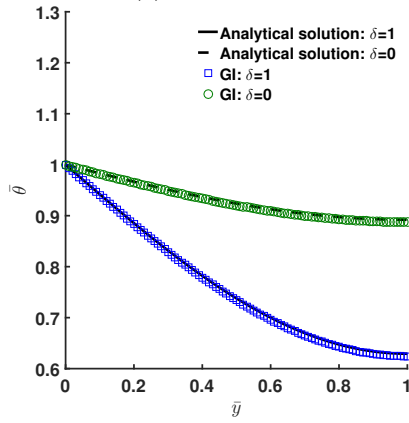
Finally, both NSNI and VC-NSNI provide both stable and accurate results, with solutions comparable to the more expensive high-order Gaussian quadrature. Here the analytical solution is available for both the coupled and uncoupled cases.



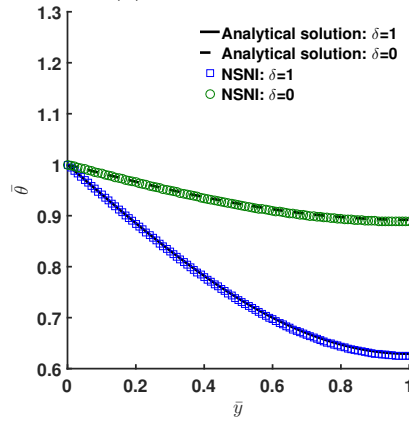
(a) DNI:  $\delta = 1$



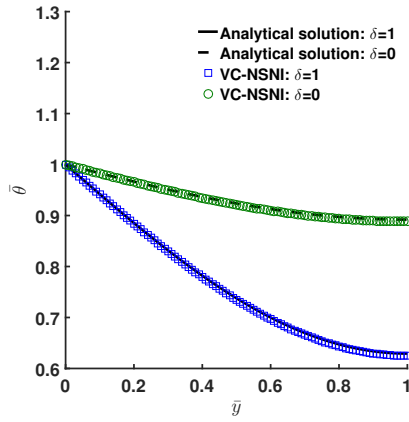
(b) VC-DNI:  $\delta = 1$



(c) GI

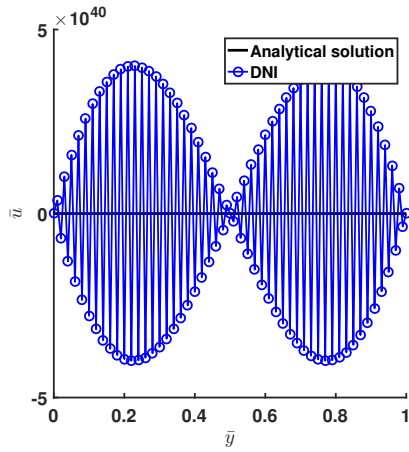


(d) NSNI

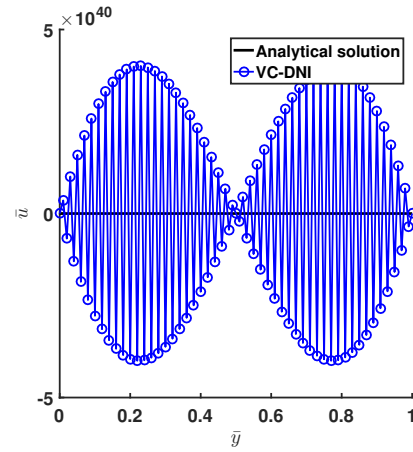


(e) VC-NSNI

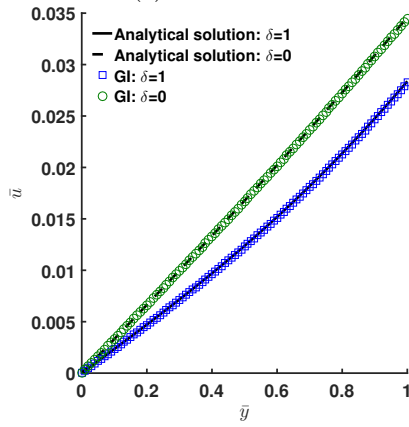
Figure 4: Temperature changes along  $\bar{y}$  at  $\bar{t} = 2$  for the first Danilovskaya problem in a quasi-static uniform discretization with various methods.



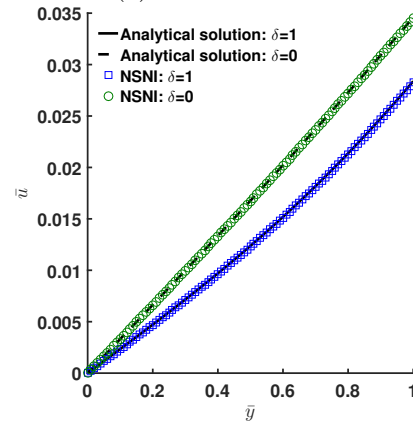
(a) DNI:  $\delta = 1$



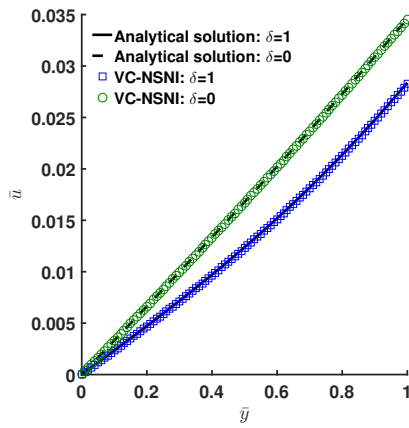
(b) VC-DNI:  $\delta = 1$



(c) GI



(d) NSNI



(e) VC-NSNI

Figure 5: Displacements along  $\bar{y}$  at  $\bar{t} = 2$  for the first Danilovskaya problem in a quasi-static uniform discretization with various methods.

Figures 6 and 7 show the time histories of temperature change and displacement at  $\bar{y} = 1$ , respectively, where explosive growth over time is seen in DNI for both fields, in both the coupled and uncoupled cases. Also seen in the figures, NSNI provides stable solutions, in both pure NSNI, and VC-NSNI. The VC correction here also does not provide much, which is expected as previously discussed.

As we have seen, Gauss integration was considered in this study. Here stable and accurate results were obtained, yet this method needs at least five-point quadrature to converge [11], which in turn is computationally demanding. On the other hand, the proposed RKPM formulation using VC-NSNI can provide comparable accuracy and stability with just one-point integration.

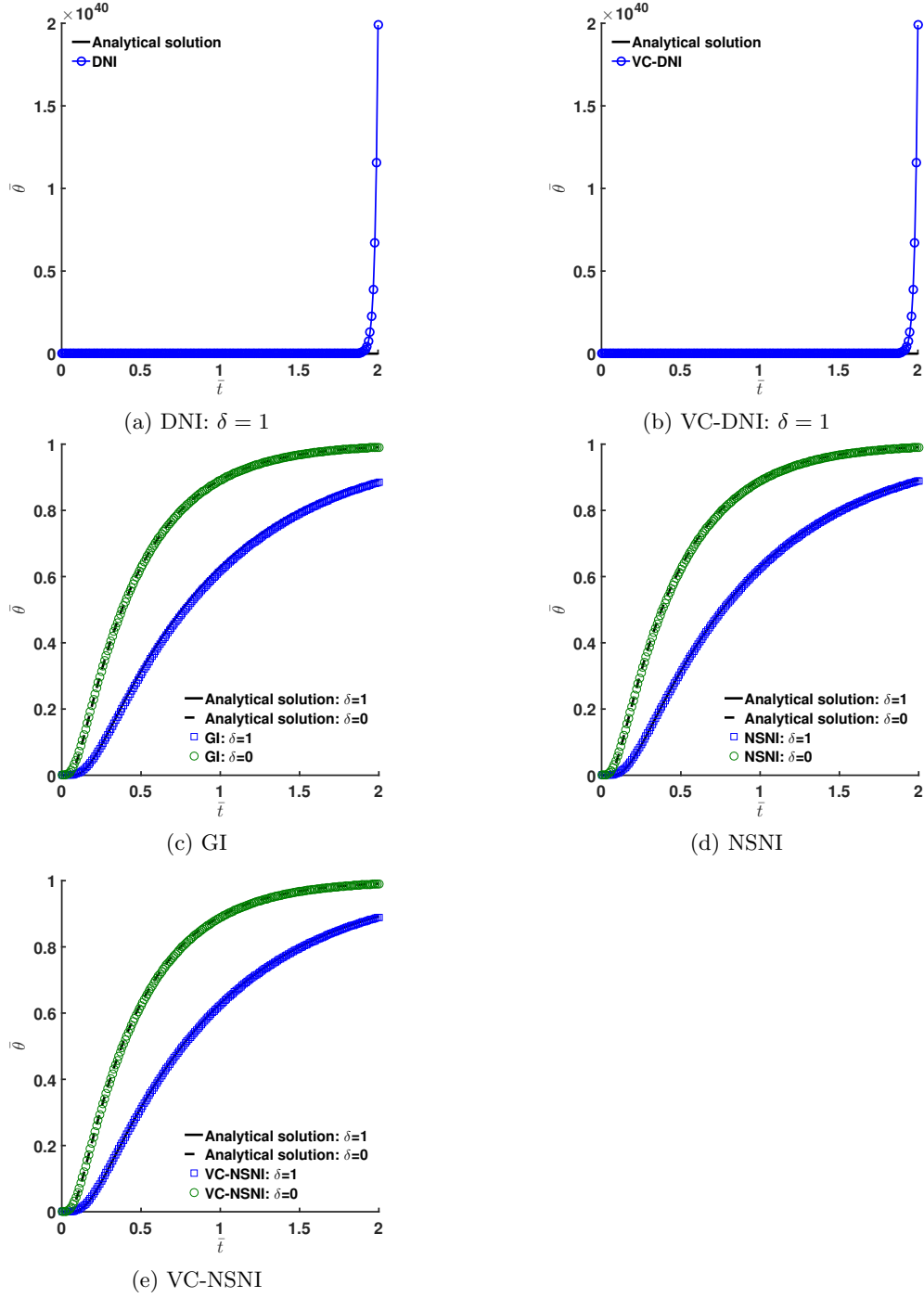


Figure 6: Time histories of temperature change at  $\bar{y} = 1$  for the first Danilovskaya problem in a quasi-static uniform discretization with various methods.

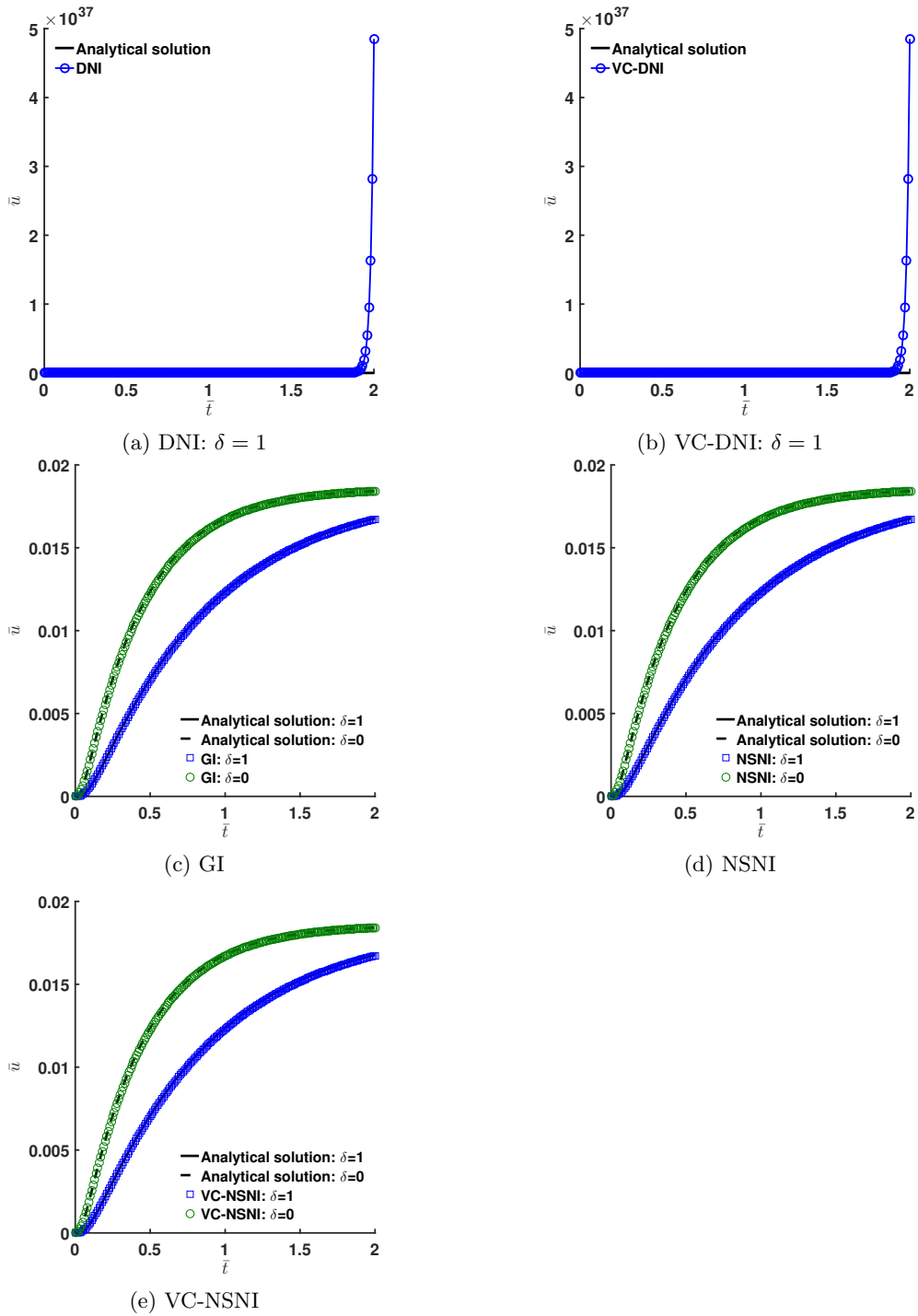


Figure 7: Time histories of displacement at  $\bar{y} = 1$  for the first Danilovskaya problem in a quasi-static uniform discretization with various methods.

### 9.2.2 Accuracy study

A non-uniform discretization is now considered to demonstrate the accuracy of the present approach. Largely, uniform discretizations are special cases where high accuracy can be obtained in meshfree methods regardless of the quadrature technique (excluding pure nodal integration which is unstable).

Here, since DNI provides completely unstable results, while Gauss integration is prohibitively expensive, only NSNI and VC techniques are considered.

Unlike in a uniform discretization, Figures 8 and 9 show that while pure NSNI can still provide stable results, it fails to provide good accuracy. There are large errors in the solution of NSNI, clearly observed in Figure 8a. The inaccuracy in the spatial distributions of the fields also manifest in the time histories shown in Figures 10 and 11. On the other hand, VC-NSNI provides both stability and high accuracy in the solution, in both spatial distributions and time histories. Thus, nodally integrated RKPM using VC-NSNI is the best candidate for integration in thermoelasticity considering all the methods tested, and VC-NSNI will be generally employed for the remainder of the examples.

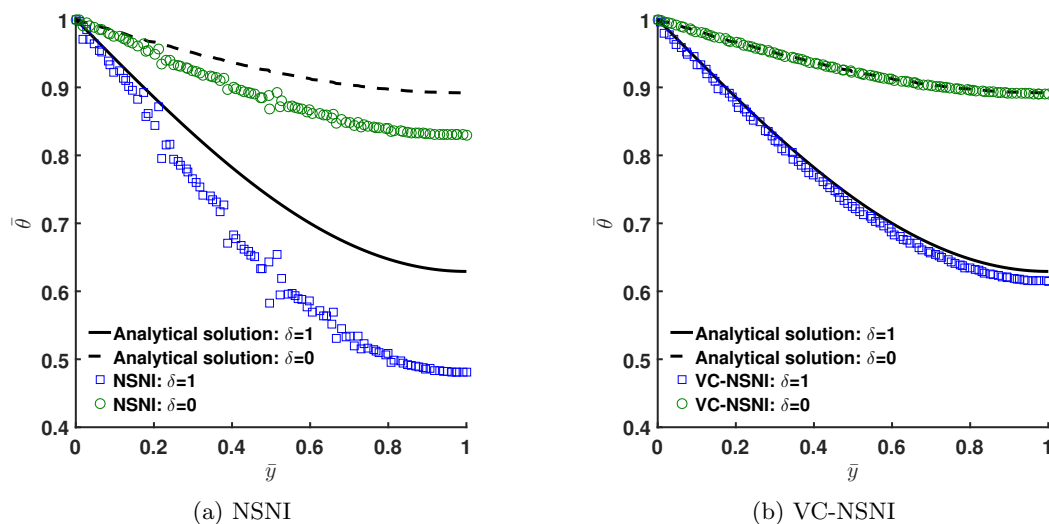


Figure 8: Temperature change along  $\bar{y}$  at  $\bar{t} = 2$  for the first Danilovskaya problem in a quasi-static nonuniform discretization and various methods.

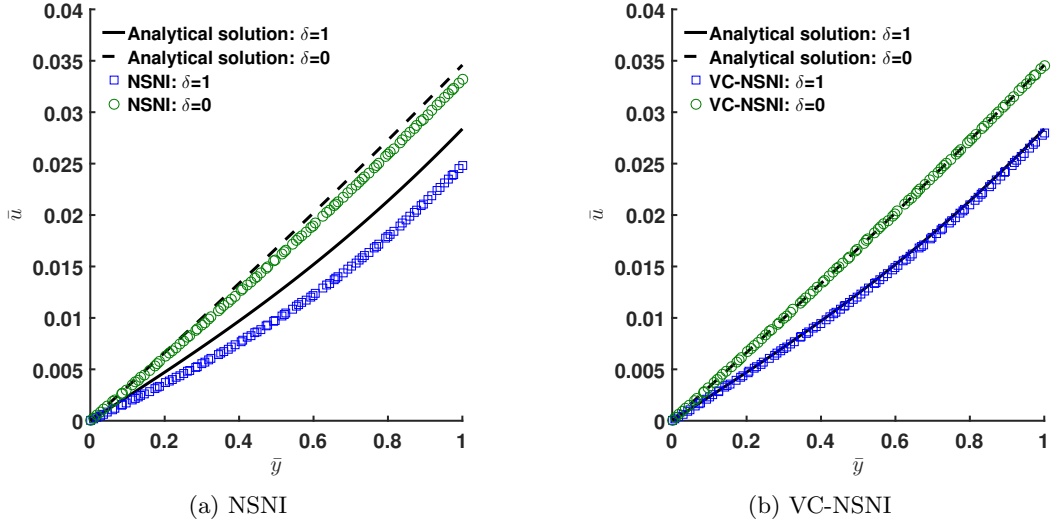


Figure 9: Displacement along  $\bar{y}$  at  $\bar{t} = 2$  for the first Danilovskaya problem in a quasi-static nonuniform discretization and various methods.

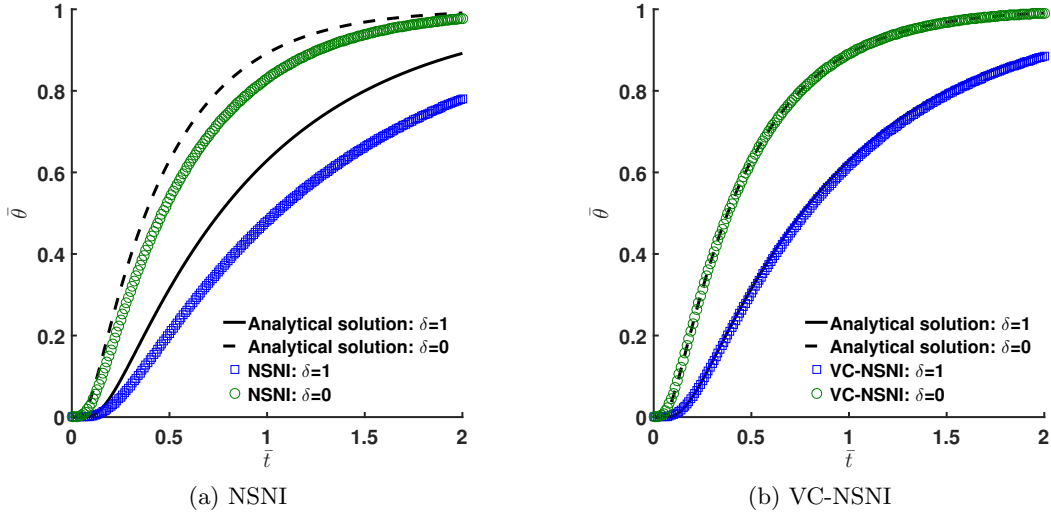


Figure 10: Time histories of temperature change at  $\bar{y} = 1$  for the first Danilovskaya problem in a quasi-static nonuniform discretization and various methods.

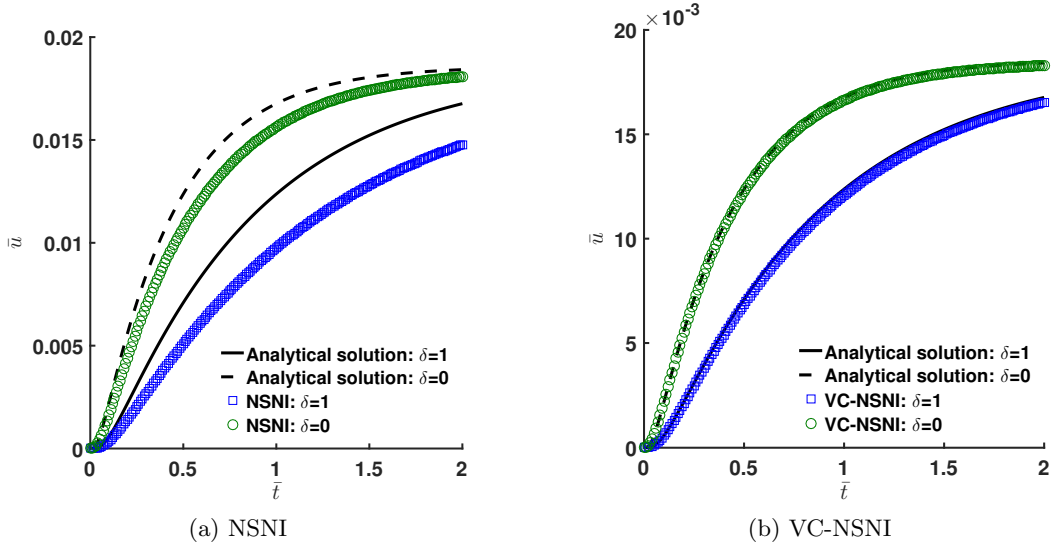
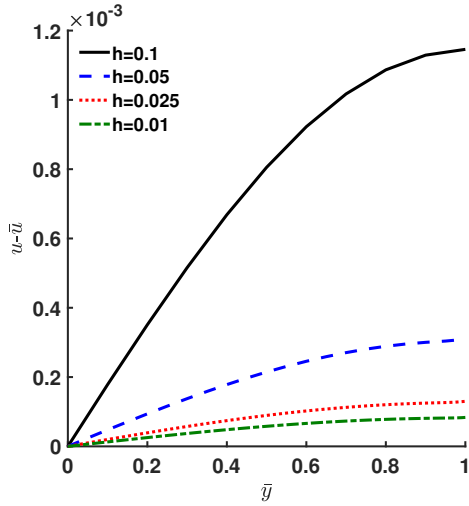


Figure 11: Time histories of displacement at  $\bar{y} = 1$  for the first Danilovskaya problem in a quasi-static nonuniform discretization and various methods.

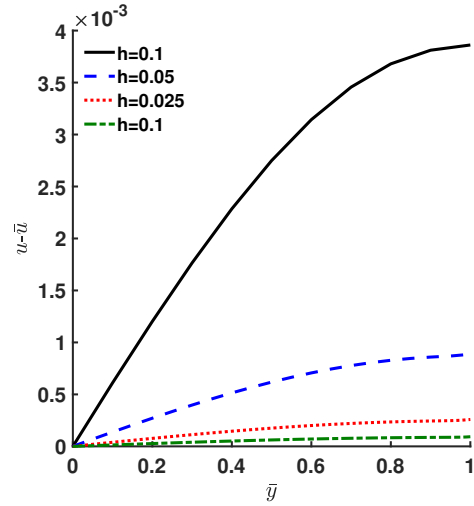
### 9.2.3 Convergence study

To study the convergence of the solution under refinement of the nodal spacing  $\Delta x$ , NSNI under a uniform nodal distribution is selected since it provides both stable and accurate results in this setting. Four NSNI discretizations of  $\Delta x = 0.1, 0.05, 0.025$ , and  $0.01$  are selected, and the results are shown in Figure 12. Clearly, the error for both fields converge, in both the coupled and uncoupled cases.

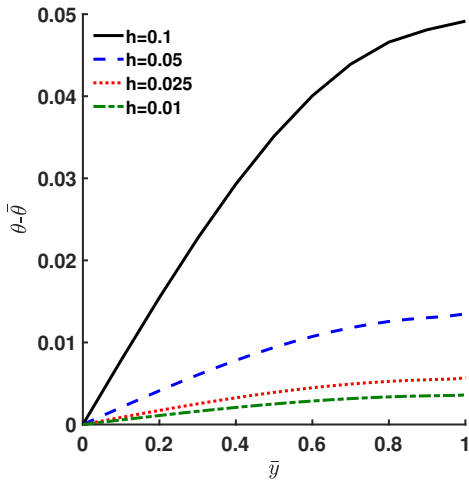
It can be seen that the displacements for both the coupled and uncoupled cases are not affected much by the nodal spacing  $\Delta x$ , since high accuracy is already obtained under course discretizations. For temperature change, both coupled and uncoupled cases are much more sensitive to  $\Delta x$ . Thus if temperature is of interest, it appears one must take care in the level of refinement necessary to obtain an acceptable solution. Here we remark that while  $\Delta x = 0.01$  provides fairly acceptable results, the previous results using  $\Delta x = 0.001$  obtained very high accuracy in VC-NSNI.



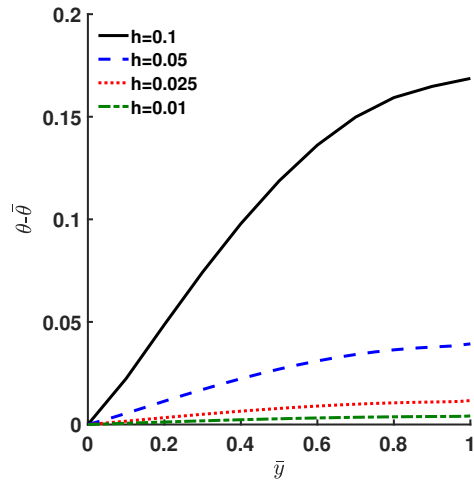
(a) Error of displacement:  $\delta = 0$



(b) Error of displacement:  $\delta = 1$



(c) Error of temperature change:  $\delta = 0$



(d) Error of temperature change:  $\delta = 1$

Figure 12: Convergence study along  $\bar{y}$  at  $\bar{t} = 2$  for the first Danilovskaya problem in a quasi-static uniform discretization with NSNI.

### 9.3 Dynamic benchmarks

The next examples consider inertial dynamic terms, where the full equation (77) is used to study dynamic thermoelasticity. VC-NSNI is employed to test the accuracy and stability of the RKPM solution.

#### 9.3.1 First Danilovskaya problem: dynamic case

The first Danilovskaya problem has analytical solutions for the dynamic uncoupled case ( $\delta = 0$ ), but not the coupled case ( $\delta = 1$ ). As such, results from the DMLPG method in [23], and FEM in [34] are used for verification of the present VC-NSNI solution.

The time histories at  $\bar{y} = 1$  for the temperature change and displacement are shown in Figures 13 and 14, respectively. For the uncoupled case, the RKPM solution matches well with the analytical solution with almost no error. The dramatic shift in displacement at  $\bar{t} = 1$  is well-captured, with no oscillations despite the weak discontinuity in time. For the coupled case, the present method agrees well with the reference numerical solutions from the literature. Moreover, RKPM can also capture the transition point well in this case, more so than the other numerical methods.

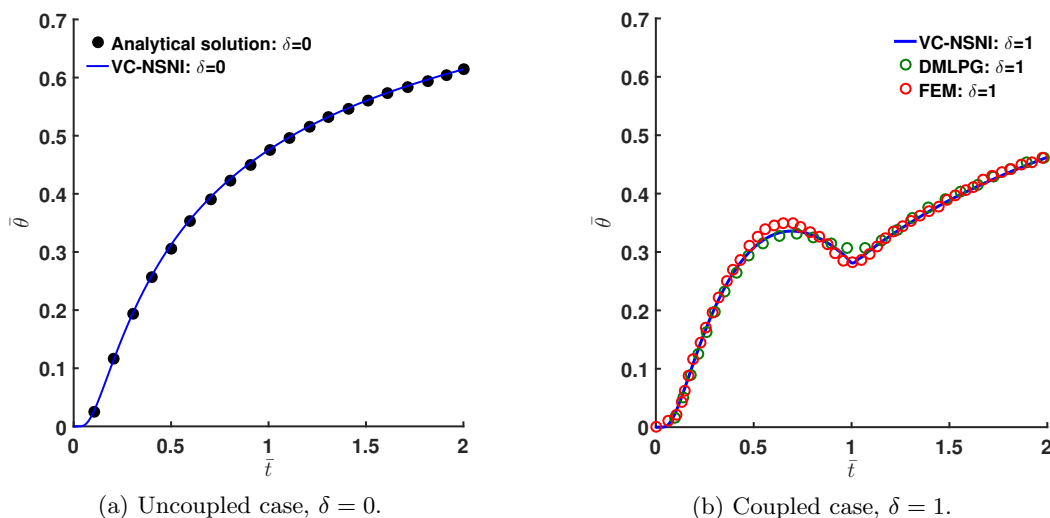


Figure 13: Temperature time history for the first Danilovskaya problem, dynamic.

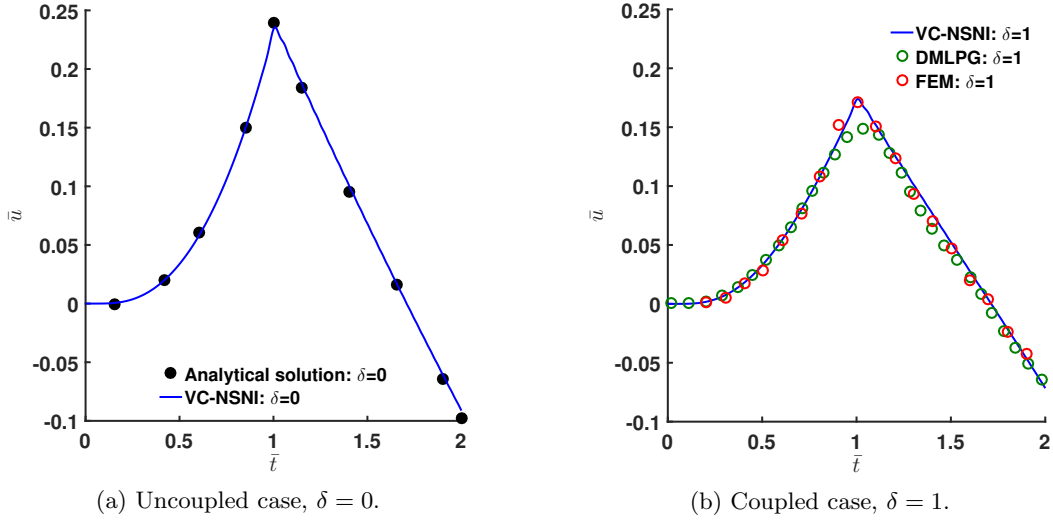


Figure 14: Displacement time history for the first Danilovskaya problem, dynamic.

Time histories for the stresses at  $\bar{y} = 1$  for the coupled and uncoupled cases are shown in Figure 15. To explain the discontinuous response: the suddenly applied temperature can be modeled as a complementary error function, so the propagation of the stress wave is discontinuous. The derivation of the stress wave front and jump discontinuity can be found in [58]. For the uncoupled case, it can be seen that the solution matches well with the analytical solution, with no observable oscillation. For the coupled case this is also true, yet here the other numerical methods do oscillate in time across the discontinuity, and MLPG also smears the wave front.

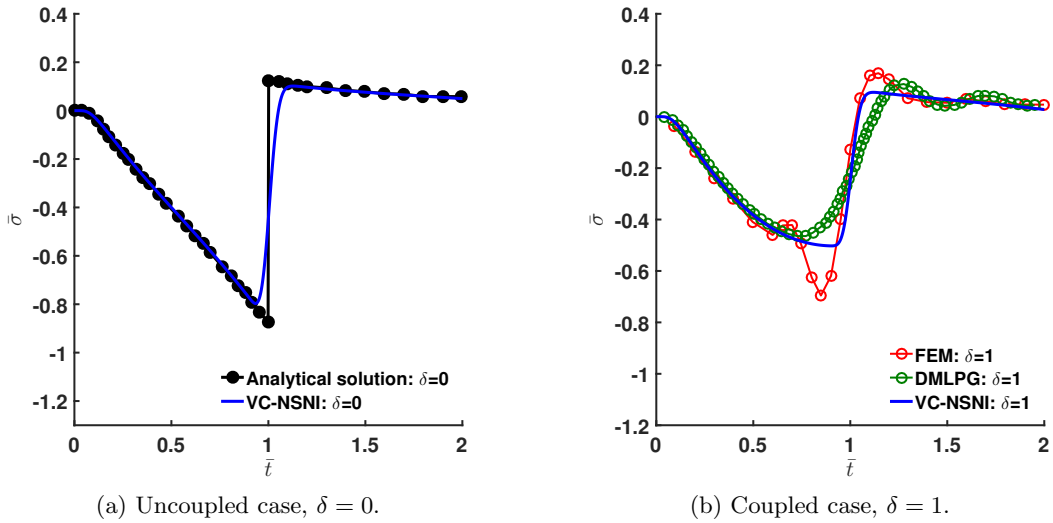


Figure 15: Stress time history for the first Danilovskaya problem, dynamic.

### 9.3.2 The second Danilovskaya problem

Next we consider a heat flux condition on the boundary  $\bar{y} = 0$ , which is the second Danilovskaya problem [19], an extended version of the first Danilovskaya problem.

The boundary conditions are

$$\begin{cases} \sigma(0, t) = 0 \\ kT_{,y} = b(T - T_\infty) \end{cases} \quad (88)$$

where  $b$  is the boundary-layer conductance and  $T_\infty$  the ambient temperature. Based on [59], these conditions can be expressed as:

$$q(y, \bar{t}) = m(1 - \theta(\bar{y}, \bar{t})) \quad \text{on} \quad \bar{y} = 0 \quad (89)$$

where

$$m = \frac{\rho\kappa b}{(\lambda + 2\mu)k}. \quad (90)$$

A parameter of  $m = 0.5$  is used in this study to select the free variable  $b$ . The temperature difference and displacement at  $\bar{y} = 1$  are shown in Figure 16. Both of the coupled and uncoupled results obtained by VC-NSNI are in agreement with analytical solutions. Although the results of temperature change are slightly smaller than analytical solutions after  $\bar{t} = 1.5$ , they still seem acceptable since they match the general trend.

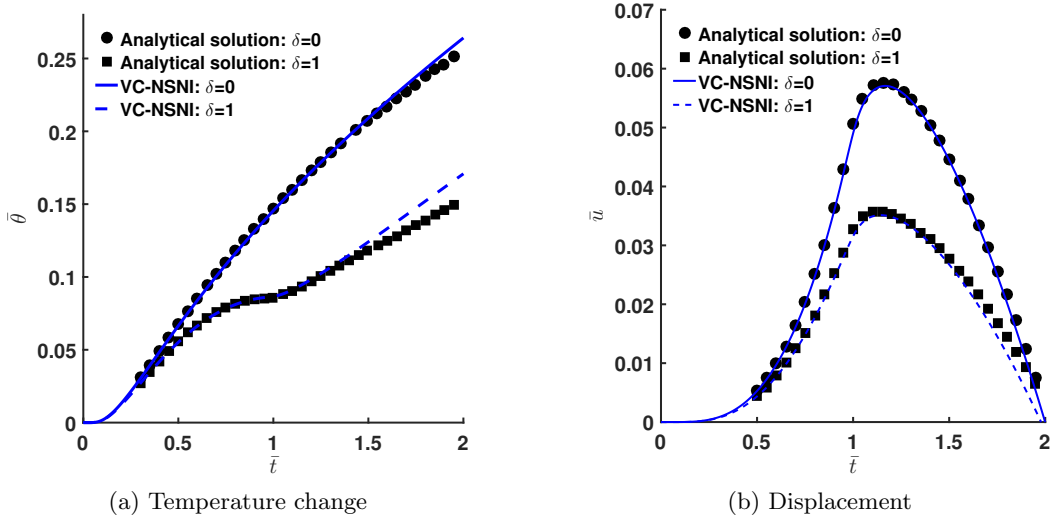


Figure 16: Time histories for the second Danilovskaya problem.

### 9.3.3 The Sternberg and Chakravorty problem

The third benchmark considered uses a ramp-type heating, a more realistic boundary condition, on the boundary  $\bar{y} = 0$ , which is the Sternberg and Chakravorty problem [56]. The boundary conditions are

$$\tilde{\theta}(\bar{y}, t) = \begin{cases} \tilde{\theta}/\theta & 0 \leq \tilde{\theta} \leq \theta \\ 1 & \tilde{\theta} \geq \theta \end{cases}. \quad (91)$$

We consider  $\tilde{\theta} = 0.25$  and the coupled case with  $\delta = 1$ . Figure 17 shows the time histories of temperature change and displacement at  $\bar{y} = 1$  obtained from the proposed nodally integrated RKPM technique, and analytical solution [46], where

the results agree well. Similar to the previous benchmark, there are small differences between numerical and analytical results for the temperature difference after  $\bar{t} = 1.5$ , yet the RKPM results are still close, and the trend agrees well.

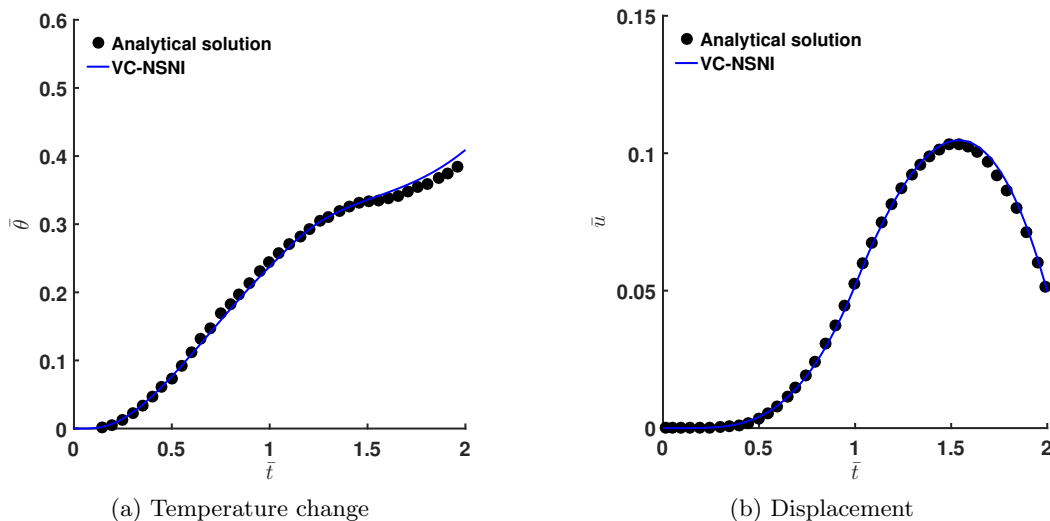


Figure 17: Time histories for the Sternberg and Chakravorty problem in the coupled case,  $\delta = 1$ .

## 10 Conclusions

In part I of this paper, a stable, efficient, and accurate nodally integrated RKPM formulation has been developed for coupled and uncoupled thermoelasticity. It was first shown that nodal integration is highly unstable, yielding oscillations in the solution orders of magnitude higher than in pure elasticity. They grow seemingly unbounded and completely destroy the results. Thus it appears in this problem, stabilization of nodal integration is absolutely necessary.

To eliminate the spurious low energy modes that cause the oscillations, the NSNI scheme has been developed for the two-field problem. Analogous to the gradient expansion of the strain in solid mechanics, stabilization is introduced into the temperature gradient for a two-field NSNI.

To improve the poor accuracy induced by nodal integration, VCI is introduced by first deriving the variational consistency conditions for the two-field problem of thermoelasticity. Here it was found that there are three integration constraints due to the two governing equations and the coupling between them. This is in contrast to pure elasticity which has only one constraint. A uniform correction was then proposed for the test function gradients.

The patch test, first and second Danilovskaya problems, and the Sternberg and Chakravorty problem have been studied. The combined approach of VC-NSNI yields a stable, accurate and efficient RKPM solution to the coupled and uncoupled static, quasi-static, and dynamic benchmark problems. This was systematically shown through comparisons of RKPM results with analytical solutions, and solutions using other existing numerical methods.

In the sequel, these methods will be extended to generalized thermoelasticity,

which provides a finite speed for the propagation of temperature, and thus a much less restrictive critical time step in explicit calculations. In addition, these techniques are developed for hyperbolic thermoplasticity, which also provides amenable conditions for explicit dynamics.

**Acknowledgments** The authors greatly acknowledge the support of this work by Penn State, and the endowment of the L. Robert and Mary L. Kimball Early Career Professorship. Proofing of this manuscript by Jennifer Dougal is also acknowledged and appreciated.

## References

- [1] J. Baek, J.-S. Chen, G. Zhou, K. Arnett, M. Hillman, G. Hegemier, and S. Hardesty. A semi-lagrangian reproducing kernel particle method with particle-based shock algorithm for explosive welding simulation. *Computational Mechanics*, 67:1601–1627, 2021.
- [2] S. Beissel and T. Belytschko. Nodal integration of the element-free Galerkin method. *Computer Methods in Applied Mechanics and Engineering*, 139:49–74, 1996.
- [3] T. Belytschko, Y. Guo, W. K. Liu, and S. P. Xiao. A unified stability analysis of meshless particle methods. *International Journal for Numerical Methods in Engineering*, 48(9):1359–1400, 2000.
- [4] F. Bobaru and S. Mukherjee. Meshless approach to shape optimization of linear thermoelastic solids. *International Journal for Numerical Methods in Engineering*, 53(4):765–796, 2002.
- [5] B. A. Boley and I. S. Tolins. Transient coupled thermoelastic boundary value problems in the half-space. *Journal of Applied Mechanics*, 29(4):637–646, 1962.
- [6] A. A. Cannarozzi and F. Ubertini. A mixed variational method for linear coupled thermoelastic analysis. *International Journal of Solids and Structures*, 38(4):717–739, 2001.
- [7] J. P. Carter and J. R. Booker. Finite element analysis of coupled thermoelasticity. *Computers and Structures*, 31(1):73–80, 1989.
- [8] J. Chen and G. F. Dargush. Boundary element method for dynamic poroelastic and thermoelastic analyses. *International Journal of Solids and Structures*, 32(15):2257–2278, 1995.
- [9] J. Chen, W. Hu, M. Puso, Y. Wu, and X. Zhang. Strain smoothing for stabilization and regularization of galerkin meshfree methods. In *Meshfree methods for partial differential equations III*, pages 57–75. Springer, 2007.
- [10] J.-S. Chen, M. Hillman, and S.-W. Chi. Meshfree methods: progress made after 20 years. *Journal of Engineering Mechanics*, 143(4):04017001, 2017.

- [11] J.-S. Chen, M. Hillman, and M. Rüter. An arbitrary order variationally consistent integration for Galerkin meshfree methods. *International Journal for Numerical Methods in Engineering*, 95(5):387–418, 2013.
- [12] J.-S. Chen, C. Pan, C.-T. Wu, and W. K. Liu. Reproducing Kernel Particle Methods for large deformation analysis of non-linear structures. *Computer Methods in Applied Mechanics and Engineering*, 139(1-4):195–227, 1996.
- [13] J.-S. Chen and H.-P. Wang. New boundary condition treatments in meshfree computation of contact problems. *Computer Methods in Applied Mechanics and Engineering*, 187(3-4):441–468, 2000.
- [14] J.-S. Chen, C.-T. Wu, S. Yoon, and Y. You. A stabilized conforming nodal integration for galerkin mesh-free methods. *International journal for numerical methods in engineering*, 50(2):435–466, 2001.
- [15] J.-S. Chen, S. Yoon, and C.-T. Wu. Non-linear version of stabilized conforming nodal integration for Galerkin mesh-free methods. *International Journal for Numerical Methods in Engineering*, 53(12):2587–2615, 2002.
- [16] J.-S. Chen, X. Zhang, and T. Belytschko. An implicit gradient model by a reproducing kernel strain regularization in strain localization problems. *Computer Methods in Applied Mechanics and Engineering*, 193(27-29):2827–2844, 2004.
- [17] H. K. Ching and S. C. Yen. Transient thermoelastic deformations of 2-D functionally graded beams under nonuniformly convective heat supply. *Composite Structures*, 73(4):381–393, 2006.
- [18] V. Danilouskaya. Thermal stresses in elastic half space due to sudden heating of its boundary. *Pelageya Yakovlevna Kochina*, 14:316–321, 1950.
- [19] V. Danilouskaya. On a dynamic problem of thermoelasticity. *Prikladnaya Matematika i Mekhanika*, 16:341–344, 1952.
- [20] J. Dolbow and T. Belytschko. Numerical integration of the galerkin weak form in meshfree methods. *Computational mechanics*, 23(3):219–230, 1999.
- [21] Q. Duan, X. Li, H. Zhang, and T. Belytschko. Second-order accurate derivatives and integration schemes for meshfree methods. *International Journal for Numerical Methods in Engineering*, 92(4):399–424, 2012.
- [22] T.-P. Fries and T. Belytschko. Convergence and stabilization of stress-point integration in mesh-free and particle methods. *International Journal for Numerical Methods in Engineering*, 74(7):1067–1087, 2008.
- [23] K. Hasanpour and D. Mirzaei. A fast meshfree technique for the coupled thermoelasticity problem. *Acta Mechanica*, 229(6):2657–2673, 2018.
- [24] M. Hillman and J.-S. Chen. An accelerated, convergent, and stable nodal integration in Galerkin meshfree methods for linear and nonlinear mechanics. *International Journal for Numerical Methods in Engineering*, 107:603–630, 2016.

- [25] M. Hillman and J.-S. Chen. Nodally integrated implicit gradient reproducing kernel particle method for convection dominated problems. *Computer Methods in Applied Mechanics and Engineering*, 299:381–400, 2016.
- [26] M. Hillman and J.-S. Chen. Performance comparison of nodally integrated galerkin meshfree methods and nodally collocated strong form meshfree methods. In *Advances in Computational Plasticity*, pages 145–164. Springer, 2018.
- [27] M. Hillman, J.-S. Chen, and S.-W. Chi. Stabilized and variationally consistent nodal integration for meshfree modeling of impact problems. *Computational Particle Mechanics*, 1(3):245–256, 2014.
- [28] M. Hillman and K.-C. Lin. Consistent weak forms for meshfree methods: Full realization of  $h$ -refinement,  $p$ -refinement, and  $a$ -refinement in strong-type essential boundary condition enforcement. *Computer Methods in Applied Mechanics and Engineering*, 373:113448, 2021.
- [29] P. Hosseini-Tehrani and M. R. Eslami. BEM analysis of thermal and mechanical shock in a two-dimensional finite domain considering coupled thermoelasticity. *Engineering Analysis with Boundary Elements*, 24(3):249–257, 2000.
- [30] H.-Y. Hu, C.-K. Lai, and J.-S. Chen. A study on convergence and complexity of reproducing kernel collocation method. *Interaction and multiscale mechanics*, 2(3):295–319, 2009.
- [31] T. J. Hughes. *The finite element method: linear static and dynamic finite element analysis*. Dover Publications, Inc., Mineola, New York, 2012.
- [32] K. K. Tamma and S. B. Railkar. On heat displacement based hybrid transfinite element formulations for uncoupled/coupled thermally induced stress wave propagation. *Computers and Structures*, 30:1025–1036, 1988.
- [33] G. A. Keramidas and E. C. Ting. A finite element formulation for thermal stress analysis. Part I: Variational formulation. *Nuclear Engineering and Design*, 39(2-3):267–275, 1976.
- [34] G. A. Keramidas and E. C. Ting. A finite element formulation for thermal stress analysis. Part II: Finite element formulation. *Nuclear Engineering and Design*, 39(2-3):277–287, 1976.
- [35] S. Li and W. K. Liu. Synchronized reproducing kernel interpolant via multiple wavelet expansion. *Computational Mechanics*, 21:28–47, 1998.
- [36] S. Li and W. K. Liu. Reproducing kernel hierarchical partition of unity, part I - formulation and theory. *International Journal for Numerical Methods in Engineering*, 288(July 1998):251–288, 1999.
- [37] S. Li and W. K. Liu. Reproducing kernel hierarchical partition of unity, Part II - applications. *International Journal for Numerical Methods in Engineering*, 45(3):289–317, 1999.

- [38] G.-R. Liu, G. Y. Zhang, Y. Y. Wang, Z. H. Zhong, G. Y. Li, and X. Han. A nodal integration technique for meshfree radial point interpolation method (NI-RPIM). *International Journal of Solids and Structures*, 44(11-12):3840–3860, 2007.
- [39] W. K. Liu, S. Jun, and Y. F. Zhang. Reproducing kernel particle methods. *International Journal for Numerical Methods in Fluids*, 20(8-9):1081–1106, 1995.
- [40] W.-K. Liu, S. Li, and T. Belytschko. Moving least-square reproducing kernel methods (i) methodology and convergence. *Computer methods in applied mechanics and engineering*, 143(1-2):113–154, 1997.
- [41] W. K. Liu, J. S.-J. Ong, and R. A. Uras. Finite element stabilization matrices — a unification approach. *Computer Methods in Applied Mechanics and Engineering*, 53(1):13–46, 1985.
- [42] A. Mahdavi, S.-W. Chi, and M. M. Atif. A two-field semi-lagrangian reproducing kernel model for impact and penetration simulation into geo-materials. *Computational Particle Mechanics*, 7(2):351–364, 2020.
- [43] A. Mahdavi, S.-W. Chi, and H. Zhu. A gradient reproducing kernel collocation method for high order differential equations. *Computational Mechanics*, 64(5):1421–1454, 2019.
- [44] G. Moutsanidis, W. Li, and Y. Bazilevs. Reduced quadrature for FEM, IGA and meshfree methods. *Computer Methods in Applied Mechanics and Engineering*, 373:113521, 2021.
- [45] T. Nagashima. Node-by-node meshless approach and its applications to structural analyses. *International Journal for Numerical Methods in Engineering*, 46(3):341–385, 1999.
- [46] J. L. Nickell, Robert E and Sackman. Approximate solutions in linear, coupled thermoelasticity. *Journal of Applied Mechanics*, 35(2):255–266, 1968.
- [47] W. Nowacki. *Dynamic problems of thermoelasticity*. Springer Science & Business Media, 1975.
- [48] J.-H. Prevost and D. Tao. Finite element analysis of dynamic coupled thermoelasticity problems with relaxation times. *Journal of applied mechanics*, 50(4a):817–822, 1983.
- [49] M. A. Puso, J.-S. Chen, E. Zywickz, and W. Elmer. Meshfree and finite element nodal integration methods. *International Journal for Numerical Methods in Engineering*, 74(3):416–446, 2008.
- [50] L. F. Qian and R. C. Batra. Transient Thermoelastic Deformations of a thick functionally graded plate. *Journal of Thermal Stresses*, 27(8):705–740, 2004.
- [51] P. W. Randles and L. D. Libersky. Normalized SPH with stress points. *Int. J. Numer. Meth. Engng*, 48(May 1999):1445–1462, 2000.

- [52] M. Rüter, M. Hillman, and J.-S. Chen. Corrected stabilized non-conforming nodal integration in meshfree methods. In *Meshfree methods for partial differential equations VI*, pages 75–92. Springer, 2013.
- [53] T. Siriaksorn, S.-W. Chi, C. Foster, and A. Mahdavi.  $u$ - $p$  semi-lagrangian reproducing kernel formulation for landslide modeling. *International Journal for Numerical and Analytical Methods in Geomechanics*, 42(2):231–255, 2018.
- [54] J. Sladek, V. Sladek, P. Sölek, C. L. Tan, and C. Zhang. Two- and three-dimensional transient thermoelastic analysis by the MLPG method. *Computer Modeling in Engineering and Sciences*, 47, 2009.
- [55] V. Sládek and J. Sládek. Boundary element method in micropolar thermoelasticity. Part II: Boundary integro-differential equations. *Engineering Analysis*, 2(2):81–91, 1985.
- [56] E. L. I. Sternberg and J. G. Chakravorty. *On inertia effects in a transient thermoelastic problem*. Brown University, 1958.
- [57] M. Tanaka, T. Matsumoto, and M. Moradi. Application of boundary element method to 3-D problems of coupled thermoelasticity. *Engineering Analysis with Boundary Elements*, 16(4):297–303, 1995.
- [58] E. A. Thornton. *Thermal structures for aerospace applications*. American Institute of Aeronautics and Astronautics, 1996.
- [59] N. Tosaka and I. G. Suh. Boundary element analysis of dynamic coupled thermoelasticity problems. *Computational Mechanics*, 8(5):331–342, 1991.
- [60] D. Wang and J. Wu. An inherently consistent reproducing kernel gradient smoothing framework toward efficient Galerkin meshfree formulation with explicit quadrature. *Computer Methods in Applied Mechanics and Engineering*, 349:628–672, 2019.
- [61] H. Wei, J.-S. Chen, F. Beckwith, and J. Baek. A naturally stabilized semi-lagrangian meshfree formulation for multiphase porous media with application to landslide modeling. *Journal of Engineering Mechanics*, 146(4):04020012, 2020.
- [62] H. Wei, J.-S. Chen, and M. Hillman. A stabilized nodally integrated meshfree formulation for fully coupled hydro-mechanical analysis of fluid-saturated porous media. *Computers & Fluids*, 141:105–115, 2016.
- [63] C.-T. Wu, S.-W. Chi, M. Koishi, and Y. Wu. Strain gradient stabilization with dual stress points for the meshfree nodal integration method in inelastic analyses. *International Journal for Numerical Methods in Engineering*, 107(1):3–30, 2016.
- [64] C.-T. Wu, M. Koishi, and W. Hu. A displacement smoothing induced strain gradient stabilization for the meshfree Galerkin nodal integration method. *Computational Mechanics*, 2015.

- [65] C. T. Wu, Y. Wu, D. Lyu, X. Pan, and W. Hu. The momentum-consistent smoothed particle Galerkin (MC-SPG) method for simulating the extreme thread forming in the flow drill screw-driving process. *Computational Particle Mechanics*, 7(2):177–191, 2020.
- [66] J. Wu and D. Wang. An accuracy analysis of Galerkin meshfree methods accounting for numerical integration. *Computer Methods in Applied Mechanics and Engineering*, 375:113631, 2021.
- [67] B. J. Zheng, X. W. Gao, K. Yang, and C. Z. Zhang. A novel meshless local Petrov-Galerkin method for dynamic coupled thermoelasticity analysis under thermal and mechanical shock loading. *Engineering Analysis with Boundary Elements*, 60:154–161, 2015.

# Nodally integrated thermomechanical RKPM: Part II — Generalized thermoelasticity and hyperbolic finite-strain thermoplasticity

Michael Hillman<sup>\*†</sup> and Kuan-Chung Lin<sup>‡</sup>

This is a post-peer-review, pre-copyedit version of an article [to be] published in Computational Mechanics. The final authenticated version is [will be] available online at: <http://dx.doi.org/10.1007/s00466-021-02048-8>.

## Abstract

In this two-part paper, a stable and efficient nodally-integrated reproducing kernel particle method (RKPM) approach for solving the governing equations of generalized thermomechanical theories is developed. Part I investigated quadrature in the weak form using classical thermoelasticity as a model problem, and a stabilized and corrected nodal integration was proposed. In this sequel, these methods are developed for generalized thermoelasticity and generalized finite-strain plasticity theories of the hyperbolic type, which are more amenable to explicit time integration than the classical theories. Generalized thermomechanical models yield finite propagation of temperature, with a so-called second sound speed. Since this speed is not well characterized for common engineering materials and environments, equating the elastic wave speed with the second sound speed is investigated to obtain results close to classical thermoelasticity, which also yields a uniform critical time step. Implementation of the proposed nodally integrated RKPM for explicit analysis of finite-strain thermoplasticity is also described in detail. Several benchmark problems are solved to demonstrate the effectiveness of the proposed approach for thermomechanical analysis.

**keywords** Meshfree methods, generalized thermoelasticity, thermoplasticity, nodal integration, coupled problems

## 1 Introduction

Part I of this paper began with investigating nodal quadrature of the Galerkin weak form in meshfree methods for thermoelasticity. It was shown that severe oscillations, orders of magnitude greater than the solution itself, were present when nodal integration was employed. This is in contrast to pure elasticity where oscillations are typically smaller than the magnitude of the true solution. This instability was also shown to be explosive in nature, yielding meaningless results for nodal integration. A naturally stabilized nodal integration (NSNI) [27] was then proposed which was

---

<sup>\*</sup>Kimball Assistant Professor, Department of Civil and Environmental Engineering, The Pennsylvania State University, University Park, PA 16802, USA.

<sup>†</sup>Corresponding author; email: [mhillman@psu.edu](mailto:mhillman@psu.edu); postal address: 224A Sackett Building, The Pennsylvania State University, University Park, PA 16802, USA.

<sup>‡</sup>Assistant Professor, Department of Civil Engineering, National Cheng Kung University, Tainan 70101, Taiwan, ROC.

shown to be effective at precluding this instability. In particular, this method provides a highly efficient solution without tunable parameters typical of stabilization approaches. The  $n$ th order variational consistency conditions were then derived for the two-field problem, and an efficient correction was proposed resulting in a variationally consistent naturally stabilized nodal integration (VC-NSNI). Importantly, as shown in [55], satisfaction of the variational consistency conditions is necessary to ensure convergence of the numerical solution, whereas traditional approaches cannot meet these conditions.

This next part focuses on the development of this stabilized and corrected nodal quadrature in RKPM for generalized thermoelasticity, and generalized finite-strain thermoplasticity. Particular emphasis is given to explicit analysis.

As discussed in Part I, the need for solving partially- or fully-coupled systems may arise due to many physical phenomena. Sub-classes of these problems also involve a large degree of material deformation, flow, and failure. Here, the traditional mesh-based methods suffer from mesh-distortion under large deformations, and are ineffective in dealing with material failure and associated topological changes in the domain present in related applications such as additive (e.g. 3-D printing — topological changes) and subtractive (e.g., machining — both) manufacturing techniques where coupling between the displacement and temperature can be present. Meshfree methods such as RKPM on the other hand, which are point-based and do not require a mesh, are quite adept at handling these phenomena [11, 13].

In Part I, the *classical* thermoelasticity theory [22] was discussed. While the equation of motion is a hyperbolic equation, the energy equation is parabolic. This provides a finite propagation speed for displacements but an infinite propagation speed for the temperature, which is non-physical: for instance, this violates the theory of special relativity by propagating information faster than light. As an alternative to the classical equations, generalized thermoelasticity theories [39, 24] have been developed, in which the energy equation is of the hyperbolic type. These theories are referred to as thermoelasticity with a so-called *second sound*. Part I of this work dealt with the classical theory; Part II will deal with these generalized theories, as well as finite-strain plasticity of the parabolic and hyperbolic types [9, 52, 20]. The numerical motivation for the use of these theories is of course, to provide efficient explicit analysis, where the time step is directly proportional to the nodal spacing rather than its square.

There are several generalized thermoelasticity theories. One popular theory is the Lord and Shulman (L-S) theory [39], based on a modified Fourier Law of heat conduction using a relaxation time. Another well-established generalized thermoelasticity theory is the Green and Lindsay (G-L) theory [24] based on an entropy production inequality. This theory uses two relaxation times, in the Duhamel-Neumann law and the entropy density. In both theories, the energy equation becomes hyperbolic, and thus the temperature propagation has a finite velocity.

Numerical solutions based on the L-S theory have been reported using FEM [44]. BEM [10, 51] also provides good results in thermoelastic problems using both the G-L theory and L-S theory. Thermoelasticity theories with a second sound have been studied in various problems, such as a layer of isotropic homogeneous material [5],

thermal shock problems with a crack [47, 40, 58, 1, 48, 30], and rotating disks [33].

For finite strain thermoplasticity, FEM methods have been developed for simulating large deformation problems, such as necking processes [50, 3, 56, 7], modelling of welding [37], ballistic penetration of metallic targets [8], and orthogonal high-speed machining [41]. Other mesh-based methods also have been used to simulate the necking process, for example, the mixed finite element method [50] and the updated enhanced assumed strain finite element formalism [2]. Of course, these finite element-based methods suffer from mesh distortion issues under large deformations, and are ineffective at dealing with material flow and separation [36, 11].

Recently, meshfree approximations have been used to study the generalized thermoelasticity theories. Various methods have been used, for example, the Meshless local Petrov–Galerkin method [29] as well as methods using radial basis functions [57]. Meshfree methods have also been developed for finite-strain thermoplasticity. Simulations have included ductile fracture [49] and friction drilling [43, 54]. Based on variational thermomechanical constitutive updates and the optimal transportation meshfree (OTM) method [34], the hot OTM method (HOTM) [53] has been developed for modeling external heating and cooling behavior. The HOTM method has mostly been applied to laser cladding technology [23]. Yet, virtually none of these meshfree approaches to thermomechanical equations discussed consider any advanced domain integration techniques other than [43, 54], regardless of the use of classical or generalized equations. For a review of existing techniques and an in-depth discussion on meshfree quadrature including [43, 54], see Part I of this paper.

In this work, the methods developed in the prequel are developed for generalized thermoelasticity, and generalized thermoplasticity. Namely, the variationally consistent naturally stabilized nodal integration (VC-NSNI) technique is extended to both of these problems. For generalized thermoelasticity, the extension of these two methods is straightforward. Strains and temperature gradients are expanded with implicit gradient approximations for stabilization as before, and the correction remains the same. In finite-strain thermoplasticity, the Cauchy stress and associated variation on strain are instead expanded to stabilize the results. Finally, since the propagation speed of temperature is not well-characterized for most engineering materials, and in most settings (typically this is reported near absolute zero for special materials such as superfluids), equating the second sound speed to the first is investigated. This yields a critical time step in explicit analysis that is the same as in pure solid mechanics problems, but meanwhile very small relaxation times such that the solution is close to the classical theory, which is widely accepted as a good model for thermomechanical problems.

The remainder of this paper is organized as follows. The general governing equations of the coupled thermomechanical theory are discussed in Section 2. In Section 3 classical and generalized thermoelasticity are introduced as special cases, with the RKPM discretization of the weak form given. Section 4 develops thermoplasticity as another more general case, with the Lagrangian RKPM discretization given along with associated explicit algorithms. In Section 5 the time-step criteria is discussed. Benchmarks are then solved for generalized thermoelasticity and classical and generalized thermoplasticity in Section 6, where equating the first and second sound speed

is also investigated. Final concluding remarks for this two-part paper are given in Section 7.

## 2 Governing equations of the coupled thermal-mechanical theory

In this section, we review the general governing equations for all of the aforementioned thermomechanical theories. Ultimately, they consist of the balance of energy, and the balance of momentum. The subsequent assumptions used in these equations yield both thermoelasticity and thermoplasticity.

### 2.1 Dissipation inequality and balance of energy

For the thermomechanical problem, the dissipation inequality can be written as

$$\frac{1}{\rho} \boldsymbol{\sigma} : \dot{\boldsymbol{\varepsilon}} - \dot{e} + \theta \eta - \frac{1}{\rho \theta} \mathbf{q} \cdot \nabla \theta \geq 0 \quad (1)$$

where  $(\dot{\phantom{x}})$  denotes a material time rate of change (herein  $(\ddot{\phantom{x}})$  will denote the second-order material time derivative; all terms are Lagrangian),  $\rho$  is the density,  $\boldsymbol{\sigma}$  is the Cauchy stress,  $\dot{\boldsymbol{\varepsilon}}$  is the rate of deformation,  $\dot{e}$  is the time rate of change of the internal energy,  $\theta \equiv T - T_0$  is the temperature change and herein is treated as a primary unknown;  $T$  is the absolute temperature,  $T_0$  is the reference temperature,  $\eta$  is the entropy, and  $\mathbf{q}$  the heat flux.

Equation (1) can be decomposed into the conductive thermal  $\Omega_{\text{con}}$ , and thermo-mechanical  $\Omega_{\text{thermech}}$ , parts as:

$$\Omega_{\text{thermech}} = \frac{1}{\rho} \boldsymbol{\sigma} : \dot{\boldsymbol{\varepsilon}} - \dot{e} + \theta \eta \geq 0 \quad (2a)$$

$$\Omega_{\text{con}} = - \frac{1}{\rho \theta} \mathbf{q} \cdot \nabla \theta \geq 0. \quad (2b)$$

From the fact that the density  $\rho$  and the absolute temperature change  $\theta$  are always positive, using (2b) one can deduce that

$$\mathbf{q} \cdot \nabla \theta \leq 0. \quad (3)$$

This is Fourier's inequality which states that heat flows from a hot region to a cold region. This can be assured by Duhamel's law of heat conduction

$$\mathbf{q} = -\mathbf{k}(\mathbf{F}, \theta) \cdot \nabla \theta \quad (4)$$

where  $\mathbf{F}$  is the deformation gradient and the thermal conductivity tensor  $\mathbf{k}$  is positive-definite. Assuming an isotropic material, one obtains Fourier's law of heat conduction  $\mathbf{k} = \mathbf{I}k$  with isotropic scalar conductivity  $k$ .

Next, we introduce the balance of energy

$$\rho \dot{e} + \nabla \cdot \mathbf{q} = \boldsymbol{\sigma} : \dot{\boldsymbol{\varepsilon}} + Q \quad (5)$$

where  $Q$  is the heat source, and here we assume the Helmholtz free energy  $\phi$  contains elastic and plastic entropy [50]:

$$\phi \equiv e - \theta(\eta - \eta^p) \quad (6)$$

where  $\eta$ ,  $\eta^p$ , and  $\eta^e = \eta - \eta^p$  are the total entropy, the plastic entropy, and the elastic entropy, respectively.

Substitution (5) and (6) into (2a) yields

$$\nabla \cdot \mathbf{q} + \theta\dot{\eta} = Q. \quad (7)$$

This is the balance of energy for both thermoelasticity and thermal plasticity.

## 2.2 Governing equations of the coupled thermal-mechanical theory

The balance of energy in the current configuration  $\Omega^{\mathbf{x}}$  with boundary  $\Gamma^{\mathbf{x}}$  over time interval  $]0, t_f[$  can thus be obtained as

$$\nabla_{\mathbf{x}} \cdot \mathbf{q} + \theta\dot{\eta} = Q \quad \text{on } \Omega^{\mathbf{x}} \times ]0, t_f[ \quad (8)$$

where  $\nabla_{\mathbf{x}}$  is the Del operator associated with current configuration with coordinates  $\mathbf{x}$ . For small-strain linear elastic problems,  $\nabla_{\mathbf{x}}$  is simply Del and there is no distinction between the current configuration and the reference configuration, and in this case we denote the domain as  $\Omega$ .

The conservation of momentum in the current configuration can be expressed as:

$$\rho\ddot{\mathbf{u}} = \nabla_{\mathbf{x}} \cdot \boldsymbol{\sigma} + \mathbf{b} \quad \text{on } \Omega^{\mathbf{x}} \times ]0, t_f[ \quad (9)$$

where  $\ddot{\mathbf{u}} \equiv \partial^2 \mathbf{u} / \partial t^2$  is the acceleration;  $\mathbf{u}$  is the displacement field and herein is treated as a primary unknown,  $\boldsymbol{\sigma}$  is the Cauchy stress tensor, and  $\mathbf{b}$  is the prescribed body force. Again for small-strain linear elastic problems, in the above  $\nabla_{\mathbf{x}} = \nabla$  and  $\Omega^{\mathbf{x}} = \Omega$ .

The boundary conditions in the current configuration are:

$$\mathbf{u} = \mathbf{g} \quad \text{on } \Gamma_{\mathbf{g}}^{\mathbf{x}} \times ]0, t_f[ \quad (10a)$$

$$\boldsymbol{\sigma} \cdot \mathbf{n} = \mathbf{h} \quad \text{on } \Gamma_{\mathbf{h}}^{\mathbf{x}} \times ]0, t_f[ \quad (10b)$$

$$\theta = \bar{\theta} \quad \text{on } \Gamma_T^{\mathbf{x}} \times ]0, t_f[ \quad (10c)$$

$$\mathbf{n} \cdot \mathbf{q} = \bar{q} \quad \text{on } \Gamma_q^{\mathbf{x}} \times ]0, t_f[ \quad (10d)$$

where  $\mathbf{g}$ ,  $\mathbf{n}$ ,  $\mathbf{h}$ ,  $\bar{\theta}$ ,  $\bar{q}$  denote prescribed displacement, outward unit normal to the surface, prescribed traction, prescribed temperature difference, and prescribed heat flux, respectively, with  $\overline{\Gamma_{\mathbf{g}}^{\mathbf{x}} \cup \Gamma_{\mathbf{h}}^{\mathbf{x}}} = \overline{\Gamma_T^{\mathbf{x}} \cup \Gamma_q^{\mathbf{x}}} = \Gamma$  and  $\Gamma_{\mathbf{g}}^{\mathbf{x}} \cap \Gamma_{\mathbf{h}}^{\mathbf{x}} = \Gamma_T^{\mathbf{x}} \cap \Gamma_q^{\mathbf{x}} = \emptyset$ . For small-strain linear thermoelastic problems, we drop the super-scripts on the boundary terms as there is no distinction between the boundary of the reference configuration and current configuration.

To complete the problem, the constitutive laws for  $\mathbf{q}$  and  $\boldsymbol{\sigma}$  need to be specified. In turn, these dictate the nature of the coupling between the displacement  $\mathbf{u}$  and temperature change  $\theta$ .

### 3 Generalized thermoelasticity

Assuming the free energy function  $\phi(\boldsymbol{\varepsilon}, \theta)$  and the entropy  $\eta^e(\boldsymbol{\varepsilon}, \theta)$  for small strain thermoelasticity, the following equations are obtained (see appendix A for assumptions) for thermoelasticity over the domain  $\Omega$  and time interval  $]0, t_f[$  :

$$\nabla \cdot \boldsymbol{\sigma} + \mathbf{b} = \rho \ddot{\mathbf{u}} \quad (11)$$

$$-\nabla \cdot \mathbf{q} - \rho c_p \dot{\theta} + Q - \beta T_0 \nabla \cdot \dot{\mathbf{u}} = 0 \quad (12)$$

where  $c_p$  is the specific heat capacity, and  $\beta = \alpha(3\lambda + 2\mu)$  is the thermal stress modulus;  $\alpha$  is the thermal expansion coefficient,  $\lambda$  and  $\mu$  are Lamé's first and second constants.

#### 3.1 Classical thermoelasticity

To outline the differences in the generalized and classical thermoelastic theories, here we review the basic assumptions in isotropic thermoelasticity. For the constitutive laws, the heat flux in (4) takes the form

$$\mathbf{q} = -k \nabla \theta \quad (13)$$

which is the Fourier law. For the stress, the Duhamel-Neumann law is adopted:

$$\boldsymbol{\sigma} = \mathbb{C} : \boldsymbol{\varepsilon} - \beta \theta \mathbb{I} \quad (14)$$

where  $\mathbb{C}$  and  $\boldsymbol{\varepsilon}$  are the isotropic fourth-order elastic tensor, and infinitesimal strain tensor, respectively, and  $\mathbb{I}$  is the second-order identity tensor. Employing (14) in the momentum equation (11) and the Fourier law (13) in the energy equation (12), the classical equations of thermoelasticity employed in Part I of this paper are obtained.

#### 3.2 Lord and Shulman's theory

Lord and Shulman (denoted as L-S) introduced a relaxation time  $t_0$  in the classical Fourier law (13) of heat conduction as follows [39]:

$$\mathbf{q} + t_0 \dot{\mathbf{q}} = -k \nabla \theta. \quad (15)$$

The classical Duhamel-Neumann law (14) is still considered. Employing (14) in (11) and the modified Fourier diffusion law (15) in the energy equation (12), the following governing equations of the Lord and Shulman theory can be written as

$$\nabla \cdot (\mathbb{C} : \boldsymbol{\varepsilon}(\mathbf{u}) - \beta \theta \mathbb{I}) + \mathbf{b} = \rho \ddot{\mathbf{u}}, \quad (16a)$$

$$-t_0 \rho c_p \ddot{\theta} - t_0 \beta T_0 \nabla \cdot \ddot{\mathbf{u}} + \nabla \cdot k \nabla \theta - \rho c_p \dot{\theta} + (Q + t_0 \dot{Q}) - \beta T_0 \nabla \cdot \dot{\mathbf{u}} = 0. \quad (16b)$$

If  $t_0 = 0$ , then classical isotropic thermoelasticity is recovered.

The corresponding finite temperature propagation speed of L-S theory,  $c_{T,LS}$ , can be obtained as

$$c_{T,LS} = \sqrt{\frac{k}{t_0 \rho c_p}}. \quad (17)$$

### 3.3 Green and Lindsay's theory

Based on an entropy production inequality, Green and Lindsay's theory (denoted as G-L) considers two relaxation times [24].

The first relaxation time  $t_1$  enters into the Duhamel-Neumann law (14):

$$\boldsymbol{\sigma} = \mathbb{C} : \boldsymbol{\varepsilon}(\mathbf{u}) - \beta(\theta + t_1\dot{\theta})\mathbb{I}. \quad (18)$$

A second relaxation time  $t_2$  is considered in the following entropy density function:

$$\eta = \eta_0 + \frac{c_p}{T_0}\theta + \frac{c_p t_2}{T_0}\dot{\theta} + \frac{1}{\rho}\beta\nabla \cdot \mathbf{u} \quad (19)$$

where  $\eta_0$  is the reference entropy density.

The Duhamel-Neumann law with relaxation time (18) and the entropy density function (19) are introduced in the equation of motion (11) and in the energy equation (12) to yield:

$$\nabla \cdot (\mathbb{C} : \boldsymbol{\varepsilon}(\mathbf{u}) - \beta(\theta + t_1\dot{\theta})\mathbb{I}) + \mathbf{b} = \rho\ddot{\mathbf{u}}, \quad (20a)$$

$$-t_2\rho c_p\ddot{\theta} + \nabla \cdot k\nabla\theta - \rho c_p\dot{\theta} + Q - \beta T_0\nabla \cdot \dot{\mathbf{u}} = 0. \quad (20b)$$

Note that if  $t_1 = t_2 = 0$ , then the classical governing equations are recovered.

The corresponding temperature propagation speed in the G-L theory,  $c_{T,GL}$ , is given as

$$c_{T,GL} = \sqrt{\frac{k}{t_2\rho c_p}}. \quad (21)$$

### 3.4 Unified generalized thermoelasticity

For convenience, the classical, G-L, and L-S theories can be expressed as a generalized thermoelasticity formulation as follows:

$$\nabla \cdot (\mathbb{C} : \boldsymbol{\varepsilon}(\mathbf{u}) - \beta(\theta + t_1\dot{\theta})\mathbb{I}) + \mathbf{b} = \rho\ddot{\mathbf{u}}, \quad (22a)$$

$$-(t_0 + t_2)\rho c_p\ddot{\theta} - t_0\beta T_0\nabla \cdot \dot{\mathbf{u}} + \nabla \cdot k\nabla\theta - \rho c_p\dot{\theta} + (Q + t_0\dot{Q}) - \beta T_0\nabla \cdot \dot{\mathbf{u}} = 0. \quad (22b)$$

In the above, when all relaxation times are zero ( $t_0 = t_1 = t_2 = 0$ ), classical thermoelasticity is recovered. The G-L theory can be obtained with  $t_0 = 0$ , and the L-S theory can be obtained by setting  $t_1 = t_2 = 0$ . In following sections, the governing equations for generalized thermoelasticity (22) are employed to make the derivations concise.

Now, to distinguish between a fully coupled and a partially coupled problem, the following thermoelasticity coupling parameter is introduced for convenience:

$$\delta = \frac{\beta^2 T_0}{\rho c(\lambda + 2\mu)}. \quad (23)$$

When  $\delta = 0$  the system is the uncoupled (or partially coupled). On the other hand, if  $\delta$  is non-zero value, it is the fully coupled case. In practice, one may select the former case when  $\delta \approx 0$ . It can be noted that this depends on the ratio of material constants at hand, and may differ for e.g., many metals  $\delta \approx 0$ , and several composites and plastics  $\delta \gg 1$ .

### 3.5 Weak form of generalized thermoelasticity

RKPM employs the weak forms of the governing equations. Using the weighted residual method, applying integration-by-parts and the divergence theorem, the weak forms can be derived as: find  $\mathbf{u} \in U_g$ ,  $U_g = \{\mathbf{u} \mid \mathbf{u} \in H^1, \mathbf{u} = \mathbf{g} \text{ on } \Gamma_g \times ]0, t_f[ \}$  and  $\theta \in \Theta_T$ ,  $\Theta_T = \{\theta \mid \theta \in H^1, \theta = \bar{\theta} \text{ on } \Gamma_T \times ]0, t_f[ \}$  such that for all  $\mathbf{v} \in U_0$ ,  $U_0 = \{\mathbf{v} \mid \mathbf{v} \in H^1, \mathbf{v} = \mathbf{0} \text{ on } \Gamma_g \times ]0, t_f[ \}$  and  $S \in \Theta_0$ ,  $\Theta_0 = \{S \mid S \in H^1, S = 0 \text{ on } \Gamma_T \times ]0, t_f[ \}$  the following equations hold:

$$\begin{aligned} & \int_{\Omega} \rho \mathbf{v} \cdot \dot{\mathbf{u}} d\Omega + \int_{\Omega} \nabla^s \mathbf{v} : \mathbb{C} : \nabla^s \mathbf{u} d\Omega - \int_{\Omega} \beta \nabla \cdot \mathbf{v} (\theta + t_1 \dot{\theta}) d\Omega = \\ & \int_{\Omega} \mathbf{v} \cdot \mathbf{b} d\Omega + \int_{\Gamma_h} \mathbf{v} \cdot \mathbf{h} d\Gamma, \quad (24a) \\ & - \int_{\Omega} (t_0 + t_2) \rho c_p S \ddot{\theta} d\Omega - \int_{\Omega} t_0 \beta T_0 S \nabla \cdot \dot{\mathbf{u}} d\Omega + \int_{\Omega} k \nabla S \cdot \nabla \theta d\Omega + \int_{\Omega} \rho c_p S \dot{\theta} d\Omega - \\ & \int_{\Omega} \beta T_0 S \nabla \cdot \dot{\mathbf{u}} d\Omega = \int_{\Omega} S (Q + t_0 \dot{Q}) d\Omega + \int_{\Gamma_q} S \bar{q} d\Gamma, \quad (24b) \end{aligned}$$

where  $\nabla^s$  denotes the symmetric part of the gradient.

As noted in Part I, both "energy" terms contain gradients of the primary unknown,  $\nabla \theta$  and  $\nabla \mathbf{u}$ , in (24a) and (24b), respectively. Thus, when discretized by meshfree shape functions, it is easy to show that an oscillatory mode with a wavelength of twice the nodal spacing, in both displacement and temperature, will not contribute to these terms when away from the influence of the boundary, and this mode can potentially grow virtually unrestricted [27]. In Part I, it was further demonstrated that in thermoelasticity, these modes do in fact grow unrestricted, and are explosive in nature yielding meaningless results without a stabilized nodal integration. It was also shown that these oscillations were many orders of magnitude worse than pure elasticity.

### 3.6 Galerkin form

The Galerkin approximation of (24) asks to find  $\mathbf{u}^h \in U^h \subset U_g^1$  and  $\theta^h \in \Theta_T^h \subset \Theta_T^1$ , such that for all  $\mathbf{v}^h \in V^h \subset U_0^1$  and  $S^h \in \Theta_0^h \subset \Theta_0^1$  the following equations hold:

$$\begin{aligned} & \int_{\Omega} \rho \mathbf{v}^h \cdot \dot{\mathbf{u}}^h d\Omega + \int_{\Omega} \nabla^s \mathbf{v}^h : \mathbb{C} : \nabla^s \mathbf{u}^h d\Omega - \int_{\Omega} \beta \nabla \cdot \mathbf{v}^h (\theta^h + t_1 \dot{\theta}^h) d\Omega = \\ & \int_{\Omega} \mathbf{v}^h \cdot \mathbf{b} d\Omega + \int_{\Gamma_h} \mathbf{v}^h \cdot \mathbf{h} d\Gamma, \quad (25a) \end{aligned}$$

$$\begin{aligned} & - \int_{\Omega} (t_0 + t_2) \rho c_p S^h \ddot{\theta}^h d\Omega - \int_{\Omega} t_0 \beta T_0 S^h \nabla \cdot \dot{\mathbf{u}}^h d\Omega + \int_{\Omega} k \nabla S^h \cdot \nabla \theta^h d\Omega + \\ & \int_{\Omega} \rho c_p S^h \dot{\theta}^h d\Omega - \int_{\Omega} \beta T_0 S^h \nabla \cdot \dot{\mathbf{u}}^h d\Omega = \int_{\Omega} S^h (Q + t_0 \dot{Q}) d\Omega + \int_{\Gamma_q} S^h \bar{q} d\Gamma. \quad (25b) \end{aligned}$$

### 3.7 Reproducing kernel approximation

In this section, the reproducing kernel (RK) approximation for the linear problem is briefly reviewed, along with its implicit gradient counterpart used in the stabilization. For more details, see Part I.

Let a domain  $\bar{\Omega} = \Omega \cup \Gamma$  be discretized by a set of  $NP$  nodes  $\mathcal{S} = \{\mathbf{x}_I | \mathbf{x}_I \in \bar{\Omega}\}_{I=1}^{NP}$  with associated set of node numbers  $\mathcal{N} = \{I | \mathbf{x}_I \in \mathcal{S}\}$ . The  $n$ th order reproducing kernel (RK) approximation  $u^h(\mathbf{x})$  of a function  $u(\mathbf{x})$  is

$$u^h(\mathbf{x}) = \sum_{I \in \mathcal{N}} \Psi_I(\mathbf{x}) u_I \quad (26)$$

where  $\{\Psi_I(\mathbf{x})\}_{I \in \mathcal{N}}$  is the set of RK shape functions, and  $\{u_I\}_{I \in \mathcal{N}}$  are the associated coefficients. The shape functions are composed of a kernel function  $\Phi_a(\mathbf{x} - \mathbf{x}_I)$  with normalized support  $a$  and a correction function [38, 15]:

$$\Psi_I(\mathbf{x}) = \mathbf{H}(\mathbf{0})^\top \mathbf{M}(\mathbf{x})^{-1} \mathbf{H}(\mathbf{x} - \mathbf{x}_I) \Phi_a(\mathbf{x} - \mathbf{x}_I). \quad (27)$$

where  $\mathbf{H}(\mathbf{0})^\top \mathbf{M}(\mathbf{x})^{-1} \mathbf{H}(\mathbf{x} - \mathbf{x}_I)$  is the correction function;  $\mathbf{H}$  is a column vector of complete  $n$ th order monomials, and  $\mathbf{M}$  is the moment matrix defined as follows:

$$\mathbf{M}(\mathbf{x}) = \sum_{I \in \mathcal{N}} \mathbf{H}(\mathbf{x} - \mathbf{x}_I) \mathbf{H}(\mathbf{x} - \mathbf{x}_I)^\top \Phi_a(\mathbf{x} - \mathbf{x}_I). \quad (28)$$

Due to the correction function, the RK approximation can be shown to satisfy the following reproducing conditions:

$$\sum_{I \in \mathcal{N}} \Psi_I(\mathbf{x}) \mathbf{H}(\mathbf{x}_I) = \mathbf{H}(\mathbf{x}) \quad (29)$$

Note that because of the product rule, taking direct derivatives of (27) becomes increasingly expensive as the order of differentiation increases. In NSNI, the gradients of gradients are necessary due to the Taylor series expansion involved. Thus, the following implicit gradient approximation to a gradient term  $u(\mathbf{x})_{,i} \equiv \partial u / \partial x_i$  is introduced to alleviate the computational burden [19, 35]:

$$u(\mathbf{x})_{,i} \approx \sum_{I \in \mathcal{N}} \Psi_{Ii}^\nabla(\mathbf{x}) u_I \quad (30)$$

where  $\Psi_{Ii}^\nabla$  is the implicit gradient shape function which takes the form:

$$\Psi_{Ii}^\nabla(\mathbf{x}) = [\mathbf{H}_i^\nabla]^\top \mathbf{M}(\mathbf{x})^{-1} \mathbf{H}(\mathbf{x} - \mathbf{x}_I) \Phi_a(\mathbf{x} - \mathbf{x}_I) \quad (31)$$

where  $\mathbf{M}$  is the same moment matrix in (28), and  $\mathbf{H}_i^\nabla$  is a column vector of the form:

$$\mathbf{H}_i^\nabla = [0, \dots, 0, -1, 0, \dots, 0]^\top \quad (32)$$

where  $-1$  is  $(i+1)^{th}$  entry. Similar to the RK approximation (27), here  $[\mathbf{H}_i^\nabla]^\top \mathbf{M}(\mathbf{x})^{-1} \mathbf{H}(\mathbf{x} - \mathbf{x}_I)$  is a correction function. It can be shown that due to this correction, the implicit gradient approximation satisfies the following gradient reproducing conditions:

$$\sum_{I \in \mathcal{N}} \Psi_{Ii}^\nabla(\mathbf{x}) \mathbf{H}(\mathbf{x}_I) = \mathbf{H}(\mathbf{x})_{,i}. \quad (33)$$

Comparing (29) to (33), it can be seen that the implicit gradient possesses the same key properties in gradient approximations, while much less computationally demanding. For more details, consult Part I, or see [11].

### 3.8 Matrix forms

Naturally stabilized nodal integration, and variationally consistent integration introduced in Part I are both straightforwardly applied to the present generalized thermoelastic problem. The natural stabilization follows the exact same derivation and formulation, since no new terms are introduced into the bilinear forms of the generalized formulation (24).

Similarly, the present formulation only introduced additional time-dependent terms. Meanwhile, the variational consistency conditions are based on the steady problem. Therefore it is easy to show that the variational consistency conditions for the generalized formulation remain the same, and the test function gradient correction from Part I thus also remains the same. That is, the integration constraints, and associated correction for (25) are identical. We refer the interested reader to Part I of this paper for the details of test and trial function construction, and related corrections and stabilization.

Proceeding to introduce the RK approximation (26) with associated NSNI stabilization and VC correction from Part I into the nodally-integrated Galerkin equation (25), one obtains the following matrix form:

$$\begin{bmatrix} \mathbf{M}_{uu} & \mathbf{0} \\ \mathbf{M}_{\theta u} & \mathbf{M}_{\theta\theta} \end{bmatrix} \begin{bmatrix} \ddot{\mathbf{u}} \\ \ddot{\boldsymbol{\theta}} \end{bmatrix} + \begin{bmatrix} \mathbf{0} & \mathbf{C}_{u\theta} \\ \mathbf{C}_{\theta u} & \mathbf{C}_{\theta\theta} \end{bmatrix} \begin{Bmatrix} \dot{\mathbf{u}} \\ \dot{\boldsymbol{\theta}} \end{Bmatrix} + \begin{bmatrix} \mathbf{K}_{uu} & \mathbf{K}_{u\theta} \\ \mathbf{0} & \mathbf{K}_{\theta\theta} \end{bmatrix} \begin{Bmatrix} \mathbf{u} \\ \boldsymbol{\theta} \end{Bmatrix} = \begin{Bmatrix} \mathbf{F}^{ext} \\ \mathbf{Q}^{ext} \end{Bmatrix} \quad (34)$$

where  $\mathbf{u}$  and  $\boldsymbol{\theta}$  are the row vectors of the unknowns  $\{\mathbf{u}_I\}_{I=1}^{NP}$  and  $\{\boldsymbol{\theta}_I\}_{I=1}^{NP}$ , respectively,

and for a homogeneous media in two dimensions:

$$\mathbf{M}_{uu} = \sum_{L=1}^{NP} \rho \mathbf{N}(\mathbf{x}_L)^\top \mathbf{N}(\mathbf{x}_L) W_L \quad (35a)$$

$$\mathbf{M}_{\theta u} = \sum_{L=1}^{NP} -t_0 T_0 \beta \Psi(\mathbf{x}_L)^\top \mathbf{I} \mathbf{B}^u(\mathbf{x}_L) W_L \quad (35b)$$

$$\mathbf{M}_{\theta\theta} = \sum_{L=1}^{NP} -\rho c_p (t_0 + t_2) \Psi(\mathbf{x}_L)^\top \Psi(\mathbf{x}_L) W_L \quad (35c)$$

$$\mathbf{C}_{u\theta} = \sum_{L=1}^{NP} -t_1 \beta \Psi(\mathbf{x}_L)^\top \mathbf{B}^\theta(\mathbf{x}_L) W_L \quad (35d)$$

$$\mathbf{C}_{\theta u} = -T_0 \mathbf{K}_{u\theta}^\top \quad (35e)$$

$$\mathbf{C}_{\theta\theta} = \sum_{L=1}^{NP} \rho c_p \Psi(\mathbf{x}_L)^\top \Psi(\mathbf{x}_L) W_L \quad (35f)$$

$$\mathbf{K}_{uu} = \sum_{L=1}^{NP} (\mathbf{B}^{uc}(\mathbf{x}_L))^\top \mathbf{D} \mathbf{B}^u(\mathbf{x}_L) W_L + \sum_{L=1}^{NP} \sum_{i=1}^2 (\mathbf{B}_i^{u\nabla}(\mathbf{x}_L))^\top \mathbf{D} \mathbf{B}_i^{u\nabla}(\mathbf{x}_L) M_{Li} \quad (35g)$$

$$\mathbf{K}_{u\theta} = - \sum_{L=1}^{NP} \beta (\mathbf{B}^{uc}(\mathbf{x}_L))^\top \mathbf{I} \Psi(\mathbf{x}_L) W_L \quad (35h)$$

$$\mathbf{K}_{\theta\theta} = \sum_{L=1}^{NP} k (\mathbf{B}^{\theta c}(\mathbf{x}_L))^\top \mathbf{B}^\theta(\mathbf{x}_L) W_L + \sum_{L=1}^{NP} \sum_{i=1}^2 k (\mathbf{B}_i^{\theta\nabla}(\mathbf{x}_L))^\top \mathbf{B}_i^{\theta\nabla}(\mathbf{x}_L) M_{Li} \quad (35i)$$

$$\mathbf{F}^{\text{ext}} = \sum_{L=1}^{NP} \mathbf{N}(\mathbf{x}_L)^\top \mathbf{b} W_L + \sum_{K=1}^{NBPu} \mathbf{N}(\mathbf{x}_K)^\top \mathbf{h} L_K^u \quad (35j)$$

$$\mathbf{Q}^{\text{ext}} = \sum_{L=1}^{NP} \Psi(\mathbf{x}_L)^\top Q W_L + \sum_{K=1}^{NBP\theta} \Psi(\mathbf{x}_K)^\top \bar{q} L_K^\theta \quad (35k)$$

where  $\mathbf{I} = [1 \ 1 \ 0 \ 0]^\top$ ,  $\mathbf{D}$  is the matrix corresponding to the tensor  $\mathbb{C}$ ,  $W_L$  is the integration weight of node  $L$ , and  $L_K^u$  and  $L_K^\theta$  denote the  $K$ th weight of one of the  $NBPu$  and  $NBP\theta$  integration points on the natural boundary, respectively. The definition of the terms  $\mathbf{N}$ ,  $\Psi$ ,  $\mathbf{B}^u$ ,  $\mathbf{B}^\theta$ ,  $\mathbf{B}^{uc}$ ,  $\mathbf{B}^{\theta c}$ ,  $\mathbf{B}_i^{u\nabla}$ , and  $\mathbf{B}_i^{\theta\nabla}$  can be found in Part I.

Compared to classical thermoelasticity, there are three additional terms in (35b), (35c), and (35d), which emanate from the relaxation times introduced. Therefore the generalized formulation can easily be introduced into existing classical thermoelasticity codes, provided time integration is taken care of.

The final semi-discrete linear time-dependent system (34) can be written in compact form as

$$\mathbf{M}\ddot{\mathbf{d}}(t) + \mathbf{C}\dot{\mathbf{d}}(t) + \mathbf{K}\mathbf{d}(t) = \mathbf{F}(t) \quad (36)$$

where

$$\mathbf{M} = \begin{bmatrix} \mathbf{M}_{uu} & \mathbf{0} \\ \mathbf{M}_{\theta u} & \mathbf{M}_{\theta\theta} \end{bmatrix}, \quad \mathbf{C} = \begin{bmatrix} \mathbf{0} & \mathbf{C}_{u\theta} \\ \mathbf{C}_{\theta u} & \mathbf{C}_{\theta\theta} \end{bmatrix}, \quad \mathbf{K} = \begin{bmatrix} \mathbf{K}_{uu} & \mathbf{K}_{u\theta} \\ \mathbf{0} & \mathbf{K}_{\theta\theta} \end{bmatrix} \quad (37)$$

and

$$\mathbf{d} = \begin{bmatrix} \mathbf{u} \\ \boldsymbol{\theta} \end{bmatrix}, \quad \mathbf{F} = \begin{bmatrix} \mathbf{F}^{\text{ext}} \\ \mathbf{Q}^{\text{ext}} \end{bmatrix}. \quad (38)$$

In this work, time integration is carried out using the Newmark method [31]. For the explicit version (central difference), since there are off-diagonal terms in the mass-type and damping-type matrices in (37), one can lump the mass and replace the velocity approximation terms with their predictors. In the numerical examples, it is shown that this has little effect on accuracy. The specific algorithms are omitted here due to their relative simplicity in the elastic case.

Later, it will be shown that the relaxation times in the generalized theories can be chosen such that critical time step for explicit time integration is the same as pure small-strain linear elasticity, thus avoiding the parabolic  $\mathcal{O}(\Delta t^2)$  time step restriction, also resulting in solutions close to the classical theory.

## 4 Thermoplasticity

### 4.1 Finite-strain formulation

A non-linear analysis generally involves either the total Lagrangian or the updated Lagrangian formulation [6]. In the total Lagrangian description, strain and stress measures are defined with respect to the undeformed or reference geometry. As opposed to the total Lagrangian description, an updated Lagrangian analysis uses the current configuration. In this work, the updated Lagrangian scheme will be employed since it is applicable to extreme deformation problems where meshfree methods are adept.

Consider a body initially occupying a region  $\Omega^{\mathbf{X}}$  with boundary  $\Gamma^{\mathbf{X}}$  and particle positions  $\mathbf{X}$  (material coordinates), deformed to a configuration occupying a region  $\Omega^{\mathbf{x}}$  with boundary  $\Gamma^{\mathbf{x}}$  and particle positions  $\mathbf{x}$ . If the deformation is one-to-one  $\mathbf{x}$  is defined by a mapping function  $\mathbf{x} = \boldsymbol{\varphi}(\mathbf{X}, t)$  which is a function of the original particle position  $\mathbf{X}$  as well as time  $t$ . The displacement  $\mathbf{u}$  in the current configuration is defined by the difference between its current coordinates in  $\Omega^{\mathbf{x}}$ , and initial material coordinates in  $\Omega^{\mathbf{X}}$ :

$$\mathbf{u} = \mathbf{x} - \mathbf{X}. \quad (39)$$

### 4.2 Governing equations

For thermoplasticity, we decompose the free energy function into an elastic energy  $\phi^e$ , a plastic energy  $\phi^p$  due to work hardening, and thermal energy  $\phi^\theta$  following [46]:

$$\phi = \phi^e(\mathbf{F}^e, \theta) + \phi^p(v, \theta) + \phi^\theta(\theta) \quad (40)$$

where  $\mathbf{F}^e$  is the elastic deformation gradient, and  $v$  is the hardening variable. The entropy for large strain can be expressed as:

$$\eta - \eta^p = -\frac{\partial\phi}{\partial\theta} = -\frac{\partial(\phi^e + \phi^p + \phi^\theta)}{\partial\theta} \quad (41)$$

and

$$\dot{\eta} = \dot{\eta}^p - c_p \dot{\theta} \quad (42)$$

where  $c_p = \frac{\partial^2\phi}{\partial\theta^2}\theta$  is the specific heat capacity.

Assuming the free energy function (40) and the entropy (41), the following equations are obtained (see Appendix B for assumptions) for thermoplasticity

$$\rho c_p \dot{\theta} = -\nabla \cdot \mathbf{q} + Q + \chi \dot{w}^p \quad (43)$$

where  $\chi \in [0, 1]$  is the Taylor-Quinney coefficient, and  $\dot{w}^p = \text{dev}(\boldsymbol{\sigma}) : \dot{\boldsymbol{\epsilon}}^p$  is the plastic power;  $\text{dev}(\boldsymbol{\sigma}) = \boldsymbol{\sigma} - \text{trace}(\boldsymbol{\sigma})\mathbb{I}$  is the deviatoric portion of the Cauchy stress, and  $\dot{\boldsymbol{\epsilon}}^p$  is the rate of plastic strain.

The classical Fourier heat flux is employed in this work with the scalar (isotropic) thermal conductivity denoted  $k$ :

$$\mathbf{q} = -k\nabla\theta. \quad (44)$$

Substituting (44) into (43), the following energy equation is obtained:

$$\rho c_p \dot{\theta} = \nabla \cdot k\nabla\theta + Q + \chi \dot{w}^p. \quad (45)$$

Obviously, the above equation implies an infinite speed for propagation of temperature information. To remedy the fact that this is physically unacceptable, and to facilitate efficient explicit calculations, a thermal sound speed can be introduced into the finite-strain problem. Here, we consider Cattaneo heat conduction [9] (or so-called relativistic heat conduction, which can also be attributed to Vernotte [52] and Chester [20]), which is directly analogous to the modified Fourier law (15):

$$\tau \dot{\mathbf{q}} + \mathbf{q} = k\nabla\theta, \quad (46)$$

where  $\tau$  is the relaxation time.

Using (46), we obtain a hyperbolic energy equation as

$$\rho c_p \tau \ddot{\theta} + \rho c_p \dot{\theta} = \nabla \cdot k\nabla\theta + Q + \tau \dot{Q} + \chi \dot{w}^p \quad (47)$$

where  $\dot{Q}$  comes from Cattaneo conduction. Note that if  $\tau = 0$ , then the parabolic energy equation (45) is recovered.

For the Cauchy stress,  $\boldsymbol{\sigma}$ , the Duhamel-Neumann law is adopted:

$$\boldsymbol{\sigma} = \mathbb{C} : (\boldsymbol{\epsilon} - \boldsymbol{\epsilon}^p - \boldsymbol{\epsilon}^\theta) \quad (48)$$

where  $\boldsymbol{\epsilon}$ ,  $\boldsymbol{\epsilon}^p$ , and  $\boldsymbol{\epsilon}^\theta = \bar{\alpha}\theta\mathbb{I}$  are the total, plastic, and thermal strains, respectively ( $\boldsymbol{\epsilon} - \boldsymbol{\epsilon}^p - \boldsymbol{\epsilon}^\theta$  is the elastic strain).

Finally, the governing equations of the conservation of linear momentum and the hyperbolic energy equation in the current configuration can be written as

$$\rho \ddot{\mathbf{u}} = \nabla_{\mathbf{x}} \cdot \boldsymbol{\sigma} + \mathbf{b} \quad \text{in } \Omega^{\mathbf{x}} \times ]0, t_f[ \quad (49a)$$

$$\rho c_p \tau \ddot{\theta} + \rho c_p \dot{\theta} = \nabla_{\mathbf{x}} \cdot k \nabla_{\mathbf{x}} \theta + Q + \tau \dot{Q} + \chi \dot{w}^p \quad \text{in } \Omega^{\mathbf{x}} \times ]0, t_f[ \quad (49b)$$

where as before,  $\nabla_{\mathbf{x}}$  is the Del operator associated with current coordinates  $\mathbf{x}$ . As can be seen, the coupling between the two fields arises from the thermal strains and possible dependence of the yield function on temperature (temperature to mechanical), and the plastic power (mechanical to temperature).

### 4.3 Weak form of thermoplasticity

RKPM employs the weak forms of the governing equations (49). Applying the weighted residual method, integration-by-parts, and the divergence theorem, the weak forms are derived as: find  $\mathbf{u} \in U_g^{\mathbf{x}}$ , and  $\theta \in \Theta_T^{\mathbf{x}}$ , such that for all  $\mathbf{v} \in U_0^{\mathbf{x}}$ , and  $S \in \Theta_0^{\mathbf{x}}$  the following equations hold:

$$\int_{\Omega^{\mathbf{x}}} \rho \mathbf{v} \cdot \ddot{\mathbf{u}} d\Omega + \int_{\Omega^{\mathbf{x}}} \nabla_{\mathbf{x}}^s \mathbf{v} : \boldsymbol{\sigma} d\Omega = \int_{\Omega^{\mathbf{x}}} \mathbf{v} \cdot \mathbf{b} d\Omega + \int_{\Gamma_h^{\mathbf{x}}} \mathbf{v} \cdot \mathbf{h} d\Gamma, \quad (50a)$$

$$\begin{aligned} \int_{\Omega^{\mathbf{x}}} \rho c_p \tau S \ddot{\theta} d\Omega + \int_{\Omega^{\mathbf{x}}} \rho c_p S \dot{\theta} d\Omega + \int_{\Omega^{\mathbf{x}}} k \nabla_{\mathbf{x}} S \cdot \nabla_{\mathbf{x}} \theta d\Omega = \\ \int_{\Omega^{\mathbf{x}}} S \chi \dot{w}^p d\Omega + \int_{\Omega^{\mathbf{x}}} S (Q + \tau \dot{Q}) d\Omega + \int_{\Gamma_q^{\mathbf{x}}} S \bar{q} d\Gamma. \end{aligned} \quad (50b)$$

where  $\nabla_{\mathbf{x}}^s$  is the symmetric part of  $\nabla_{\mathbf{x}}$ ,  $U_g^{\mathbf{x}} = \{\mathbf{u} \mid \mathbf{u} \in H^1, \mathbf{u} = \mathbf{g} \text{ on } \Gamma_g^{\mathbf{x}} \times ]0, t_f[ \}$ ,  $\Theta_T^{\mathbf{x}} = \{\theta \mid \theta \in H^1, \theta = \bar{\theta} \text{ on } \Gamma_T^{\mathbf{x}} \times ]0, t_f[ \}$ ,  $U_0^{\mathbf{x}} = \{\mathbf{v} \mid \mathbf{v} \in H^1, \mathbf{v} = \mathbf{0} \text{ on } \Gamma_g^{\mathbf{x}} \times ]0, t_f[ \}$ , and  $\Theta_0^{\mathbf{x}} = \{S \mid S \in H^1, S = 0 \text{ on } \Gamma_T^{\mathbf{x}} \times ]0, t_f[ \}$ .

### 4.4 Galerkin approximation

The Galerkin approximation of (50) asks to find  $\mathbf{u}^h \in U^h \subset U_g^{\mathbf{x}}$  and  $\theta^h \in \Theta_T^h \subset \Theta_T^{\mathbf{x}}$ , such that for all  $\mathbf{v}^h \in V^h \subset U_0^{\mathbf{x}}$  and  $S^h \in \Theta_0^h \subset \Theta_0^{\mathbf{x}}$  the following equations hold:

$$\int_{\Omega^{\mathbf{x}}} \rho \mathbf{v}^h \cdot \ddot{\mathbf{u}}^h d\Omega + \int_{\Omega^{\mathbf{x}}} \nabla_{\mathbf{x}}^s \mathbf{v}^h : \boldsymbol{\sigma} d\Omega = \int_{\Omega^{\mathbf{x}}} \mathbf{v}^h \cdot \mathbf{b} d\Omega + \int_{\Gamma_h^{\mathbf{x}}} \mathbf{v}^h \cdot \mathbf{h} d\Gamma, \quad (51a)$$

$$\begin{aligned} \int_{\Omega^{\mathbf{x}}} \rho c_p \tau S^h \ddot{\theta}^h d\Omega + \int_{\Omega^{\mathbf{x}}} \rho c_p S^h \dot{\theta}^h d\Omega + \int_{\Omega^{\mathbf{x}}} k \nabla_{\mathbf{x}} S^h \cdot \nabla_{\mathbf{x}} \theta^h d\Omega = \\ \int_{\Omega^{\mathbf{x}}} S^h \chi \dot{w}^p d\Omega + \int_{\Omega^{\mathbf{x}}} S^h (Q + \tau \dot{Q}) d\Omega + \int_{\Gamma_q^{\mathbf{x}}} S^h \bar{q} d\Gamma. \end{aligned} \quad (51b)$$

### 4.5 Finite-strain RK formulation

#### 4.5.1 Lagrangian RK approximation

The Lagrangian reproducing kernel approximation is constructed with reference to the material configuration  $\mathbf{X}$ . Following procedures analogous to Section 3.7, the

shape functions are obtained as [15, 14]:

$$\Psi_I(\mathbf{X}) = \mathbf{H}^\top(\mathbf{0})\mathbf{M}^{-1}(\mathbf{X})\mathbf{H}(\mathbf{X} - \mathbf{X}_I)\phi_a(\mathbf{X} - \mathbf{X}_I) \quad (52)$$

where  $\mathbf{X}_I$  is the nodal coordinate in the material configuration.

For the Lagrangian approximation, the displacement and temperature change are constructed (in 2-D as before) as:

$$\mathbf{u}^h(\mathbf{X}) = \sum_{I=1}^{NP} \mathbf{N}_I(\mathbf{X})\mathbf{u}_I, \quad \theta^h(\mathbf{X}) = \sum_{I=1}^{NP} \Psi_I(\mathbf{X})\theta_I \quad (53)$$

where

$$\mathbf{N}_I(\mathbf{X}) = \begin{bmatrix} \Psi_I(\mathbf{X}) & 0 \\ 0 & \Psi_I(\mathbf{X}) \end{bmatrix}, \quad (54)$$

and the test functions are approximated as

$$\mathbf{v}^h(\mathbf{X}) = \sum_{I=1}^{NP} \mathbf{N}_I(\mathbf{X})\mathbf{v}_I, \quad S^h(\mathbf{X}) = \sum_{I=1}^{NP} \Psi_I(\mathbf{X})S_I \quad (55)$$

where  $\{\Psi_I(\mathbf{X})\}_{I=1}^{NP}$  are the Lagrangian RK shape functions (52), and  $\mathbf{u}_I$ ,  $\theta_I$ ,  $\mathbf{v}_I$ , and  $S_I$  are the nodal coefficients in the Galerkin equation.

#### 4.5.2 Stabilized non-conforming nodal integration (SNNI)

While the formulation of the VC correction technique is straight-forward, the actual coding for large-scale three-dimensional nonlinear codes is somewhat non-trivial. An alternative is to use SCNI [16] which uses conforming cells to satisfy the VC constraints. The main idea of SCNI is to replace the nodal gradient by a smoothed gradient constructed via a Voronoi diagram, as shown in Figure 1, to avoid instability from DNI and inherently satisfy the first-order VC conditions. However, this implementation is also somewhat non-trivial in three-dimensions due to data structures and book-keeping needed. Instead, the stabilized non-conforming nodal integration (SNNI) [25, 26] is adopted here, which utilizes non-conforming cells with a sphere or brick shape as shown in Figure 1.

In SNNI, a direct gradient  $\nabla_{\mathbf{X}}$  is replaced with a smoothed gradient  $\tilde{\nabla}_{\mathbf{X}}$ , constructed as:

$$\tilde{\nabla}_{\mathbf{X}}(\cdot)|_{\mathbf{X}_L} = \frac{1}{\tilde{W}_L^{\mathbf{X}}} \int_{\tilde{\Omega}_L^{\mathbf{X}}} \nabla_{\mathbf{X}}(\cdot) d\Omega = \frac{1}{\tilde{W}_L^{\mathbf{X}}} \int_{\tilde{\Gamma}_L^{\mathbf{X}}} (\cdot) \tilde{\mathbf{n}}^{\mathbf{X}} d\Gamma \quad (56)$$

where  $\mathbf{X}_L$  is the nodal point,  $\tilde{\Omega}_L^{\mathbf{X}}$  is the smoothing domain associated with each node in the material configuration with boundary  $\tilde{\Gamma}_L^{\mathbf{X}}$ ,  $\tilde{W}_L^{\mathbf{X}} \equiv |\tilde{\Omega}_L^{\mathbf{X}}|$  is the smoothing weight of the nodal domain, and  $\tilde{\mathbf{n}}^{\mathbf{X}}$  is the unit normal to the nodal smoothing domain. Here, the gradient at a nodal location (as in nodal integration) is smoothed over its representative nodal domain and then the domain integral is converted to a surface integral using the divergence theorem. While relaxation of the conforming condition on the smoothing cells results in loss of variational consistency, so long as the domain is sufficiently uniform, optimal convergence can be achieved [4]. In this work, we

utilize semi-uniform discretizations in the numerical examples. The VC corrections should be implemented if accuracy is desired across all types of discretizations, as shown in Part I.

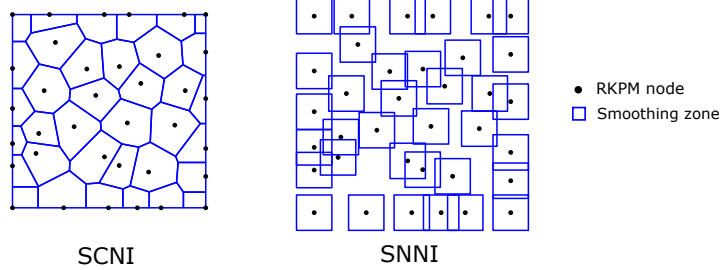


Figure 1: Smoothing cells: conforming nodal integration with SCNI and non-conforming nodal integration with SNNI.

When SNNI is applied to nodal gradient terms, the following approximations result (all smoothed quantities and related variables are denoted with a tilde ( $\tilde{\cdot}$ ) herein):

$$\begin{aligned}\tilde{\boldsymbol{\varepsilon}}(\mathbf{u}^h(\mathbf{X}_L)) &= \sum_{I=1}^{NP} \tilde{\mathbf{B}}_I^u(\mathbf{X}_L) \mathbf{u}_I, & \tilde{\nabla} \theta^h(\mathbf{X}_L) &= \sum_{I=1}^{NP} \tilde{\mathbf{B}}_I^\theta(\mathbf{X}_L) \theta_I \\ \tilde{\boldsymbol{\varepsilon}}(\mathbf{v}^h(\mathbf{X}_L)) &= \sum_{I=1}^{NP} \tilde{\mathbf{B}}_I^v(\mathbf{X}_L) \mathbf{v}_I, & \tilde{\nabla} S^h(\mathbf{X}_L) &= \sum_{I=1}^{NP} \tilde{\mathbf{B}}_I^S(\mathbf{X}_L) S_I\end{aligned}\quad (57)$$

where

$$\begin{aligned}\tilde{\mathbf{B}}_I^u(\mathbf{X}_L) &= \begin{bmatrix} \tilde{b}_{1I}^L & 0 \\ 0 & \tilde{b}_{2I}^L \\ \tilde{b}_{2I}^L & \tilde{b}_{1I}^L \end{bmatrix}, \\ \tilde{\mathbf{B}}_I^\theta(\mathbf{X}_L) &= [\tilde{b}_{1I}^L, \tilde{b}_{2I}^L]^\top, \\ \tilde{b}_{iI}^L &= \frac{1}{\tilde{W}_L^{\mathbf{X}}} \int_{\tilde{\Gamma}_L^{\mathbf{X}}} \Psi_I \tilde{n}_i^{\mathbf{X}} d\Gamma\end{aligned}\quad (58)$$

In the updated Lagrangian formulation, the spatial gradients are required, and here are computed using the smoothed gradient approximation [18]:

$$\begin{aligned}\tilde{\nabla}_{\mathbf{x}} \otimes \mathbf{u}^h(\mathbf{X}_L) &= \frac{\partial \mathbf{X}}{\partial \mathbf{x}}(\mathbf{X}_L) \cdot \left( \tilde{\nabla}_{\mathbf{X}} \otimes \mathbf{u}^h(\mathbf{X}_L) \right) \approx \tilde{\mathbf{F}}(\mathbf{X}_L)^{-\top} \cdot \left( \tilde{\nabla}_{\mathbf{X}} \otimes \mathbf{u}^h(\mathbf{X}_L) \right), \\ \tilde{\nabla}_{\mathbf{x}} \theta(\mathbf{X}_L) &= \frac{\partial \mathbf{X}}{\partial \mathbf{x}}(\mathbf{X}_L) \cdot \left( \tilde{\nabla}_{\mathbf{X}} \theta(\mathbf{X}_L) \right) \approx \tilde{\mathbf{F}}(\mathbf{X}_L)^{-\top} \cdot \left( \tilde{\nabla}_{\mathbf{X}} \theta(\mathbf{X}_L) \right),\end{aligned}\quad (59)$$

where the smoothed deformation gradient  $\tilde{\mathbf{F}}$  is computed as:

$$\tilde{\mathbf{F}}(\mathbf{X}_L) = \mathbf{I} + \sum_{I=1}^{NP} \tilde{\nabla}_{\mathbf{X}} \Psi_I(\mathbf{X}_L) \otimes \mathbf{u}_I.\quad (60)$$

For the inverse of the deformation gradient  $\tilde{\mathbf{F}}^{-1}$ , the mapping must exist between the undeformed and deformed configuration. For material separation where the mapping does not exist everywhere, the semi-Lagrangian formulation can be introduced [26]. In this work, the Lagrangian approximation (52) is employed since the deformations are not severe in the chosen benchmarks.

Finally, we note for nodal quadrature of the Updated Lagrangian formulation, nodal weights in the current configuration also employ  $\tilde{\mathbf{F}}$  and are computed as  $W_L^x = \det(\tilde{\mathbf{F}})W_L^X$  where  $W_L^X$  is the weight in the undeformed configuration.

## 4.6 Naturally stabilized nodal integration in thermoplasticity

In this section, the nodal stabilization given in Part I is extended to nonlinear problems. Most of the procedures are a straightforward analogy, so particular emphasis is only given to key differences. Here as in the rest of the text, two dimensions are considered without loss of generality.

### 4.6.1 Stabilization of the mechanical field

To start, the variation on strains in nodal domains are expanded about the current nodal position  $\mathbf{x}_L$  using a Taylor series expansion truncated to first order [27]:

$$\boldsymbol{\varepsilon}(\mathbf{v}^h) \approx \boldsymbol{\varepsilon}_L(\mathbf{v}^h) + \sum_{i=1}^2 \{(x_i - x_{Li})\boldsymbol{\varepsilon}_L(\mathbf{v}^h)_{,\bar{i}}\}. \quad (61)$$

where  $\boldsymbol{\varepsilon}_L(\mathbf{v}^h) \equiv \boldsymbol{\varepsilon}(\mathbf{v}^h(\mathbf{x}_L))$  and  $(\ )_{,\bar{i}} \equiv \partial(\ )/\partial x_i$ . Now, rather than the strain, the Cauchy stress is instead expanded:

$$\boldsymbol{\sigma}(\mathbf{u}^h) \approx \boldsymbol{\sigma}_L(\mathbf{u}^h) + \sum_{i=1}^2 \{(x_i - x_{Li})\boldsymbol{\sigma}_L(\mathbf{u}^h)_{,\bar{i}}\}. \quad (62)$$

where  $\boldsymbol{\sigma}_L(\mathbf{u}^h) \equiv \boldsymbol{\sigma}(\mathbf{u}^h(\mathbf{x}_L))$ . As in Part I, we have considered the linear ( $n = 1$ ) case and only retain first-order terms. Substituting (61) and (62) into (51a) with nodal quadrature and employing the smoothed (56) and implicit (30) gradient approximations, the following smoothed naturally stabilized nodal quadrature version of the bilinear form is obtained as:

$$a_{SN}^x \langle \mathbf{v}^h, \mathbf{u}^h \rangle = a_S^x \langle \mathbf{v}^h, \mathbf{u}^h \rangle + a_N^x \langle \mathbf{v}^h, \mathbf{u}^h \rangle \quad (63)$$

where  $a_S^x \langle \cdot, \cdot \rangle$  is the SNNI quadrature version of the bilinear form using strain smoothing:

$$a_S^x \langle \mathbf{v}^h, \mathbf{u}^h \rangle = \sum_{L=1}^{NP} \tilde{\boldsymbol{\varepsilon}}_L(\mathbf{u}^h) : \tilde{\boldsymbol{\sigma}}_L(\mathbf{v}^h) W_L^x \quad (64)$$

where  $\tilde{\boldsymbol{\sigma}}$  denotes the Cauchy stress computed using the smoothed strain, and the stabilization term  $a_N^x \langle \cdot, \cdot \rangle$  is

$$a_N^x \langle \mathbf{v}^h, \mathbf{u}^h \rangle = \sum_{L=1}^{NP} \sum_{i=1}^2 \hat{\boldsymbol{\varepsilon}}_{L\bar{i}}(\mathbf{v}^h) : \tilde{\boldsymbol{\sigma}}_{L\bar{i}}(\mathbf{u}^h) M_{Li}^x \quad (65)$$

where  $\hat{\boldsymbol{\varepsilon}}_{L\bar{i}}(\mathbf{v}^h)$  is the smoothed implicit gradient approximation of  $\boldsymbol{\varepsilon}_L(\mathbf{v}^h)_{,\bar{i}}$ ,  $\tilde{\boldsymbol{\sigma}}_{L\bar{i}}(\mathbf{u}^h)$  is the approximation to  $\boldsymbol{\sigma}_L(\mathbf{u}^h)_{,\bar{i}}$  using  $\hat{\boldsymbol{\varepsilon}}_{L\bar{i}}(\mathbf{u}^h)$  and

$$M_{Li}^{\mathbf{x}} = \int_{\Omega_L^{\mathbf{x}}} (x_i - x_{Li})^2 d\Omega, \quad (66)$$

which are the second moments of inertia of each integration zone in the current configuration. For the Lagrangian formulation, to avoid recomputing the spatial moments in (66), these are pre-computed just as other quantities, and are approximated at the current time step by:

$$M_{Li}^{\mathbf{x}} \approx \det(\tilde{\mathbf{F}}(\mathbf{X}_I)) \int_{\Omega_L^{\mathbf{X}}} (X_i - X_{Li})^2 d\Omega. \quad (67)$$

The smoothed nodal terms in (64) are constructed using SNNI as in (57). Additional terms containing the derivatives of strains are approximated by *smoothed* implicit gradients (in contrast to Part I) as

$$\begin{aligned} \hat{\boldsymbol{\varepsilon}}_{L\bar{i}}(\mathbf{u}^h) &= \sum_{I=1}^{NP} \mathbf{B}_{I\bar{i}}^{u\tilde{\nabla}}(\mathbf{x}_L) \mathbf{u}_I, & \hat{\boldsymbol{\varepsilon}}_{L\bar{i}}(\mathbf{v}^h) &= \sum_{I=1}^{NP} \mathbf{B}_{I\bar{i}}^{v\tilde{\nabla}}(\mathbf{x}_L) \mathbf{v}_I, \\ \mathbf{B}_{I\bar{i}}^{u\tilde{\nabla}}(\mathbf{x}) &= \begin{bmatrix} \Psi_{I\bar{i}1}^{\tilde{\nabla}}(\mathbf{x}) & 0 \\ 0 & \Psi_{I\bar{i}2}^{\tilde{\nabla}}(\mathbf{x}) \\ \Psi_{I\bar{i}2}^{\tilde{\nabla}}(\mathbf{x}) & \Psi_{I\bar{i}1}^{\tilde{\nabla}}(\mathbf{x}) \end{bmatrix} \end{aligned} \quad (68)$$

where the spatial derivatives  $\Psi_{I\bar{i}j}$  are mapped as in (59) from

$$\Psi_{I\bar{i}j}^{\tilde{\nabla}} = \frac{1}{2\tilde{W}_L^{\mathbf{X}}} \int_{\tilde{\Gamma}_L^{\mathbf{X}}} (\Psi_{I\bar{i}}^{\nabla} \tilde{n}_j^{\mathbf{X}} + \Psi_{I\bar{i}j}^{\nabla} \tilde{n}_i^{\mathbf{X}}) d\Gamma. \quad (69)$$

The above averaging enforces the mathematical property of true second-order derivatives  $\Psi_{I\bar{i}j}^{\tilde{\nabla}} = \Psi_{I\bar{i}j}^{\tilde{\nabla}}$ .

Note that in this formulation, no direct derivatives are involved, which is computationally efficient. Further details and enhanced algorithms for smoothed Lagrangian natural stabilization will be presented in a forthcoming paper.

Finally, the stress updates in this paper follow the Hughes-Winget algorithm [32] in order to maintain objectivity, while the updates of the derivative of stresses in (62) use the strains in (68) following the procedure given in the Appendix of [27].

#### 4.6.2 Stabilization of temperature field

Following the procedures for the displacement field, expanding the temperature gradient in nodal domains is proposed in this work to achieve stabilization of the temperature field:

$$\nabla_{\mathbf{x}} \theta^h(\mathbf{x}) \approx \nabla_{\mathbf{x}} \theta_L^h + \sum_{i=1}^2 \{(x_i - x_{Li})(\nabla_{\mathbf{x}} \theta_L^h)_{,\bar{i}}\} \quad (70)$$

where  $\nabla_{\mathbf{x}}\theta_L^h \equiv \nabla_{\mathbf{x}}\theta^h(\mathbf{x}_L)$ . The test function gradient follows the same form:

$$\nabla_{\mathbf{x}}S^h(\mathbf{x}) \approx \nabla_{\mathbf{x}}S_L^h + \sum_{i=1}^2 \{(x_i - x_{Ii})(\nabla_{\mathbf{x}}S_L^h)_{,\bar{i}}\} \quad (71)$$

where  $\nabla_{\mathbf{x}}S_L^h \equiv \nabla_{\mathbf{x}}S^h(\mathbf{x}_L)$ .

Employing (70) and (71) in (51b) with nodal quadrature and employing the smoothed (56) and implicit (30) gradient approximations, the following stabilized bilinear form is obtained for the temperature field:

$$\bar{a}_{SN}^{\mathbf{x}} \langle S^h, \theta^h \rangle = \bar{a}_S^{\mathbf{x}} \langle S^h, \theta^h \rangle + \bar{a}_N^{\mathbf{x}} \langle S^h, \theta^h \rangle \quad (72)$$

where  $\bar{a}_S^{\mathbf{x}} \langle \cdot, \cdot \rangle$  is the SNNI quadrature version of the bilinear form using gradient smoothing (56):

$$\bar{a}_S^{\mathbf{x}} \langle S^h, \theta^h \rangle = \sum_{L=1}^{NP} k(\tilde{\nabla}_{\mathbf{x}}S_L^h) \cdot (\tilde{\nabla}_{\mathbf{x}}\theta_L^h)M_{Li}^{\mathbf{x}} \quad (73)$$

and the stabilization term for temperature  $\bar{a}_N^{\mathbf{x}} \langle \cdot, \cdot \rangle$  is computed as

$$\bar{a}_N^{\mathbf{x}} \langle S^h, \theta^h \rangle = \sum_{L=1}^{NP} \sum_{i=1}^2 k(\hat{\nabla}S_{L\bar{i}}^h) \cdot (\hat{\nabla}\theta_{L\bar{i}}^h)M_{Li} \quad (74)$$

where  $\hat{\nabla}S_{L\bar{i}}^h$  and  $\hat{\nabla}\theta_{L\bar{i}}^h$  denote the smoothed implicit approximations to  $\nabla S_{L,\bar{i}}^h$  and  $\nabla\theta_{L,\bar{i}}^h$ , respectively.

The nodal gradients in the SNNI term are computed using (57). For the stabilization terms in (74), smoothed implicit gradients are utilized as follows:

$$\begin{aligned} \hat{\nabla}S_{L\bar{i}}^h &= \sum_{I=1}^{NP} \mathbf{B}_{I\bar{i}}^{\theta\hat{\nabla}}(\mathbf{x}_L)S_I, & \hat{\nabla}\theta_{L\bar{i}}^h &= \sum_{I=1}^{NP} \mathbf{B}_{I\bar{i}}^{\theta\hat{\nabla}}(\mathbf{x}_L)\theta_I, \\ \mathbf{B}_{I\bar{i}}^{\theta\hat{\nabla}}(\mathbf{x}) &= [\Psi_{I\bar{i}1}^{\hat{\nabla}}(\mathbf{x}) \quad \Psi_{I\bar{i}2}^{\hat{\nabla}}(\mathbf{x})]^{\top}. \end{aligned} \quad (75)$$

Note that the weights  $W_L^{\mathbf{x}}$  and second moments of inertia  $M_{Li}^{\mathbf{x}}$  are the same as in Section 4.6.1.

## 4.7 Semi-discrete matrix equations

Herein, we consider the explicit formulation for thermoplasticity. First, the semi-discrete form using SNNI and NSNI can be stated as:

$$\mathbf{M}_u \mathbf{a}_u(t) = \mathbf{f}_u^{\text{ext}}(t) - \mathbf{f}_u^{\text{int}}(t) \quad (76a)$$

$$\mathbf{M}_\theta \mathbf{a}_\theta(t) + \mathbf{C}_\theta \mathbf{v}_\theta(t) = \mathbf{f}_\theta^{\text{ext}}(t) + \mathbf{f}_\theta^{\text{diss}}(t) - \mathbf{f}_\theta^{\text{int}}(t) \quad (76b)$$

where we have adopted the notation  $\mathbf{a}_u \equiv \ddot{\mathbf{u}}$ ,  $\mathbf{v}_u \equiv \dot{\mathbf{u}}$ ,  $\mathbf{d}_u \equiv \mathbf{u}$ ,  $\mathbf{a}_\theta \equiv \ddot{\boldsymbol{\theta}}$ ,  $\mathbf{v}_\theta \equiv \dot{\boldsymbol{\theta}}$ , and  $\mathbf{d}_\theta \equiv \boldsymbol{\theta}$ ;  $\mathbf{u}$  and  $\boldsymbol{\theta}$  are the row vectors of  $\{\mathbf{u}_I\}_{I=1}^{NP}$  and  $\{\theta_I\}_{I=1}^{NP}$ , respectively, and the

matrix entries of the above are

$$\mathbf{M}_{uIJ} = \sum_{L=1}^{NP} \rho(\mathbf{X}_L) \bar{\mathbf{I}} \Psi_I(\mathbf{X}_L) \Psi_J(\mathbf{X}_L) W_L^x \quad (77a)$$

$$M_{\theta IJ} = \sum_{L=1}^{NP} \tau \rho(\mathbf{X}_L) c_p(\mathbf{X}_L) \Psi_I(\mathbf{X}_L) \Psi_J(\mathbf{X}_L) W_L^x \quad (77b)$$

$$C_{\theta IJ} = \sum_{L=1}^{NP} \rho(\mathbf{X}_L) c_p(\mathbf{X}_L) \Psi_I(\mathbf{X}_L) \Psi_J(\mathbf{X}_L) W_L^x \quad (77c)$$

$$\mathbf{f}_{uI}^{\text{int}} = \sum_{L=1}^{NP} \left( (\tilde{\mathbf{B}}_I^u(\mathbf{X}_L))^{\top} \Sigma(\mathbf{X}_L) W_L^x + \sum_{i=1}^2 (\mathbf{B}_i^{u\nabla}(\mathbf{x}_L))^{\top} \Sigma(\mathbf{X}_L)_{,\bar{i}}(\mathbf{x}_L) M_{Li}^x \right) \quad (77d)$$

$$\mathbf{f}_{uI}^{\text{ext}} = \sum_{K=1}^{NBPu} \Psi_I(\mathbf{x}_K) \mathbf{h}(\mathbf{X}_K) L_K^u + \sum_{L=1}^{NP} \Psi_I(\mathbf{X}_L) \mathbf{b}(\mathbf{X}_L) W_L^x \quad (77e)$$

$$f_{\theta I}^{\text{int}} = \sum_{L=1}^{NP} \left( (\tilde{\mathbf{B}}_I^{\theta}(\mathbf{X}_L))^{\top} k(\mathbf{X}_L) \tilde{\nabla}_{\mathbf{x}} \theta(\mathbf{X}_L) W_L^x + \sum_{i=1}^2 k(\mathbf{X}_L) (\mathbf{B}_i^{\theta\nabla}(\mathbf{x}_L))^{\top} \hat{\nabla} \theta_{L\bar{i}}^h M_{Li}^x \right) \quad (77f)$$

$$f_{\theta I}^{\text{ext}} = \sum_{K=1}^{NBP\theta} \Psi_I(\mathbf{x}_K) q(\mathbf{X}_K) L_K^{\theta} + \sum_{L=1}^{NP} \Psi_I(\mathbf{X}_L) (Q(\mathbf{X}_L) + \tau Q(\dot{\mathbf{X}}_L)) W_L^x \quad (77g)$$

$$f_{\theta I}^{\text{diss}} = \sum_{L=1}^{NP} \Psi_I(\mathbf{X}_L) \chi \dot{w}^p(\mathbf{X}_L) W_L^x \quad (77h)$$

with

$$\bar{\mathbf{I}} = \begin{bmatrix} 1 & 0 \\ 0 & 1 \end{bmatrix}, \quad (78)$$

$$\Sigma(\mathbf{X}_L) = [\tilde{\sigma}_{11}(\mathbf{X}_L), \tilde{\sigma}_{22}(\mathbf{X}_L), \tilde{\sigma}_{12}(\mathbf{X}_L)]^{\top},$$

$\mathbf{b}$  and  $\mathbf{h}$  are the matrix forms of  $\mathbf{b}$  and  $\mathbf{h}$ , respectively, and  $L_K^u$  and  $L_K^{\theta}$  denote the  $K$ th weight of one of the  $NBPu$  and  $NBP\theta$  integration points on the natural boundaries for the displacement and temperature change in the current configuration, respectively. As described in Section 4.6, the stress gradient  $\Sigma(\mathbf{X}_L)_{,\bar{i}}$  is not computed directly but instead approximated.

#### 4.8 Fully discrete matrix equations for explicit hyperbolic analysis

In this section, we introduce the fully discrete matrix equations for explicit hyperbolic analysis following the Newmark method with the central difference scheme [31]. For the parabolic version, the heat equation just follows the forward Euler algorithm on temperature. First, denote the approximation of displacement variables at time  $t_n$  as  $\mathbf{a}_u^n \approx \mathbf{a}_u(t_n)$ ,  $\mathbf{v}_u^n \approx \mathbf{v}_u(t_n)$ , and  $\mathbf{d}_u^n \approx \mathbf{d}_u(t_n)$ .

The approximate temperature changes and their rates at  $t_n$  are  $\mathbf{a}_{\theta}^n \approx \mathbf{a}_{\theta}(t_n)$ ,  $\mathbf{v}_{\theta}^n \approx \mathbf{v}_{\theta}(t_n)$ , and  $\mathbf{d}_{\theta}^n \approx \mathbf{d}_{\theta}(t_n)$ . Then the following algorithm is obtained for the central difference method at time  $t_{n+1}$ :

**Predictor phase** Compute predicted quantities ( $\hat{\cdot}$ ):

$$\hat{\mathbf{d}}_u^{n+1} = \mathbf{d}_u^n + \Delta t \mathbf{v}_u^n + \frac{\Delta t^2}{2} \mathbf{a}_u^n, \quad (79a)$$

$$\hat{\mathbf{v}}_u^{n+1} = \mathbf{v}_u^n + \frac{\Delta t}{2} \mathbf{a}_u^n, \quad (79b)$$

$$\hat{\mathbf{d}}_\theta^{n+1} = \mathbf{d}_\theta^n + \Delta t \mathbf{v}_\theta^n + \frac{\Delta t^2}{2} \mathbf{a}_\theta^n, \quad (79c)$$

$$\hat{\mathbf{v}}_\theta^{n+1} = \mathbf{v}_\theta^n + \frac{\Delta t}{2} \mathbf{a}_\theta^n. \quad (79d)$$

Note that in the central difference method, some of the predicted values are the corrected values such that  $\mathbf{d}_u^{n+1} = \hat{\mathbf{d}}_u^{n+1}$  and  $\mathbf{d}_\theta^{n+1} = \hat{\mathbf{d}}_\theta^{n+1}$ . This makes the internal force-type terms possible to compute exactly at any given time step and are thus moved to the right-hand side.

**Solve the governing equations** Solve for the accelerations and their temperature counterparts from the Governing equations.

For the hyperbolic version, to keep the method explicit, the following "mass" matrices are lumped using the row-sum method, and the predictor for the velocity-type temperature terms are employed and moved to the right-hand side:

$$\mathbf{M}_u^l \mathbf{a}_u^{n+1} = \mathbf{f}_u^{\text{ext}} - \mathbf{f}_u^{\text{int}}, \quad (80a)$$

$$\mathbf{M}_\theta^l \mathbf{a}_\theta^{n+1} = \mathbf{f}_\theta^{\text{ext}} + \mathbf{f}_\theta^{\text{diss}} - \mathbf{f}_\theta^{\text{int}} - \mathbf{C}_\theta \tilde{\mathbf{v}}_\theta^{n+1}. \quad (80b)$$

Since the mass matrices are lumped (80) is simply a set of row equations and needs no solver. Also note, the coupling between mechanical fields and temperature is given by the source term  $\dot{\omega}^p$  in the energy equation in  $\mathbf{f}_\theta^{\text{diss}}$ , the temperature strain in the Cauchy stress  $\boldsymbol{\sigma}$  in  $\mathbf{f}_u^{\text{int}}$ , and the possible effect of the temperature on the yield stress in plasticity in  $\mathbf{f}_u^{\text{int}}$ .

**Corrector phase** Compute corrected quantities:

$$\mathbf{d}_u^{n+1} = \hat{\mathbf{d}}_u^{n+1} \quad (\text{no correction}), \quad (81a)$$

$$\mathbf{v}_u^{n+1} = \hat{\mathbf{v}}_u^{n+1} + \frac{\Delta t}{2} \mathbf{a}_u^{n+1}, \quad (81b)$$

$$\mathbf{d}_\theta^{n+1} = \hat{\mathbf{d}}_\theta^{n+1} \quad (\text{no correction}), \quad (81c)$$

$$\mathbf{v}_\theta^{n+1} = \hat{\mathbf{v}}_\theta^{n+1} + \frac{\Delta t}{2} \mathbf{a}_\theta^{n+1}. \quad (81d)$$

Hence, the algorithm follows the typical explicit scheme for pure solid mechanics, with no special treatments. Therefore existing explicit solids codes can benefit from the present approach if thermomechanical coupling is desired. In addition, when the second sound speed is equated with the first (see the Sections 5 and 6), the time step requirement also remains the same.

## 5 Time-step criteria

In this section we examine the time-step criteria for the G-L theory using the explicit Newmark Method (the extension to L-S is straightforward), and compare it to the classical theory with the explicit generalized trapezoidal rule (forward Euler) method with lumped mass, as has been used in the past for explicit thermomechanical analysis (e.g., see [43]). We note that the coupled system for the generalized theory (80) is not solved in a matrix fashion monolithically, so we examine the limitation on the time step due to the temperature field alone.

There are three main methods typically considered in stability analysis: (1) modal analysis, (2) the Von Neumann Method, and (3) the energy method. Here we use modal analysis based on linear finite elements (as a proxy for a linear meshfree discretization, with nodal spacing  $\Delta x$ , which is conservative for nodal integration methods [17]) to examine the critical time step,  $\Delta t_{\text{cr}}$ . We solve the following problem to determine the maximum magnitude of the element eigenvalues, which governs the time step:

$$(\mathbf{K}^e - \lambda_i^2 \mathbf{M}^e) \boldsymbol{\phi}_i = \mathbf{0}, \quad i = 1, 2 \quad (82)$$

where  $\boldsymbol{\phi}_i$  is an eigenvector and  $\lambda_i$  is the associated eigenvalue, and for the element eigenvalue problem:

$$\mathbf{M}^e = \frac{t_2 \rho c_p l^e}{2} \begin{bmatrix} 1 & 0 \\ 0 & 1 \end{bmatrix} \quad \mathbf{K}^e = \frac{k}{l^e} \begin{bmatrix} 1 & -1 \\ -1 & 1 \end{bmatrix}. \quad (83)$$

where  $l^e$  is the length of an element. For simplicity, damping is neglected here, since this does not effect the time step estimate with the standard selection of  $\gamma = 1/2$ , which is needed for second order accuracy [31].

Following standard procedures, one can obtain two solutions:

$$\lambda = 0, \quad \text{and} \quad \lambda = \frac{4k}{t_2 \rho c_p (l^e)^2}. \quad (84)$$

Since  $\Delta t_{\text{cr}} = 2/\sqrt{\max(\lambda)}$  in the central difference method [31], the critical time step of the hyperbolic heat equation using lumped mass is:

$$\Delta t \leq \Delta t_{\text{cr}} = \frac{2}{\sqrt{\max(\lambda)}} = \sqrt{\frac{t_2 \rho c_p}{k}} l^e = \frac{l^e}{c_{\text{T,GL}}}, \quad (85)$$

where  $c_{\text{T,GL}}$  is the temperature propagation speed for the G-L theory (21). So, the critical time step of the hyperbolic heat equation is  $\Delta t_{\text{cr}} \propto l^e$ , and mimics the requirement for pure solid mechanics problems. That is, the critical time step is exactly the time it takes for a wave to pass through one element. This time, it is the second sound speed. Therefore for efficiency, relaxation times can be based on equating the second sound speed with the first. This seems to be also a practical solution, since this data is generally unavailable for most materials, and this also results in very small relaxation times yielding results close to the classical theory.

L-S follows a similar derivation, with the critical time step governed by the associated wave speed with

$$\Delta t \leq \Delta t_{\text{cr}} = \frac{l^e}{c_{\text{T,LS}}}. \quad (86)$$

For comparison, using forward Euler with lumped element "heat mass" matrix  $\mathbf{C}^e$  (the explicit generalized trapezoidal rule), the critical time step of the classic parabolic theory can be determined using eigenvalue strategies as in (82):

$$(\mathbf{K}^e - \lambda_i^p \mathbf{C}^e) \phi_i^p = \mathbf{0}, \quad i = 1, 2 \quad (87)$$

where  $\phi_i^p$  is an eigenvector and  $\lambda_i^p$  is the associated eigenvalue, and for the element eigenvalue problem:

$$\mathbf{C}^e = \frac{\rho c_p l^e}{2} \begin{bmatrix} 1 & 0 \\ 0 & 1 \end{bmatrix} \quad \mathbf{K}^e = \frac{k}{l^e} \begin{bmatrix} 1 & -1 \\ -1 & 1 \end{bmatrix}. \quad (88)$$

Stability for the Forward Euler algorithm is  $\Delta t_{\text{cr}} = 2/\max(\lambda)$  [31]. Thus, the critical time step governed by the associated wave speed with

$$\Delta t \leq \Delta t_{\text{cr}} = \frac{2}{\max(\lambda)} = \frac{(l^e)^2 \rho c_p}{2k} \quad (89)$$

Based on (85), (86) and (89), the time step for parabolic equation will always be smaller than the hyperbolic equation as  $l^e \rightarrow 0$ .

## 6 Numerical examples

In this section numerical examples are presented to demonstrate the accuracy of stability of the proposed method. For generalized thermoelasticity, four different integration methods are used for comparison to demonstrate the necessity of both stabilization and variationally consistent integration. Three benchmarks of thermoelasticity and a thermoplastic benchmark are solved, and the results are compared with numerical methods such as FEM and BEM, and experimental data when available.

### 6.1 Generalized thermoelasticity

In this section the accuracy of stability of the proposed method in generalized thermoelasticity is studied. The following numerical integration methods are employed in this section:

1. Direct nodal integration (denoted DNI)
2. Variationally consistent integration with direct nodal integration (denoted VC-DNI)
3. Naturally stabilized nodal integration (denoted NSNI)
4. Variationally consistent integration with naturally stabilized nodal integration (denoted VC-NSNI)

Unless otherwise stated, for the RK approximation, linear basis with cubic B-spline kernels with a normalized support size of 2 are employed in all problems, using a uniform node distribution with a nodal spacing of  $\Delta x = 0.001$ . The implicit and unconditionally stable backward difference method [44] is employed with a time step of  $\Delta t = 0.001$  to discretize the time domain in all examples in this section. The transformation method [15] is used for the imposition of essential boundary conditions. The solutions are presented in terms of the dimensionless variables

$$\bar{y} = \frac{y}{\bar{a}}, \quad \bar{\theta} = \frac{\theta}{\theta_0}, \quad \bar{t} = \frac{\kappa}{\bar{a}^2}t, \quad \bar{u} = \frac{(\lambda + 2\mu)}{\bar{a}\beta\theta_0}u, \quad \bar{t}_0 = \frac{\kappa}{\bar{a}^2}t_0, \quad \bar{t}_1 = \frac{\kappa}{\bar{a}^2}t_1, \quad \bar{t}_2 = \frac{\kappa}{\bar{a}^2}t_2, \quad (90)$$

where  $\bar{a} = \kappa/c_s\rho c_p$ ;  $\kappa = k/\rho c_p$ , and  $c_s = \sqrt{(\lambda + 2\mu)/\rho}$ .

We consider a linear elastic half-space  $y \geq 0$  subjected to a uniform sudden temperature change on its boundary plane, free of traction. This initial boundary value problem is the first Danilovskaya's problem [21]. The boundary conditions in this problem are given as

$$\theta(0, t) = \theta_0, \quad (91a)$$

$$\sigma(0, t) = 0. \quad (91b)$$

The above problem can be treated as one-dimensional coupled and uncoupled generalized thermoelasticity. Unless otherwise stated, all material properties used in the studies are given in Table 1, and for the L-S theory, the relaxation time  $\bar{t}_0 = 2$  s is used, and for the G-L theory, the relaxation times  $\bar{t}_1$  and  $\bar{t}_2$  are 2.25 s. The full inertial dynamic representation of the problem is employed.

	$k$	$\rho$	$c_p$	$\beta$	$\lambda + 2\mu$
value	$1.7 \times 10^3$	$7.82 \times 10^{-3}$	$4.61 \times 10^6$	$3.34 \times 10^4$	$1.99 \times 10^9$
unit	$\text{kg} \times \text{cm}/\text{K}/\text{s}^3$	$\text{kg}/\text{cm}^3$	$\text{cm}^2/\text{K}/\text{s}^3$	$\text{kg}/\text{cm}/\text{K}/\text{s}^2$	$\text{kg}/\text{cm}/\text{s}^2$

Table 1: Parameters for numerical examples in generalized thermoelasticity unless otherwise stated.

### 6.1.1 Stability and accuracy study

The stability and accuracy of the proposed VC-NSNI method is first studied. Later, the need for both VC and NSNI techniques will be examined and confirmed.

Consider the G-L theory. Figure 2 shows that the comparison of RKPM with BEM [10] and FEM [44] for the coupled ( $\delta = 1$ ) and uncoupled ( $\delta = 0$ ) cases. The results are clearly stable, and both the displacement and temperature change are very close to the BEM and FEM solutions.

Interesting features of this problem include the fact that the peak of displacement in the coupled model is smaller and flatter than uncoupled model. For the temperature change, the coupled results have smaller magnitude, and show a longer delay before the large rise in temperature.

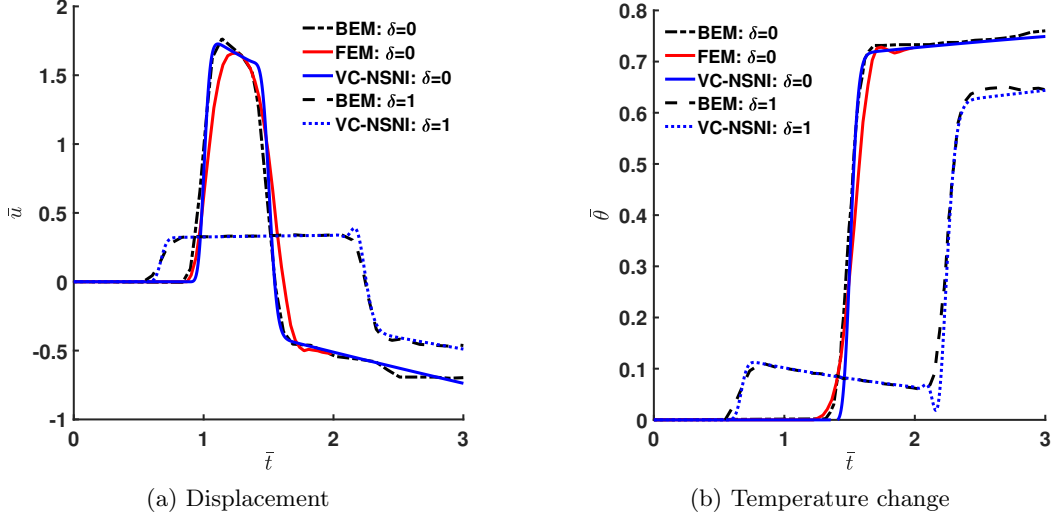


Figure 2: Time histories for the first Danilovskaya problem with the G-L theory.

Figure 3 shows the comparison of RKPM with BEM [10] for the coupled ( $\delta = 1$ ) and uncoupled ( $\delta = 0$ ) cases for the L-S theory. Both displacement and temperature change are stable, and also close to reference results. The temperature change profile is similar to the G-L theory. For the displacement, peaks are easily seen in both the coupled and uncoupled cases, and the transition is well-captured.

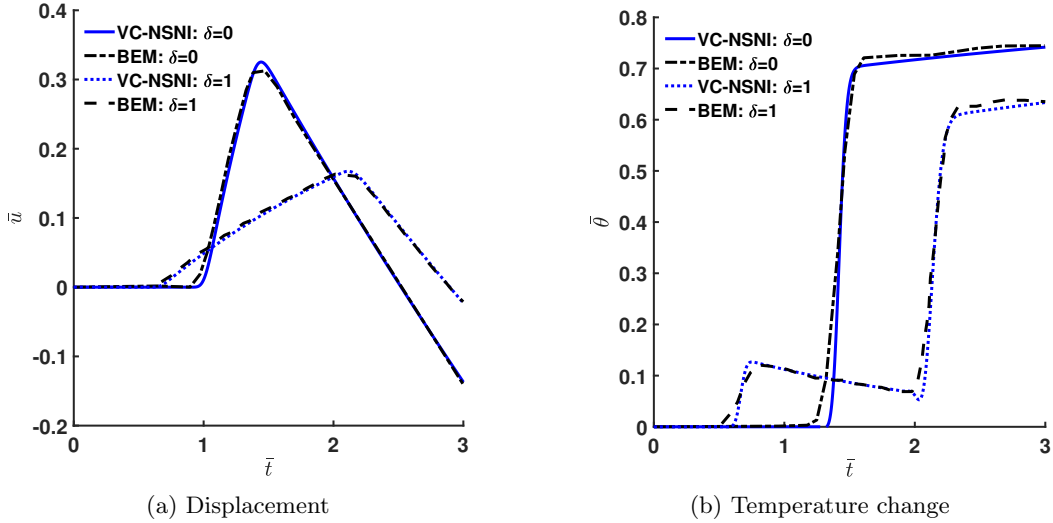


Figure 3: Time histories for the first Danilovskaya problem with the L-S theory.

In summary, the results using RKPM with VC-NSNI are stable for both the G-L and L-S theories, and are close to the available reference solutions.

### 6.1.2 Node distribution study

A non-uniform discretization is now considered to demonstrate the accuracy of the present approach, and necessity for stabilization and variationally consistent integration. Largely, uniform discretizations (as in the previous example) are special

cases where high accuracy can be obtained in meshfree methods regardless of the quadrature technique (excluding pure nodal integration which is unstable).

Consider a transition ( $\Delta x = 0.005, \Delta x = 0.01$ ) in nodal spacing, as shown in Figure 4. In [28] it was shown that this type of spatial discretization is very challenging for nodal integration in meshfree methods for dynamic problems, so it is selected.



Figure 4: Node distribution with transition in one dimension.

DNI, VC-DNI, NSNI, and VC-NSNI are employed for domain integration. Since the G-L and L-S theories do not have exact solutions, VC-NSNI with a uniform node distribution ( $\Delta x = 0.005$ ) is employed as reference (denoted as Reference).

The time histories for displacement and temperature for the G-L and L-S theories are shown in Figures 5-8. Here it is seen that DNI provides quite spurious behavior in all cases, particularly in displacements. Meanwhile, NSNI and VCI can provide more accuracy in both displacement and temperature compared to DNI. However, each alone can not achieve the accuracy of the reference solution. While NSNI seems to provide fairly acceptable results, there are still some discrepancies later in time ( $\bar{t} > 2$ ). Only when the combined VC-NSNI is employed solutions can be obtained that are very close to the reference solutions for all fields and all cases.

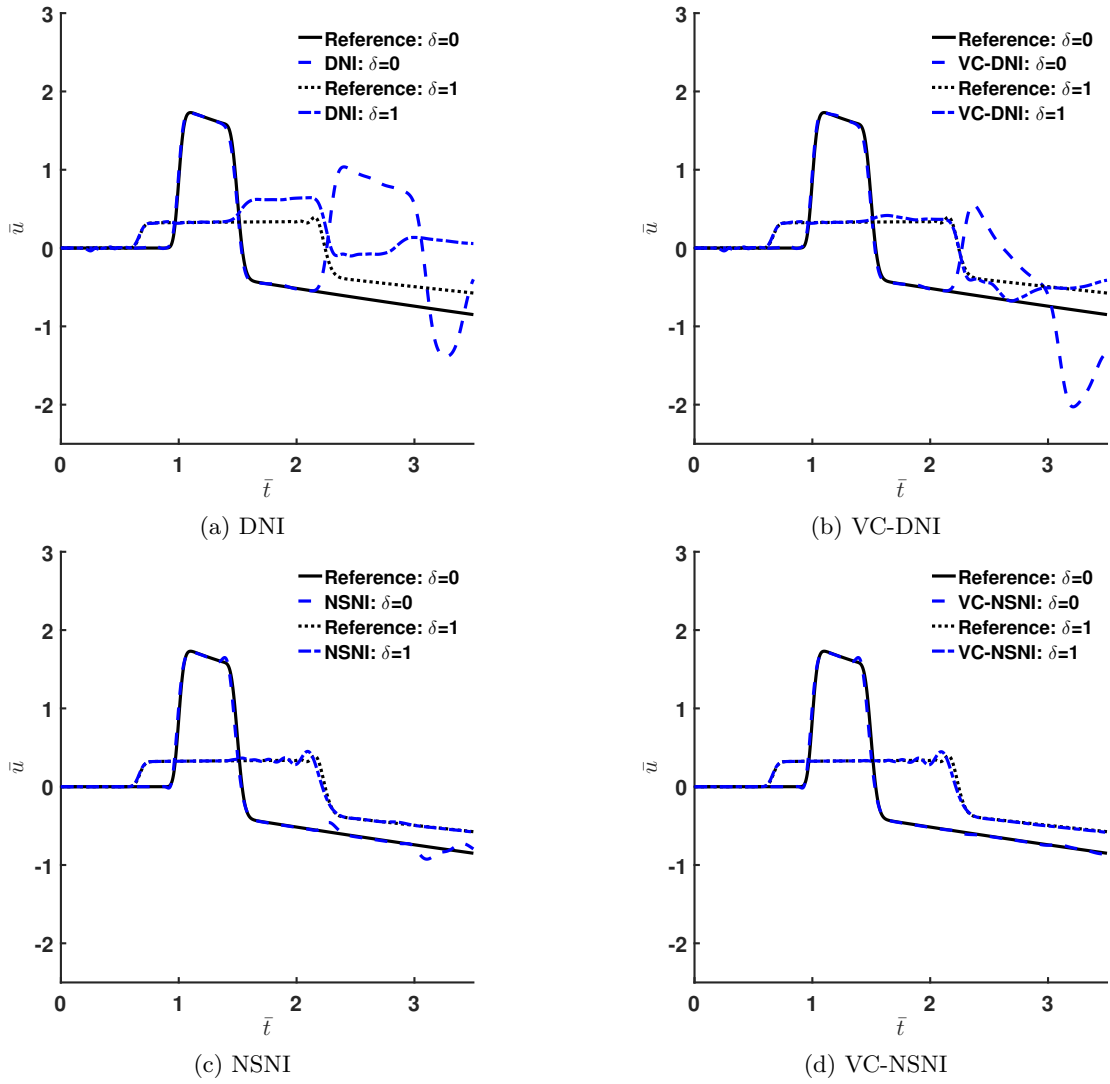


Figure 5: Displacement time histories using the G-L theory with various integration methods.

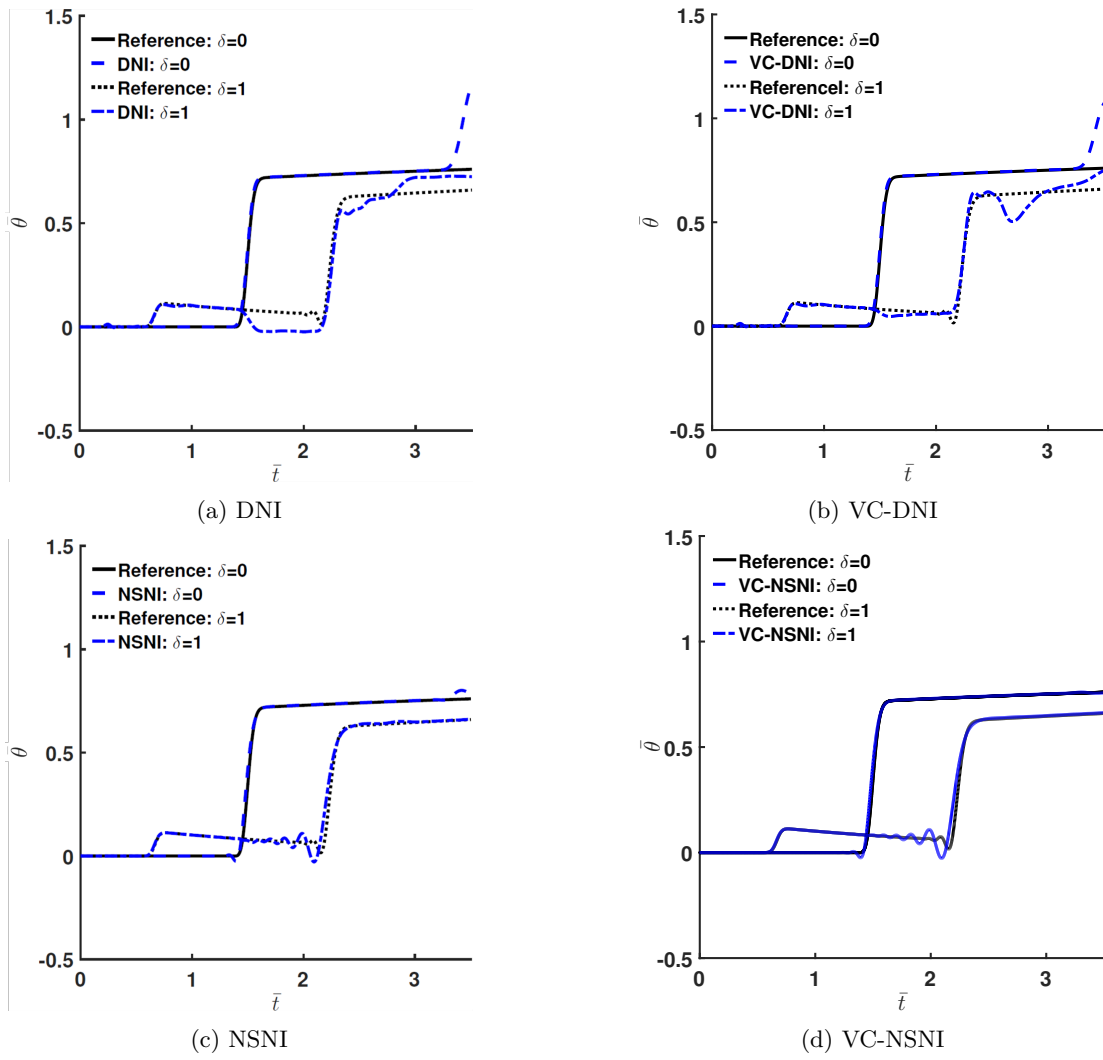


Figure 6: Time histories of temperature change using the G-L theory with various integration methods.

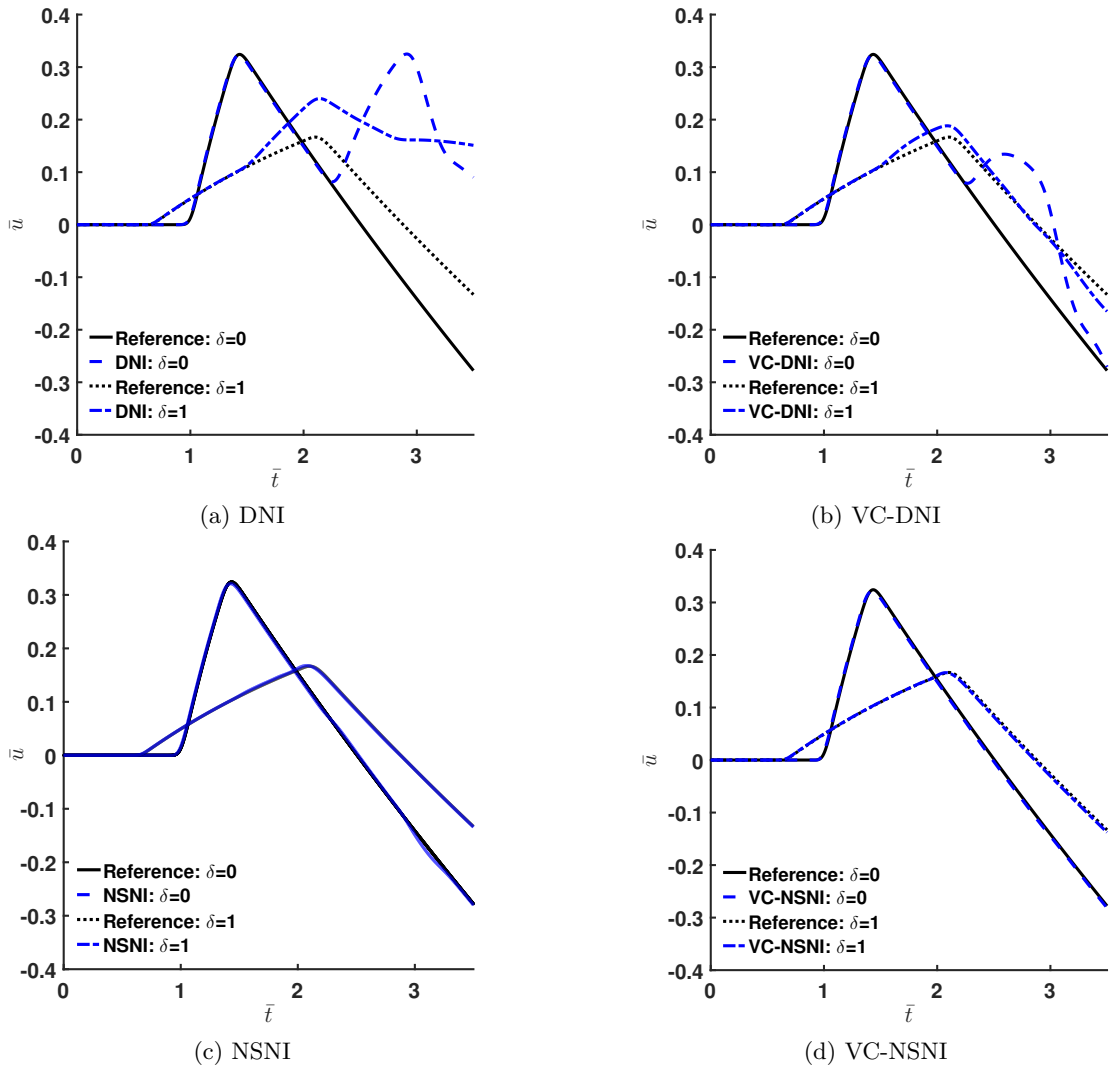


Figure 7: Displacement time histories using the L-S theory with various integration methods.

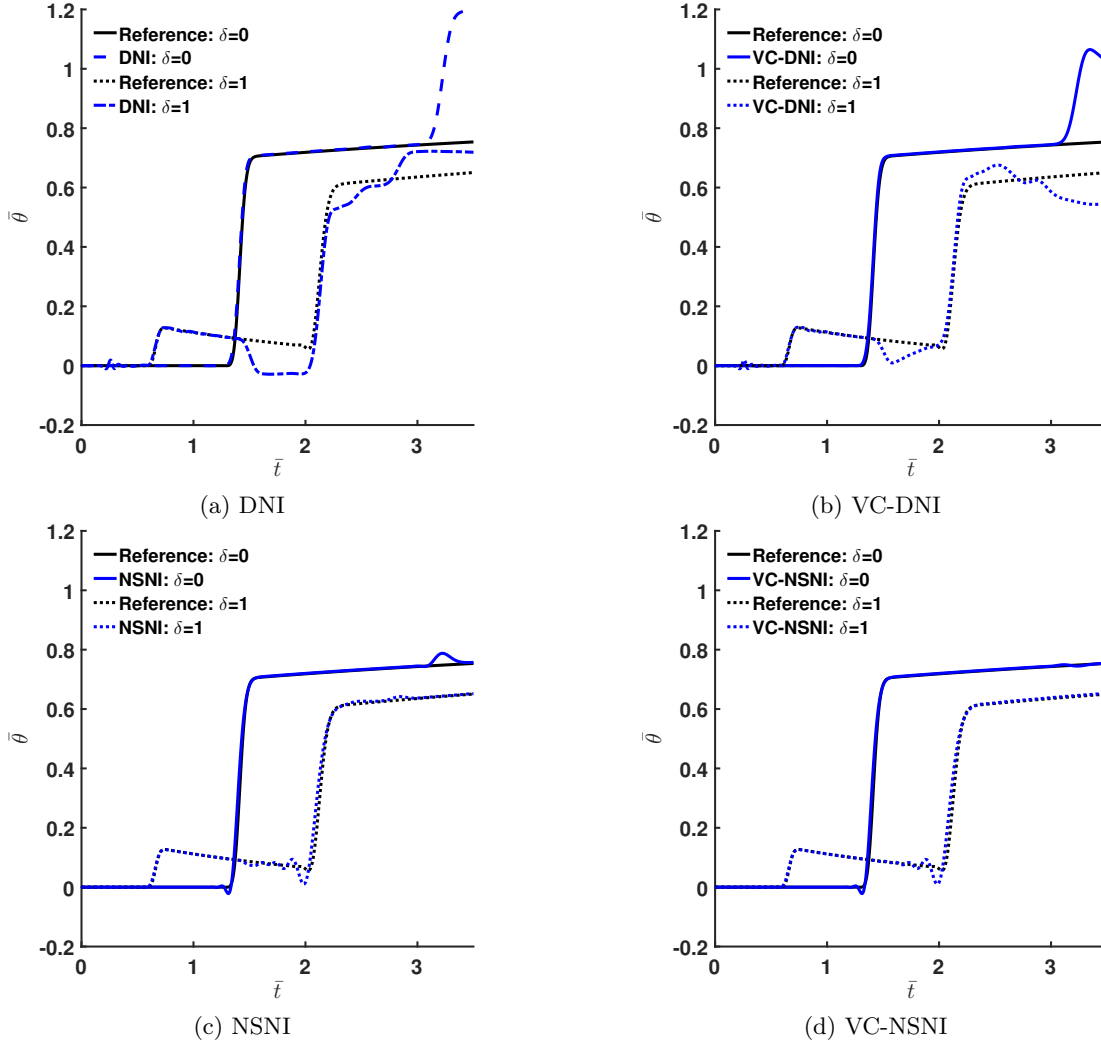


Figure 8: Time histories of temperature change using the L-S theory with various integration methods.

### 6.1.3 Relaxation time study

In the explicit numerical time integration scheme, the critical time step of the hyperbolic equation is of linear order of the nodal spacing,  $\Delta x$ , or the length of an element in FEM. In contrast, parabolic equations require a time step that is proportional to the square of the nodal spacing, and explicit methods are widely considered to be impractical since spatially refined solutions are always desired for accuracy.

To use a larger time step and obtain solutions close to the classical thermoelasticity theory, we have found that one can select relaxation times in the G-L and L-S theories by setting the thermal wave speed equal to the solid elastic wave speed  $c_s$ . Further impetus is provided by the fact that this second sound speed is generally available for most materials, and this also yields a single critical time step for uniformly solving the coupled equations monolithically in time. Here we select the relaxations times

using the following:

$$\begin{aligned}
c_s &= \sqrt{\frac{\lambda + 2\mu}{\rho}} = c_{T,GL} = \sqrt{\frac{k}{t_2 \rho c_p}}, & \rightarrow t_2 &= \frac{k}{(\lambda + 2\mu)c_p}, \\
c_s &= \sqrt{\frac{\lambda + 2\mu}{\rho}} = c_{T,LS} = \sqrt{\frac{k}{t_0 \rho c_p}}, & \rightarrow t_0 &= \frac{k}{(\lambda + 2\mu)c_p}.
\end{aligned} \tag{92}$$

The above selection of relaxation times yields the single critical time step  $\Delta t_{cr} = \Delta x/c_s$ .

For the problem at hand, the material properties result in the relaxation times  $t_2 = 1.05 \times 10^{-12}$  s and  $t_0 = 1.05 \times 10^{-12}$  s for the G-L and L-S theories, respectively. For the G-L theory with a second relaxation time  $t_1$ , we set the two relaxation times equal to each other as  $t_1 = t_2$ . Time histories for classical and generalized thermoelasticity for the displacement and temperature change are shown in Figures 9 and 10. It can be seen from the figures that when the relaxation times are defined using the elastic wave speed, the results are indistinguishable from the classical results for both the coupled and uncoupled cases, and both the G-L and L-S theories. By setting both sound speeds equal, the relaxation times are small enough such that the classical theory is nearly recovered. However here, results close to the classical theory are obtained without a severe time step restriction.

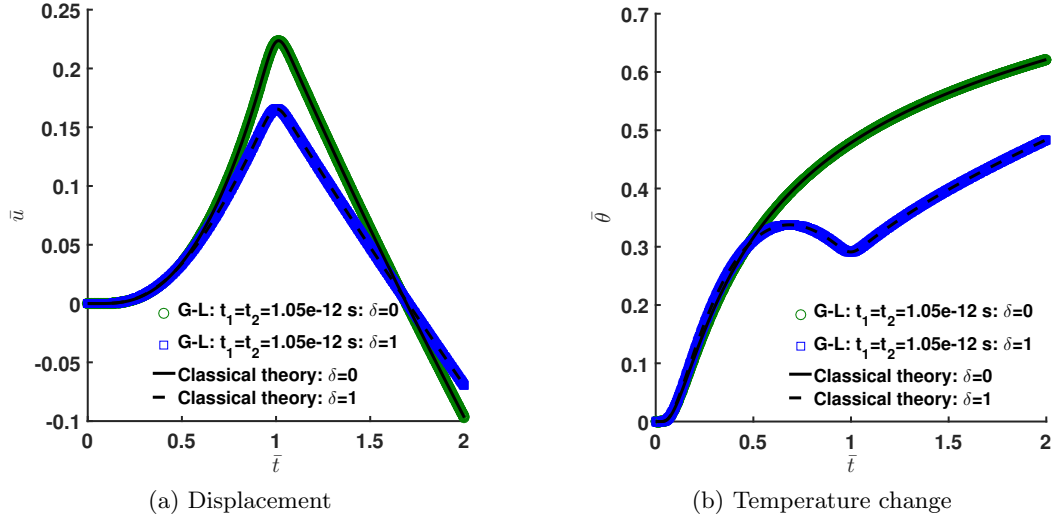


Figure 9: Time histories for the first Danilovskaya problem with the classical theory, and the G-L theory with relaxation times  $t_1 = t_2 = 1.05 \times 10^{-12}$  s.

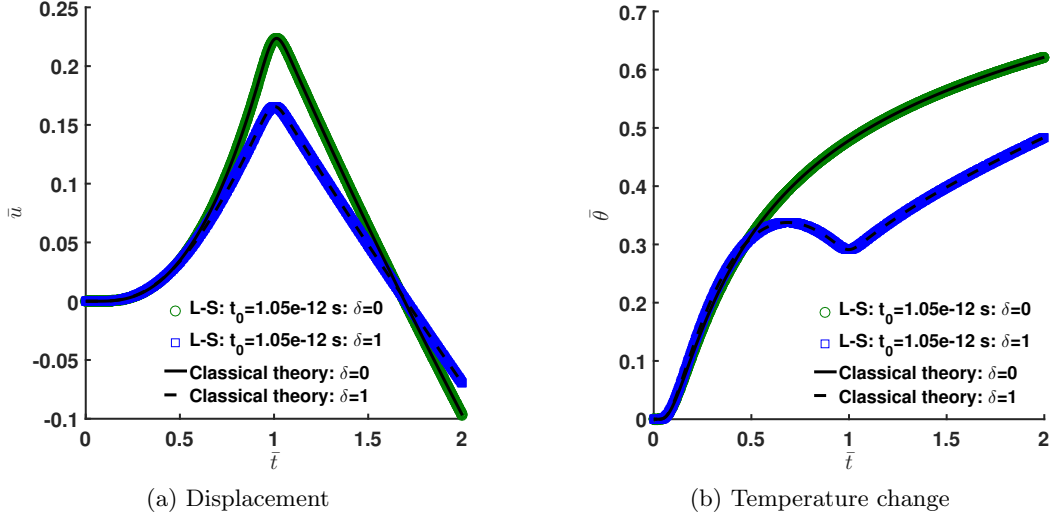


Figure 10: Time histories for the first Danilovskaya problem with the classical theory, and the L-S theory with relaxation time  $t_0 = 1.05 \times 10^{-12}$  s.

## 6.2 Thermoplasticity: necking of an isotropic bar

The necking of an isotropic bar including thermal effects is used as a benchmark for thermoplasticity. For saving computational cost, we use a half bar (with symmetry condition) to perform the simulation. The dimensions of the half-bar shown in Figure 11 are  $L_0 = 5.334$  cm,  $a_0 = 0.6298$  cm, and  $a_1 = 0.6413$  cm.

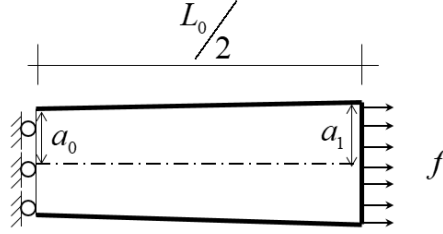


Figure 11: Depiction of tension test with force  $f$  and dimensions indicated.

The properties of the bar are density  $\rho = 7,800$  kg/m<sup>3</sup>, Young's modulus  $E = 206.9$  GPa, Poisson's ratio  $\nu = 0.29$ , heat capacity  $c_p = 460$  m<sup>2</sup>/(s<sup>2</sup>K), thermal conductivity  $k = 45$  m · kg/(s<sup>3</sup>K), thermal expansion coefficient  $\alpha = 10^{-5}$  K<sup>-1</sup>, Taylor-Quinney factor  $\chi = 0.9$ , initial temperature  $T_0 = 293$  K, and the yield stress is

$$K(\bar{e}_p) = \sigma_y^0 + \alpha_y \bar{e}_p + (\sigma_y^\infty - \sigma_y^0)(1 - e^{\beta_1 \bar{e}_p}) \quad (93)$$

where  $\bar{e}_p$  is the equivalent plastic strain,  $\alpha_y = 0.12924$  GPa,  $\sigma_y^0 = 0.45$  GPa,  $\sigma_y^\infty = 0.715$  GPa, and  $\bar{\beta}_1 = 16.93$ .

When the thermal effect is considered, the yield stress can be modified as

$$K(\bar{e}_p, \theta) = \sigma_y^0(\theta) + \alpha_y(\theta) \bar{e}_p + (\sigma_y^\infty(\theta) - \sigma_y^0(\theta))(1 - e^{\beta_1 \bar{e}_p}) \quad (94)$$

where

$$\sigma_y^0(\theta) = \sigma_y^0(1 - \omega_0\theta) \quad (95a)$$

$$\sigma_y^\infty(\theta) = \sigma_y^\infty(1 - \omega_h\theta) \quad (95b)$$

$$\alpha_y(\theta) = \alpha_y(1 - \omega_h\theta) \quad (95c)$$

and here  $\omega_0 = 0.002$ , and  $\omega_h = 0.002$ .

Linear basis, a normalized support of 2.0, and a cubic B-spline kernel are used to construct the RK approximation. Figure 12 shows the RKPM discretization with 5,771 nodes. We found for this simulation SNNI suffices for both stability and accuracy, which can likely be attributed to the coarseness and uniformity of the discretization [45, 12]. For non-uniform particles or finer nodal spacing, VC-NSNI should be used as demonstrated in the previous examples.

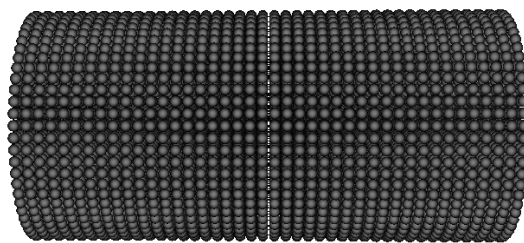


Figure 12: RKPM discretization.

We first consider the classical parabolic energy equation (44). Figure 13 depicts the deformation with the equivalent plastic strain values at 26% elongation. The elongation rate is set to 3 m/s with the time step  $\Delta t = 1 \times 10^{-8}$  s. The maximum value of the equivalent plastic strain in this study is close to the numerical results by other methods [27, 46].

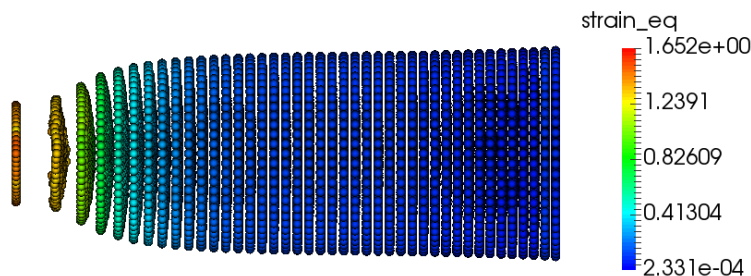


Figure 13: Final elongation with equivalent plastic strain values.

Figure 14 shows the evolution of the radius at the center of the bar and the force-displacement relationship, along with experimental data. It can be seen that RKPM agrees with the reference FEM results (denoted as Seitz et al.) [46], and the experimental data in [42]. For the reduction in radius, RKPM is in better agreement with experimental data than the reference.

For the temperature field, no experimental data is available, so the computational results from [46] are employed as a reference. Figure 15a shows that the thermal

response in the necking region by the proposed nodally integrated RKPM is in agreement with the reference result.

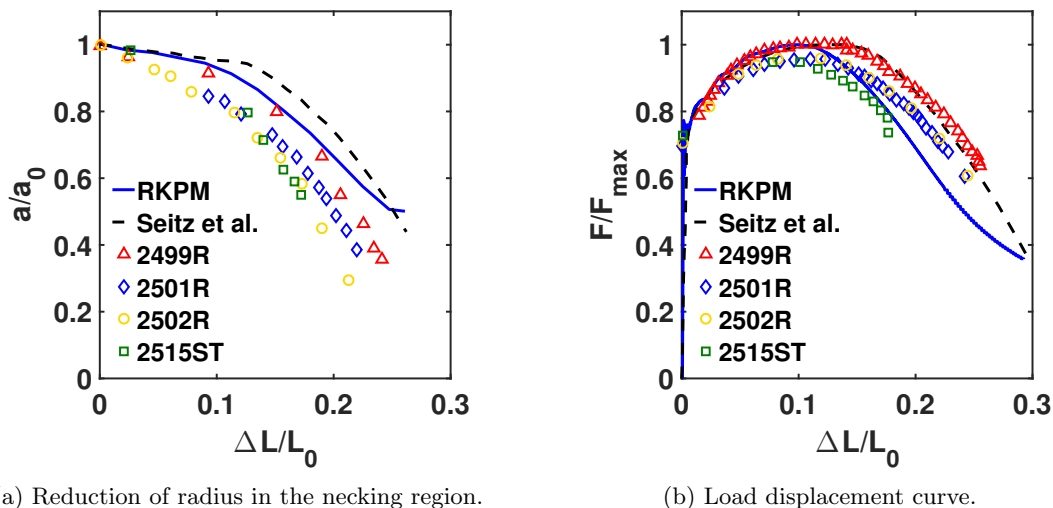


Figure 14: Comparison of RKPM mechanical response in the necking problem with experimental data.

To release the time step restriction of the parabolic equation, we now consider the hyperbolic energy equation (denoted as RKPM-Hyperbolic) with Cattaneo heat conduction (46).

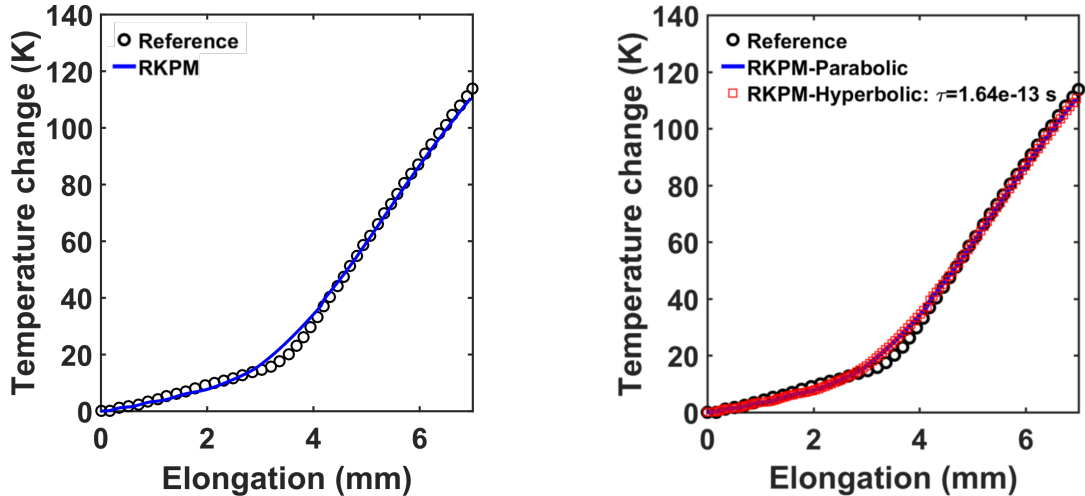
As before, we set the thermal wave speed equal to the elastic wave speed to yield a single critical time step of linear order in the nodal spacing (using linear one-dimensional finite elements as a reference):

$$c_s = \sqrt{E/\rho} = c_{T,C} = \sqrt{k/\tau c_p \rho} \quad \rightarrow \quad \tau = \frac{k}{E c_p} = 4.7282 \times 10^{-13} \text{ s} \quad (96)$$

where  $c_{T,C} = \sqrt{k/(\tau \rho c_p)}$  is the wave speed for Cattaneo heat conduction. Thus the critical time step is  $\Delta t_{\text{cr}} = \Delta x/c_{T,C} = \Delta x/c_s$ . For general considerations, one should consider the  $p$ -wave and shear wave velocity for a sharper estimate.

Figure 15b shows the RKPM response using the parabolic and hyperbolic formulations. Both agree with the reference solution, as well as each other. The parabolic and hyperbolic results are virtually indistinguishable.

This example, that uses properties of a real material, seems to indicate that the strategy of setting the thermal sound speed to the solid sound speed is a reasonable approach to achieve explicit analysis with a less restrictive (and uniform) critical time step, meanwhile achieving results similar to the classical theory. In addition, since the data for second sound speeds is not generally available for most materials in typical engineering environments, this is also one way to select the relaxation times for the hyperbolic formulation such that the classical results are achieved for all intents and purposes.



(a) Comparison of RKPM thermal response in the necking problem with results from [46]. (b) Temperatures for the classical theory and the hyperbolic theory equating sound speeds.

Figure 15: Comparisons of RKPM thermal response in the necking problem.

## 7 Conclusions

In this two-part paper, a stable, accurate, and efficient nodally integrated RKPM approach for thermomechanical problems has been presented. First, the instability in pure nodal quadrature was investigated using thermoelasticity as a model problem. It was shown that this results in node-to-node oscillations typical of nodal integration of meshfree methods in solid mechanics problems, yet the magnitude of the oscillations is several orders of magnitude higher. A naturally stabilized nodal integration (NSNI) was then proposed to stabilize the solution in an efficient manner. This approach of using implicit gradient expansions, has previously been shown to provide accelerated computations, with a 10-20 times CPU speed-up over stress-point type methods. The method was clearly shown to provide stability in both classical and generalized thermoelasticity theories. However, it was also shown that pure NSNI is insufficient for acceptable accuracy in both theories. Therefore, the variational consistency (VC) conditions for  $n$ th order exactness and convergence for the two-field problem were derived, and a uniform correction on test function gradients for both fields was adopted. This correction is performed node-by-node with small symmetric systems of equations, and hence increases the computational cost minimally. It should be noted that this approach alone does not provide stability, since it does not address the issue with the trial functions admitting spurious modes. Nevertheless, the combined VC-NSNI method was shown to provide both stability and accuracy in classical and generalized thermoelasticity. These techniques were also shown to be essentially uncoupled, so that no additional issues arise with the implementation of the two combined. These methods were then extended to thermoplasticity. Good agreement with analytical and numerical reference solutions was achieved, as well as agreement with experimental data.

For efficient explicit analysis, hyperbolic theories for both thermoelasticity and

thermoplasticity were investigated. In these models, rather than an infinite propagation of temperature information, a so-called second sound exists, and the use of these theories is well justified from a physical standpoint. Yet, this second sound speed is not well characterized for most engineering materials in most temperature environments. Therefore, equating the second sound speed with the first was investigated. The basis of this approach is the fact that the critical time step for both the equation of motion and generalized thermomechanical models are governed by the nodal spacing and the first and second sound speeds, respectively. While purely a numerical approach for selecting the associated relaxation times in the generalized equations, it was shown that this approach yields results very close to the classical theory since the resulting relation times are extremely small, at least for the problems tested herein. Therefore, since the classical thermomechanical theories are well-accepted in terms of their predictive capabilities, this provides an approach to solve coupled thermomechanical problems without a severe time step restriction.

Now that a stable and effective thermomechanical RKPM has been established, future work will entail applying this method to coupled problems where finite elements encounter great difficulty, e.g., additive manufacturing where topological changes in the domain are present, and subtractive manufacturing such as machining with material failure and separation.

**Acknowledgments** Both authors greatly acknowledge the support of this work by Penn State, and the endowment of the L. Robert and Mary L. Kimball Early Career Professorship. The first author also acknowledges the support of the Missile Defence Agency through Karagozian and Case Inc. subcontract #PSU 190337.000. Proofing of this manuscript by Jennifer Dougal is also acknowledged and appreciated.

## References

- [1] A. E. Abouelregal and A. M. Zenkour. The effect of fractional thermoelasticity on a two-dimensional problem of a mode I crack in a rotating fiber-reinforced thermoelastic medium. *Chinese Physics B*, 22(10):108102, 2013.
- [2] L. Adam and J.-P. Ponthot. Thermomechanical modeling of metals at finite strains: First and mixed order finite elements. *International Journal of Solids and Structures*, 42(21-22):5615–5655, 2005.
- [3] F. Armero and J. C. Simo. A priori stability estimates and unconditionally stable product formula algorithms for nonlinear coupled thermoplasticity. *International Journal of Plasticity*, 9(6):749–782, 1993.
- [4] J. Baek, J. Chen, G. Zhou, K. Arnett, M. Hillman, G. Hegemier, and S. Hardesty. A semi-Lagrangian RKPM with node-based shock algorithm for explosive welding simulation. *Computational Mechanics*, In press.
- [5] A. Bagri, H. Taheri, M. R. Eslami, and S. Fariborz. Generalized coupled thermoelasticity of a layer. *Journal of Thermal Stresses*, 29(4):359–370, 2006.

- [6] K.-J. Bathe. *Finite element procedures*. Klaus-Jurgen Bathe, 2006.
- [7] Y. T. Beni and M. R. Movahhedy. Consistent arbitrary Lagrangian Eulerian formulation for large deformation thermo-mechanical analysis. *Materials & Design*, 31(8):3690–3702, 2010.
- [8] G. T. Camacho and M. Ortiz. Adaptive Lagrangian modelling of ballistic penetration of metallic targets. *Computer methods in applied mechanics and engineering*, 142(3-4):269–301, 1997.
- [9] C. Cattaneo. On a form of the heat equation eliminating the paradox of an instantaneous propagation. *Account. Render*, 247:431–433, 1958.
- [10] J. Chen and G. F. Dargush. Boundary element method for dynamic poroelastic and thermoelastic analyses. *International Journal of Solids and Structures*, 32(15):2257–2278, 1995.
- [11] J.-S. Chen, M. Hillman, and S.-W. Chi. Meshfree Methods: Progress Made after 20 Years. *Journal of Engineering Mechanics*, 2016.
- [12] J.-S. Chen, M. Hillman, and M. Rüter. An arbitrary order variationally consistent integration for Galerkin meshfree methods. *International Journal for Numerical Methods in Engineering*, 95(5):387–418, 2013.
- [13] J.-S. Chen, W. K. Liu, M. Hillman, S. W. Chi, Y. Lian, and M. A. Bessa. Reproducing Kernel Approximation and Discretization. In E. Stein, R. de Borst, and T. J. R. Hughes, editors, *Encyclopedia of Computational Mechanics*. John Wiley & Sons, Ltd., Chichester, 2nd edition, 2017.
- [14] J.-S. Chen, C. Pan, C. Roque, and H.-P. Wang. A lagrangian reproducing kernel particle method for metal forming analysis. *Computational mechanics*, 22(3):289–307, 1998.
- [15] J.-S. Chen, C. Pan, C.-T. Wu, and W. K. Liu. Reproducing Kernel Particle Methods for large deformation analysis of non-linear structures. *Computer Methods in Applied Mechanics and Engineering*, 139(1-4):195–227, 1996.
- [16] J.-S. Chen, C.-T. Wu, S. Yoon, and Y. You. A stabilized conforming nodal integration for galerkin mesh-free methods. *International journal for numerical methods in engineering*, 50(2):435–466, 2001.
- [17] J.-S. Chen and Y. Wu. Stability in lagrangian and semi-lagrangian reproducing kernel discretizations using nodal integration in nonlinear solid mechanics. In *Advances in meshfree techniques*, pages 55–76. Springer, 2007.
- [18] J.-S. Chen, S. Yoon, and C.-T. Wu. Non-linear version of stabilized conforming nodal integration for Galerkin mesh-free methods. *International Journal for Numerical Methods in Engineering*, 53(12):2587–2615, 2002.
- [19] J.-S. Chen, X. Zhang, and T. Belytschko. An implicit gradient model by a reproducing kernel strain regularization in strain localization problems. *Computer Methods in Applied Mechanics and Engineering*, 193(27-29):2827–2844, 2004.

- [20] M. Chester. Second sound in solids. *Physical Review*, 131(5):2013, 1963.
- [21] V. Danilouskaya. Thermal stresses in elastic half space due to sudden heating of its boundary. *Pelageya Yakovlevna Kochina*, 14:316–321, 1950.
- [22] A. C. Eringen. *Mechanics of continua*. Robert E. Krieger Publishing Co., Huntington, New York, 1980.
- [23] Z. Fan and B. Li. Meshfree simulations for additive manufacturing process of metals. *Integrating Materials and Manufacturing Innovation*, 8(2):144–153, 2019.
- [24] A. E. Green and K. A. Lindsay. Thermoelasticity. *Journal of Elasticity*, 2(1):1–7, 1972.
- [25] P.-C. Guan, J.-S. Chen, Y. Wu, H. Teng, J. Gaidos, K. Hofstetter, and M. Al-saleh. Semi-Lagrangian reproducing kernel formulation and application to modeling earth moving operations. *Mechanics of Materials*, 41(6):670–683, 2009.
- [26] P.-C. Guan, S.-W. Chi, J.-S. Chen, T. Slawson, and M. J. Roth. Semi-Lagrangian reproducing kernel particle method for fragment-impact problems. *International Journal of Impact Engineering*, 38(12):1033–1047, 2011.
- [27] M. Hillman and J.-S. Chen. An accelerated, convergent, and stable nodal integration in Galerkin meshfree methods for linear and nonlinear mechanics. *International Journal for Numerical Methods in Engineering*, 107:603–630, 2016.
- [28] M. Hillman, J.-S. Chen, and S.-W. Chi. Stabilized and variationally consistent nodal integration for meshfree modeling of impact problems. *Computational Particle Mechanics*, 1(3):245–256, 2014.
- [29] S. M. Hosseini, J. Sladek, and V. Sladek. Meshless local Petrov–Galerkin method for coupled thermoelasticity analysis of a functionally graded thick hollow cylinder. *Engineering analysis with boundary elements*, 35(6):827–835, 2011.
- [30] P. Hosseini-Tehrani, M. R. Eslami, and S. Azari. Analysis of thermoelastic crack problems using Green–Lindsay Theory. *Journal of Thermal Stresses*, 29(4):317–330, 2006.
- [31] T. J. Hughes. *The finite element method: linear static and dynamic finite element analysis*. Dover Publications, Inc., Mineola, New York, 2012.
- [32] T. J. R. Hughes and J. Winget. Finite rotation effects in numerical integration of rate constitutive equations arising in large deformation analysis. *International Journal for Numerical Methods in Engineering*, 15(12):1862–1867, 1980.
- [33] M. A. Kouchakzadeh and A. Entezari. Analytical solution of classic coupled thermoelasticity problem in a rotating disk. *Journal of Thermal Stresses*, 38(11):1267–1289, 2015.
- [34] B. Li, F. Habbal, and M. Ortiz. Optimal transportation meshfree approximation schemes for fluid and plastic flows. *International journal for numerical methods in engineering*, 83(12):1541–1579, 2010.

- [35] S. Li and W. K. Liu. Synchronized reproducing kernel interpolant via multiple wavelet expansion. *Computational Mechanics*, 21:28–47, 1998.
- [36] S. Li and W. K. Liu. Meshfree and particle methods and their applications. *Appl. Mech. Rev.*, 55(1):1–34, 2002.
- [37] L.-E. Lindgren. Numerical modelling of welding. *Computer Methods in Applied Mechanics and Engineering*, 195(48):6710–6736, 2006.
- [38] W. K. Liu, S. Jun, and Y. F. Zhang. Reproducing kernel particle methods. *International Journal for Numerical Methods in Fluids*, 20(8-9):1081–1106, 1995.
- [39] H. W. Lord and Y. Shulman. A generalized dynamical theory of thermoelasticity. *Journal of the Mechanics and Physics of Solids*, 15(5):299–309, 1967.
- [40] S. H. Mallik and M. Kanoria. A unified generalized thermoelasticity formulation: application to penny-shaped crack analysis. *Journal of Thermal stresses*, 32(9):943–965, 2009.
- [41] T. D. Marusich and M. Ortiz. Modelling and simulation of high-speed machining. *International Journal for Numerical Methods in Engineering*, 38(21):3675–3694, 1995.
- [42] D. M. Norris Jr, B. Moran, J. K. Scudder, and D. F. Quinones. A computer simulation of the tension test. *Journal of the Mechanics and Physics of Solids*, 26(1):1–19, 1978.
- [43] X. Pan, C. T. Wu, W. Hu, and Y. Wu. A momentum-consistent stabilization algorithm for Lagrangian particle methods in the thermo-mechanical friction drilling analysis. *Computational Mechanics*, 64(3):625–644, 2019.
- [44] J.-H. Prevost and D. Tao. Finite element analysis of dynamic coupled thermoelasticity problems with relaxation times. *Journal of applied mechanics*, 50(4a):817–822, 1983.
- [45] M. A. Puso, E. Zywicz, and J. S. Chen. A new stabilized nodal integration approach. *Lecture Notes in Computational Science and Engineering*, 57:207–217, 2007.
- [46] A. Seitz, W. A. Wall, and A. Popp. A computational approach for thermoelasto-plastic frictional contact based on a monolithic formulation using non-smooth nonlinear complementarity functions. *Advanced Modeling and Simulation in Engineering Sciences*, 5(1):5, 2018.
- [47] H. H. Sherief and N. M. El-Maghraby. A mode-I crack problem for an infinite space in generalized thermoelasticity. *Journal of Thermal Stresses*, 28(5):465–484, 2005.
- [48] H. H. Sherief, N. M. El-Maghraby, and A. A. Allam. Stochastic thermal shock problem in generalized thermoelasticity. *Applied Mathematical Modelling*, 37(3):762–775, 2013.

- [49] D. C. Simkins and S. Li. Meshfree simulations of thermo-mechanical ductile fracture. *Computational Mechanics*, 38(3):235–249, 2006.
- [50] J. C. Simo and C. Miehe. Associative coupled thermoplasticity at finite strains: Formulation, numerical analysis and implementation. *Computer Methods in Applied Mechanics and Engineering*, 98(1):41–104, 1992.
- [51] P. H. Tehrani and M. R. Eslami. Boundary element analysis of coupled thermoelasticity with relaxation times in finite domain. *AIAA journal*, 38(3):534–541, 2000.
- [52] P. Vernotte. Les paradoxes de la theorie continue de l’equation de la chaleur. *Comptes rendus*, 246:3154–3155, 1958.
- [53] H. Wang, H. Liao, Z. Fan, J. Fan, L. Stainier, X. Li, and B. Li. The Hot Optimal Transportation Meshfree (HOTM) method for materials under extreme dynamic thermomechanical conditions. *Computer Methods in Applied Mechanics and Engineering*, 364:112958, 2020.
- [54] C. T. Wu, Y. Wu, D. Lyu, X. Pan, and W. Hu. The momentum-consistent smoothed particle Galerkin (MC-SPG) method for simulating the extreme thread forming in the flow drill screw-driving process. *Computational Particle Mechanics*, 7(2):177–191, 2020.
- [55] J. Wu and D. Wang. An accuracy analysis of Galerkin meshfree methods accounting for numerical integration. *Computer Methods in Applied Mechanics and Engineering*, 375:113631, 2021.
- [56] Q. Yang, L. Stainier, and M. Ortiz. A variational formulation of the coupled thermo-mechanical boundary-value problem for general dissipative solids. *Journal of the Mechanics and Physics of Solids*, 54(2):401–424, 2006.
- [57] H. Yousefi, A. T. Kani, and I. M. Kani. Multiscale RBF-based central high resolution schemes for simulation of generalized thermoelasticity problems. *Frontiers of Structural and Civil Engineering*, 13(2):429–455, 2019.
- [58] A. Zamani, R. B. Hetnarski, and M. R. Eslami. Second sound in a cracked layer based on Lord–Shulman theory. *Journal of Thermal Stresses*, 34(3):181–200, 2011.

## Appendix A: Small-strain thermoelasticity

With  $\eta^p = 0$ , the Helmholtz free energy function (6) for thermoelasticity can be written as

$$\phi = e - \theta\eta \tag{97}$$

For small-strain thermoelasticity, the free energy function is a function of strain and the temperature  $\phi(\boldsymbol{\varepsilon}, \theta)$  with

$$\dot{\phi}(\boldsymbol{\varepsilon}, \theta) = \frac{\partial \phi}{\partial \boldsymbol{\varepsilon}} \dot{\boldsymbol{\varepsilon}} + \frac{\partial \phi}{\partial \theta} \dot{\theta}. \tag{98}$$

With the assumption (97) and (98), the dissipation inequality (2a) becomes

$$\Omega_{\text{thermech}} = \left( \frac{1}{\rho} \boldsymbol{\sigma} - \frac{\partial \phi}{\partial \boldsymbol{\varepsilon}} \right) : \dot{\boldsymbol{\varepsilon}} + \left( \eta + \frac{\partial \phi}{\partial \theta} \right) \dot{\theta} \geq 0. \quad (99)$$

Which yields the constitutive relations

$$\eta = - \frac{\partial \phi}{\partial \theta} \quad (100)$$

and

$$\boldsymbol{\sigma} = \rho \frac{\partial \phi}{\partial \boldsymbol{\varepsilon}}. \quad (101)$$

Assuming  $\boldsymbol{\varepsilon} = \mathbf{0}$  and  $\theta = \theta_0$  in the reference state, (101) becomes

$$\boldsymbol{\sigma} = \mathbf{D} : \boldsymbol{\varepsilon} - \boldsymbol{\beta} \theta, \quad \text{or} \quad \boldsymbol{\sigma} = \mathbf{D} : (\boldsymbol{\varepsilon} - \boldsymbol{\alpha} \theta), \quad \text{or} \quad \boldsymbol{\sigma} = 2\mu \text{dev}(\boldsymbol{\varepsilon}) + K \text{tr}(\boldsymbol{\varepsilon}) - 3\alpha(\theta - \theta_0) \mathbf{I} \quad (102)$$

where  $\boldsymbol{\alpha}$  contains the thermal expansion coefficients,  $K$  is bulk modulus and

$$\mathbf{D} = \rho \frac{\partial^2 \phi}{\partial \boldsymbol{\varepsilon}^2}, \quad (103a)$$

$$\boldsymbol{\beta} = \mathbf{D} : \boldsymbol{\alpha} = -\rho \frac{\partial^2 \phi}{\partial \boldsymbol{\varepsilon} \partial \theta}. \quad (103b)$$

Also, the entropy for small strain can be expressed as

$$\eta(\boldsymbol{\varepsilon}, \theta) = - \frac{\partial \phi}{\partial \theta} = - \frac{\partial \phi}{\partial \theta} \Big|_0 - \frac{\partial^2 \phi}{\partial \boldsymbol{\varepsilon} \partial \theta} \Big|_0 : \boldsymbol{\varepsilon} - \frac{\partial^2 \phi}{\partial \theta^2} \Big|_0 (\theta - \theta_0) \quad (104)$$

where  $|_0$  means that the quantity is evaluated at the reference state. With (100), (102), (103), and  $(\theta - \theta_0)/\theta \approx (\theta - \theta_0)/\theta_0$ , and The specific heat capacity is  $c_p = \theta \frac{\partial \eta}{\partial \theta} \approx \theta_0 \frac{\partial \eta}{\partial \theta}$  the entropy (104) can be written as

$$\eta(\boldsymbol{\varepsilon}, \theta) = \eta_0 + \frac{3K\alpha}{\rho} \text{tr}(\boldsymbol{\varepsilon}) + \frac{\theta - \theta_0}{\theta_0} c_p, \quad (105a)$$

$$\dot{\eta}(\boldsymbol{\varepsilon}, \theta) = \frac{3K\alpha}{\rho} \text{tr}(\dot{\boldsymbol{\varepsilon}}) + \frac{\dot{\theta}}{\theta_0} c_p. \quad (105b)$$

Substitution of (105b) and  $\boldsymbol{\beta} = 3K\alpha$  into (7) with the Fourier's law (4) yields

$$\rho c_p \frac{\theta}{\theta_0} \dot{\theta} + \theta \boldsymbol{\beta} \text{tr}(\dot{\boldsymbol{\varepsilon}}) = k \nabla \cdot \nabla \theta + Q. \quad (106)$$

With the assumption  $\theta \approx \theta_0$ , the energy equation becomes

$$\rho c_p \dot{\theta} + \theta_0 \boldsymbol{\beta} \text{tr}(\dot{\boldsymbol{\varepsilon}}) = k \nabla \cdot \nabla \theta + Q \quad (107)$$

which is the same as (12).

## Appendix B: Finite-strain thermoplasticity

First, taking time derivative of the Helmholtz free energy function one obtains

$$\dot{\phi} = \dot{e} - \dot{\theta}\eta - \theta\dot{\eta} + \dot{\theta}\eta^p + \theta\dot{\eta}^p. \quad (108)$$

With the assumption (108) and (40), the dissipation inequality (2a) becomes

$$\begin{aligned} \Omega_{\text{thermech}} = \rho(\mathbf{P} - \frac{\partial\phi^e}{\partial\mathbf{F}^e} \frac{\mathbf{F}^e}{\mathbf{F}}) : \dot{\mathbf{F}} + (-(\eta - \eta^p) + \rho \frac{\partial\phi}{\partial\theta})\dot{\theta} + \\ \rho \frac{\partial\phi^e}{\partial\mathbf{F}^e} \frac{\mathbf{F}^e}{\mathbf{F}^p} : \dot{\mathbf{F}}^p + \rho \frac{\partial\phi^p}{\partial v} \dot{v} + \theta\dot{\eta}^p \geq 0. \end{aligned} \quad (109)$$

where  $\mathbf{F} = \mathbf{F}^e \mathbf{F}^p$ ;  $\mathbf{F}^e$  is the deformation gradient;  $\mathbf{F}^e$  and  $\mathbf{F}^p$  are the elastic and plastic part of the deformation gradient, respectively. Since  $\mathbf{F}$ ,  $\dot{\mathbf{F}}$ ,  $\theta$ , and  $\dot{\theta}$  are arbitrary values, we obtain the constitutive relations of

$$\mathbf{P} = \frac{\partial\phi}{\partial\mathbf{F}^e} \frac{\partial\mathbf{F}^e}{\partial\mathbf{F}}, \quad \eta - \eta^p = \rho \frac{\partial\phi}{\partial\theta} \quad (110)$$

where  $\mathbf{P}$  is the first Piola-Kirchhoff stress.

Here we define (109) into two parts

$$\mathbf{D}_{\text{mech}} = \rho \frac{\partial\phi^e}{\partial\mathbf{F}^e} \frac{\mathbf{F}^e}{\mathbf{F}^p} : \dot{\mathbf{F}}^p + \rho \frac{\partial\phi^p}{\partial v} \dot{v} = \boldsymbol{\Sigma} : \mathbf{D}^p + \rho \frac{\partial\phi^p}{\partial v} \dot{v}, \quad (111a)$$

$$\mathbf{D}_{\text{ther}} = \theta\dot{\eta}^p \quad (111b)$$

where  $\boldsymbol{\Sigma} = 2\mathbf{C}^e \frac{\partial\phi^e}{\partial\mathbf{C}^e}$  is the Mandel stress tensor;  $\mathbf{C} = \mathbf{F}^T \mathbf{F}$  denotes the right Cauchy-Green tensor and  $\mathbf{C}^e$  is the elastic part, and  $\mathbf{D}^p = \text{sym}(\dot{\mathbf{F}}^p \mathbf{F}^{p-1})$  is the symmetric part of the plastic velocity gradient. Substitution (108), (42), and (111) into (7) with the Fourier's law (4) yields

$$\rho c_p \dot{\theta} = k \nabla \cdot \nabla \theta + Q + \mathbf{D}_{\text{mech}} + \theta \frac{\partial(\mathbf{P} : \dot{\mathbf{F}} - \mathbf{D}_{\text{mech}})}{\partial\theta} \quad (112)$$

where the last term is the elasto-plastic heating.

The simplification can be written with a dissipation factor  $\chi$  and  $\mathbf{D}_{\text{mech}} - \theta \frac{\partial\mathbf{D}_{\text{mech}}}{\partial\theta}$  is replaced to a total plastic power  $\dot{w}^p$  as following

$$\rho c_p \dot{\theta} = k \nabla \cdot \nabla \theta + Q + \theta \frac{\partial(\mathbf{P} : \dot{\mathbf{F}})}{\partial\theta} + \chi \dot{w}^p. \quad (113)$$

In applications of metal thermoplasticity, the plastic dissipation is much greater than thermoelastic heating. Therefore, we rewrite the energy equation neglecting the thermoelastic heating

$$\rho c_p \dot{\theta} = k \nabla \cdot \nabla \theta + Q + \chi \dot{w}^p$$

which is (43).

# Consistent weak forms for meshfree methods: Full realization of $h$ -refinement, $p$ -refinement, and $a$ -refinement in strong-type essential boundary condition enforcement

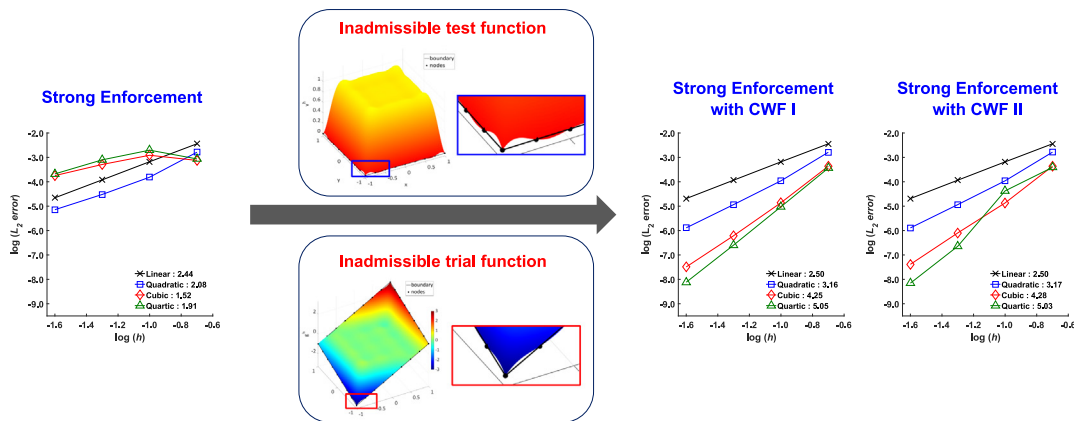
Michael Hillman\*, Kuan-Chung Lin

Department of Civil and Environmental Engineering, The Pennsylvania State University, University Park, PA 16802, USA

Received 14 May 2020; received in revised form 14 September 2020; accepted 15 September 2020

Available online xxx

## Graphical Abstract



## Abstract

Enforcement of essential boundary conditions in many Galerkin meshfree methods is non-trivial due to the fact that field variables are not guaranteed to coincide with their coefficients at nodal locations. A common approach to overcome this issue is to strongly enforce the boundary conditions at these points by employing a technique to modify the approximation such that this is possible. However, with these methods, test and trial functions do not strictly satisfy the requirements of the conventional weak formulation of the problem, as the desired imposed values can actually deviate between nodes on the boundary. In this work, it is first shown that this inconsistency results in the loss of Galerkin orthogonality and the best approximation property, and correspondingly, failure to pass the patch test. It is also shown that this induces an  $\mathcal{O}(h)$  error in the energy norm in the solution of second-order boundary value problems that is independent of the order of completeness in the approximation. As a result, this places a barrier on the global order of accuracy of Galerkin meshfree solutions to that of linear consistency. That

\* Correspondence to: 224A Sackett Building, The Pennsylvania State University, University Park, PA 16802, USA  
E-mail address: [mhillman@psu.edu](mailto:mhillman@psu.edu) (M. Hillman).

is, with these methods, it is not possible to attain the higher order accuracy offered by meshfree approximations in the solution of boundary-value problems. To remedy this deficiency, two new weak forms are introduced that relax the requirements on the test and trial functions in the traditional weak formulation. These are employed in conjunction with strong enforcement of essential boundary conditions at nodes, and several benchmark problems are solved to demonstrate that optimal accuracy and convergence rates associated with the order of approximation can be restored using the proposed method. In other words, this approach allows  $p$ -refinement, and  $h$ -refinement with  $p$ th order rates with strong enforcement of boundary conditions beyond linear ( $p > 1$ ) for the first time. In addition, a new concept termed  $a$ -refinement is introduced, where improved accuracy is obtained by increasing the kernel measure in meshfree approximations, previously unavailable.

© 2020 Elsevier B.V. All rights reserved.

*Keywords:* Meshfree methods; Essential boundary conditions; Refinement; Transformation method

---

## 1. Introduction

Galerkin meshfree methods [1] are a unique class of numerical approaches based on a purely point-based discretization. They offer advantages in classes of problems where mesh-based finite elements encounter difficulty, such as those involving extreme-deformation, multi-body evolving contact, fragmentation, among others; they also offer other attractive features like arbitrary smoothness or roughness uncoupled with the order of accuracy, ease of discretization, ease of adaptivity, and intrinsic enrichment [1–4]. However, their implementation is less trivial than the finite element method. For instance, careful attention needs to be paid to numerical quadrature, and enforcement of essential boundary conditions (cf. [1]). The focus of this work is the latter issue.

Enforcement of essential (or Dirichlet) boundary conditions is non-trivial in Galerkin meshfree methods since the nodal coefficients of shape functions do not coincide with their field variables at nodal locations in the general case. Colloquially, this is described as lacking the Kronecker delta property, or weak-Kronecker delta property (although an even weaker condition is sufficient to impose values at nodes on the boundary as will be discussed). Therefore, unlike the finite element method, essential boundary conditions cannot be directly enforced on the shape functions' coefficients. Several techniques have been proposed to overcome this difficulty.

In general, these methods can be classified into two categories: (1) strong enforcement of essential boundary conditions at nodal locations [5–9], and (2) weak enforcement of boundary conditions, such as the Lagrange multiplier method [10], the penalty method [7] and Nitsche's method [11,12]. In the first category, the idea is to modify the approximations such that nodal coefficients correspond to field variables on the essential boundary. For the second, these methods allow test and trial functions which do not need to satisfy any particular requirement related to the essential boundary, and instead impose boundary conditions weakly, i.e., in the sense of a distribution.

The first method proposed for enforcing essential boundary conditions in meshfree methods was the Lagrange multiplier approach used in the element free Galerkin (EFG) method [10]. While this circumvents the aforementioned difficulties in a relatively straight-forward manner, additional degrees of freedom are introduced, and the stiffness matrix is also positive semi-definite. The choice of the approximation for these multipliers is also subject to the *Ladyzhenskaya-Babuška-Brezzi (LBB) stability condition*, which is an inf-sup condition necessary for well-posedness of the discrete problem [13,14]; an approximation to the multiplier that is not "well-balanced" with the discretization of the primary variable will not yield a stable solution. Shortly after, a modified variational principle [15] was proposed to overcome these shortcomings. In this method, the idea is to substitute the physical meaning of the Lagrange multiplier (the constraint "forces") in terms of the primary variable back into the weak form; thus, the problem does not involve any additional degrees of freedom. However, this method does not guarantee stability either as it is equivalent to using a penalty value of zero in Nitsche's method, while a minimum penalty value is necessary for stability [16].

The penalty method is also a straight-forward way to enforce essential boundary conditions, which augments the potential with a weak penalty on the constraint. However, the solution is strongly dependent on the value of the penalty parameter: lower values lead to large errors on the essential boundary, while large values lead to an ill-conditioned system matrix [12]. Nitsche's method can be viewed, in some sense, as a combination of the modified variational principle and the penalty method. The solution error is much less sensitive to the value of the penalty parameter than the penalty method, as the penalty parameter plays an alternate role of ensuring solution stability rather than enforcing boundary conditions. Nevertheless, an extremely large or small parameter also leads

to the same issues as the penalty method [12]. A reliable way to select the parameter is based on an eigenvalue problem related to the discretization [16]. However, an important corollary is that the parameter depends on the discretization, and for meshfree methods that have a variety of free parameters, this entails the distribution of points, order of approximation, kernel measure, kernel function, etc. In the authors' experience, it is difficult to choose a suitable penalty parameter (to maintain desired convergence rates) *a priori* for accuracy higher than linear. More details on the effect and choice of the penalty value for these methods can be found in [12,16].

So far, the methods discussed are all in the class of weak enforcement of essential boundary conditions. Strong methods have been developed as well, which modify the approximation such that their enforcement is similar to the finite element method. The *transformation method* also known as the *collocation method* was first introduced in [5]. This method constructs the relationship between nodal coefficients and their field values in order to achieve the Kronecker delta property in the approximation. This however requires the inverse of a system-size matrix to solve the problem at hand. This technique was independently derived and discussed by several researchers later [6–9]. To avoid inverting a system-size matrix, a technique has been introduced to greatly reduce the size of the matrix involved in this method that needs to be inverted [7,17], which has been termed the *mixed transformation method*. It is worth mentioning the work in [17] offers convenient and simple implementations of these transformation methods with row-swap operations on the system matrix. Using these techniques is equivalent to employing Lagrange multipliers to enforce the essential boundary constraint point-wise at nodal locations [17].

Alternatively, approximations can also be constructed so that direct imposition of essential boundary conditions can be performed without inverting any matrices. These techniques are most convenient for explicit dynamic calculations for obvious reasons. Approaches include coupling of meshfree shape functions with finite elements near the essential boundary [18–20], employing singular kernel functions for nodes on the essential boundary of the domain [17], and constructing moving-least squares approximations with the interpolation property via primitive functions [21]. Forcing the correction function to be zero on the essential boundary has also been introduced [22], which yields the interpolation property (for a discussion on this aspect of meshfree approximations see [23]), but this technique is difficult to use in high dimensions and complex geometry. More recently a conforming kernel approximation has been introduced which possesses the weak Kronecker delta property, and can thus strictly satisfy the requirements on the test function (and for simple boundary conditions, the trial function) in the weak formulation [24]. Finally, outside of these two classes of methods, a novel way to impose boundary conditions using D'Alembert's principle was introduced in [25].

The most common method employed in the literature appears to be strong enforcement at nodal points. To the best of the authors' knowledge, there has been only one paper [21] examining the accuracy of higher-order meshfree approximations used with these strong-form type methods. There it was reported that while using quadratic basis *to approximate a function* can yield expected convergence rates, *employing it in the Galerkin equation* results in only first-order accuracy, a discrepancy which was attributed to a lack of verifying the desired conditions for test and trial functions in between the nodes.

In this paper, this assertion, and the effect of this discrepancy in the strong-type approach is closely examined, where it is shown that the requirements on test and trial functions in the weak form are indeed not verified between nodal locations. And, in fact, the difference between the desired values is of order  $h$  on the boundary ( $h$  is the nodal spacing), independent of the approximation order  $p$ . It is further shown that this discrepancy results in failure to pass the patch test, and loss of Galerkin orthogonality. Patch tests performed demonstrate that the  $L_2$  norm of the error in the domain is restricted to order  $\mathcal{O}(h^2)$  due to these inconsistencies, and order  $\mathcal{O}(h)$  in the energy norm, regardless of the order of approximation employed.

Correspondingly, convergence rates much lower than expected are obtained for meshfree basis functions of order higher than linear ( $p > 1$ ), and the rate of convergence is limited to that of employing approximations of linear consistency. To remedy these deficiencies, two weak forms are introduced that allow for larger spaces of test and trial functions. When employed with the strong-type methods, optimal convergence rates (for sufficiently regular solutions) are obtained. This technique thus allows, for the first time using strong methods,  $p$ -refinement, and  $h$ -refinement with  $p$ th order optimal rates beyond linear. Further, it is shown that the proposed method provides improved accuracy by increasing the kernel measure  $a$  in the meshfree approximation, previously unavailable, which is termed  $a$ -refinement.

The remainder of this paper is organized as follows. The reproducing kernel approximation is first introduced in Section 2 as a basis for examination of a typical meshfree method, and issues with strong essential boundary

condition enforcement are discussed. In Section 3, two weak forms are introduced which allow the enlargement of the approximation spaces to include meshfree approximations constructed under the strong-type enforcement techniques. Numerical procedures are described in Section 4, and numerical results are then given in Section 5 to demonstrate the effectiveness of the proposed methods. Section 6 provides concluding remarks.

## 2. Background

### 2.1. Reproducing kernel approximation

In this work, the reproducing kernel is chosen as a model approximation that does not strictly meet the requirements of the commonly used weak statement of a problem that includes Dirichlet boundary conditions.

Let a domain  $\bar{\Omega} = \Omega \cup \partial\Omega$  be discretized by a set of  $Np$  nodes  $S = \{\mathbf{x}_1, \dots, \mathbf{x}_{Np} | \mathbf{x}_I \in \bar{\Omega}\}$  with corresponding node numbers  $\eta = \{I | \mathbf{x}_I \in S\}$ . The  $p$ th order discrete reproducing kernel (RK) approximation  $u^h(\mathbf{x})$  of a function  $u(\mathbf{x})$  is defined as [5,26]:

$$u^h(\mathbf{x}) = \sum_{I \in \eta} \Psi_I^{[p]}(\mathbf{x}) u_I \tag{1}$$

where  $\{\Psi_I^{[p]}(\mathbf{x})\}_{I \in \eta}$  is the set of RK shape functions, and  $\{u_I\}_{I \in \eta}$  are the associated coefficients.

The shape functions (1) are constructed by the product of a kernel function  $\Phi_a(\mathbf{x} - \mathbf{x}_I)$  and a correction function  $C^{[p]}(\mathbf{x}; \mathbf{x} - \mathbf{x}_I)$ :

$$\Psi_I^{[p]}(\mathbf{x}) = \Phi_a(\mathbf{x} - \mathbf{x}_I) C^{[p]}(\mathbf{x}; \mathbf{x} - \mathbf{x}_I). \tag{2}$$

The correction function is composed of a linear combination of monomials up to order  $p$ , which allows the exact reproduction of these monomials and  $p$ th order accuracy in the approximation (1). In matrix form this function can be expressed as:

$$C^{[p]}(\mathbf{x}; \mathbf{x} - \mathbf{x}_I) = \mathbf{H}^{[p]}(\mathbf{x} - \mathbf{x}_I)^\top \mathbf{b}^{[p]}(\mathbf{x}) \tag{3}$$

where  $\mathbf{H}^{[p]}(\mathbf{x})$  is a column vector of complete  $p$ th order monomials and  $\mathbf{b}^{[p]}(\mathbf{x})$  is a column vector of coefficients. The coefficients are obtained by enforcing the following reproducing conditions:

$$\sum_{I \in \eta} \Psi_I^{[p]}(\mathbf{x}) \mathbf{H}^{[p]}(\mathbf{x}_I) = \mathbf{H}^{[p]}(\mathbf{x}), \tag{4}$$

or equivalently,

$$\sum_{I \in \eta} \Psi_I^{[p]}(\mathbf{x}) \mathbf{H}^{[p]}(\mathbf{x} - \mathbf{x}_I) = \mathbf{H}^{[p]}(\mathbf{0}). \tag{5}$$

Employing (2)–(5), the RK shape functions in (1) are constructed as:

$$\Psi_I^{[p]}(\mathbf{x}) = \mathbf{H}^{[p]}(\mathbf{0})^\top \{\mathbf{M}^{[p]}(\mathbf{x})\}^{-1} \mathbf{H}^{[p]}(\mathbf{x} - \mathbf{x}_I) \Phi_a(\mathbf{x} - \mathbf{x}_I) \tag{6}$$

where

$$\mathbf{M}^{[p]}(\mathbf{x}) = \sum_{I \in \eta} \mathbf{H}^{[p]}(\mathbf{x} - \mathbf{x}_I) \mathbf{H}^{[p]}(\mathbf{x} - \mathbf{x}_I)^\top \Phi_a(\mathbf{x} - \mathbf{x}_I) \tag{7}$$

and is called the moment matrix. Without modification, the approximation is in general non-interpolatory, that is,  $u^h(\mathbf{x}_I) \neq u_I$ . A simple demonstration of this property is given in Fig. 1.

### 2.2. Strong enforcement of essential boundary conditions at nodal locations

#### 2.2.1. Model problem: Poisson’s equation

Without loss of generality, in this work we consider the strong form (S) of Poisson’s equation as a model boundary value problem, which asks: given  $s : \Omega \rightarrow \mathbb{R}$ ,  $t : \partial\Omega_t \rightarrow \mathbb{R}$ , and  $g : \partial\Omega_g \rightarrow \mathbb{R}$ , find  $u : \bar{\Omega} \rightarrow \mathbb{R}$  such that the following conditions hold:

$$\nabla^2 u + s = 0 \quad \text{in } \Omega \tag{8a}$$

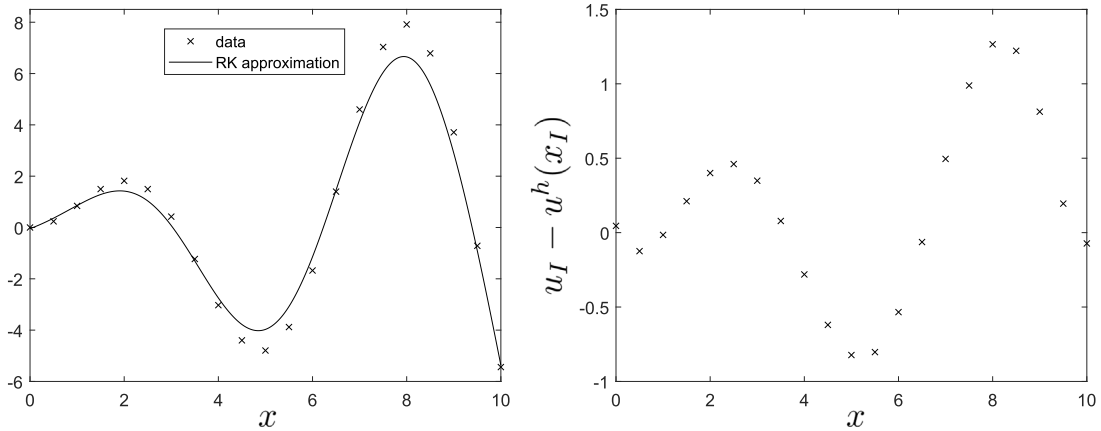


Fig. 1. Example of a meshfree approximation of data  $u_I = x_I \sin(x_I)$ .

$$\nabla u \cdot \mathbf{n} = t \quad \text{on } \partial\Omega_t \tag{8b}$$

$$u = g \quad \text{on } \partial\Omega_g \tag{8c}$$

where  $\nabla^2 \equiv \nabla \cdot \nabla$ , and  $\partial\Omega_t$  and  $\partial\Omega_g$  denote the natural boundary and essential boundary, respectively, with  $\partial\Omega_g \cap \partial\Omega_t = \emptyset$ ,  $\partial\Omega = \overline{\partial\Omega_g} \cup \overline{\partial\Omega_t}$ , and  $\bar{\Omega} = \Omega \cup \partial\Omega$ .

2.2.2. Conventional Galerkin approximation

A weak form (W) of Poisson’s equation (8) can be constructed that seeks  $u \in H_g^1$ ,  $H_g^1 = \{u | u \in H^1(\Omega), u = g \text{ on } \partial\Omega_g\}$  such that for all  $v \in H_0^1$ ,  $H_0^1 = \{v | v \in H^1(\Omega), v = 0 \text{ on } \partial\Omega_g\}$  the following equation holds:

$$a(v, u)_\Omega = (v, s)_\Omega + (v, t)_{\partial\Omega_t} \tag{9}$$

where

$$a(v, u)_\Omega = \int_\Omega \nabla v \cdot \nabla u \, d\Omega, \tag{10a}$$

$$(v, s)_\Omega = \int_\Omega v s \, d\Omega, \tag{10b}$$

$$(v, t)_{\partial\Omega_t} = \int_{\partial\Omega_t} v t \, d\Gamma. \tag{10c}$$

With approximations  $v^h$  of test functions  $v$  and  $u^h$  of trial functions  $u$ , with  $v^h = 0$  on  $\partial\Omega_g$  and  $u^h = g$  on  $\partial\Omega_g$ , a proper Galerkin approximation to (9) can be constructed which employs finite-dimensional subsets  $\mathcal{S}_g \subset H_g^1$  and  $\mathcal{S}_0 \subset H_0^1$ , and seeks  $u^h \in \mathcal{S}_g$  such that for all  $v^h \in \mathcal{S}_0$  the following equation holds:

$$a(v^h, u^h)_\Omega = (v^h, s)_\Omega + (v^h, t)_{\partial\Omega_t}. \tag{11}$$

In approximations which possess the Kronecker delta property, and in particular the weak Kronecker delta property, a subset of  $H_0^1$  is usually easily constructed. For instance, in linear finite elements, the boundary of the computational domain is defined by element edges where nodal values are linearly interpolated, so enforcement of a value of zero at nodes on the boundary ensures  $v^h = 0$  on  $\partial\Omega_g$ . For any method with the weak Kronecker delta property and the partition of unity, the same argument follows. For construction of a subset of  $H_g^1$ , a common choice is to let the approximation interpolate values of  $g$  on the essential boundary, and  $\mathcal{S}_g$  is also subset of  $H_g^1$ , or closely resembles a subset of  $H_g^1$ .

For meshfree methods which generally do not possess these properties, it is apparent from these discussions that the construction of subsets of  $H_0^1$  and  $H_g^1$  is non-trivial.

### 2.3. Strong nodal imposition in meshfree methods

Strong imposition of essential boundary conditions at nodal locations is a popular choice in meshfree methods to (approximately, as will be shown) construct admissible test and trial functions for the conventional weak formulation (9). Essentially, these entail a modification of meshfree shape functions such that nodal degrees of freedom on the essential boundary coincide with their field variables. For this to be the case, the Kronecker delta property is not actually necessary [17,21], and instead the set of modified shape functions  $\{\hat{\Psi}_I^{[p]}(\mathbf{x})\}_{I \in \eta}$  only need to verify the requirements:

$$\hat{\Psi}_J^{[p]}(\mathbf{x}_I) = 0 \quad \forall \quad I \in \eta_g, \quad J \in \eta \setminus \eta_g \tag{12}$$

and

$$\hat{\Psi}_I^{[p]}(\mathbf{x}_J) = \delta_{IJ} \quad \forall \quad I \in \eta_g, \quad J \in \eta_g \tag{13}$$

where  $\delta_{IJ}$  is the Kronecker delta function, and  $\eta \setminus \eta_g$  is the complement of the set of node numbers  $\eta_g = \{I | \mathbf{x}_I \in S_g\}$  for nodes  $S_g = \{\mathbf{x}_I | \mathbf{x}_I \in \partial\Omega_g\}$  located on the essential boundary. The above means that all “inside nodes” should not contribute to the approximation at “boundary nodes”, while all “boundary nodes” need to verify the delta property at nodal locations on the boundary.

It is important to note that (12) and (13) only verify the prescribed conditions at nodal locations, but not in between nodes. Therefore one may enforce boundary conditions on nodal coefficients, as is done in the literature, but cannot ensure proper approximation spaces are constructed.

In contrast, the above properties are distinct from the weak Kronecker delta property, where only boundary shape functions contribute to the approximation on the *entire essential boundary*:

$$\hat{\Psi}_J^{[p]}(\mathbf{x}) = 0 \quad \forall \quad \mathbf{x} \in \partial\Omega_g, \quad J \in \eta \setminus \eta_g. \tag{14}$$

From the above, it is apparent that approximations with (14) will have little issue with constructing proper subsets (or very close approximations) necessary for the weak formulation (9). Meanwhile for meshfree approximations with only (12) and (13), and not (14), as is most common, constructing proper subsets is not possible.

#### 2.3.1. Test function construction

Using these modified shape functions, in an attempt to construct a test space satisfying  $S_0 \subset H_0^1$ , the following approximation is typically employed:

$$v^h(\mathbf{x}) = \sum_{I \in \eta \setminus \eta_g} \hat{\Psi}_I^{[p]}(\mathbf{x}) v_I \tag{15}$$

where  $\{\hat{\Psi}_I^{[p]}(\mathbf{x})\}_{I \in \eta}$  is the set of modified shape functions with properties (12) and (13), and  $\{v_I\}_{I \in \eta \setminus \eta_g}$  are coefficients of the test function.

Due to (12) and (13), the test functions verify  $v^h(\mathbf{x}_I) = 0 \quad \forall \quad I \in \eta_g$ . However, for these meshfree approximations, the value of  $v^h(\mathbf{x})$  is in the general case, non-zero *between* nodes on the essential boundary and therefore violates the construction  $S_0 \subset H_0^1$ .

To illustrate this, consider a domain  $\bar{\Omega} = [-1, 1] \times [-1, 1]$  discretized uniformly in each direction by 9 nodes with  $9 \times 9 = 81$  nodes total. A linear RK approximation ( $p = 1$  in (15)) is employed using a cubic B-spline kernel function with a normalized support of 3. A test function with the arbitrary coefficients set to unity is constructed using the transformation method, with  $\partial\Omega = \partial\Omega_g$ . As seen in Fig. 2, the test functions are in fact non-zero between nodes along  $\partial\Omega_g$  with the employment of (15). According to the norms computed in Table 1, the “error” (defined as non-zero values on the essential boundary) does converge at about a rate of one ( $\mathcal{O}(h)$ ) in the  $L^2(\partial\Omega_g)$  norm, yet the magnitude of the error (in  $L^\infty(\partial\Omega_g)$ ) stays about the same regardless of the discretization. According to [27], the  $L^2(\partial\Omega_g)$  error should be  $\mathcal{O}(h^{3/2})$ , however it seems to be  $\mathcal{O}(h)$  when observed numerically, at least for meshfree approximations.

Next, the same setup is tested with  $p = 2$  and  $p = 3$ , since a “linear” error occurs for the previous test, and linear basis was employed. The same norms are computed, shown in Tables 2 and 3, respectively for the two cases. Again an  $\mathcal{O}(h)$  error is observed, and it is seen that this error is apparently independent of the order of approximation.

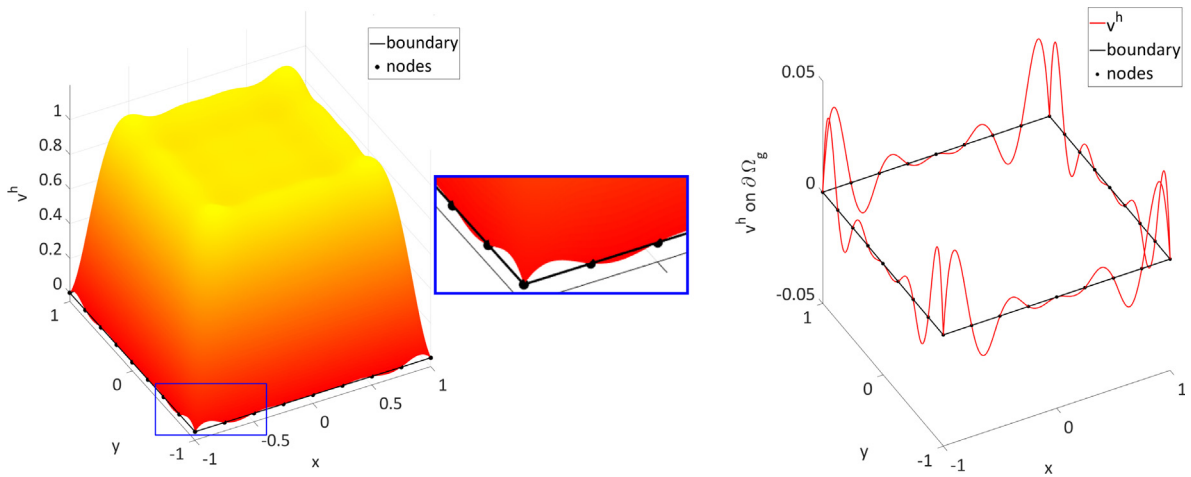


Fig. 2. Example of a test function in meshfree methods using the transformation method.

Table 1

Norms of error for boundary conditions imposed by test and trial functions,  $p = 1$ , varying  $h$ .

$h$	$L^2(\partial\Omega_g)$				$L^\infty(\partial\Omega_g)$	
	Test	Rate	Trial	Rate	Test	Trial
<b>0.5000</b>	0.01821	–	0.03615	–	0.03516	0.08443
<b>0.2500</b>	0.01014	0.84513	0.02137	0.75856	0.03645	0.10125
<b>0.1250</b>	0.00523	0.95507	0.01119	0.93372	0.03630	0.10495
<b>0.0625</b>	0.00262	0.99535	0.00573	0.96561	0.03628	0.10688

Table 2

Norms of error for boundary conditions imposed by test and trial functions,  $p = 2$ , varying  $h$ .

$h$	$L^2(\partial\Omega_g)$				$L^\infty(\partial\Omega_g)$	
	Test	Rate	Trial	Rate	Test	Trial
<b>0.5000</b>	0.01105	–	0.01935	–	0.02249	0.05458
<b>0.2500</b>	0.00352	1.65251	0.00640	1.59508	0.01476	0.03715
<b>0.1250</b>	0.00172	1.03368	0.00330	0.95787	0.01441	0.03723
<b>0.0625</b>	0.00086	1.00177	0.00176	0.90788	0.01440	0.03990

Table 3

Norms of error for boundary conditions imposed by test and trial functions,  $p = 3$ , varying  $h$ .

$h$	$L^2(\partial\Omega_g)$				$L^\infty(\partial\Omega_g)$	
	Test	Rate	Trial	Rate	Test	Trial
<b>0.5000</b>	0.00666	–	0.00975	–	0.01241	0.02231
<b>0.2500</b>	0.01016	–0.60978	0.01614	–0.72816	0.04419	0.09271
<b>0.1250</b>	0.00317	1.68073	0.00702	1.20050	0.02588	0.07773
<b>0.0625</b>	0.00163	0.95634	0.00353	0.99222	0.02653	0.07701

Later, it will be shown that this error can be directly related to the error in the energy norm of the problem—which will limit the rate of convergence for higher order ( $p > 1$ ) approximations. This will then be confirmed numerically.

Finally, as a test, the kernel measure  $a$  is varied, with  $p = 1$  and  $h = 1/4$  fixed; the results are shown in Table 4. One can first observe that if  $a \approx 1$  then the error (not shown to full significant digits) is machine precision; in this case the RK approximation closely resembles a bilinear finite element discretization. Then, as the kernel

**Table 4**

Norms of error for boundary conditions imposed by test and trial functions,  $h = 1/4$ ,  $p = 1$ , varying  $a$ .

$a$	$L^2(\partial\Omega_g)$		$L^\infty(\partial\Omega_g)$	
	Test	Trial	Test	Trial
<b>1.01</b>	0.00000	0.00000	0.00000	0.00000
<b>1.50</b>	0.00118	0.00207	0.00592	0.01363
<b>2.00</b>	0.00483	0.00873	0.01821	0.04438
<b>2.50</b>	0.00863	0.01693	0.03007	0.08018
<b>3.00</b>	0.01014	0.02137	0.03645	0.10125
<b>3.50</b>	0.01085	0.02303	0.04106	0.11543
<b>4.00</b>	0.01207	0.02563	0.04533	0.13379

measure increases, the error on the boundary increases as well. It is generally expected that in the solution of partial differential equations (PDEs), that increasing the measure of an approximation will increase the accuracy of the solution; however this is not observed in practice, and an “optimal” value is observed in meshfree methods [26]. The increasing error on the boundary can explain that there exists two competing mechanisms: increasing error with increasing  $a$  due to failure to satisfy the requirements of test functions, and increasing the accuracy of the approximation with increasing  $a$ .

2.3.2. Trial function construction

Strong enforcement at boundary nodes  $u^h(\mathbf{x}_I) = g(\mathbf{x}_I)$  is also typically introduced, and in an attempt to construct  $\mathcal{S}_g \subset H_g^1$ , the following approximation is employed:

$$u^h(\mathbf{x}) = \sum_{I \in \eta \setminus \eta_g} \hat{\Psi}_I^{[p]}(\mathbf{x})u_I + g^h(\mathbf{x}), \tag{16}$$

where

$$g^h(\mathbf{x}) = \sum_{I \in \eta_g} \hat{\Psi}_I^{[p]}(\mathbf{x})g_I, \tag{17}$$

the values  $\{u_I\}_{I \in \eta \setminus \eta_g}$  are the trial functions coefficients, and  $g_I \equiv g(\mathbf{x}_I)$  is the prescribed value of  $g(\mathbf{x})$  at an essential boundary node  $\mathbf{x}_I \in \mathcal{S}_g$ . Because of the properties (12) and (13), the trial functions verify  $u^h(\mathbf{x}_I) = g(\mathbf{x}_I) \forall I \in \eta_g$ .

While essential boundary conditions for trial functions are verified at nodal locations, the condition  $u^h = g$  is again not enforced *between* the nodes. Fig. 3 depicts a linear function prescribed as  $g(\mathbf{x}) = x + 2y$  and approximated by (17) using the same discretization that was employed for the test function. Again it can be seen that along the boundary, the solution is collocated only at nodal points. As shown in Table 1, the  $L^2(\partial\Omega_g)$  norm of the difference between  $g$  and  $g^h$  also converges at a rate of approximately one ( $\mathcal{O}(h)$ ) just as the test function, while the magnitude of error (in  $L^\infty(\partial\Omega_g)$ ) also stays roughly the same, despite refinement. It should be noted that even though linear bases are employed, the function is not exactly represented due to the influence of the interior nodes on the value of the meshfree approximation on the essential boundary between nodes. That is, it should be clear from Fig. 3 that the RK approximation under the transformation framework does not possess the weak Kronecker delta property.

Next,  $p = 2$ , and  $p = 3$  are tested, with the same norms computed and shown in Tables 2 and 3, respectively. Again an  $\mathcal{O}(h)$  error is observed, and it is seen that this error in representing the essential boundary conditions is also apparently independent of the order of approximation. The kernel measure  $a$  is again varied, with  $p = 1$  and  $h = 1/4$  fixed, and the results are shown in Table 4. Again for  $a \approx 1$  the boundary conditions are represented quite well, as the RK approximation simply interpolates the boundary condition in the limit of  $a \rightarrow 1$ . Then, as the kernel measure increases, the error on the boundary increases as before.

In the next section, it will be shown that the errors on the boundary in the test and trial functions are directly related to the error in the solution of PDEs. That is, while  $\mathcal{O}(h)$  in  $L^2(\partial\Omega_g)$ , the errors manifest as errors of  $\mathcal{O}(h^2)$  in  $L^2(\Omega)$  and  $\mathcal{O}(h)$  in  $H_1(\Omega)$ , limiting the rate of convergence of the solution.

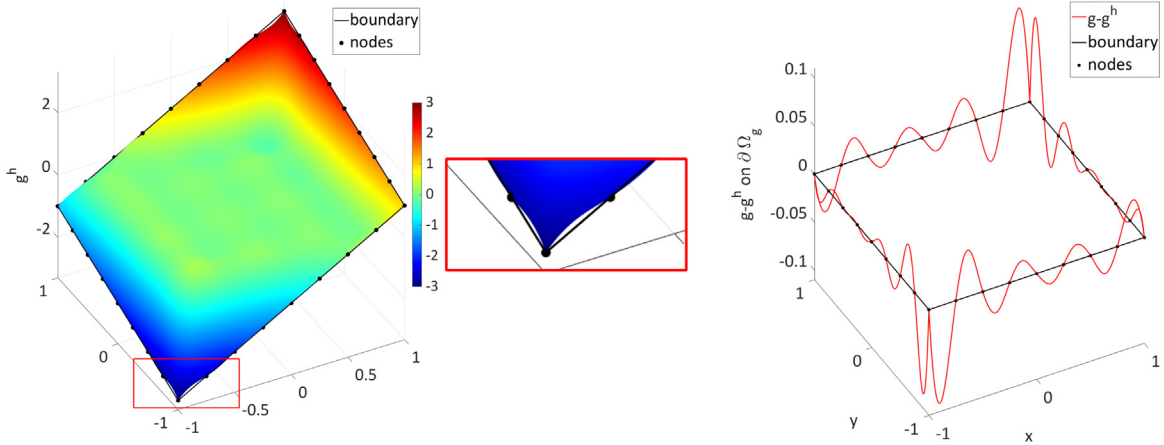


Fig. 3. Approximation  $g^h(\mathbf{x})$  in meshfree methods using the transformation method.

### 2.3.3. Error assessment of inconsistencies

As a point of departure in considering the error induced by these inconsistencies, we first examine the weighted residual formulation, which is more a more general way to arrive at a weak formulation than a potential. The latter point of view will be revisited.

Integrating the product of an arbitrary weight function  $v$  and the residual of (8a) over  $\Omega$  we have:

$$(v, \nabla^2 u + s)_\Omega = 0. \tag{18}$$

Integrating (18) by parts and employing divergence theorem one obtains

$$a(v, u)_\Omega = (v, s)_\Omega + (v, \mathbf{n} \cdot \nabla u)_{\partial\Omega}. \tag{19}$$

Per the usual procedures, employing (8b),  $v = 0$  on  $\partial\Omega_g$ , and the boundary decomposition, we have the weak form (W) in (9) which asks to find  $u \in H_g^1$  such that for all  $v \in H_0^1$  the following equation holds:

$$a(v, u)_\Omega = (v, s)_\Omega + (v, t)_{\partial\Omega_t}.$$

Provided  $u$  is sufficiently smooth, the above equation can be integrated by parts to obtain

$$(v, \nabla^2 u + s) + (v, t - \nabla u \cdot \mathbf{n})_{\partial\Omega_t} - (v, \nabla u \cdot \mathbf{n})_{\partial\Omega_g} = 0 \tag{20}$$

where

$$(v, \nabla u \cdot \mathbf{n})_{\partial\Omega_g} = \int_{\partial\Omega_g} v \nabla u \cdot \mathbf{n} \, d\Gamma. \tag{21}$$

Employing the fact that  $v = 0$  on  $\partial\Omega_g$ ,  $u = g$  on  $\partial\Omega_g$ , and the arbitrary nature of  $v$  one obtains the strong form (8), that is we have the following equivalence

$$(W) \Leftrightarrow (S)$$

However, in meshfree methods it is difficult to achieve  $v^h = 0$  on  $\partial\Omega_g$  in the Galerkin discretization as discussed previously. And, in fact, as shown in [17], the transformation method is actually consistent with a weak formulation that only attests to strong enforcement of essential boundary conditions at nodal locations, rather than the entire essential boundary in the true strong form.

Either way, to demonstrate one significant consequence of employing (9), consider the following relation found by using Green's first identity and the conditions in (8):

$$\begin{aligned} a(v^h, u)_\Omega &= -(v^h, \nabla^2 u)_\Omega + (v^h, \mathbf{n} \cdot \nabla u)_{\partial\Omega} \\ &= (v^h, s)_\Omega + (v^h, t)_{\partial\Omega_t} + (v^h, \mathbf{n} \cdot \nabla u)_{\partial\Omega_g}. \end{aligned} \tag{22}$$

Subtracting (22) from (9) gives

$$a(v^h, u^h - u)_\Omega = (v^h, \mathbf{n} \cdot \nabla u^h)_{\partial\Omega_g} \tag{23}$$

which is the relation given in [27], and demonstrates that if  $v^h \neq 0$  on  $\partial\Omega_g$  Galerkin orthogonality is lost. It can be easily shown that using this relation, the best approximation property no longer holds, i.e., the minimum error in the norm induced by  $a(\cdot, \cdot)$  is not obtained for the Galerkin solution. One immediate consequence is that the patch test will fail.

Now, as discussed in [27], the left hand side is bounded by  $a(u^h - u, u^h - u)_\Omega^{1/2}$ . Since the discrepancy on the boundary induced by the inadmissibility of test functions has been numerically observed as  $\mathcal{O}(h)$ , one should expect  $\mathcal{O}(h)$  error in the energy norm of the problem, independent of the order of approximation. This will be confirmed numerically in the next Subsection.

**Remark 1.** To further elucidate the failure of the patch test, consider the viewpoint of variational consistency presented in [28]. Starting from (9), and following [28], it can be shown using (8) and (4), that the requirements for obtaining an exact solution  $u^{[p]}$  of order  $p$  using the traditional weak formulation is

$$a\langle v^h, u^{[p]} \rangle_\Omega = -\langle v^h, \nabla^2 u^{[p]} \rangle_\Omega + \langle v^h, \mathbf{n} \cdot \nabla u^{[p]} \rangle_{\partial\Omega_t} \tag{24}$$

where  $a\langle \cdot, \cdot \rangle$ ,  $\langle \cdot, \cdot \rangle_\Omega$ , and  $\langle \cdot, \cdot \rangle_{\partial\Omega_t}$  denote the quadrature versions of  $a(\cdot, \cdot)$ ,  $(\cdot, \cdot)_\Omega$ , and  $(\cdot, \cdot)_{\partial\Omega_t}$ , respectively. However, using integration by parts, with sufficiently high order (e.g. machine precision) quadrature it is obvious that

$$a\langle v^h, u^{[p]} \rangle_\Omega \approx -\langle v^h, \nabla^2 u^{[p]} \rangle_\Omega + \langle v^h, \mathbf{n} \cdot \nabla u^{[p]} \rangle_{\partial\Omega} \neq -\langle v^h, \nabla^2 u^{[p]} \rangle_\Omega + \langle v^h, \mathbf{n} \cdot \nabla u^{[p]} \rangle_{\partial\Omega_t} \approx -\langle v^h, \nabla^2 u^{[p]} \rangle_\Omega + \langle v^h, \mathbf{n} \cdot \nabla u^{[p]} \rangle_{\partial\Omega_t} \tag{25}$$

and a patch test will fail unless  $v^h = 0$  on  $\partial\Omega_g$ . That is, no matter how high order the quadrature (or even with exact integration), one will not be able to pass the patch test. In addition, even if variationally consistent integration (VCI) is employed (which was developed to pass the patch test), one will still not be able to pass the patch test with strong-type essential boundary condition enforcement (unless  $v^h = 0$  on  $\partial\Omega_g$ ), since VCI-based methods are based on consistent weak forms (Nitsche’s method, Lagrange multiplier, etc., see [28] for details) and one obtains:

$$a\langle v^h, u^{[p]} \rangle_\Omega = -\langle v^h, \nabla^2 u^{[p]} \rangle_\Omega + \langle v^h, \mathbf{n} \cdot \nabla u^{[p]} \rangle_{\partial\Omega} \neq -\langle v^h, \nabla^2 u^{[p]} \rangle_\Omega + \langle v^h, \mathbf{n} \cdot \nabla u^{[p]} \rangle_{\partial\Omega_t} \tag{26}$$

where  $\langle \cdot, \cdot \rangle_{\partial\Omega}$  denotes the quadrature version of  $(\cdot, \cdot)_{\partial\Omega}$ . That is, these methods are incompatible with the inconsistent (traditional) weak form. On the other hand, as will be seen later in the text, the consistent weak forms proposed in Section 3 are in fact compatible with VCI methods.

### 2.3.4. Numerical assessment of the order of errors in boundary value problems

To examine the effect of these inconsistencies on the numerical solution to PDEs, and verify the assertions made in the previous section, a few patch tests are first performed, with the solution obtained using the transformation method.

Consider the Poisson problem (8) on the domain  $\bar{\Omega} = [-1, 1] \times [-1, 1]$  with the pure essential boundary condition  $\partial\Omega_g = \partial\Omega$ . First, let the prescribed body force and boundary conditions be consistent with the linear solution  $u = 0.1x + 0.3y$ :

$$u = 0.1x + 0.3y \quad \text{on } \partial\Omega_g, \tag{27a}$$

$$s = 0 \quad \text{in } \Omega. \tag{27b}$$

Since the patch test in meshfree methods is intimately related with quadrature [28], the effect of the order of quadrature is first considered. That is, according to conventional wisdom, a failure of the patch test in meshfree methods is generally attributed to the lack of quadrature accuracy in the weak formulation. However, as has been discussed, no matter the accuracy of quadrature employed, one will not be able to pass the patch test with the weak formulation in conjunction with a strong-type boundary method. In addition, as discussed in Remark 1, the VCI technique used to patch past tests will not succeed.

To demonstrate this, the patch test is first performed with varying orders of quadrature denoted  $NQ$ . Gauss cells with  $NQ \times NQ$  rules are employed that are coincident with the nodal spacing such that each cell is associated

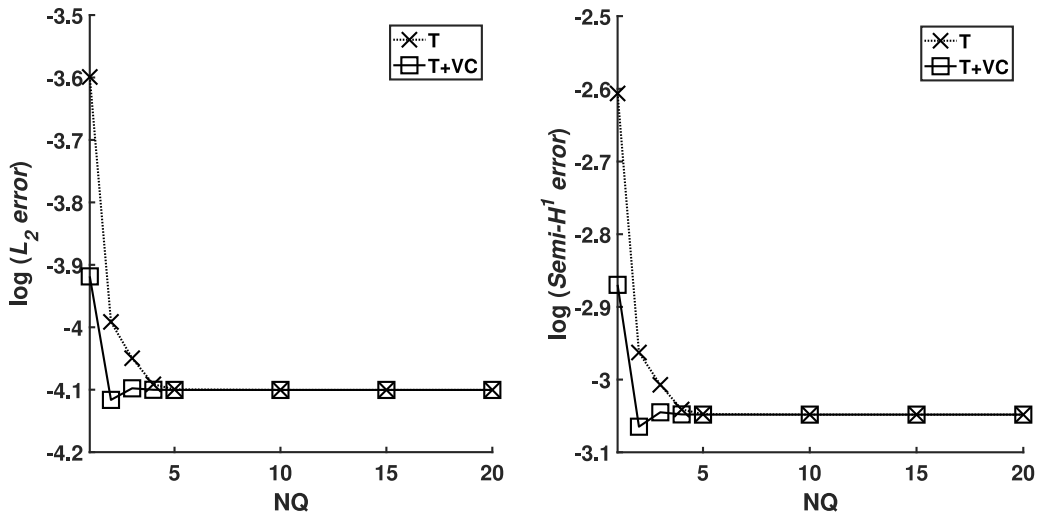


Fig. 4. Norms of error for the transformation method in a linear patch test in Poisson’s problem with respect to number of quadrature points “NQ”. “T” denotes transformation, “T+VC” denotes transformation using VCI.

with four nodes, with boundary Gauss points defined by the outer segments of cells intersecting  $\partial\Omega$  for integration of boundary terms. Cubic B-spline kernels are employed for the RK approximation, with normalized supports of  $p + 1$ . This integration scheme and choice of kernel functions will be employed throughout this manuscript unless otherwise stated.

Linear basis is used in the RK approximation so that the solution can be represented exactly. VCI is also employed to verify the relations stated in Remark 1. The domain is discretized uniformly with a nodal spacing of  $h = 1/5$ . As seen in Fig. 4, no matter the order of accuracy of quadrature, the patch test cannot be passed (error on the level of machine precision). Increasing the quadrature accuracy does not result in a better solution, and in fact, the solution error converges at  $NQ = 5$ . That is, increasing the order quadrature past this point has little effect on the solution. In addition, it can be seen that the VCI technique also does not pass the patch test with strong-type essential boundary condition enforcement.

As a result of this study,  $NQ = 5$  will be employed for the following patch test studies in this Subsection, and any remaining error should be due to other *variational crimes*: the only inconsistency present in the formulation then is the inability to satisfy the requirements on test and trial functions in the weak form [27].

Standard convergence of the solution (with respect to  $h$ ) is now tested, with the errors in the  $L_2(\Omega)$  norm and  $H^1(\Omega)$  semi-norm shown in Fig. 5. VCI is again employed to verify the relations stated in Remark 1. First, it can be seen that the patch tests are indeed not passed, which can be attributable to the errors in constructing the proper approximation spaces, since there are no other variational crimes committed (the quadrature error should be negligible according to Fig. 4). Also, with the addition of VCI, one is still not able to pass the patch test, and the error is generally unaffected.

Importantly, it is also seen that through refinement of the discretization (decreasing  $h$ ), the order of error induced by the inconsistency in the boundary conditions on the test and trial functions manifest as  $\mathcal{O}(h^2)$  and  $\mathcal{O}(h)$ , for the  $L_2(\Omega)$  norm and  $H^1(\Omega)$  semi-norm, respectively. That is, the errors reduce with refinement, at a rate consistent with employing linear basis. One may thus expect that these errors will have no influence on the convergence rates in the solution of PDEs with linear basis, but will have influence on solutions using higher order basis, which will be confirmed later.

Next, consider a quadratic patch test with quadratic basis with the same test of  $h$ -refinement. Here the following quadratic solution is considered:  $u = 0.1x + 0.3y + 0.8x^2 + 1.2xy + 0.6y^2$ . The following conditions result in this solution:

$$u = 0.1x + 0.3y + 0.8x^2 + 1.2xy + 0.6y^2 \quad \text{on } \partial\Omega_g, \tag{28a}$$

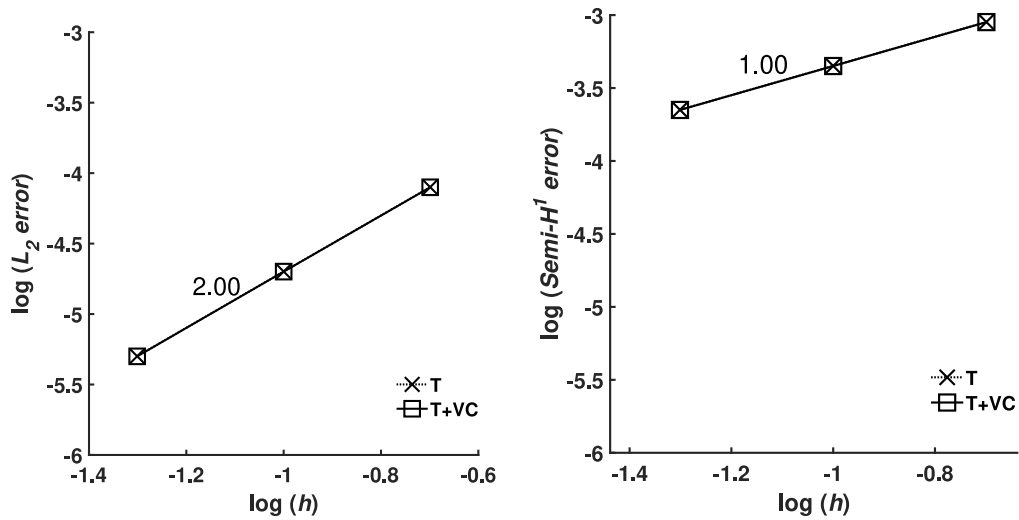


Fig. 5. Norms of error for the transformation method in a linear patch test in Poisson’s problem, rate of convergence indicated. “T” denotes transformation, “T+VC” denotes transformation using VCI.

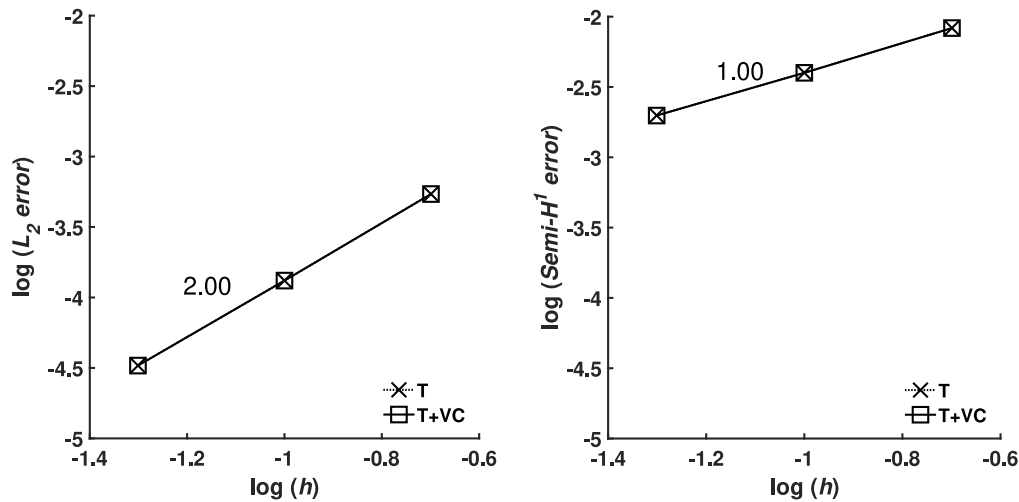


Fig. 6. Norms of error for the transformation method in a quadratic patch test in Poisson’s problem, rate of convergence indicated. “T” denotes transformation, “T+VC” denotes transformation using VCI.

$$s = -2.8 \quad \text{in } \Omega. \tag{28b}$$

The error in the  $L_2(\Omega)$  norm and  $H^1(\Omega)$  semi-norm are shown in Fig. 6. First, it can be seen that indeed no method can pass the patch test, even when VCI is employed. This is again attributable to the inconsistency of the weak formulation used in conjunction with the strong approach to boundary conditions.

It can also be seen that the inconsistent enforcement of boundary conditions results in errors  $\mathcal{O}(h^2)$  and  $\mathcal{O}(h)$  in the previously mentioned norms, respectively. That is, the errors again decrease at a rate consistent with “linear” accuracy, despite the fact that higher-order accurate basis functions are employed. One may then expect that these errors will limit the order of convergence in the solution of PDEs, which again, will be confirmed later.

To conclude, these results indicate that quadrature is not the only factor that influences the ability to pass the patch test, and in fact, using the strong-type enforcement of boundary conditions in conjunction with the conventional weak formulation precludes this. The failure of the patch test using VCI also indicates that the transformation method must be corrected in some way in order to use VCI effectively for these strong methods. Importantly, the inability

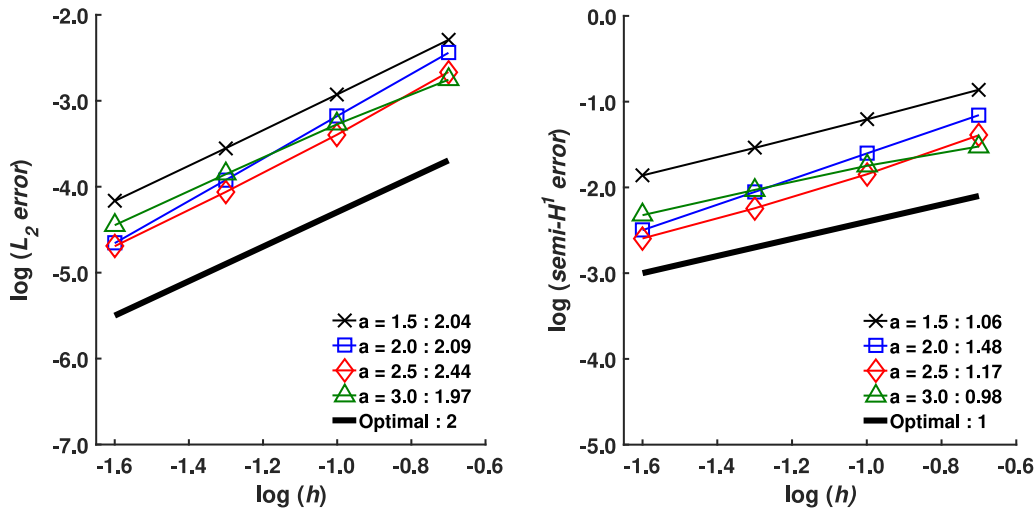


Fig. 7. Convergence of transformation method with linear basis with various kernel measures  $a$ : rates indicated in legend.

to construct proper approximation spaces also yields errors of linear order in the solution of PDEs, independent of the order of completeness employed.

To examine the possible, and now expected, effect on convergence rates, consider (8) with the source term and pure essential boundary  $\partial\Omega_g = \partial\Omega$  with domain  $\Omega = [0, 1] \times [0, 1]$ :

$$g(x, 0) = \sin(\pi x), \quad g(x, 1) = g(0, y) = g(1, y) = 0 \quad \text{on } \partial\Omega_g, \tag{29a}$$

$$s = 0 \quad \text{in } \Omega. \tag{29b}$$

The exact solution of this problem is high order [12]:

$$u = \{\cosh(\pi y) - \coth(\pi) \sinh(\pi y)\} \sin(\pi x). \tag{30}$$

Linear, quadratic, and cubic bases are employed with the transformation method, with uniform refinements of the domain. Various normalized support sizes (denoted “ $a$ ” in the Figure legends) are employed, to examine the effect of varying the measure of  $\Phi_a(x - x_I)$ , as it is well known that linear basis degenerates to linear finite elements as the normalized measure  $a$  approaches unity. Thus, larger values of  $a$  are expected to show more pronounced error due to boundary condition enforcement, since finite elements have little to no difficulty in constructing proper approximation spaces, or at least ones which do not induce significant solution errors. In these convergence tests,  $20 \times 20$  quadrature is employed to isolate the effects of the boundary condition enforcement completely (see Fig. 4).

Fig. 7 shows the convergence for linear basis in the  $L_2(\Omega)$  norm and  $H^1(\Omega)$  semi-norm; it can be seen that the optimal rates of two and one are essentially maintained, regardless of the kernel measure.

For quadratic basis, it can be seen in Fig. 8 that these same linear rates are also generally obtained, yet the optimal rates for quadratic basis should be three and two for the  $L_2(\Omega)$  norm and  $H^1(\Omega)$  semi-norm, respectively. Therefore optimal rates are not obtained in this case, and rather, the solution exhibits linear accuracy rather than quadratic.

For the case of cubic basis, shown in Fig. 9, it can again be seen that the rates obtained are far lower than expected; the linear rates of two and one are again obtained in most cases for the  $L_2(\Omega)$  norm and  $H^1(\Omega)$  semi-norm, respectively, when the optimal convergence rates associated with employing approximations with cubic completeness are four and three, respectively. Again, the solution exhibits linear accuracy, rather than cubic.

Higher order bases were also tested but are not shown here for conciseness of presenting the present study. The transformation method also provided only linear solution accuracy.

To conclude, the numerical results in this section indicate that the error due to the inability to satisfy the requirements of the conventional weak form (9) is characterized as  $\mathcal{O}(h^2)$  error in the  $L_2(\Omega)$  norm and  $\mathcal{O}(h)$  error in the  $H^1(\Omega)$  semi-norm, limiting the rate of convergence for bases higher than linear.

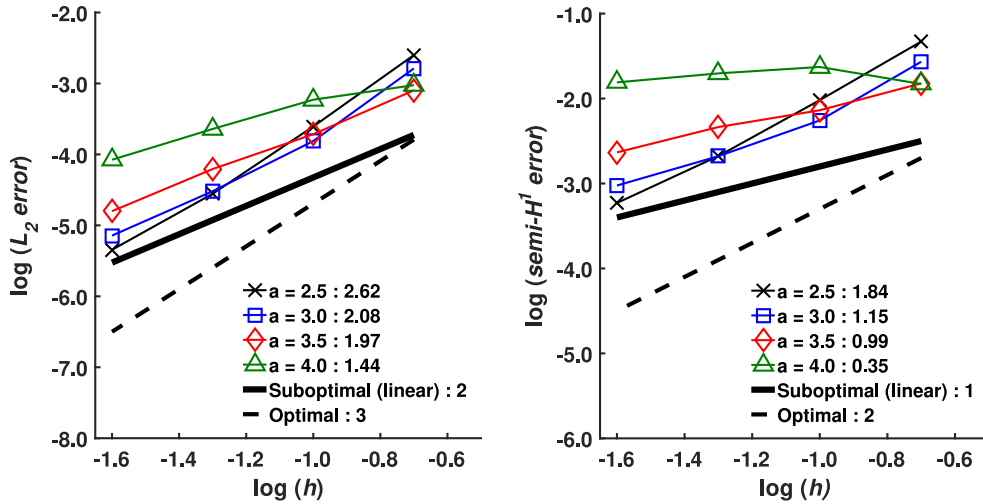


Fig. 8. Convergence of transformation method with quadratic basis with various kernel measures  $a$ : rates indicated in legend.

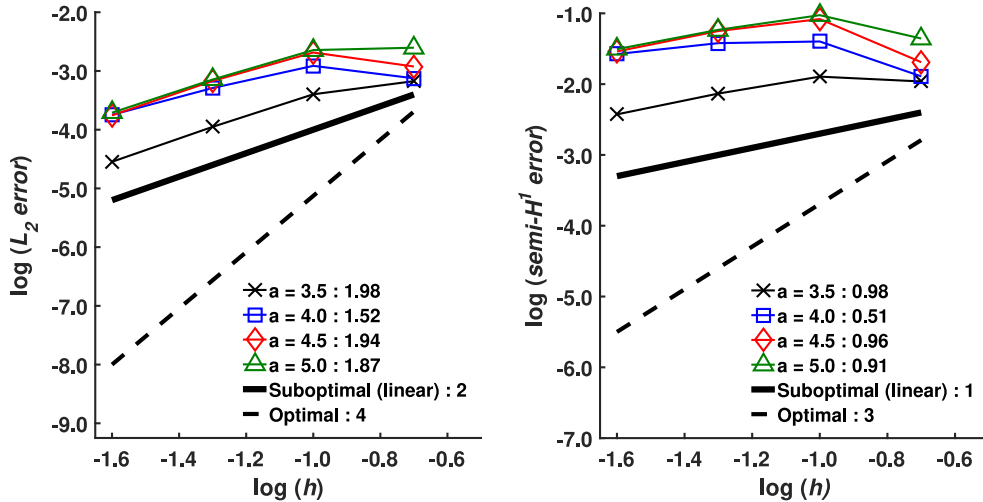


Fig. 9. Convergence of transformation method with cubic basis with various kernel measures  $a$ : rates indicated in legend.

It seems that through the popular choice of linear basis in meshfree approximations over the past two decades, this observation has somehow been overlooked, or hardly reported in the literature. To the best of the authors' knowledge, only [21] reports results with quadratic basis and strong enforcement of boundary conditions (using the RK approximation with interpolation property), where the same trend was observed.

### 3. Consistent weak forms for meshfree methods

#### 3.1. Consistent weak form I: A consistent weak formulation for inadmissible test functions

A consistent weak formulation for test functions inadmissible in the conventional weak form can be derived by considering the possibility of  $v^h \neq 0$  on  $\partial\Omega_g$  in between nodes. First, consider the weighted residual of (8), as before:

$$(v, \nabla^2 u + s)_{\Omega} = 0.$$

Integrating by parts and employing divergence theorem one obtains

$$a(v, u)_\Omega = (v, s)_\Omega + (v, \mathbf{n} \cdot \nabla u)_{\partial\Omega}.$$

Now, by employing (8b) and allowing  $v \neq 0$  on  $\partial\Omega_g$ , a consistent weak form which we denote ( $\mathbb{W}_C^1$ ) is arrived at, which asks to find  $u \in H_g^1$ , such that for all  $v \in H^1$ , the following equation holds:

$$a(v, u)_\Omega - (v, \mathbf{n} \cdot \nabla u)_{\partial\Omega_g} = (v, s)_\Omega + (v, t)_{\partial\Omega_t} \tag{31}$$

where the requirement on  $v \in H_0^1$  has been relaxed to simply  $v \in H^1$  where  $H^1 = H^1(\Omega)$ , which allows the employment of (15) for the test function without committing a variational crime.

It is important to note, that when (31) is integrated by parts, it is straightforward to show the weak form (31) attests to (8), and the equivalence of the weak form and the strong form is verified, that is,  $\mathbb{W}_C^1 \Leftrightarrow \mathbb{S}$ :

$$(v, \nabla^2 u + s) + (v, h - \nabla u \cdot \mathbf{n})_{\partial\Omega_t}. \tag{32}$$

Since  $v$  in the above is arbitrary and  $u \in H_g^1$ , the strong form (8) is recovered.

The corresponding Galerkin approximation seeks  $u^h \in \mathcal{S}_g$ ,  $\mathcal{S}_g \subset H_g^1$  such that for all  $v^h \in \mathcal{S}$ ,  $\mathcal{S} \subset H^1$  the following holds

$$a(v^h, u^h)_\Omega - (v^h, \mathbf{n} \cdot \nabla u^h)_{\partial\Omega_g} = (v^h, s)_\Omega + (v^h, t)_{\partial\Omega_t} \tag{33}$$

where  $v^h$  is constructed from (15) and  $u^h$  is constructed from (16).

In this formulation, we have relaxed the condition on the test function, but still attempt to construct approximation spaces that satisfy the usual conditions. That is, the present weak formulation ( $\mathbb{W}_C^1$ ) can be considered a consistent way to employ the condition  $v^h = 0$  on  $\partial\Omega_g$  strongly at nodes.

So far, the inconsistency in the construction of the trial function is neglected, yet in the numerical examples in Section 5 it is shown that this has little consequence on the solution accuracy. The reason for this is discussed in the Remark below.

**Remark 2.** Subtracting (22) from (33) gives

$$a(v^h, u^h - u)_\Omega = (v^h, \mathbf{n} \cdot \nabla(u^h - u))_{\partial\Omega_g} \tag{34}$$

and a type of Galerkin orthogonality is restored (compare to (23)). If one recalls that the left hand side is bounded by  $a(u^h - u, u^h - u)_\Omega^{1/2}$ , this indicates that the limiting term on the boundary in (23) will be released and proper convergence rates associated with the approximation space should be achieved. To emphasize, the additional term in (31) corrects for a non-zero test function on  $\partial\Omega_g$ , and appears to be the most important correction to the strong-type methods since it eliminates the  $\mathcal{O}(h)$  term that limits the rate of convergence. The possibility that  $u \neq g$  on  $\partial\Omega_g$  does not seem to be as problematic, since it does not show up in (23).

**Remark 3.** The consistent weighted residual procedure generalizes easily to various boundary value problems (see the Appendix).

### 3.2. Consistent weak form II: A consistent weak formulation for inadmissible test and trial functions with symmetry

The employment of (31) yields a non-symmetric stiffness matrix which is often undesirable. In addition, unless trial functions can satisfy the essential boundary conditions exactly, we do not have  $\mathbb{W}_C^1 \Leftrightarrow \mathbb{S}$ , and strictly speaking  $\mathbb{W}_C^1$  is still not consistent with a meshfree discretization (although as discussed previously, this may not be as problematic).

To address these two issues, consider a more general form of the weighted residual formulation with weights  $v_\Omega$  on  $\Omega$  and  $v_g$  on  $\partial\Omega_g$ :

$$(v_\Omega, \nabla^2 u + s)_\Omega + (v_g, u - g)_{\partial\Omega_g} = 0. \tag{35}$$

Various weights can be chosen, however the choice of  $v_\Omega = v$  and  $v_g = \mathbf{n} \cdot \nabla v$  yields a symmetric weak form which will be shown as follows. Further impetus is provided by the fact that a flux term  $\mathbf{n} \cdot \nabla u$  is the “work-conjugate”

to  $u$  in terms of the potential associated with (8) and yields consistent “units” of the problem at hand. With this choice, (35) is expressed as

$$(v, \nabla^2 u + s)_\Omega + (\mathbf{n} \cdot \nabla v, u - g)_{\partial\Omega_g} = 0. \tag{36}$$

Integrating (36) by parts and employing the natural boundary condition (8b), one obtains a symmetric weak form that we denote  $(\mathbb{W}_C^2)$ , which asks to find  $u \in H^1$  such that for all  $v \in H^1$ , the following equation holds

$$a(v, u)_\Omega - (v, \mathbf{n} \cdot \nabla u)_{\partial\Omega_g} - (\mathbf{n} \cdot \nabla v, u)_{\partial\Omega_g} = (v, s)_\Omega + (v, t)_{\partial\Omega_t} - (\mathbf{n} \cdot \nabla v, g)_{\partial\Omega_g}. \tag{37}$$

The above allows the complete relaxations of simply requiring  $v \in H^1$  and  $u \in H^1$ , and now both (15) and (16) can be employed without committing a variational crime.

Applying integration by parts to  $a(\cdot, \cdot)$  in (37) yields:

$$(v, \nabla^2 u + s)_{\partial\Omega} + (v, \mathbf{n} \cdot \nabla u - t)_{\partial\Omega_t} + (v, u - g)_{\partial\Omega_g} = 0 \tag{38}$$

where it is immediately apparent that the strong form of the problem can be recovered, hence  $(\mathbb{W}_C^2) \Leftrightarrow (\mathbb{S})$ .

The weak form  $(\mathbb{W}_C^2)$  is the same one identified in Ref. [15], and can be also derived from a variational viewpoint. Here, the key difference between this work and that in [15], is that the weak form is employed with (15) and (16) as to rectify the deficiencies of the standard use of these approximations. We also note that employing (37) alone does not guarantee stability [16].

The corresponding Galerkin approximation seeks  $u^h \in \mathcal{S}$  such that for all  $v^h \in \mathcal{S}$ ,  $\mathcal{S} \subset H^1$  the following holds

$$a(v^h, u^h)_\Omega - (v^h, \mathbf{n} \cdot \nabla u^h)_{\partial\Omega_g} - (\mathbf{n} \cdot \nabla v^h, u^h)_{\partial\Omega_g} = (v^h, s)_\Omega + (v^h, t)_{\partial\Omega_t} - (\mathbf{n} \cdot \nabla v^h, g)_{\partial\Omega_g} \tag{39}$$

where  $v^h$  is again constructed from (15) and  $u^h$  is constructed from (16). It is easy to see that when a Bubnov–Galerkin approximation is employed, (39) leads to a symmetric system matrix.

With the complete relaxation on test and trial functions, this weak formulation  $(\mathbb{W}_C^2)$  can be considered a consistent way to employ both the conditions  $v^h = 0$  on  $\partial\Omega_g$  and  $u^h = g$  on  $\partial\Omega_g$  strongly at nodes.

**Remark 4.** Rather than satisfying Galerkin orthogonality, by employing (22), the Galerkin discretization of the consistent weak form  $(\mathbb{W}_C^2)$  satisfies the following:

$$a(v^h, u^h - u)_\Omega = (\mathbf{n} \cdot \nabla v^h, u^h - g)_{\partial\Omega_g} + (v^h, \mathbf{n} \cdot \nabla(u^h - g))_{\partial\Omega_g}. \tag{40}$$

Note that if  $u^h = g$  on  $\partial\Omega_g$ , then the standard orthogonality relation is recovered.

**Remark 5.** The relation (40) leads to the insight that a Galerkin discretization of  $(\mathbb{W}_C^2)$  minimizes the error in the norm induced by  $a(\cdot, \cdot)$  augmented by the “work” of the error on the essential boundary:

$$\Pi_{(\mathbb{W}_C^2)}(u^h) = \frac{1}{2} a(u^h - u, u^h - u)_\Omega - (u^h - u, \mathbf{n} \cdot \nabla(u^h - u))_{\partial\Omega_g}. \tag{41}$$

That is,  $(\mathbb{W}_C^2)$  can be obtained by minimization of the above potential with respect to  $u^h$ . This illuminates the possibility of balancing errors on the domain and boundary, following [29], although the numerical examples in Section 5 indicate that this is likely not necessary since optimal rates are obtained—that is, with (41), the order of errors due to the imposition of conditions on the domain and boundary may already be balanced. It should also be noted that an immediate consequence of this property is this proposed weak form also restores the ability to pass the patch test in strong-type essential boundary condition methods.

**Remark 6.** The potential associated with (39) can also be stated in a more conventional manner:

$$\Pi_{(\mathbb{W}_C^2)}(u^h) = \frac{1}{2} a(u^h, u^h)_\Omega - (u^h, s)_\Omega - (u^h, t)_{\partial\Omega_t} - (u^h - g, \mathbf{n} \cdot \nabla u^h)_{\partial\Omega_g} \tag{42}$$

where it can be seen that the last term accounts for the work done by the error on the essential boundary. Thus, considering the possibility of error on the boundary is yet another way to arrive at a consistent weak form. The other, is to minimize the error in both the domain and boundary, in terms of appropriate work-conjugates, as in (41).

**Remark 7.** This weak form can also be generalized to other boundary value problems, for a discussion, refer to the [Appendix](#).

**Remark 8.** The employment of  $(\mathbb{W}_C^2)$  or  $(\mathbb{W}_C^1)$  is consistent with the variationally consistent framework proposed in [28], which requires the weak form attest to the strong form. In contrast, the strong-type of boundary condition enforcement does not. As a result a VCI method employing either of the consistent weak formulations can pass the patch test. To demonstrate this, starting from (31) or (37), and following [28], it can be shown using (8) and (4), that the requirements for obtaining an exact solution  $u^{[p]}$  of order  $p$  using a *consistent* weak formulation are the same as given in [28]:

$$a\langle v^h, u^{[p]} \rangle_\Omega = -\langle v^h, \nabla^2 u^{[p]} \rangle_\Omega + \langle v^h, \mathbf{n} \cdot \nabla u^{[p]} \rangle_{\partial\Omega}. \tag{43}$$

Now, using integration by parts, with sufficiently high order (e.g. machine precision) quadrature one obtains:

$$a\langle v^h, u^{[p]} \rangle_\Omega \approx a(v^h, u^{[p]})_\Omega = -(v^h, \nabla^2 u^{[p]})_\Omega + (v^h, \mathbf{n} \cdot \nabla u^{[p]})_{\partial\Omega} \approx -\langle v^h, \nabla^2 u^{[p]} \rangle_\Omega + \langle v^h, \mathbf{n} \cdot \nabla u^{[p]} \rangle_{\partial\Omega} \tag{44}$$

and the pass test will be passed with higher order quadrature even if  $v^h \neq 0$  on  $\partial\Omega_g$  (compare to (25)). In addition, since VCI methods inherently satisfy the requirements in (43), the patch tests can be passed using (31) or (37) with any order of quadrature. This is also applicable to other variationally consistent methods such as the popular stabilized conforming nodal integration [30], or the quadratically-consistent method [31].

In summary, two weak forms have been developed, which are consistent with the inability of an approximation to meet the requirements of the conventional weak form. The first considers the fact that the weight function is possibly non-zero on the essential boundary, but that the essential boundary conditions still hold strongly. This results in a non-symmetric stiffness matrix, but is more consistent with meshfree approximations. This weak form attests to the strong form, and is shown to restore a type of Galerkin orthogonality. The second weak form relaxes the requirements on both the test and trial functions, and they only need to be constructed to possess square-integrable derivatives. The particular form taken here results in a symmetric system, at least for the model problem at hand (see the [Appendix](#) for a brief discussion). This weak form attests to the strong form, and is shown to satisfy a different orthogonality relation, which illuminates that it minimizes the error in the domain in terms of the energy norm, as well as the error on the boundary in terms of the field variable and its corresponding “flux” (or work-conjugate) term.

#### 4. Numerical procedures

In this section, the matrix forms for the consistent weak forms are given and boundary condition enforcement procedures are discussed. As a starting point, let us first define terms common to the weak formulations discussed: let  $\mathbf{d}$  denote a column vector of  $\{u_I\}_{I \in \eta}$ ,  $\Psi_I$  and  $\mathbf{B}_I$  denote the  $I$ th shape function and the column vector of its derivatives respectively, and let  $\mathbf{n}$  represent the unit normal to  $\partial\Omega_g$  in column vector form. In two dimensions this yields:

$$\mathbf{d} = \begin{bmatrix} d_1 \\ d_2 \\ \vdots \\ d_{N_p} \end{bmatrix}, \quad \mathbf{B}_I = \begin{bmatrix} \Psi_{I,1} \\ \Psi_{I,2} \end{bmatrix}, \quad \mathbf{n} = \begin{bmatrix} n_1 \\ n_2 \end{bmatrix}. \tag{45}$$

The following final system of matrix equations is also common to all formulations:

$$\mathbf{K}\mathbf{d} = \mathbf{f} \tag{46}$$

where the system size is  $N_p \times N_p$ . The above system is left statically uncondensed purposefully, as special procedures are needed to apply boundary conditions in meshfree methods. These techniques are discussed in Section 4.4.

##### 4.1. Conventional weak formulation

Under the conventional weak formulation (9), the scalar entries of  $\mathbf{K}$  and  $\mathbf{f}$  in (46) are computed as

$$K_{IJ} = \int_\Omega \mathbf{B}_I^T(\mathbf{x})\mathbf{B}_J(\mathbf{x}) \, d\Omega, \tag{47a}$$

$$f_I = \int_{\Omega} \Psi_I(\mathbf{x})s \, d\Omega + \int_{\partial\Omega_t} \Psi_I(\mathbf{x})t \, d\Gamma. \quad (47b)$$

#### 4.2. Consistent weak form I (CFW I)

For the Consistent weak form I (33), the scalar entries of  $\mathbf{K}$  and  $\mathbf{f}$  in (46) are computed as

$$K_{IJ} = \int_{\Omega} \mathbf{B}_I^T(\mathbf{x})\mathbf{B}_J(\mathbf{x}) \, d\Omega - \int_{\partial\Omega_g} \Psi_I(\mathbf{x})\mathbf{n}^T \mathbf{B}_J(\mathbf{x}) \, d\Gamma, \quad (48a)$$

$$f_I = \int_{\Omega} \Psi_I(\mathbf{x})s \, d\Omega + \int_{\partial\Omega_t} \Psi_I(\mathbf{x})t \, d\Gamma. \quad (48b)$$

Comparing (48) to (47), it can be seen that only one new term is added to the stiffness matrix of the system. Later, it will be seen that the addition of this *one term* results in a drastic increase in solution accuracy and is able to restore optimal convergence rates. Indeed, the main problem with the inability to construct proper subspaces in the conventional weak formulation is due to the term in (23), which this weak form corrects for.

#### 4.3. Consistent weak form II (CFW II)

For the discretization of consistent weak form II (39), the scalar entries of  $\mathbf{K}$  and  $\mathbf{f}$  in (46) are computed as

$$K_{IJ} = \int_{\Omega} \mathbf{B}_I^T(\mathbf{x})\mathbf{B}_J(\mathbf{x}) \, d\Omega - \int_{\partial\Omega_g} \mathbf{B}_I^T(\mathbf{x})\mathbf{n} \Psi_J(\mathbf{x}) \, d\Gamma - \int_{\partial\Omega_g} \Psi_I(\mathbf{x})\mathbf{n}^T \mathbf{B}_J(\mathbf{x}) \, d\Gamma, \quad (49a)$$

$$f_I = \int_{\Omega} \Psi_I(\mathbf{x})s \, d\Omega + \int_{\partial\Omega_t} \Psi_I(\mathbf{x})t \, d\Gamma - \int_{\partial\Omega_g} \mathbf{B}_I^T(\mathbf{x})\mathbf{n}g \, d\Gamma. \quad (49b)$$

In the above, it can be seen that compared to (47), both the stiffness matrix and the force vector contain new terms. For the stiffness matrix, the two additional terms are the transpose of each other, so that only one of these matrices needs to be constructed for the analysis (or just the upper triangle of the entire system matrix). In addition, since the original stiffness matrix is symmetric, the resulting system matrix will also be symmetric, and efficient solvers can be employed with this method.

#### 4.4. Enforcement of boundary conditions

Procedurally, due to the nature of the approximations involved, it is uncommon to employ the formal definitions of test and trial approximations in (15) and (16) directly in the weak form for meshfree methods. Rather, the full systems are formed with the RK approximation defined over all nodes (1) leading to (46), and boundary conditions are applied after. That is to say, the system in (46) represents a statically uncondensed system and cannot be solved directly.

Instead, two favorable possibilities to enforce boundary conditions on the uncondensed systems are recommended here: (1) meshfree transformation procedures can be applied—the reader is referred to [17] for more details, where a simple and convenient row-swap implementation of the transformation method is presented; or (2) straightforward static condensation with direct enforcement of boundary conditions is possible (equivalent of course to using (15) and (16) directly in the weak form), provided either singular kernels [17] or shape functions with interpolation property [21] are introduced for nodes that lie on the essential boundary.

## 5. Numerical examples

For the following examples, the parameters of the RK approximation and the numerical integration method have been discussed in Section 2.3.4 in detail, but are briefly recalled here: twenty-by-twenty Gaussian integration per background cell is employed with cells aligned with uniformly distributed nodes. Cubic B-spline kernels are used in the RK approximation, with varying nodal spacing denoted  $h$ , kernel measures normalized with respect to  $h$  denoted  $a$ , and order of bases denoted  $p$ .

Three main methods are compared in terms of the transformation method [17]:

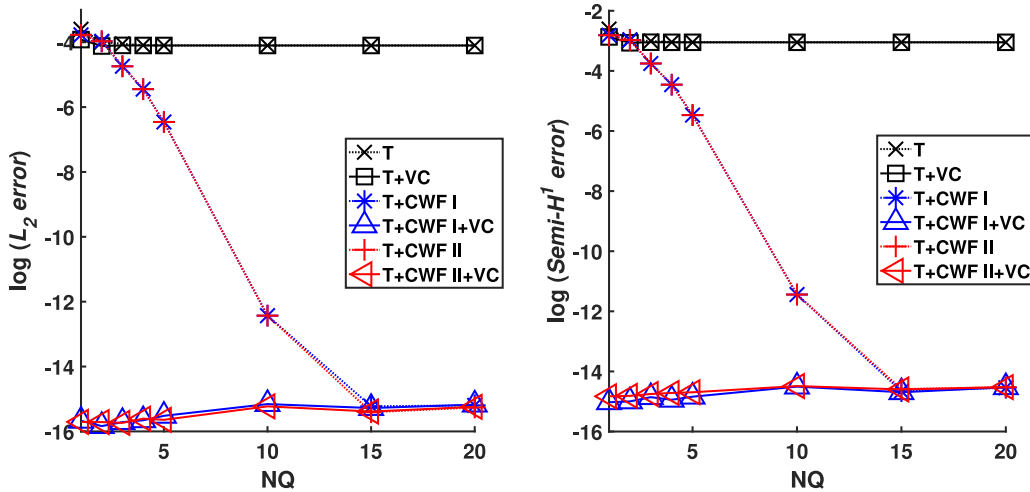


Fig. 10. Norms of error for various methods in the linear patch test. “+VC” denotes methods using VCI.

- The transformation method (denoted as T)
- The transformation method with consistent weak form I (denoted as T+CWF I)
- The transformation method with consistent weak form II (denoted as T+CWF II)

Later, the boundary singular kernel method [17] is employed to complete the study to demonstrate the method works with other types of strong enforcement, with permutations denoted following the same convention:

- The boundary singular kernel method (denoted as B)
- The boundary singular kernel method with consistent weak form I (denoted as B+CWF I)
- The boundary singular kernel method with consistent weak form II (denoted as B+CWF II)

The error in the  $L_2(\Omega)$  norm and the  $H^1(\Omega)$  semi-norm are assessed, computed using the same quadrature rules as forming the system matrices.

### 5.1. Patch test for the 2D Poisson equation

Consider the Poisson problem (8) on the domain  $\bar{\Omega} = [-1, 1] \times [-1, 1]$  with the pure essential boundary condition  $\partial\Omega_g = \partial\Omega$ . Let the prescribed body force and boundary conditions be consistent with an exact linear solution  $u = 0.1x + 0.3y$  (see (27) for the conditions).

The quadrature study in Section 2.3.4 is carried out, now with all three weak forms, to examine the effect of quadrature and use of T, T+CWF I, and T+CWF II, and VCI on the solution error in the patch test: an increasing number of quadrature points  $NQ$  is employed with these methods as before.

The error in the  $L_2(\Omega)$  and  $H^1(\Omega)$  semi-norm for the three versions of the transformation method are shown in Fig. 10. First, it is seen that both the proposed T+CWF I and T+CWF II are able to pass the linear patch test (with machine precision error) with sufficient quadrature. Again, the transformation method fails to pass the patch test no matter how high the order of quadrature employed.

The ability to pass the patch test by both T+CWF I and T+CWF II, and failure to pass the patch test by the transformation method alone, is consistent with the orthogonality relations (23), (34), and (40), where the resulting projection properties, or lack thereof, indicate which methods should or should not pass the patch tests. Thus the results of the patch tests are consistent with the discussions in Sections 2 and 3.

It is also seen that the variationally consistent integration technique can now pass the patch tests with any order of quadrature, provided a consistent weak form is employed (CWF I or CWF II), which is also in agreement with the discussions in Sections 2 and 3. Thus, in order to effectively use VCI to enhance solution accuracy in strong-type essential boundary condition enforcement, one must use one of the proposed consistent weak forms.

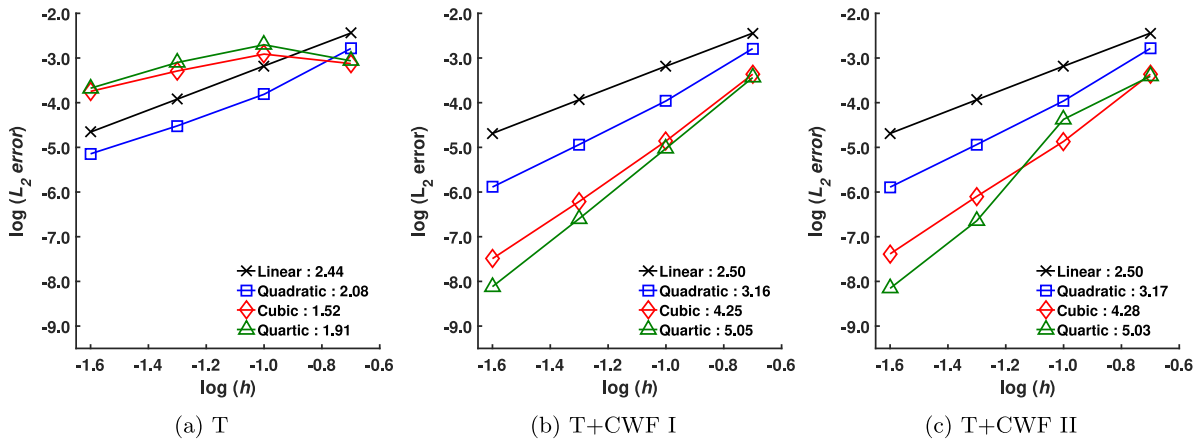


Fig. 11. Convergence with various bases in the  $L_2$  norm: rates indicated in legend.

5.2. Poisson equation with high-order solution

Now consider the Poisson problem (8), on  $\bar{\Omega} = [0, 1] \times [0, 1]$ , with source term and the pure essential boundary condition as the same as (29):

$$g(x, 0) = \sin(\pi x), \quad g(x, 1) = g(0, y) = g(1, y) = 0 \quad \text{on } \partial\Omega_g,$$

$$s = 0 \quad \text{in } \Omega.$$

The exact solution of this problem is high order:

$$u = \{\cosh(\pi y) - \coth(\pi) \sinh(\pi y)\} \sin(\pi x).$$

In this study, the effect of the three weak forms is examined in terms of convergence rates with respect to varying the support sizes  $a$ , order of basis functions  $p$ , and nodal spacing  $h$ .  $20 \times 20$  quadrature is employed in all of the following studies in order to put aside the issue of quadrature.

5.2.1.  $p$ -refinement and  $h$ -refinement

First consider linear, quadratic, cubic, and quartic bases (denoted with  $p = 1$ ,  $p = 2$ ,  $p = 3$ , and  $p = 4$ , respectively), with normalized support sizes of  $a = p + 1$ .  $h$ -refinement is performed for each of the basis, starting with an  $11 \times 11$  uniform node distribution. The solution errors in the  $L_2(\Omega)$  norm and  $H^1(\Omega)$  semi-norm of the various bases are plotted in Figs. 11–12, showing that T+CWF I and T+CWF II can yield optimal convergence rates ( $p + 1$  in  $L_2$  and  $p$  in semi- $H^1$ ), while the traditional weak form (T) only yields linear rates (2 in  $L_2$  and 1 in semi- $H^1$ ), regardless of the order of basis. Therefore the present approach can yield  $h$ -refinement with  $p$ th order optimal rates of convergence.

In addition, it can be seen in Figs. 11b 11c, 12b, and 12c, that by increasing  $p$ , for any given  $h$  (with the exception of one case), more accuracy can be obtained, yielding the ability to also provide  $p$ -refinement. These two features of the present approach are in stark contrast to the results in Figs. 11a and 12a, where increasing  $p$  does not give consistently more accurate results, and in fact moving from  $p = 1$  to  $p = 2$  provides only marginal improvement in accuracy, while increasing  $p$  from two to three and three to four actually provides worse results. Comparing to Tables 1, 2, and 3, it can be inferred that this is due to the additional error in the representation of boundary conditions in the test and trial functions, decreasing from  $p = 1$  to  $p = 2$ , and increasing from  $p = 2$  to  $p = 3$ .

Finally, it can be noted that both T+CWF I and T+CWF II can provide  $p$ -refinement and  $h$ -refinement with  $p$ th order optimal rates with nearly the same levels of error, and one may select either based on need or preference (T+CWF I has only one new term, but yields a non-symmetric system, while T+CWF II yields a symmetric system, but has three additional terms).

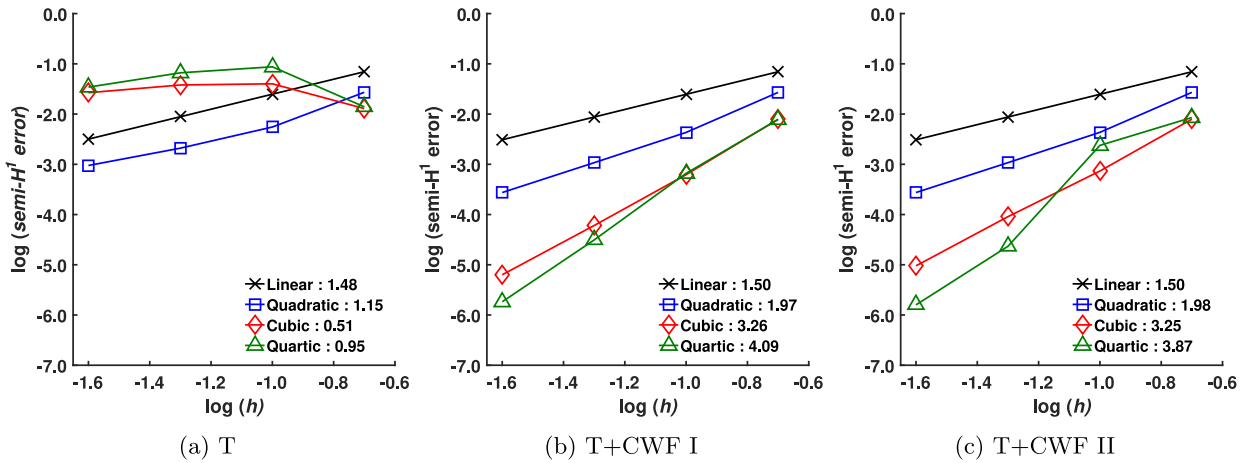


Fig. 12. Convergence with various bases in the  $H^1$  semi-norm: rates indicated in legend.

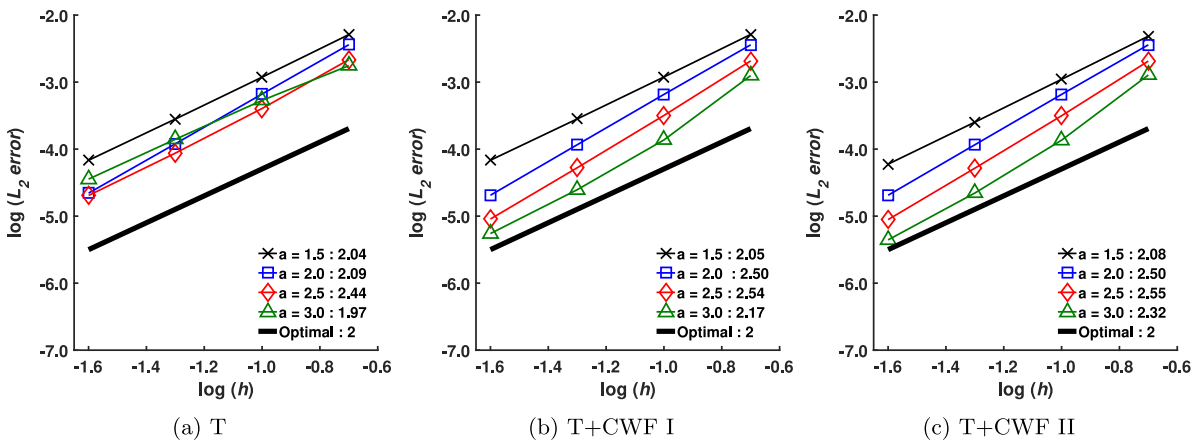


Fig. 13. Convergence for linear basis ( $p = 1$ ) with various  $a$  in the  $L_2$  norm: rates indicated in legend.

5.2.2. Dilation analysis

The effect of varying normalized support sizes in the proposed method is now examined, since as shown previously, increased support sizes in the RK approximation can yield different behavior on the essential boundary of the domain for both test and trial functions. In addition, the present test is to show that the previous results were not a special case—window functions and their measure can have an effect on accuracy and convergence rates [26], and even super-convergence can be obtained for special values of window functions [32,33]. Thus the current permutations on  $a$  and  $p$  will examine the robustness of the formulation under the variety of free parameters in the RK approximation. For this study, the discretizations and solution technique for the previous example are employed, refining  $h$  as before, while varying  $a$  and  $p$ .

First, linear basis ( $p = 1$ ) is tested. The errors in the  $L_2(\Omega)$  norm and  $H^1(\Omega)$  semi-norm are plotted in Figs. 13 and 14 respectively, for T, T+CWF I, and T+CWF II. First it can be seen that optimal rates are obtained for all cases of  $a$ , for all methods. Also, when comparing to the results for the transformation alone (T), much lower levels of error can be obtained with the present approach: nearly an order of magnitude when  $a$  is sufficiently large. The error also decreases monotonically with increasing  $a$ —this point will be revisited. Finally, it is seen that little difference in the solution error is observed for T+CWF I and T+CWF II, as in the previous cases.

Next, quadratic ( $p = 2$ ) basis is tested for various values of  $a$ ; the same error measures are presented in Figs. 15 and 16. Here it can be seen that the use of T+CWF I and T+CWF II provides a large improvement in performance over T alone, regardless of the value of  $a$ . The proposed methods provide optimal convergence rates consistently,

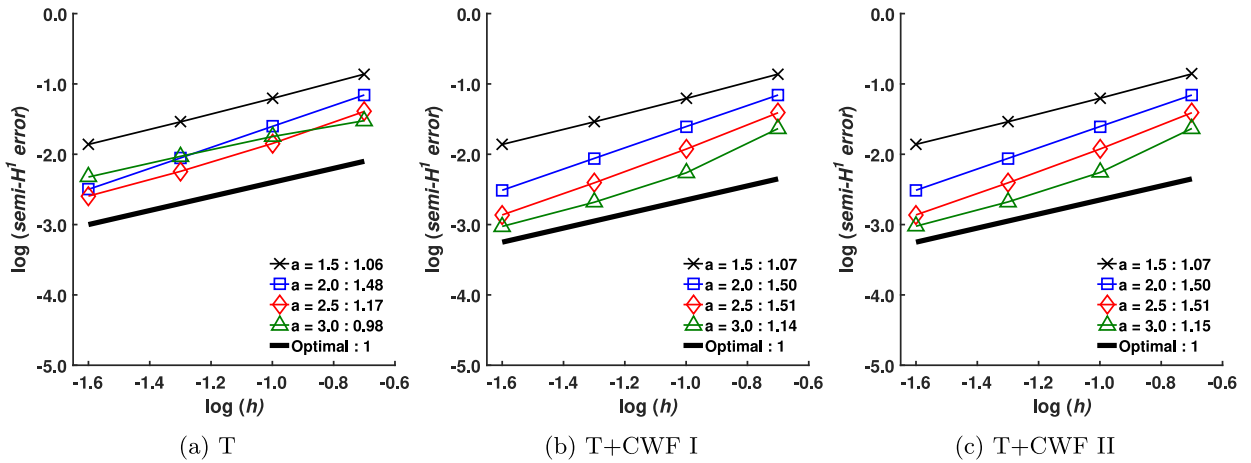


Fig. 14. Convergence for linear basis ( $p = 1$ ) with various  $a$  in the  $H^1$  semi-norm: rates indicated in legend.

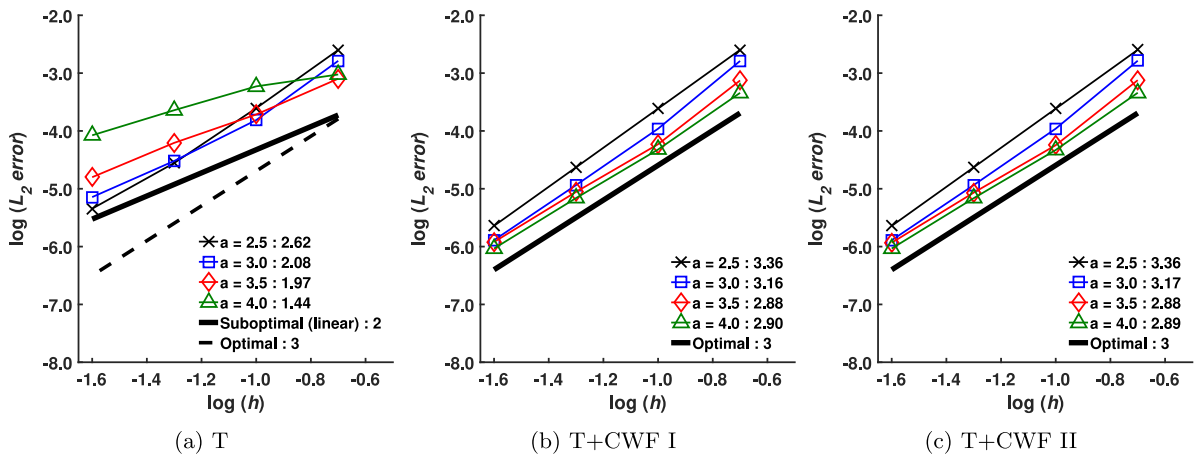


Fig. 15. Convergence for quadratic basis ( $p = 2$ ) with various  $a$  in the  $L_2$  norm: rates indicated in legend.

and do not depend on the dilation parameter. Meanwhile, with T alone, consistently worse rates are obtained with increasing the kernel measure  $a$ . Finally, from the figures, it is starkly apparent that the magnitude of error can be reduced anywhere from one to two orders of magnitude by employing the proposed techniques.

Finally, cubic ( $p = 3$ ) basis is tested. The same error measures are presented in Figs. 17 and 18 for all cases. Again, the two proposed methods consistently provide optimal convergence rates regardless of the value of  $a$ . However in this case, it seems that the actual value has little effect on solution accuracy. On the other hand, the transformation method (T) provides only linear rates, as expected, while the value of  $a$  also has little effect. Similar to the last example, it is apparent from Figs. 17 and 18 that these techniques provide the ability to reduce the solution error by several orders of magnitude, in this case, by three orders, or 99.9%.

5.2.3. A new concept:  $a$ -refinement

From the previous study, it can be noted that increasing the support size tends to yield lower error. This seems to run counter-intuitive as reported results in the meshfree community seem to indicate an “optimal” dilation (e.g., see [26]); this contradiction motivates the current study.

Here, a fixed distribution of the nodal spacing  $h = 1/10$  is employed, while varying the normalized support  $a$  for different values of  $p$ . Fig. 19 shows the error for linear basis, where it is seen that by increasing  $a$ , lower error

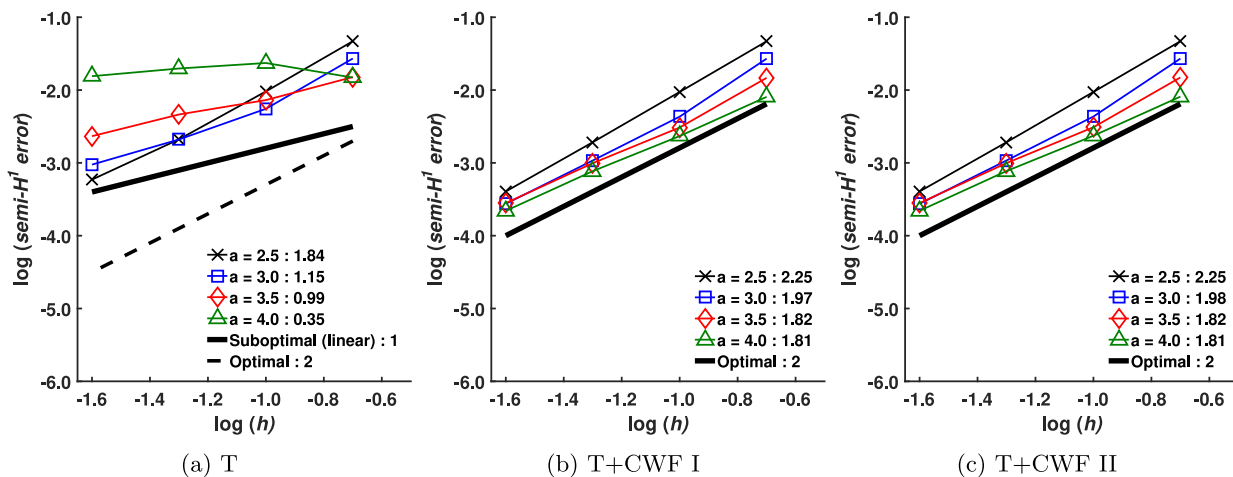


Fig. 16. Convergence for quadratic basis ( $p = 2$ ) with various  $a$  in the  $H^1$  semi-norm: rates indicated in legend.

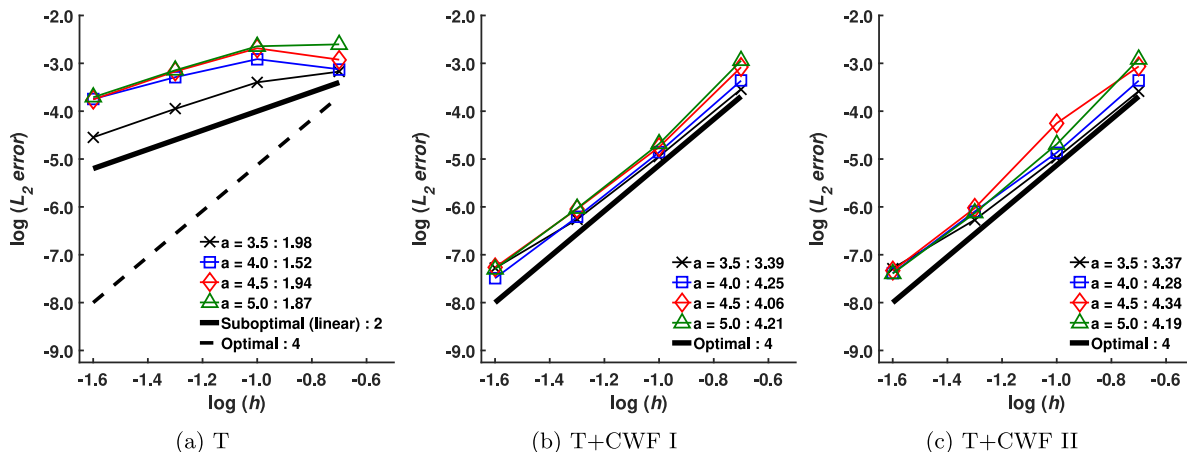


Fig. 17. Convergence for cubic basis ( $p = 3$ ) with various  $a$  in the  $L_2$  norm: rates indicated in legend.

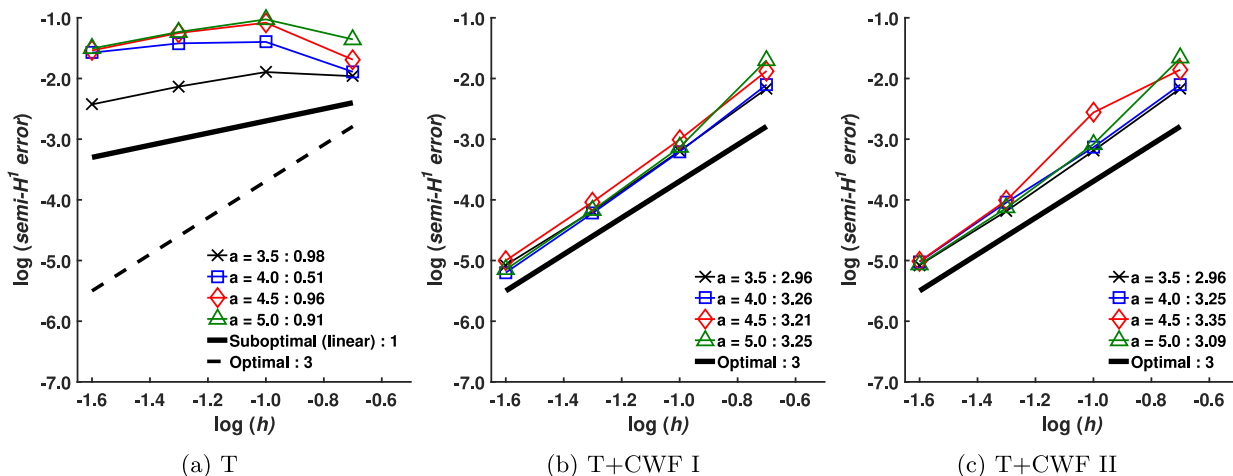


Fig. 18. Convergence for cubic basis ( $p = 3$ ) with various  $a$  in the  $H^1$  semi-norm: rates indicated in legend.

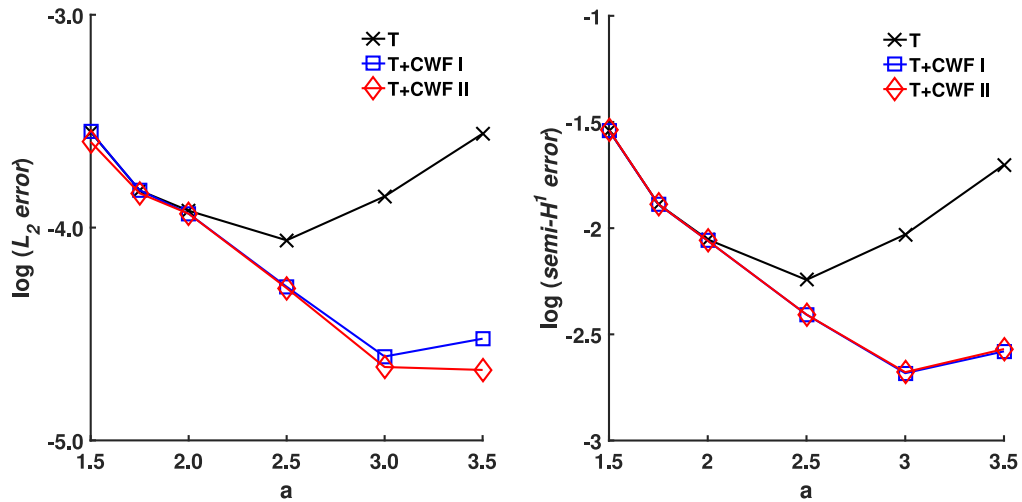


Fig. 19. Norms of error of various methods with linear basis and various kernel measures  $a$ .

can be obtained with T+CWF I and T+CWF II. On the other hand, with T alone, the optimal value appears to be  $a = 2.5$ , which likely strikes a balance between approximation accuracy, and error due to the inability to construct proper spaces required of the weak form.

As shown in Fig. 20, the trends are similar for quadratic basis. However this time, increasing  $a$  consistently yields larger errors for the transformation method. Meanwhile, for both T+CWF I and T+CWF II, the error is generally monotonically reduced by increasing  $a$ .

Finally, the results for cubic basis are presented in Fig. 21. Here it is seen that the kernel measure has little effect on solution accuracy, for all three methods. However for the transformation method, increasing the kernel measure monotonically increases the error. At least, the present method can obtain robust results for any selection of  $a$  in cubic basis.

To conclude, with the transformation method alone, there is an optimal value of  $a$  for linear basis. For higher-order approximations, increasing the kernel measure seems to always increase the solution error. For the proposed method, increasing  $a$  for both linear and quadratic basis very consistently yields lower error. Meanwhile, for cubic basis, the solution is relatively unaffected. In this work, we term the former effect, the ability to decrease the solution error by increasing the kernel measure,  $a$ -refinement. Thus with the proposed method, users may have confidence in consistent behavior of meshfree approximations in the Galerkin solution.

### 5.3. Boundary singular kernel method

The boundary singular kernel method is another strong type of boundary condition enforcement. Singular kernels for the reproducing kernel shape functions are introduced for essential boundary nodes, which recovers the properties (12)–(13). The imposition of boundary conditions in this method is therefore similar to the finite element method. However, since (12)–(13) do not imply the weak Kronecker delta property, values imposed may actually deviate between the nodes, just as in the transformation method.

Here we also consider the Poisson equation with high-order solution given in Section 5.2: with the boundary singular kernel method (B), boundary singular kernel method with consistent weak form one (B+CWF I), and boundary singular kernel method with consistent weak form two (B+CWF II).  $h$ -refinement is performed as before, varying  $p$ , with  $a = p + 1$  fixed.

Figs. 22 and 23 show the errors in the  $L_2(\Omega)$  norm and  $H^1(\Omega)$  semi-norm, respectively. Here it can be seen that for B alone, the convergence rates are far from optimal, as expected from previous results and the previous discussions, and are in fact, linear. When CWFs are considered, both B+CWF I and B+CWF II can yield optimal convergence rates. That is, they allow  $h$ -refinement with  $p$ th order rates in the boundary singular kernel method. In addition, since accuracy can be increased monotonically with increasing  $p$  (again with one case as an exception), both B+CWF I and B+CWF II offer the ability to perform  $p$ -refinement.

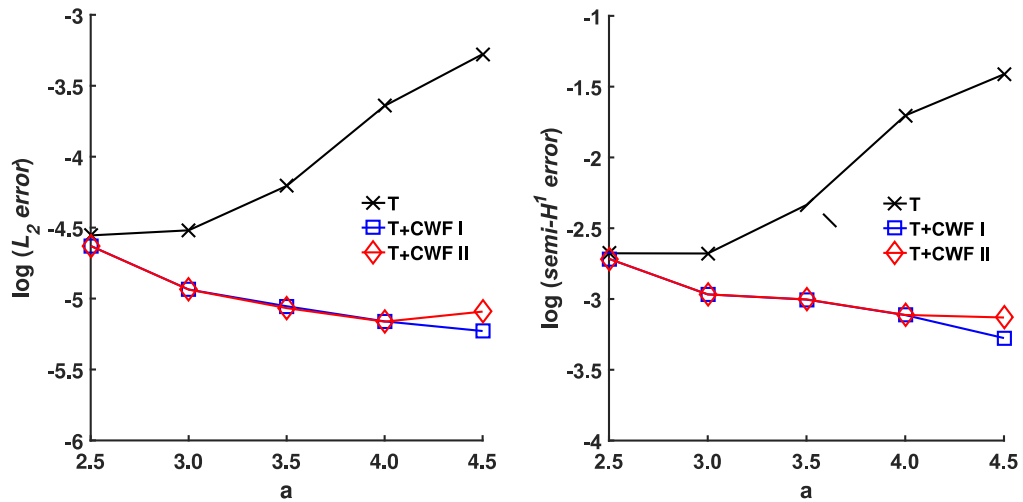


Fig. 20. Norms of error of various methods with quadratic basis and various kernel measures  $a$ .

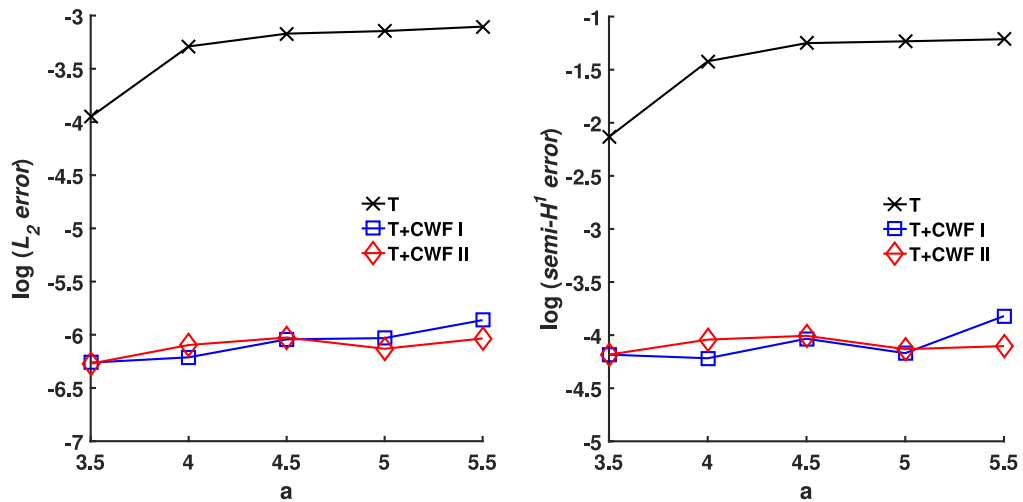


Fig. 21. Norms of error of various methods with cubic basis and various kernel measures  $a$ .

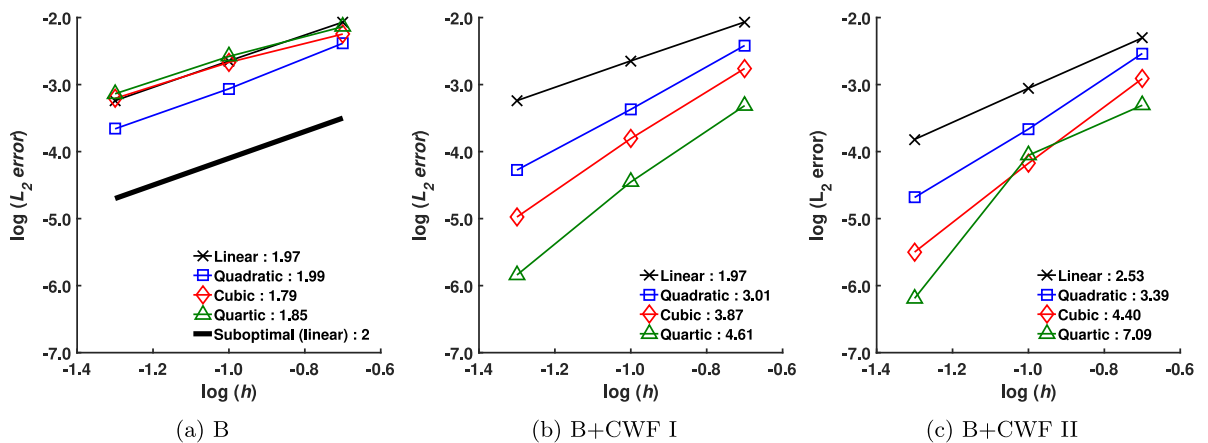


Fig. 22. Convergence with various bases in the  $L_2$  norm for the boundary singular kernel method: rates indicated in legend.

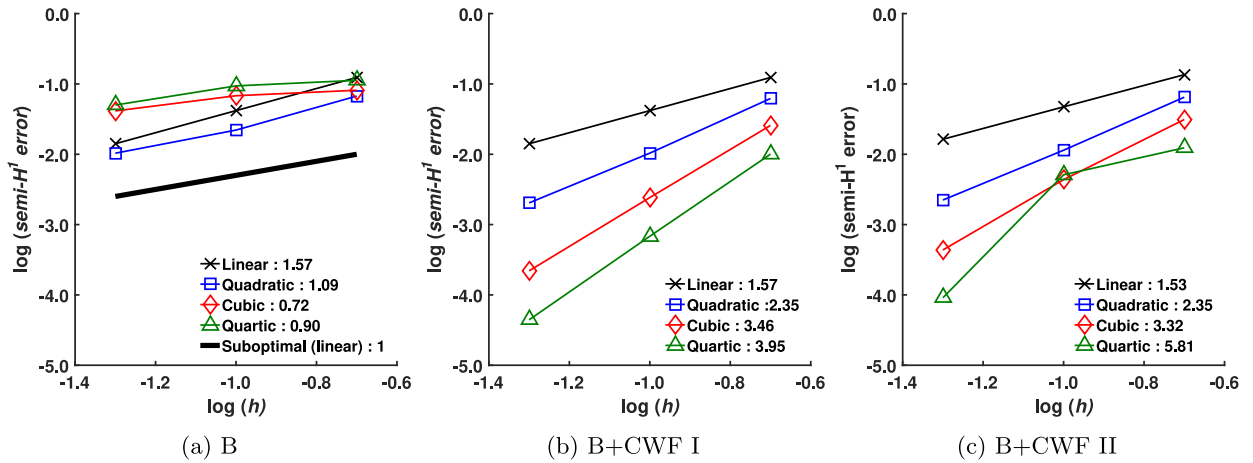


Fig. 23. Convergence with various bases in the  $H^1$  semi-norm for the boundary singular kernel method: rates indicated in legend.

### 6. Conclusion

In this work, it has first been shown that traditional strong enforcement of boundary conditions at nodal locations in meshfree methods is inconsistent with the traditional weak formulation of the problem. That is, without the weak Kronecker delta property, large, non-trivial deviations between the desired conditions on test and trial functions exist between nodes. This was shown to result loss of Galerkin orthogonality, and an  $\mathcal{O}(h)$  error in the  $L^2(\partial\Omega_g)$  norm, which in turn resulted in an  $\mathcal{O}(h)$  error in the energy norm of the problem at hand. This error was also shown to be independent of the order of approximation employed. Thus, when solving PDEs, it was expected that this error would limit the rate of convergence in the numerical solution.

It was then demonstrated through patch tests, and convergence tests, that indeed this  $\mathcal{O}(h)$  energy norm error appeared in the solution, limiting the rate of convergence in meshfree methods to that of linear basis. Thus, this inconsistency resulted in a barrier for meshfree approximations, to solutions with linear accuracy in the energy norm of the problem.

To remedy this deficiency, two new weak forms were introduced. The first accounts for the inconsistency in the test function construction. Here, the weak form relaxes the requirements on the test functions, to include the approximations introduced in the Galerkin equation under the strong-form enforcement framework. This weak form attests to the strong form of the problem at hand, and also was shown to restore a type of Galerkin orthogonality. Only one new term is required in the matrix formulation, however this results in a non-symmetric system matrix for self-adjoint systems.

The second weak form introduced relaxes the requirements on both the test and trial functions, to include both approximations in the strong-form enforcement methods. This weak form also attests to the strong form, and results in a symmetric system, which is favorable. Interestingly, this method results in an another orthogonality relation related to the boundary conditions, and an alternate best approximation property. The latter feature demonstrates that the method simultaneously minimizes the error in the energy norm, and the error on the boundary.

In numerical tests, it was first shown that the two proposed methods can restore the ability to pass the patch test for both high-order quadrature, and any order quadrature when VCI is employed. It was then demonstrated that  $p$ th-order optimal convergence rates under  $h$ -refinement could be obtained, which is in stark contrast to the existing strong-type methods under the conventional weak formulation. In addition, by increasing  $p$  for a fixed  $h$ , it was shown that lower error can be obtained, thus providing the ability to perform  $p$ -refinement for the first time under this framework. It was also shown that these results were independent of the particular dilation  $a$  chosen, and in fact, lower error can be obtained by increasing  $a$ , which was termed  $a$ -refinement. Taken together, the proposed method provides the ability to perform  $p$ -refinement,  $h$ -refinement with  $p$ th order rates, and a new capability called  $a$ -refinement.

Compared to other existing methods, it is apparent that the present approach is clearly superior to inconsistent strong enforcement of essential boundary conditions. In fact, this approach appears to remedy deficiencies in any

strong approach, as evidenced by the examples. Compared to weak-type methods, the present approach does not involve tunable parameters, nor does it involve additional degrees of freedom or stability conditions. However, since the present approach includes Nitsche-type terms, it is possible that with the proper selection of the penalty parameter in Nitsche’s approach, it would be less efficient. However, by comparison, the present approach does not require computation or user selection of any parameters, and can still ensure optimal convergence.

Finally, it should be noted that in this work, high-order quadrature was employed, which is atypical of a practical meshfree implementation. In future work, this aspect should be investigated: for instance, what is the lowest order quadrature required to maintain these high-order properties? And, with methods such as variationally consistent integration, which can greatly reduce the burden of quadrature, what would be the order required? It is noteworthy that the present technique is compatible with the variationally consistent approach, in that the weak forms attest to the strong form of the problem, which is in contrast to traditional strong enforcement of boundary conditions. Lastly, this method was tested for the Poisson equation, but can be applied to other boundary value problems as well, as described in the [Appendix](#).

**Acknowledgments**

The authors greatly acknowledge the support of this work by the L. Robert and Mary L. Kimball Early Career Professorship.

**Declaration of competing interest**

The authors declare that they have no known competing financial interests or personal relationships that could have appeared to influence the work reported in this paper.

**Appendix**

Consider the following abstract boundary value problem governing a scalar  $u$ :

$$Lu + s = 0 \quad \text{in } \Omega \tag{51a}$$

$$Bu = t \quad \text{on } \partial\Omega_t \tag{51b}$$

$$u = g \quad \text{on } \partial\Omega_g \tag{51c}$$

where  $L$  is scalar differential operator acting in the domain  $\Omega \subset \mathbb{R}^d$ ,  $s$  is a source term,  $B$  is a scalar boundary operator acting on the natural boundary  $\partial\Omega_t$ ,  $t$  is the prescribed values of  $Bu$  on  $\partial\Omega_t$ ,  $g$  is the prescribed values of  $u$  on the essential boundary  $\partial\Omega_g$ ,  $\partial\Omega_g \cap \partial\Omega_t = \emptyset$  and  $\partial\Omega = \overline{\partial\Omega_g} \cup \overline{\partial\Omega_t}$ .

Consider the weighted residual of the boundary value problem:

$$(v, Lu + s)_\Omega = 0. \tag{52}$$

Manipulation yields a bilinear form  $a(\cdot, \cdot)$  which results from the integration by parts formula  $(v, Lu)_\Omega = (v, Bu)_{\partial\Omega} - a(v, u)_\Omega$ , and the following problem statement for  $(\mathbb{W}_C^1)$ : find  $u \in H_g^k$ ,  $H_g^k = \{u | u \in H^k(\Omega), u = g \text{ on } \partial\Omega_g\}$  such that for all  $v \in H^k$  the following equation holds:

$$a(v, u)_\Omega - (v, Bu)_{\partial\Omega_g} = (v, s)_\Omega + (v, t)_{\partial\Omega_t} \tag{53}$$

where  $H^k$  is an adequate Sobolev space. The above is a consistent weighted residual of the boundary value problem as  $v = 0$  on  $\partial\Omega_g$  is not required to verify it. Note that this procedure does not require the governing equation to emanate from a potential.

To take a concrete example, consider the equations for elasticity:

$$\nabla \cdot \boldsymbol{\sigma} + \mathbf{b} = \mathbf{0} \quad \text{in } \Omega \tag{54a}$$

$$\boldsymbol{\sigma} \cdot \mathbf{n} = \mathbf{t} \quad \text{on } \partial\Omega_t \tag{54b}$$

$$\mathbf{u} = \mathbf{g} \quad \text{on } \partial\Omega_g \tag{54c}$$

where  $\mathbf{u}$  is the displacement,  $\mathbf{b}$  is the body force,  $\mathbf{t}$  is the traction,  $\mathbf{g}$  is the prescribed displacement,  $\mathbf{n}$  is the unit normal to the domain,  $\boldsymbol{\sigma} = \mathbb{C} : \nabla^s \mathbf{u}$  is the Cauchy stress tensor;  $\mathbb{C}$  is the elasticity tensor and  $\nabla^s \mathbf{u} = 1/2(\nabla \otimes \mathbf{u} + \mathbf{u} \otimes \nabla)$  is the strain tensor.

The following form for  $(\mathbb{W}_C^1)$  can be obtained following the given procedures: find  $\mathbf{u} \in \mathcal{S}_g$ ,  $\mathcal{S}_g = \{\mathbf{u} | \mathbf{u} \in H^1(\Omega), u_i = g_i \text{ on } \partial\Omega_{g_i}\}$  such that for all  $\mathbf{w} \in H^1$  the following equation holds:

$$a(\mathbf{w}, \mathbf{u})_\Omega - (\mathbf{w}, \mathbf{n} \cdot \sigma(\mathbf{u}))_{\partial\Omega_g} = (\mathbf{w}, \mathbf{b})_\Omega + (\mathbf{w}, \mathbf{t})_{\partial\Omega_t} \tag{55}$$

where

$$a(\mathbf{w}, \mathbf{u})_\Omega = \int_\Omega \nabla^s \mathbf{w} : \mathbb{C} : \nabla^s \mathbf{u} \, d\Omega, \tag{56a}$$

$$(\mathbf{w}, \mathbf{b})_\Omega = \int_\Omega \mathbf{w} \cdot \mathbf{b} \, d\Omega, \tag{56b}$$

$$(\mathbf{w}, \mathbf{t})_{\partial\Omega_t} = \int_{\partial\Omega_t} \mathbf{w} \cdot \mathbf{t} \, d\Gamma, \tag{56c}$$

$$(\mathbf{w}, \mathbf{n} \cdot \sigma(\mathbf{u}))_{\partial\Omega_g} = \int_{\partial\Omega_g} \mathbf{w} \cdot (\mathbf{n} \cdot \sigma(\mathbf{u})) \, d\Gamma. \tag{56d}$$

For the symmetric weak form of the abstract scalar boundary value problem, consider a more general weighted residual:

$$(v_\Omega, Lu + s)_\Omega + (v_g, u - g)_{\partial\Omega_g} = 0. \tag{57}$$

Choosing  $v_\Omega = v$  and  $v_g = Bv$  one obtains the following formulation for  $(\mathbb{W}_C^2)$ : find  $u \in H^k$  such that for all  $v \in H^k$  the following equation holds

$$a(v, u)_\Omega - (v, Bu)_{\partial\Omega_g} - (Bv, u)_{\partial\Omega_g} = (w, s)_\Omega + (v, t)_{\partial\Omega_t} - (Bv, g)_{\partial\Omega_g} \tag{58}$$

where  $H^k$  is again an adequate Sobolev space. The above verifies the boundary value problem without the use of  $v = 0$  on  $\partial\Omega_g$  and  $u = g$  on  $\partial\Omega_g$ . Note that if  $L$  is non-self-adjoint  $a(\cdot, \cdot)$  is not symmetric, and the resulting Galerkin system matrix will not be symmetric.

To take an example, consider the elasticity equations again. The  $(\mathbb{W}_C^2)$  can be derived as: find  $\mathbf{u} \in H^1$ , such that for all  $\mathbf{w} \in H^1$  the following equation holds:

$$a(\mathbf{w}, \mathbf{u})_\Omega - (\mathbf{w}, \sigma(\mathbf{u}) \cdot \mathbf{n})_{\partial\Omega_g} - (\sigma(\mathbf{w}) \cdot \mathbf{n}, \mathbf{u})_{\partial\Omega_g} = (\mathbf{w}, \mathbf{b})_\Omega + (\mathbf{w}, \mathbf{h})_{\partial\Omega_h} - (\sigma(\mathbf{w}) \cdot \mathbf{n}, \mathbf{g})_{\partial\Omega_g}. \tag{59}$$

Again, this procedure does not require the governing equation to emanate from a potential, although from the discussions in the manuscript, it seems that this is likely always possible to do so if the original governing equation does.

## References

- [1] J.-S. Chen, M. Hillman, S.-W. Chi, Meshfree methods: Progress made after 20 years, *J. Eng. Mech.* 143 (4) (2016) 04017001.
- [2] T. Belytschko, Y. Krongauz, D. Organ, M. Fleming, P. Krysl, Meshless methods: An overview and recent developments, *Comput. Methods Appl. Mech. Engrg.* 139 (1–4) (1996) 3–47.
- [3] S. Li, W.K. Liu, Meshfree and particle methods and their applications, *Appl. Mech. Rev.* 55 (1) (2002) 1–34.
- [4] J.-S. Chen, S.-W. Chi, H.-Y. Hu, Recent developments in stabilized Galerkin and collocation meshfree methods, *Comput. Assist. Methods Eng. Sci.* 18 (1/2) (2017) 3–21.
- [5] J.-S. Chen, C. Pan, C.-T. Wu, W.K. Liu, Reproducing kernel particle methods for large deformation analysis of non-linear structures, *Comput. Methods Appl. Mech. Engrg.* 139 (1–4) (1996) 195–227.
- [6] Y.X. Mukherjee, S. Mukherjee, On boundary conditions in the element-free Galerkin method, *Comput. Mech.* 19 (4) (1997) 264–270.
- [7] T.L. Zhu, S.N. Atluri, A modified collocation method and a penalty formulation for enforcing the essential boundary conditions in the element free Galerkin method, *Comput. Mech.* 21 (3) (1998) 211–222.
- [8] S.N. Atluri, J.Y. Cho, H.G. Kim, Analysis of thin beams, using the meshless local Petrov–Galerkin method, with generalized moving least squares interpolations, *Comput. Mech.* 24 (5) (1999) 334–347.
- [9] G.J. Wagner, W.K. Liu, Application of essential boundary conditions in mesh-free methods: A corrected collocation method, *Internat. J. Numer. Methods Engrg.* 47 (8) (2000) 1367–1379.
- [10] T. Belytschko, Y.Y. Lu, L. Gu, Element-free Galerkin methods, *Internat. J. Numer. Methods Engrg.* 37 (2) (1994) 229–256.
- [11] J. Nitsche, Über ein Variationsprinzip zur Lösung von Dirichlet-Problemen bei Verwendung von Teilräumen, die keinen Randbedingungen unterworfen sind, *Abh. Math. Semin. Univ. Hambg.* 36 (1) (1971) 9–15.
- [12] S. Fernández-Méndez, A. Huerta, Imposing essential boundary conditions in mesh-free methods, *Comput. Methods Appl. Mech. Engrg.* 193 (12) (2004) 1257–1275.
- [13] I. Babuška, The finite element method with Lagrangian multipliers, *Numer. Math.* 20 (3) (1973) 179–192.

- [14] F. Brezzi, On the existence, uniqueness and approximation of saddle-point problems arising from Lagrangian multipliers, *Publ. Math. Inform. Rennes* (S4) (1974) 1–26.
- [15] Y.Y. Lu, T. Belytschko, L. Gu, A new implementation of the element free Galerkin method, *Comput. Methods Appl. Mech. Engrg.* 113 (3–4) (1994) 397–414.
- [16] M. Griebel, M.A. Schweitzer, A particle-partition of unity method part V: boundary conditions, in: *Geometric Analysis and Nonlinear Partial Differential Equations*, Springer, Berlin, Heidelberg, 2003, pp. 519–542.
- [17] J.-S. Chen, H.-P. Wang, New boundary condition treatments in meshfree computation of contact problems, *Comput. Methods Appl. Mech. Engrg.* 187 (3–4) (2000) 441–468.
- [18] T. Belytschko, D. Organ, Y. Krongauz, A coupled finite element-element-free Galerkin method, *Comput. Mech.* 17 (3) (1995) 186–195.
- [19] Y. Krongauz, T. Belytschko, Enforcement of essential boundary conditions in meshless approximations using finite elements, *Comput. Methods Appl. Mech. Engrg.* 131 (1–2) (1996) 133–145.
- [20] L.T. Zhang, G.J. Wagner, W.K. Liu, A parallelized meshfree method with boundary enrichment for large-scale CFD, *J. Comput. Phys.* 176 (2) (2002) 483–506.
- [21] J.-S. Chen, W. Han, Y. You, X. Meng, A reproducing kernel method with nodal interpolation property, *Internat. J. Numer. Methods Engrg.* 56 (7) (2003) 935–960.
- [22] J. Gosz, W.K. Liu, Admissible approximations for essential boundary conditions in the reproducing kernel particle method, *Comput. Mech.* 19 (1) (1996) 120–135.
- [23] B. Nayroles, G. Touzot, P. Villon, Generalizing the finite element method: Diffuse approximation and diffuse elements, *Comput. Mech.* 10 (5) (1992) 307–318.
- [24] J.J. Koester, J.-S. Chen, Conforming window functions for meshfree methods, *Comput. Methods Appl. Mech. Engrg.* 347 (2019) 588–621.
- [25] F.C. Günther, W.K. Liu, Implementation of boundary conditions for meshless methods, *Comput. Methods Appl. Mech. Engrg.* 163 (1–4) (1998) 205–230.
- [26] W.K. Liu, S. Jun, Y.F. Zhang, Reproducing kernel particle methods, *Internat. J. Numer. Methods Fluids* 20 (8–9) (1995) 1081–1106.
- [27] G.J. Strang, Gilbert, Fix, *An Analysis of the Finite Element Method*, Prentice-hall, Englewood Cliffs, NJ, 1973.
- [28] J.-S. Chen, M. Hillman, M. Rüter, An arbitrary order variationally consistent integration for Galerkin meshfree methods, *Internat. J. Numer. Methods Engrg.* 95 (5) (2013) 387–418.
- [29] H.Y. Hu, J.S. Chen, W. Hu, Weighted radial basis collocation method for boundary value problems, *Internat. J. Numer. Methods Engrg.* 69 (13) (2007) 2736–2757.
- [30] J.-S. Chen, C.-T. Wu, S. Yoon, Y. You, A stabilized conforming nodal integration for Galerkin mesh-free methods, *Internat. J. Numer. Methods Engrg.* 50 (2) (2001) 435–466.
- [31] Q. Duan, X. Li, H. Zhang, T. Belytschko, Second-order accurate derivatives and integration schemes for meshfree methods, *Internat. J. Numer. Methods Engrg.* 92 (4) (2012) 399–424.
- [32] S. Li, W.K. Liu, Moving least-square reproducing kernel method part ii: Fourier analysis, *Comput. Methods Appl. Mech. Engrg.* 139 (1–4) (1996) 159–193.
- [33] Y. Leng, X. Tian, J.T. Foster, Super-convergence of reproducing kernel approximation, *Comput. Methods Appl. Mech. Engrg.* 352 (2019) 488–507.

# An arbitrary order variationally consistent integration for Galerkin meshfree methods

Jiun-Shyan Chen<sup>\*,†</sup>, Michael Hillman and Marcus Rüter

*Department of Civil and Environmental Engineering, University of California, Los Angeles, CA 90095, USA*

## SUMMARY

Because most approximation functions employed in meshfree methods are rational functions with overlapping supports, sufficiently accurate domain integration becomes costly, whereas insufficient accuracy in the domain integration leads to suboptimal convergence. In this paper, we show that it is possible to achieve optimal convergence by enforcing variational consistency between the domain integration and the test functions, and optimal convergence can be achieved with much less computational cost than using higher-order quadrature rules. In fact, stabilized conforming nodal integration is variationally consistent, whereas Gauss integration and nodal integration are not. In this work the consistency conditions for arbitrary order exactness in the Galerkin approximation are set forth explicitly. The test functions are then constructed to be variationally consistent with the integration scheme up to a desired order. Attempts are also made to correct methods that are variationally inconsistent via modification of test functions, and several variationally consistent methods are derived under a unified framework. It is demonstrated that the solution errors of PDEs due to quadrature inaccuracy can be significantly reduced when the variationally inconsistent methods are corrected with the proposed method, and consequently the optimal convergence rate can be either partially or fully restored. Copyright © 2013 John Wiley & Sons, Ltd.

Received 2 December 2012; Revised 26 March 2013; Accepted 28 March 2013

**KEY WORDS:** integration constraint; domain integration; meshfree methods; variationally consistent integration

## 1. INTRODUCTION

In recent decades, meshfree methods have become of growing interest due to the applicability of the method to classes of problems that present difficulty in traditional mesh-based methods. Examples include large deformation problems such as metal forming processes [1], moving discontinuities in fracture mechanics [2, 3], penetration processes [4], and earth moving simulations [5], among others. Although significant progress in meshfree methods has been made over the years, issues in domain integration remain to be addressed.

In meshfree methods, the shape functions are typically rational, and their supports overlap. Therefore it is difficult to develop accurate and efficient numerical integration for these methods. Roughly speaking, this results in two major issues in meshfree methods with inappropriate domain integration: the deterioration of accuracy and convergence rates, and a spatial instability in some node-based integration techniques.

In early literature [6, 7], background cells were used for Gauss integration and no special treatment was taken to alleviate the problems associated with integration. Dolbow and Belytschko [8] first investigated the integration issue in the element-free Galerkin method and showed that although moving least squares (MLS) shape functions are rational and thus more difficult to integrate, the

<sup>\*</sup>Correspondence to: Jiun-Shyan Chen, Department of Civil and Environmental Engineering, University of California, Los Angeles, CA 90095, USA.

<sup>†</sup>E-mail: jschen@seas.ucla.edu

main source of error in domain integration with Gauss quadrature is the misalignment of shape function supports with integration cells. They proposed an integration scheme where supports and integration cells are aligned for enhanced accuracy and convergence. Various other methods have been proposed to address integration in meshfree methods. The meshless local Petrov–Galerkin method [9] uses the local weak form such that the support of each shape function can be used as integration cells with proper quadrature rules for the local integration domain. A similar technique has been used in the method of finite spheres, as introduced in [10, 11]. However, these methods are expensive, as many integration points are repeatedly evaluated. More recently, Liu and Belytschko [12] devised a method on the basis of this idea, combined with satisfaction of the linear patch test. Methods based on the partition of unity have also been proposed [13, 14] to construct a method that is free of background integration cells. In these methods, the domain integration is separated into a series of integrands that cover the domain, each weighted by the partition of unity function.

If nodal integration is employed for domain integration to maintain the meshfree character of the method, a well-known spatial instability arises [15, 16]. This is because first derivatives of shape functions are zero or nearly zero at nodes, resulting in spurious modes from underestimating the energy associated with small (two times the nodal spacing) wavelength modes. In this situation, modes of alternating nodal displacements are left virtually unchecked as their contribution to the bilinear form is small. Beissel and Belytschko [15] introduced a least squares residual-based method where the second-order derivatives stabilize the rank instability. The approach eliminates the oscillatory behavior but at the cost of increasing the completeness of the basis functions to quadratic, and thus requiring a larger support and further increasing computational cost. Chen *et al.* [16] introduced a stabilized conforming nodal integration method (SCNI) that uses strain smoothing to achieve Galerkin linear exactness and to take derivatives away from the nodes to circumvent rank instability. More recently, it has been shown that SCNI generates nonzero low energy modes because of the loss of coercivity in the limit of discretization, and a correction has been proposed to enhance the stability [17, 18]. The SCNI approach has also been introduced as a nodal integration technique in finite elements [19]. Stress point methods have also been proposed [20] for SPH where derivatives are taken away from the nodes so that the spurious modes are not present.

To address the error induced by quadrature, a model problem of interest has been the patch test. The conditions on the domain and boundary integration for passing the linear patch test as to yield linear exactness in the Galerkin approximation have been investigated in [16, 21, 22] and were termed integration constraints [16]. Several corrections based on these conditions have been proposed. Bonet and Kulasegaram [22] have arrived at the condition for SPH, and a correction of the bilinear form was proposed based on the satisfaction of the integration constraints which involved an iterative procedure. Chen *et al.* [16] derived the integration constraint by enforcing linear exactness in the Galerkin approximation with quadrature and proposed SCNI where the strains are smoothed with divergence operation on a set of conforming subdomains such that the integration constraint is satisfied. SCNI has been applied to various problems such as plate and shell problems [23–25], where an integration constraint to achieve bending exactness so as to avoid shear locking has been derived, and a strain smoothing on the curvature has been proposed. This approach was further extended by Wang and Chen [25] to introduce a subdomain stabilized conforming integration to achieve a locking free solution while maintaining spatial stability. Duan *et al.* [26] extended the linear exactness of SCNI to quadratic exactness by solving for the shape function derivatives at each integration point. Similar to SCNI, conforming integration cells are adapted to meet integration constraints. Error analysis of quadrature in meshfree methods has been carried out in [27, 28], where a zero row-sum condition for improving convergence behavior has been introduced, and a correction on diagonal terms of the stiffness matrix to achieve the zero row-sum condition has been proposed.

In this work, we focus on obtaining the requirements in domain integration to achieve arbitrary order exactness in the Galerkin meshfree methods as an extension of linear integration constraints [16] to higher-order constraints. Assuming the  $n^{\text{th}}$  order completeness of the trial functions is attained, close examination reveals that the conditions for  $n^{\text{th}}$  order exactness are related to both the integration scheme and the choice of test functions. These conditions state that using the chosen numerical integration, integration by parts holds for the inner product of the test functions and the differential operator acting on the  $n^{\text{th}}$  order monomials. The domain integration methods that

meet these conditions are referred to as variationally consistent integration (VCI) methods herein. By using this as a basis, we construct a set of test functions consistent with the integration scheme for satisfaction of the integration constraints. The method allows for arbitrarily high order exactness for arbitrary types of integration methods, and it is demonstrated numerically that convergence rates predicted by exact integration are either partially or fully restored, and the integration error is significantly reduced when the integration constraints are met.

The outline of the paper is as follows. Section 2 gives a basic overview of domain integration for Galerkin meshfree methods, and demonstrates that some commonly used numerical integration methods can severely deteriorate accuracy and convergence. In Section 3 the integration constraints for  $n^{th}$  order exactness are derived and applied to several BVPs. Section 4 introduces ways to construct test functions consistent with the integration scheme and proposes an assumed strain method to satisfy the  $n^{th}$  order integration constraints. Section 5 discusses the stability of the proposed method for meeting integration constraints. In Section 6, the method is applied to several problems demonstrating improved error and convergence over standard methods. Finally, concluding remarks are given in Section 7.

## 2. BACKGROUND

In this section, we identify the issues in the domain integration of Galerkin meshfree methods. We show how several commonly used domain integration methods such as nodal integration and Gauss integration exhibit suboptimal convergence behavior under certain discretizations. The reproducing kernel particle method (RKPM) will be used to demonstrate the integration issues, but the same applies to other Galerkin meshfree methods. The discussions in this section serve as the motivation of the present work.

### 2.1. Reproducing kernel approximation

We consider the reproducing kernel (RK) approximation herein to demonstrate the nature of approximation functions commonly used in meshfree methods. Let the closed domain  $\bar{\Omega} \subset \mathbb{R}^d$  with dimension  $d$  be discretized by a set of  $NP$  nodes  $\{\mathbf{x}_I | \mathbf{x}_I \in \bar{\Omega}\}_{I=1}^{NP}$ . The RK approximation of a function  $u(\mathbf{x})$  in  $\bar{\Omega}$  denoted by  $u^h(\mathbf{x})$  is constructed by the product of a kernel function  $\Phi_a(\mathbf{x} - \mathbf{x}_I)$  with compact support and a correction function composed of a linear combination of basis functions in the following form [29]:

$$u^h(\mathbf{x}) = \sum_{I=1}^{NP} \left\{ \sum_{|\alpha| \leq n} (\mathbf{x} - \mathbf{x}_I)^\alpha b_\alpha(\mathbf{x}) \right\} \Phi_a(\mathbf{x} - \mathbf{x}_I) u_I \equiv \sum_{I=1}^{NP} \Psi_I(\mathbf{x}) u_I. \tag{1}$$

Here we have introduced the multi-index notation  $\alpha = (\alpha_1, \alpha_2, \dots, \alpha_d)$  with the length of  $\alpha$  defined as  $|\alpha| = \sum_{i=1}^d \alpha_i$ ,  $\mathbf{x}^\alpha \equiv x_1^{\alpha_1} \cdot x_2^{\alpha_2} \cdot \dots \cdot x_d^{\alpha_d}$ ,  $\mathbf{x}_I^\alpha \equiv x_{I1}^{\alpha_1} \cdot x_{I2}^{\alpha_2} \cdot \dots \cdot x_{Id}^{\alpha_d}$ ,  $b_\alpha = b_{\alpha_1 \alpha_2 \dots \alpha_d}$ , and  $u_I$  are the coefficients of approximation. The term  $\{(\mathbf{x} - \mathbf{x}_I)^\alpha\}_{|\alpha| \leq n}$  is the set of basis functions, and  $\{b_\alpha(\mathbf{x})\}_{|\alpha| \leq n}$  are coefficients that are determined by meeting the reproducing conditions

$$\sum_{I=1}^{NP} \Psi_I(\mathbf{x}) \mathbf{x}_I^\alpha = \mathbf{x}^\alpha, \quad |\alpha| \leq n. \tag{2}$$

With  $\{b_\alpha(\mathbf{x})\}_{|\alpha| \leq n}$  obtained from (2), the RK shape functions are obtained as

$$u^h(\mathbf{x}) = \sum_{I=1}^{NP} \Psi_I(\mathbf{x}) u_I \tag{3}$$

where

$$\Psi_I(\mathbf{x}) = \mathbf{H}(\mathbf{0})^T \mathbf{M}^{-1}(\mathbf{x}) \mathbf{H}(\mathbf{x} - \mathbf{x}_I) \Phi_a(\mathbf{x} - \mathbf{x}_I) \quad (4)$$

$$\mathbf{M}(\mathbf{x}) = \sum_{I=1}^{NP} \mathbf{H}(\mathbf{x} - \mathbf{x}_I) \mathbf{H}^T(\mathbf{x} - \mathbf{x}_I) \Phi_a(\mathbf{x} - \mathbf{x}_I). \quad (5)$$

Here, the vector  $\mathbf{H}^T(\mathbf{x} - \mathbf{x}_I)$  is the corresponding row vector of  $\{(\mathbf{x} - \mathbf{x}_I)^\alpha\}_{|\alpha| \leq n}$  and  $\mathbf{M}(\mathbf{x})$  is the moment matrix. In this construction, the reproducing conditions (2) are met provided the moment matrix (5) is invertible, and this requires sufficient nodes under the cover of  $\Phi_a$  so that the reproducing equations are linearly independent [30]. By direct differentiation, the shape functions also satisfy the gradient property

$$\sum_{I=1}^{NP} \nabla \Psi_I(\mathbf{x}) \mathbf{x}_I^\alpha = \nabla \mathbf{x}^\alpha, \quad |\alpha| \leq n. \quad (6)$$

The gradient completeness in (6) is one of the necessary conditions to pass the patch test. It is important to note that meshfree shape functions such as the RK shape functions in (3) can be rational functions, and the shape function supports are often overlapping. This adds complexity to domain integration in meshfree methods.

## 2.2. Issues in domain integration

When shape functions are rational such as the RK shape functions in (3), exact domain integration may not be possible. Exactness in the Galerkin approximation is not guaranteed even if the test functions possess sufficient completeness to represent the solution. As shown in [16], the exactness in the Galerkin approximation is guaranteed provided additional integration constraints are met. For first order Galerkin exactness, the linear integration constraint is the condition to numerically integrate the divergence equality [16]:

$$\langle \nabla \Psi_I \rangle_\Omega = \langle \Psi_I \mathbf{n} \rangle_{\partial\Omega} \quad \forall I, \quad (7)$$

where  $\langle \cdot \rangle_\Omega = \int_\Omega \cdot \, d\Omega$  and  $\langle \cdot \rangle_{\partial\Omega} = \int_{\partial\Omega} \cdot \, d\Gamma$  denote numerical versions of domain and boundary integrals, respectively, with ‘ $\hat{\cdot}$ ’ denoting numerical integration, and  $\Psi_I$  is a shape function with first-order completeness used in the Galerkin equation. Passing the patch tests (Galerkin exactness) for meshfree methods is in general not straightforward. Even high order Gauss integration (GI) is in general unable to meet the integration constraint, and therefore it cannot provide Galerkin exactness in meshfree methods. Methods such as stabilized conforming nodal integration [16, 23, 24, 31, 32] have been proposed that are specifically formulated to meet the integration constraints and therefore pass the associated patch tests.

Let us examine the effect of various conventional domain integration techniques on the accuracy of Galerkin meshfree methods. The patch test requires that the exact solution of a certain order be obtained for the BVP at hand. If the shape functions possess sufficient completeness, then this is achievable provided the additional integration constraints are met.

As an example, consider a linear patch test for the Poisson equation:

$$\nabla^2 u + s = 0 \quad \text{in } \Omega \quad (8a)$$

$$\nabla u \cdot \mathbf{n} = h \quad \text{on } \partial\Omega_h \quad (8b)$$

$$u = g \quad \text{on } \partial\Omega_g, \quad (8c)$$

where  $\Omega : (-1, 1) \times (-1, 1)$ ,  $\partial\Omega_h : -1 \leq x \leq 1, y = 1$ ,  $\partial\Omega_g = \partial\Omega \setminus \partial\Omega_h$ . Let the prescribed conditions to (8) be

$$s = 0 \quad (9a)$$

$$h = n_1 + 2n_2 \quad (9b)$$

$$g = x + 2y. \quad (9c)$$

The solution to the BVP (8) with conditions (9) is  $u = x + 2y$ .

The domain  $\Omega$  is discretized with uniform and nonuniform node distributions. For the generation of the nonuniform discretization, a perturbation parameter  $\beta$  is introduced to perturb the nodes away from a uniform distribution with spacing  $\Delta x_i$  by  $x_{iI} = x_{iI}^0 + \eta_{Ii} \Delta x_i$ ,  $-\beta \leq \eta_{Ii} \leq \beta$ , where  $x_{iI}^0$  is the uniform nodal position,  $x_{iI}$  is the perturbed node position, and  $\eta_{Ii}$  is generated randomly for each node in each direction. In nonuniform node distributions, the integration constraint tends to be violated more because of the asymmetry of the location of the integration points with respect to nodes and the asymmetry of the shape functions themselves. Figure 1 shows the domain discretizations used with integration schemes for GI and direct nodal integration (DNI).

Because both Gauss integration and direct nodal integration fail to meet the linear integration constraint, they fail the patch test as seen in Table I. Although linear bases are used, meeting the linear completeness requirement alone is not sufficient for passing linear patch test. DNI performs poorly, whereas GI is seen to provide better results as the number of integration points increases. However, when the number of Gauss points is increased from  $1 \times 1$  to  $5 \times 5$ , the error still remains. Although the patch test can be ‘nearly’ passed for high order integration, the cost increase can be significant. Here, it is seen that for  $\beta = 1$ , the error is reduced by an order of magnitude from  $1 \times 1$  GI to  $3 \times 3$  GI and an additional order from  $3 \times 3$  to  $5 \times 5$  GI. Lastly, it can be seen that for irregular node distributions, the error can be several orders of magnitude larger than in the uniform case.

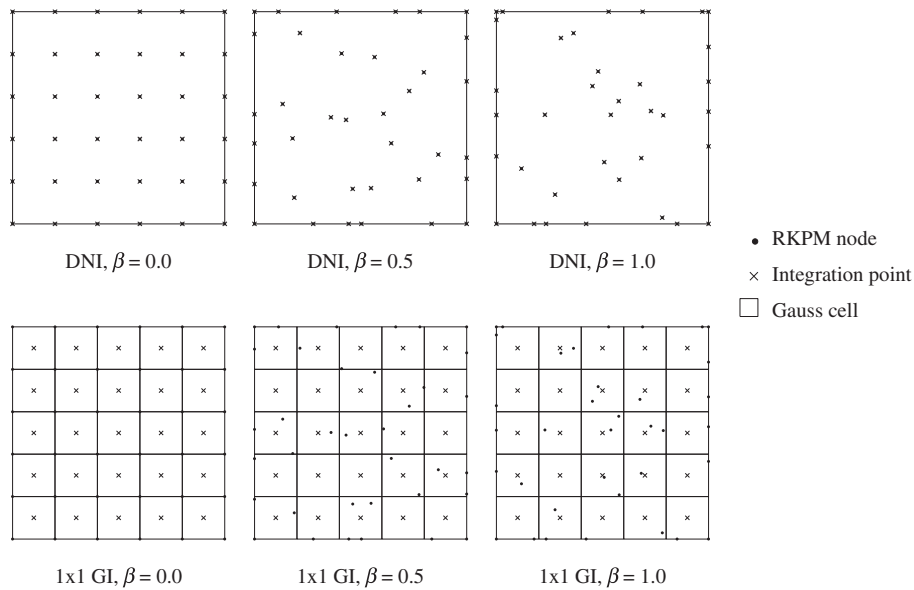


Figure 1. Integration schemes for direct nodal integration (DNI) and  $1 \times 1$  Gauss integration (GI) for uniform and nonuniform node distributions.

Table I.  $L^2$  norm of error for various integration methods.

Method	$\beta$		
	0.0	0.5	1.0
DNI	0.0236688	0.7213156	0.6750119
$1 \times 1$ GI	0.0071572	0.3163669	1.6402035
$2 \times 2$ GI	0.0001916	0.0649164	0.0782014
$3 \times 3$ GI	0.0000333	0.0115104	0.0241756
$4 \times 4$ GI	0.0000087	0.0053343	0.0066763
$5 \times 5$ GI	0.0000013	0.0015578	0.0019404

DNI, direct nodal integration; GI, Gauss integration.

Under integration can result in suboptimal convergence. To demonstrate this, consider a convergence study for the same BVP (8) with the source term and pure essential boundary condition:

$$s = \sin(\pi x) \sin(\pi y) \tag{10a}$$

$$g = 0. \tag{10b}$$

Here, the entire boundary is subjected to  $g = 0$ . The exact solution of this problem is

$$u = \frac{1}{2\pi^2} \sin(\pi x) \sin(\pi y). \tag{11}$$

First, the domain is discretized uniformly with 36, 121, 441, and 1681 nodes, and an RK approximation with linear bases and a normalized support of 1.75 is employed. In this case, the integration constraint is met for nodes with kernel functions that do not cover the boundary of the domain, because GI and direct integration points are symmetric with respect to the shape functions. Consequently, as seen in Figure 2 (numbers in the legends indicate rates of convergence), the convergence behavior is optimal. It is noted here that the  $H^1$  semi-norm turns into the energy norm for this particular problem.

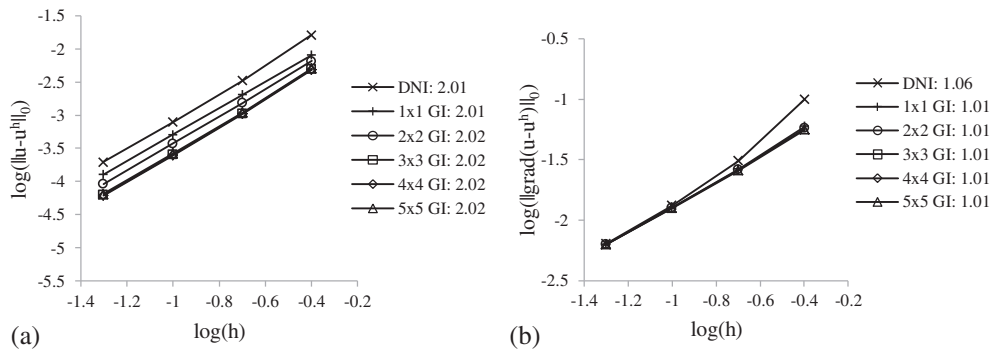


Figure 2. Convergence of error in (a) the  $L^2$  norm and (b) the  $H^1$  semi-norm for uniform discretization for Gauss integration (GI) and direct nodal integration (DNI).

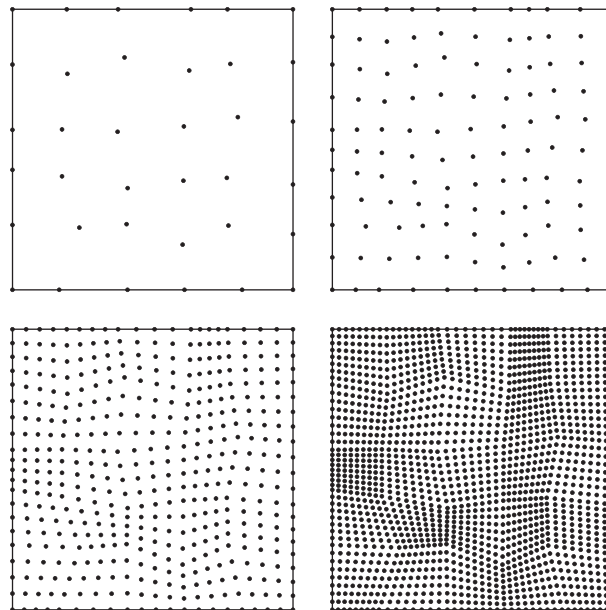


Figure 3. Uniform refinement of irregular node distribution.

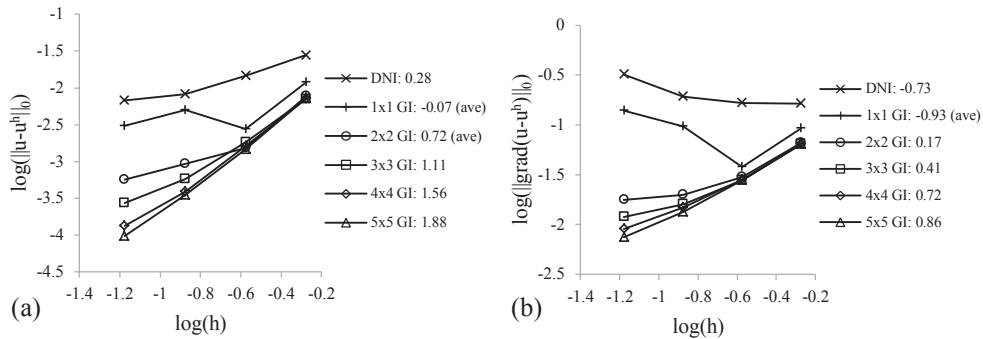


Figure 4. Convergence of error in (a) the  $L^2$  norm and (b) the  $H^1$  semi-norm for nonuniform discretization for Gauss integration (GI) and direct nodal integration (DNI).

The domain is then discretized with a nonuniform node distribution with the random generation parameter  $\beta = 0.2$  in the coarse discretization and refined uniformly as shown in Figure 3. Herein, the characteristic length for convergence  $h$  is taken as the maximum nodal spacing for the first discretization and halved for each subsequent discretization.

Direct nodal integration and GI are again employed; the error in the  $L^2$  norm and  $H^1$  semi-norm are shown in Figure 4. In nonuniform convergence studies, when the convergence is erratic, the average rate is taken as indicated in the figure. It can be seen that although the shape functions possess linear completeness, the optimal convergence rates of 2 in the  $L^2$  norm and 1 in the  $H^1$  semi-norm are not obtained, and can in fact be much lower than these optimal rates. The two methods of simple integration ( $1 \times 1$  GI and DNI) behave erratically with respect to the convergence and accuracy, as it is seen that the  $H^1$  semi-norm of the error actually diverges with refinement. It is also seen that the convergence rate can be partially restored, but even with  $5 \times 5$  GI, the rate is not full in the  $H^1$  semi-norm.

2.3. Stabilized conforming and nonconforming nodal integration

Stabilized conforming nodal integration has been introduced [16] to meet the linear integration constraint (7) and to remedy rank instability in DNI. In this method, gradients are smoothed over conforming cells that partition the domain as shown in Figure 5(a). The cells can be generated by using Voronoi diagrams or Delaunay triangulations. SCNI considers gradient smoothing with divergence in each nodal representative domain by

$$\tilde{\nabla}u^h(x_L) = \frac{1}{A_L} \int_{\Omega_L} \nabla u^h(x) \, d\Omega = \frac{1}{A_L} \int_{\partial\Omega_L} u^h(x) \mathbf{n}(x) \, d\Gamma. \tag{12}$$

Here  $A_L = \int_{\Omega_L} d\Omega$  and  $\Omega_L$  is the representative domain of node  $L$ .

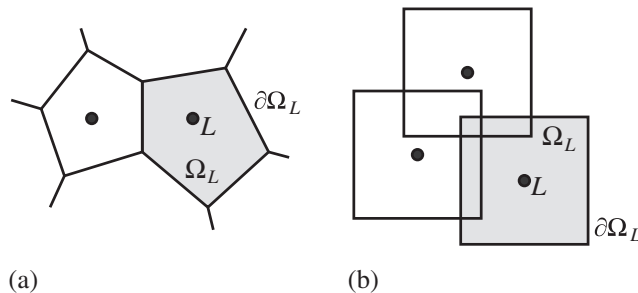


Figure 5. Nodal representative domain (a) by Voronoi diagram for stabilized conforming nodal integration (b) for stabilized nonconforming nodal integration smoothing scheme.

With (3), the approximation of the gradient at each node can be expressed in terms of the averaged (smoothed) shape function gradient

$$\tilde{\nabla}u^h(x_L) = \sum_{I=1}^{NP} \tilde{\nabla}\Psi_I(x_L)u_I, \tag{13}$$

where

$$\tilde{\nabla}\Psi_I(x_L) = \frac{1}{A_L} \int_{\partial\Omega_L} \Psi_I(x)\mathbf{n}(x) \, d\Gamma. \tag{14}$$

If numerical integration is employed, (14) is expressed as

$$\tilde{\nabla}\Psi_I(x_L) = \frac{1}{A_L} \langle \Psi_I \mathbf{n} \rangle_{\partial\Omega_L}. \tag{15}$$

It is easily shown that nodal integration with the smoothed gradient in (15) meets the integration constraint (7) if the smoothing domains  $\{\Omega_L\}_{L=1}^{NINT}$  are conforming [16]:

$$\langle \tilde{\nabla}\Psi_I \rangle_{\Omega} = \sum_{L=1}^{NINT} \tilde{\nabla}\Psi_I(x_L)A_L = \sum_{L=1}^{NINT} \langle \Psi_I \mathbf{n} \rangle_{\partial\Omega_L} = \langle \Psi_I \mathbf{n} \rangle_{\partial\Omega}, \tag{16}$$

where  $NINT$  is the number of integration points. To yield linear exactness in the Galerkin approximation of second-order PDEs by using SCNI, the boundary integration rules used in  $\langle \Psi_I \mathbf{n} \rangle_{\partial\Omega_L}$  in (15) should be used for natural or essential boundary terms in the weak form as can be understood from (7) and the Galerkin weak form of (8).

The formation of conforming strain smoothing domains in SCNI can be cumbersome in problems subjected to topological change in geometry, and stabilized nonconforming nodal integration (SNNI) has been introduced [4, 5] as a simplification of SCNI. Figure 5(b) depicts a typical smoothing scheme for SNNI where the smoothing zones are nonconforming. For illustration, SCNI and SNNI are employed for solving the patch test problem described by (8) and (9). Figure 6 shows the gradient smoothing schemes by conforming Voronoi cells and nonconforming cells for the discretizations. The integration weights used in both methods are the nodal areas in the Voronoi diagram.

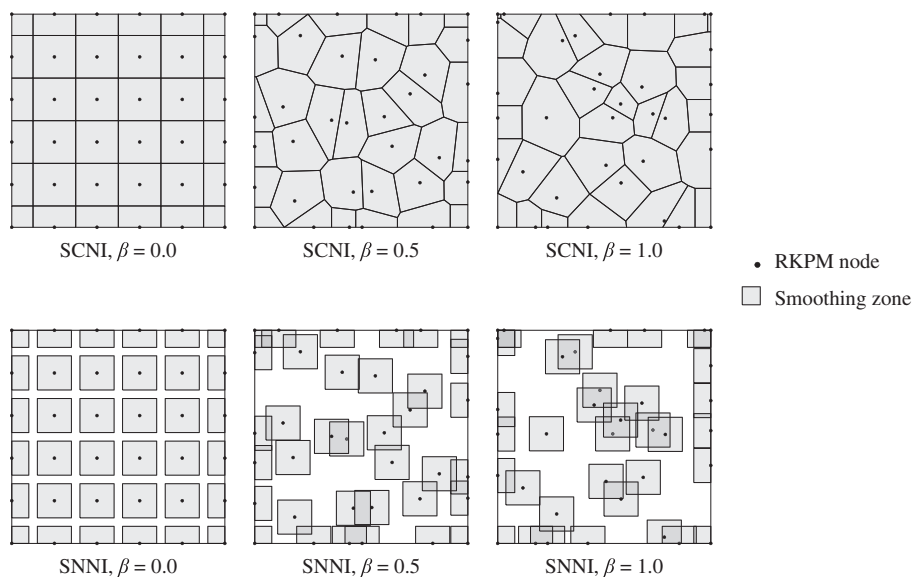


Figure 6. Gradient smoothing domains in smoothed nodal integration methods.

Table II.  $L^2$  norm of error for smoothed integration methods.

Method	$\beta$		
	0.0	0.5	1.0
SCNI	1.34E-15	3.51E-14	1.06E-14
SNNI	0.0259761	0.4509896	0.9459201

SCNI, stabilized conforming nodal integration; SNNI, stabilized nonconforming nodal integration.

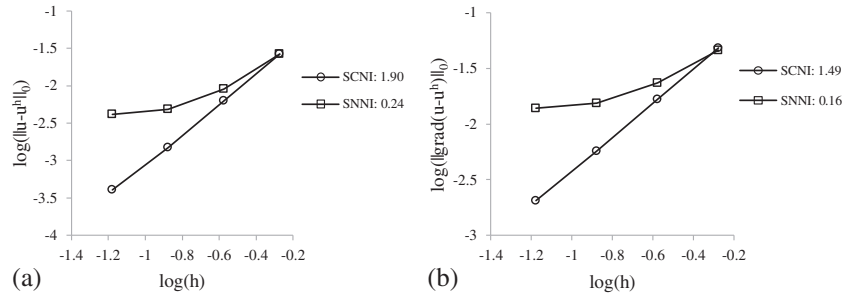


Figure 7. Convergence of error in (a) the  $L^2$  norm and (b) the  $H^1$  semi-norm for nonuniform discretization for stabilized conforming nodal integration (SCNI) and stabilized nonconforming nodal integration (SNNI).

Table II shows the error of patch test by using nodal integration with the two gradient smoothing methods. For SCNI, the result passes the patch test to machine precision, whereas SNNI does not pass the patch test. The consequence of passing or violating patch test can be demonstrated in the convergence test described by Equations (8) and (10), with the nonuniform discretizations shown in Figure 3. The  $L^2$  norm and  $H^1$  semi-norm of the errors are plotted in Figure 7, showing that SCNI provides optimal convergence in the  $L^2$  norm and in derivatives, whereas SNNI converges at a much lower rate in the  $L^2$  norm and in the  $H^1$  semi-norm. It is noted that, similar to the cases of DNI and GI, optimal convergence can be obtained when a uniform discretization is employed.

Remarks 2.1

- (1) To satisfy linear completeness, which is the first requirement to meet Galerkin exactness, it is sufficient to take single point integration on each boundary face in the smoothed methods so that

$$\langle \mathbf{n} \rangle_{\partial\Omega_L} = \langle \nabla 1 \rangle_{\Omega_L} \tag{17a}$$

$$\langle \mathbf{n}x \rangle_{\partial\Omega_L} = \langle \nabla x \rangle_{\Omega_L} \tag{17b}$$

$$\langle \mathbf{n}y \rangle_{\partial\Omega_L} = \langle \nabla y \rangle_{\Omega_L}. \tag{17c}$$

Using (17a), the smoothed gradients meet the gradient partition of nullity

$$\sum_{I=1}^{NP} \tilde{\nabla} \Psi_I(x_L) = \frac{1}{A_L} \left\langle \left( \sum_{I=1}^{NP} \Psi_I \right) \mathbf{n} \right\rangle_{\partial\Omega_L} = \frac{1}{A_L} \langle \mathbf{n} \rangle_{\partial\Omega_L} = \mathbf{0}. \tag{18}$$

Similarly, the smoothed gradients meet the first-order gradient reproducing condition by using (17b) and (17c) and if the approximation is first-order complete

$$\sum_{I=1}^{NP} \tilde{\nabla} \Psi_I x_I(x_L) = \frac{1}{A_L} \left\langle \left( \sum_{I=1}^{NP} \Psi_I x_I \right) \mathbf{n} \right\rangle_{\partial\Omega_L} = \frac{1}{A_L} \langle \mathbf{n}x \rangle_{\partial\Omega_L} = \begin{Bmatrix} 1 \\ 0 \end{Bmatrix} \tag{19a}$$

and

$$\sum_{I=1}^{NP} \tilde{\nabla} \Psi_I y_I(\mathbf{x}_L) = \frac{1}{A_L} \left\langle \left( \sum_{I=1}^{NP} \Psi_I y_I \right) \mathbf{n} \right\rangle_{\partial\Omega_L} = \frac{1}{A_L} \langle \mathbf{n} y \rangle_{\partial\Omega_L} = \begin{Bmatrix} 0 \\ 1 \end{Bmatrix}. \quad (19b)$$

- (2) For smoothed integration methods, an additional condition analogous to (17) is required to meet quadratic gradient reproducing conditions:

$$\langle \mathbf{n} x^2 \rangle_{\partial\Omega_L} = \langle \nabla x^2 \rangle_{\Omega_L} \quad (20a)$$

$$\langle \mathbf{n} y^2 \rangle_{\partial\Omega_L} = \langle \nabla y^2 \rangle_{\Omega_L} \quad (20b)$$

$$\langle \mathbf{n} x y \rangle_{\partial\Omega_L} = \langle \nabla x y \rangle_{\Omega_L}. \quad (20c)$$

Further, let the nodes coincide with the centroid  $\mathbf{x}_c$  of the smoothing zones defined by

$$x_c = \frac{1}{A_L} \langle x \rangle_{\Omega_L} = \frac{1}{2A_L} \langle x^2 n_1 \rangle_{\partial\Omega_L} \quad (21a)$$

$$y_c = \frac{1}{A_L} \langle y \rangle_{\Omega_L} = \frac{1}{2A_L} \langle y^2 n_2 \rangle_{\partial\Omega_L}. \quad (21b)$$

Here, (20) has been used to result in (21). By using (20) and (21), the second-order gradient reproducing conditions are satisfied at each nodal position  $\mathbf{x}_c$  by

$$\sum_{I=1}^{NP} \tilde{\nabla} \Psi_I x_I^2(\mathbf{x}_c) = \frac{1}{A_L} \langle \mathbf{n} x^2 \rangle_{\partial\Omega_L} = \begin{Bmatrix} 2x_c \\ 0 \end{Bmatrix} \quad (22a)$$

$$\sum_{I=1}^{NP} \tilde{\nabla} \Psi_I y_I^2(\mathbf{x}_c) = \frac{1}{A_L} \langle \mathbf{n} y^2 \rangle_{\partial\Omega_L} = \begin{Bmatrix} 0 \\ 2y_c \end{Bmatrix} \quad (22b)$$

$$\sum_{I=1}^{NP} \tilde{\nabla} \Psi_I x_I y_I(\mathbf{x}_c) = \frac{1}{A_L} \langle \mathbf{n} x y \rangle_{\partial\Omega_L} = \begin{Bmatrix} y_c \\ x_c \end{Bmatrix}. \quad (22c)$$

In two dimensions, the above relationships can be satisfied by using the two-point GI for each boundary segment of arbitrary polygon smoothing zones and single point integration for each boundary segment of square smoothing zones, provided the nodal location is at  $\mathbf{x}_c$  for both cases.

### 3. VARIATIONALLY CONSISTENT INTEGRATION FOR HIGH ORDER EXACTNESS IN THE GALERKIN APPROXIMATION

In this section, we demonstrate how arbitrary order exactness in the Galerkin approximation can be achieved if the test function and domain integration are variationally consistent. This concept is a generalization of the integration constraint for first-order Galerkin exactness for the second-order PDE as introduced in [16]. These constraint conditions serve as the basis for deriving variationally consistent domain integrations to be discussed in Section 4.

#### 3.1. Model problem

Here, the integration constraint for linear exactness in the Galerkin approximation of second-order PDEs (7) is generalized to high order solutions and general PDEs. Consider the following abstract boundary value problem:

$$Lu + s = 0 \quad \text{in } \Omega \quad (23a)$$

$$Bu = h \quad \text{on } \partial\Omega_h \quad (23b)$$

$$u = g \quad \text{on } \partial\Omega_g. \quad (23c)$$

In the above,  $L$  is a differential operator acting in the domain  $\Omega \subset \mathbb{R}^d$ ,  $s$  is a source term,  $g$  is the prescribed values of  $u$  on the essential boundary  $\partial\Omega_g$ ,  $B$  is a boundary operator acting on the natural boundary  $\partial\Omega_h$ , and the boundary of the domain  $\partial\Omega$  admits the decomposition  $\partial\Omega_g \cap \partial\Omega_h = \emptyset$  and  $\partial\Omega = \partial\Omega_g \cup \partial\Omega_h$ .

Although traditionally essential boundary terms are omitted in the weighted residual because of the availability of the kinematically admissible trial space, in meshfree methods this may not be the case and the essential boundary conditions should be imposed as constraints by, for example, Lagrange multiplier methods, Nitsche’s method, or the modified variational principle. To keep the formulation general, Lagrange multipliers shall be employed for the enforcement of boundary conditions herein, but what follows applies to all consistent weak forms, that is, all weak forms that attest to the strong form (23).

The weak form of the BVP seeks  $(u, \lambda) \in U \times \Lambda$  such that for all  $(v, \gamma) \in V \times \Gamma$  the following equation holds:

$$a(v, u)_\Omega = (v, s)_\Omega + (v, h)_{\partial\Omega_h} + (v, \lambda)_{\partial\Omega_g} + (\gamma, u - g)_{\partial\Omega_g}, \tag{24}$$

where  $U, \Lambda, V$ , and  $\Gamma$  are adequate Sobolev spaces associated with the differential operator  $L$ . Here  $(v, s)_\Omega = \int_\Omega v s \, d\Omega$  denotes the  $L^2$  inner product in  $\Omega$ ,  $(v, h)_{\partial\Omega_h} = \int_{\partial\Omega_h} v h \, d\Gamma$  and  $(v, \lambda)_{\partial\Omega_g} = \int_{\partial\Omega_g} v \lambda \, d\Gamma$  denote  $L^2$  inner products on the natural and essential boundaries of  $\Omega$ , respectively, and  $a$  is a bilinear form which results from the integration by parts formula  $(v, Lu)_\Omega = (v, Bu)_{\partial\Omega} - a(v, u)_\Omega$ . Note that using the equivalence of the weak and strong forms, the Lagrange multiplier is obtained as

$$\lambda = Bu \quad \text{on } \partial\Omega_g. \tag{25}$$

Substitution of (25) into (24) gives the modified variational principle [33]. However for illustration, the Lagrange multiplier form shall be used.

3.2. Variational consistency condition: a generalization of the linear integration constraint

Consider the abstract boundary value problem (23) where the solution is complete monomials with degree  $n$ :

$$u = \sum_{|\alpha| \leq n} c_\alpha \mathbf{x}^\alpha \equiv u^n, \tag{26}$$

where the multi-index notation is that used in (1). The source term and boundary conditions consistent with this solution are

$$s = -Lu^n \quad \text{in } \Omega \tag{27a}$$

$$h = Bu^n \quad \text{on } \partial\Omega_h \tag{27b}$$

$$g = u^n \quad \text{on } \partial\Omega_g. \tag{27c}$$

That is, when the boundary conditions and source term are prescribed as (27), the solution to the BVP of (23) is (26). For this solution the Lagrange multiplier takes the form

$$\lambda^n = Bu^n \quad \text{on } \partial\Omega_g. \tag{28}$$

The Galerkin approximation seeks  $(u^h, \lambda^h) \in U^h \times \Lambda^h$  such that for all  $(v^h, \gamma^h) \in V^h \times \Gamma^h$  the following equation holds:

$$a(v^h, u^h)_\Omega = (v^h, s)_\Omega + (v^h, h)_{\partial\Omega_h} + (v^h, \lambda^h)_{\partial\Omega_g} + (\gamma^h, u^h - g)_{\partial\Omega_g}, \tag{29}$$

where  $U^h \subset U$ ,  $V^h \subset V$ ,  $\Lambda^h \subset \Lambda$ , and  $\Gamma^h \subset \Gamma$  are suitable finite-dimensional subspaces. Let the trial and test functions be approximated as

$$u^h = \sum_{I=1}^{NP} \Psi_I u_I \quad (30a)$$

$$v^h = \sum_{I=1}^{NP} \hat{\Psi}_I v_I \quad (30b)$$

$$\lambda^h = \sum_{I=1}^{NC} \varphi_I \lambda_I \quad (30c)$$

$$\gamma^h = \sum_{I=1}^{NC} \hat{\varphi}_I \gamma_I, \quad (30d)$$

where  $NC$  is the number of constraint nodes associated with the essential boundary condition. Note that in the Bubnov–Galerkin method,  $\hat{\Psi}_I = \Psi_I$  and  $\hat{\varphi}_I = \varphi_I$ , and for a Petrov–Galerkin method they are different from each other. Consider the  $n^{\text{th}}$  order completeness in  $u^h$  in (2):

$$\sum_{I=1}^{NP} \Psi_I u_I^n = u^n, \quad (31)$$

where  $u^n$  is the complete  $n^{\text{th}}$  order monomial defined in (26), and  $u_I^n = \sum_{|\alpha| \leq n} c_\alpha \mathbf{x}_I^\alpha$ . By using the approximations (30), inserting  $u_J = u_J^n$  into the last term in (29), using the essential boundary condition (27c), and the completeness condition (31), we have

$$\sum_{J=1}^{NP} a(\hat{\Psi}_I, \Psi_J u_J)_{\Omega} = (\hat{\Psi}_I, s)_{\Omega} + (\hat{\Psi}_I, h)_{\partial\Omega_h} + \sum_{J=1}^{NC} (\hat{\Psi}_I, \varphi_J \lambda_J)_{\partial\Omega_g} \quad \forall I. \quad (32)$$

By taking  $\lambda_I = \lambda_I^n = (Bu^n)_I$ , inserting  $u_J = u_J^n$ , and using the completeness condition in the approximation of  $\lambda^h = \sum_{I=1}^{NC} \varphi_I \lambda_I^n = \sum_{I=1}^{NC} \varphi_I (Bu^n)_I = Bu^n$  we arrive at

$$\sum_{J=1}^{NP} a(\hat{\Psi}_I, \Psi_J u_J^n)_{\Omega} = (\hat{\Psi}_I, s)_{\Omega} + (\hat{\Psi}_I, h)_{\partial\Omega_h} + (\hat{\Psi}_I, Bu^n)_{\partial\Omega_g} \quad \forall I. \quad (33)$$

Finally, by using the source term (27a) and boundary conditions (27b) and (27c), considering all orders of completeness from 1 to  $n$ , and employing numerical integration in (33), we have

$$a\langle \hat{\Psi}_I, \mathbf{x}^\alpha \rangle_{\Omega} = -\langle \hat{\Psi}_I, L\mathbf{x}^\alpha \rangle_{\Omega} + \langle \hat{\Psi}_I, B\mathbf{x}^\alpha \rangle_{\partial\Omega} \quad \forall I, |\alpha| = 0, 1, \dots, n, \quad (34)$$

where  $a\langle \cdot, \cdot \rangle_{\Omega}$  is the quadrature version of  $a(\cdot, \cdot)_{\Omega}$ , and  $\langle \cdot, \cdot \rangle_{\Omega}$  and  $\langle \cdot, \cdot \rangle_{\partial\Omega}$  are the quadrature versions of  $(\cdot, \cdot)_{\Omega}$  and  $(\cdot, \cdot)_{\partial\Omega}$ , respectively. The equations in (34) are a generalization of the linear integration constraints to arbitrary order of Galerkin exactness. Domain integration that meets (34) yields Galerkin exactness with a desired order and is called VCI herein.

### Remarks 3.1

- (1) To arrive at the  $n^{\text{th}}$  order integration constraints in (34),  $n^{\text{th}}$  order completeness in the trial functions has been used. The integration constraint states that the numerical integration of the domain and boundary integrals for Galerkin approximation of a PDE with differential operator  $L$  has to be consistent with the test functions  $\hat{\Psi}_I$  in the form of (34) for an  $n^{\text{th}}$  order complete numerical method to achieve the  $n^{\text{th}}$  order exactness in the Galerkin approximation (passing the  $n^{\text{th}}$  order patch test).

- (2) For  $n = 1$ , (34) is the integration constraint for the linear patch test as given in [16], which reduces to a divergence condition for a second-order differential operator  $L$  such as the elasticity or Poisson problem. Further, stabilized conforming nodal integration introduced in [16] meets the constraint for  $n = 1$ .
- (3) The constraint for constant exactness for self-adjoint PDEs is automatically satisfied when the trial functions possess the partition of unity property.
- (4) The integration constraints in (34) act on the test functions  $\hat{\Psi}_I$ . It is therefore possible, for a given set of  $n^{th}$  order complete trial functions and numerical integration methods, to construct test functions, different from the trial functions, to meet the integration constraints. This is demonstrated in Section 4.

3.3. Integration constraint for the Poisson equation

For illustration, consider the two-dimensional Poisson equation, where the operators in (23) and the bilinear form in (24) are defined by

$$L = \nabla^2 \tag{35a}$$

$$B = \mathbf{n} \cdot \nabla \tag{35b}$$

$$a(v, u)_\Omega = (\nabla v, \nabla u)_\Omega, \tag{35c}$$

and the trial and test spaces are defined as  $U = V = H^1(\Omega)$  and  $\Lambda = \Gamma = L^2(\partial\Omega_g)$ . Substitution of (35) into (34) gives

$$a\langle \hat{\Psi}_I, \mathbf{x}^\alpha \rangle_\Omega = -\langle \hat{\Psi}_I, \nabla^2 \mathbf{x}^\alpha \rangle_\Omega + \langle \hat{\Psi}_I, \nabla \mathbf{x}^\alpha \cdot \mathbf{n} \rangle_{\partial\Omega} \quad \forall I, |\alpha| = 0, 1, \dots, n. \tag{36}$$

By letting  $n = 1$ , the linear constraints are obtained as

$$\langle \nabla \hat{\Psi}_I \rangle_\Omega = \langle \hat{\Psi}_I \mathbf{n} \rangle_{\partial\Omega} \quad \forall I. \tag{37}$$

The integration constraint in (37) is a divergence condition with numerical integration acting on  $\hat{\Psi}_I$ . Similarly, the quadratic integration constraints are obtained as

$$\langle \hat{\Psi}_{I,1x} \rangle_\Omega = -\langle \hat{\Psi}_I \rangle_\Omega + \langle \hat{\Psi}_I x n_1 \rangle_{\partial\Omega} \quad \forall I \tag{38a}$$

$$\langle \hat{\Psi}_{I,2y} \rangle_\Omega = -\langle \hat{\Psi}_I \rangle_\Omega + \langle \hat{\Psi}_I y n_2 \rangle_{\partial\Omega} \quad \forall I \tag{38b}$$

$$\langle \hat{\Psi}_{I,1y} + \hat{\Psi}_{I,2x} \rangle_\Omega = \langle \hat{\Psi}_I (y n_1 + x n_2) \rangle_{\partial\Omega} \quad \forall I, \tag{38c}$$

and the third order integration constraints are

$$\langle \hat{\Psi}_{I,1x^2} \rangle_\Omega = -\langle 2\hat{\Psi}_I x \rangle_\Omega + \langle \hat{\Psi}_I x^2 n_1 \rangle_{\partial\Omega} \quad \forall I \tag{39a}$$

$$\langle \hat{\Psi}_{I,2y^2} \rangle_\Omega = -\langle 2\hat{\Psi}_I y \rangle_\Omega + \langle \hat{\Psi}_I y^2 n_2 \rangle_{\partial\Omega} \quad \forall I \tag{39b}$$

$$\langle 2\hat{\Psi}_{I,1xy} + \hat{\Psi}_{I,2x^2} \rangle_\Omega = -\langle 2\hat{\Psi}_I y \rangle_\Omega + \langle \hat{\Psi}_I (2xy n_1 + x^2 n_2) \rangle_{\partial\Omega} \quad \forall I \tag{39c}$$

$$\langle \hat{\Psi}_{I,1y^2} + 2\hat{\Psi}_{I,2xy} \rangle_\Omega = -\langle 2\hat{\Psi}_I x \rangle_\Omega + \langle \hat{\Psi}_I (y^2 n_1 + 2xy n_2) \rangle_{\partial\Omega} \quad \forall I. \tag{39d}$$

Note that for high order exactness, the constraints of each lower order should be satisfied.

3.4. Integration constraint for linear elasticity

The elasticity boundary value problem is stated as:

$$\nabla \cdot \boldsymbol{\sigma} + \mathbf{b} = \mathbf{0} \quad \text{in } \Omega \tag{40a}$$

$$\boldsymbol{\sigma} \cdot \mathbf{n} = \mathbf{h} \quad \text{on } \partial\Omega_h \tag{40b}$$

$$\mathbf{u} = \mathbf{g} \quad \text{on } \partial\Omega_g. \tag{40c}$$

Here,  $\mathbf{u}$  is the displacement field,  $\boldsymbol{\sigma} = \mathbb{C} : \nabla^s \mathbf{u}$  is the Cauchy stress tensor, where  $\mathbb{C}$  is the elasticity tensor and  $\nabla^s \mathbf{u} = 1/2(\nabla \otimes \mathbf{u} + \mathbf{u} \otimes \nabla)$  is the strain tensor. Thus for elasticity we have the following tensorial operators:

$$\mathbf{L} = \nabla \cdot \mathbb{C} : \nabla^s \quad (41a)$$

$$\mathbf{B} = \mathbf{n} \cdot (\mathbb{C} : \nabla^s). \quad (41b)$$

The weak form asks to find  $(\mathbf{u}, \boldsymbol{\lambda}) \in U \times \Lambda$  such that for all  $(\mathbf{v}, \boldsymbol{\gamma}) \in V \times \Gamma$ , with  $U = V = [H^1(\Omega)]^d$  and  $\Lambda = \Gamma = [L^2(\partial\Omega_g)]^d$ , the following equation holds:

$$a(\mathbf{v}, \mathbf{u})_\Omega = (\mathbf{v}, \mathbf{b})_\Omega + (\mathbf{v}, \mathbf{h})_{\partial\Omega_h} + (\mathbf{v}, \boldsymbol{\lambda})_{\partial\Omega_g} + (\boldsymbol{\gamma}, \mathbf{u} - \mathbf{g})_{\partial\Omega_g}, \quad (42)$$

where the bilinear form and linear forms for elasticity are

$$a(\mathbf{v}, \mathbf{u})_\Omega = \int_\Omega \nabla^s \mathbf{v} : \mathbb{C} : \nabla^s \mathbf{u} \, d\Omega \quad (43a)$$

$$(\mathbf{v}, \mathbf{b})_\Omega = \int_\Omega \mathbf{v} \cdot \mathbf{b} \, d\Omega \quad (43b)$$

$$(\mathbf{v}, \mathbf{h})_{\partial\Omega_h} = \int_{\partial\Omega_h} \mathbf{v} \cdot \mathbf{h} \, d\Gamma \quad (43c)$$

$$(\mathbf{v}, \boldsymbol{\lambda})_{\partial\Omega_g} = \int_{\partial\Omega_g} \mathbf{v} \cdot \boldsymbol{\lambda} \, d\Gamma. \quad (43d)$$

Consider (40) with the following  $n^{th}$  order solution  $\mathbf{u} = \sum_{|\alpha| \leq n} \mathbf{c}_\alpha \mathbf{x}^\alpha \equiv \mathbf{u}^n$  by using the multi-index notation. Denote the stress tensor corresponding to the displacement field as  $\boldsymbol{\sigma}^n = \mathbb{C} : \nabla^s \mathbf{u}^n$ , and the stress corresponding to  $\mathbf{x}^\alpha$  as  $\boldsymbol{\sigma}^\alpha = \mathbb{C} : \nabla^s \mathbf{x}^\alpha$ . The boundary conditions and body force associated with this displacement field are

$$\mathbf{b} = -\nabla \cdot \boldsymbol{\sigma}^n \quad \text{in } \Omega \quad (44a)$$

$$\mathbf{h} = \boldsymbol{\sigma}^n \cdot \mathbf{n} \quad \text{on } \partial\Omega_h \quad (44b)$$

$$\mathbf{g} = \mathbf{u}^n \quad \text{on } \partial\Omega_g. \quad (44c)$$

That is, when the body force and boundary conditions are prescribed as in (44), the solution to (40) is  $\mathbf{u}^n$ . Furthermore, the Lagrange multiplier consistent with the solution  $\mathbf{u}^n$  is

$$\boldsymbol{\lambda}^n = \boldsymbol{\sigma}^n \cdot \mathbf{n} \quad \text{on } \partial\Omega_g, \quad (45)$$

which is the traction on the essential boundary. For the Galerkin form, let us introduce the following approximations:

$$\mathbf{u}^h = \sum_{I=1}^{NP} \Psi_I \mathbf{u}_I \quad (46a)$$

$$\mathbf{v}^h = \sum_{I=1}^{NP} \hat{\Psi}_I \mathbf{v}_I \quad (46b)$$

$$\boldsymbol{\lambda}^h = \sum_{I=1}^{NC} \varphi_I \boldsymbol{\lambda}_I \quad (46c)$$

$$\boldsymbol{\gamma}^h = \sum_{I=1}^{NC} \hat{\varphi}_I \boldsymbol{\gamma}_I. \quad (46d)$$

By substituting the approximations (46) into (42) with the exact nodal solution; employing  $n^{th}$  order completeness; using prescribed conditions in (44) and the Lagrange multiplier in (45); and

employing numerical integration on (42), the following integration constraints are obtained for elasticity following similar procedures for the scalar equations:

$$\langle \nabla \hat{\Psi}_I \cdot \sigma^\alpha \rangle_\Omega = -\langle \hat{\Psi}_I \nabla \cdot \sigma^\alpha \rangle_\Omega + \langle \hat{\Psi}_I \sigma^\alpha \cdot \mathbf{n} \rangle_{\partial\Omega} \quad \forall I, |\alpha| = 0, 1, \dots, n. \quad (47)$$

For illustration purposes, let us consider the two-dimensional ( $d = 2$ ) case. Further manipulation of (47) gives the general two-dimensional integration constraint for elasticity for all  $I$  and  $|\alpha| = 0, 1, \dots, n$ :

$$\langle \hat{\Psi}_{I,1} \sigma_{11}^\alpha + \hat{\Psi}_{I,2} \sigma_{21}^\alpha \rangle_\Omega = -\langle \hat{\Psi}_I (\sigma_{11,1}^\alpha + \sigma_{21,2}^\alpha) \rangle_\Omega + \langle \hat{\Psi}_I (n_1 \sigma_{11}^\alpha + n_2 \sigma_{21}^\alpha) \rangle_{\partial\Omega} \quad (48a)$$

$$\langle \hat{\Psi}_{I,1} \sigma_{21}^\alpha + \hat{\Psi}_{I,2} \sigma_{22}^\alpha \rangle_\Omega = -\langle \hat{\Psi}_I (\sigma_{21,1}^\alpha + \sigma_{22,2}^\alpha) \rangle_\Omega + \langle \hat{\Psi}_I (n_1 \sigma_{21}^\alpha + n_2 \sigma_{22}^\alpha) \rangle_{\partial\Omega}. \quad (48b)$$

For the linear integration constraint, consider the linear displacement field

$$u_1 = a_{11}x + a_{12}y \quad (49a)$$

$$u_2 = a_{21}x + a_{22}y. \quad (49b)$$

Note that constant terms are omitted because partition of unity in the trial function in general satisfies constant exactness. The stress associated with this displacement is constant:

$$\sigma_{ij} = \mathbb{C}_{ij11}a_{11} + \frac{1}{2}\mathbb{C}_{ij12}(a_{12} + a_{21}) + \frac{1}{2}\mathbb{C}_{ij21}(a_{12} + a_{21}) + \mathbb{C}_{ij22}a_{22}. \quad (50)$$

Substituting (50) into (48) the constraint is reduced to

$$\langle \hat{\Psi}_{I,1} \rangle_\Omega = \langle \hat{\Psi}_I n_1 \rangle_{\partial\Omega} \quad \forall I \quad (51a)$$

$$\langle \hat{\Psi}_{I,2} \rangle_\Omega = \langle \hat{\Psi}_I n_2 \rangle_{\partial\Omega} \quad \forall I, \quad (51b)$$

which is the same as the divergence condition in the Poisson equation (37).

For quadratic exactness, consider the additional quadratic components of the displacement field by

$$u_1 = a_{13}x^2 + a_{14}y^2 + a_{15}xy \quad (52a)$$

$$u_2 = a_{23}x^2 + a_{24}y^2 + a_{25}xy, \quad (52b)$$

which gives the linear stress

$$\begin{aligned} \sigma_{ij} = & \mathbb{C}_{ij11}(2a_{13}x + a_{15}y) + \frac{1}{2}\mathbb{C}_{ij12}(2a_{14}y + a_{15}x + 2a_{23}x + a_{25}y) \\ & + \frac{1}{2}\mathbb{C}_{ij21}(2a_{14}y + a_{15}x + 2a_{23}x + a_{25}y) + \mathbb{C}_{ij22}(2a_{24}y + a_{25}x). \end{aligned} \quad (53)$$

Substitution of (53) into the constraint (48) results in the following conditions:

$$\langle \hat{\Psi}_{I,1x} \rangle_\Omega = -\langle \hat{\Psi}_I \rangle_\Omega + \langle \hat{\Psi}_I x n_1 \rangle_{\partial\Omega} \quad \forall I \quad (54a)$$

$$\langle \hat{\Psi}_{I,2y} \rangle_\Omega = -\langle \hat{\Psi}_I \rangle_\Omega + \langle \hat{\Psi}_I y n_2 \rangle_{\partial\Omega} \quad \forall I \quad (54b)$$

$$\langle \hat{\Psi}_{I,2x} \rangle_\Omega = \langle \hat{\Psi}_I x n_2 \rangle_{\partial\Omega} \quad \forall I \quad (54c)$$

$$\langle \hat{\Psi}_{I,1y} \rangle_\Omega = \langle \hat{\Psi}_I y n_1 \rangle_{\partial\Omega} \quad \forall I, \quad (54d)$$

which are similar to, but slightly more restrictive than the Poisson equation's constraints (38). Note that for passing quadratic patch test, both (51) and (54) are needed.

Higher-order constraints can be obtained similarly as shown in Appendix A.

#### 4. VARIATIONALLY CONSISTENT INTEGRATION METHODS

Several variationally consistent integration methods are presented in this section. Methods discussed in this section include corrections of existing integration methods that are variationally inconsistent, as well as an extension of SCNI to achieve higher-order exactness.

#### 4.1. Basic ideas

The integration constraints in Section 3 provide a basis for developing a variationally consistent integration method. Completeness of the trial space can be met by using standard shape functions such as the reproducing kernel function given in (1). Straightforward examination of (34) shows that it is possible to select a set of test functions to meet the integration constraints. Here, a procedure is introduced to this end, and it can be applied to arbitrary types of integration.

Let the approximations of scalar trial and test functions be expressed as

$$u^h = \sum_{I=1}^{NP} \Psi_I u_I \quad (55a)$$

$$v^h = \sum_{I=1}^{NP} \hat{\Psi}_I v_I, \quad (55b)$$

where  $\Psi_I$  is the trial function which possesses  $n^{th}$  order completeness, and consider the test function approximations as

$$\hat{\Psi}_I = \Psi_I + \sum_{|\beta| \leq n} \xi_{\beta I} \hat{\Psi}_I^\beta. \quad (56)$$

Here, it is required that  $\{\Psi_I, \hat{\Psi}_I^\beta\}_{|\beta|=1}^n$  be linearly independent. Inserting the trial function and the test functions into the integration constraint for the scalar BVP in (23) yields

$$\begin{aligned} \sum_{|\beta|=1}^n \xi_{\beta I} \left( a \langle \hat{\Psi}_I^\beta, \mathbf{x}^\alpha \rangle_\Omega + \langle \hat{\Psi}_I^\beta, L\mathbf{x}^\alpha \rangle_\Omega - \langle \hat{\Psi}_I^\beta, B\mathbf{x}^\alpha \rangle_{\partial\Omega} \right) = \\ - \left( a \langle \Psi_I, \mathbf{x}^\alpha \rangle_\Omega + \langle \Psi_I, L\mathbf{x}^\alpha \rangle_\Omega - \langle \Psi_I, B\mathbf{x}^\alpha \rangle_{\partial\Omega} \right) \quad \forall I, |\alpha| = 0, 1, \dots, n \end{aligned} \quad (57)$$

which can be expressed as

$$\sum_{|\beta|=1}^n A_{\alpha\beta I} \xi_{\beta I} = r_{\alpha I} \quad \forall I, |\alpha| = 0, 1, \dots, n \quad (58)$$

where

$$A_{\alpha\beta I} = a \langle \hat{\Psi}_I^\beta, \mathbf{x}^\alpha \rangle_\Omega + \langle \hat{\Psi}_I^\beta, L\mathbf{x}^\alpha \rangle_\Omega - \langle \hat{\Psi}_I^\beta, B\mathbf{x}^\alpha \rangle_{\partial\Omega} \quad (59a)$$

$$r_{\alpha I} = - \left( a \langle \Psi_I, \mathbf{x}^\alpha \rangle_\Omega + \langle \Psi_I, L\mathbf{x}^\alpha \rangle_\Omega - \langle \Psi_I, B\mathbf{x}^\alpha \rangle_{\partial\Omega} \right). \quad (59b)$$

The unknown coefficients  $\xi_{\beta I}$  are straightforwardly obtained from (58).

The method resulting from the chosen integration method with trial function and test function formed using (56)–(59) is variationally consistent.

#### Remarks 4.1

- (1) The method is driven from the residual of the numerical integration. If the numerical integration is variationally consistent, that is,  $\boldsymbol{\xi}_I = \mathbf{0}$ , the method is the same as the unmodified method.
- (2) The type of numerical integration in the method is arbitrary.
- (3) The method allows arbitrarily high order exactness in the Galerkin approximation.
- (4) The set of  $\{\Psi_I, \hat{\Psi}_I^\beta\}_{|\beta|=1}^n$  is not arbitrary for general problems where solutions may not be in the trial space, and conditions on these functions should be chosen on the basis of stability considerations to be discussed in Section 5.

4.2. Assumed strain variationally consistent integration

The basic approach for constructing the VCI method given in the last section requires solving a local linear system. In this section we seek to decouple the correction equations (58) for enhanced computational efficiency. An assumed strain method is proposed, and this involves a construction of the gradient field to achieve the integration constraints. First, let the test and trial functions be approximated by shape functions with  $n^{th}$  order completeness:

$$u^h = \sum_{I=1}^{NP} \Psi_I u_I \tag{60a}$$

$$v^h = \sum_{I=1}^{NP} \Psi_I v_I. \tag{60b}$$

A direct gradient and an assumed gradient are then introduced to the trial and test functions, respectively:

$$\nabla u^h = \sum_{I=1}^{NP} \nabla \Psi_I u_I \tag{61a}$$

$$\tilde{\nabla} v^h = \sum_{I=1}^{NP} \left( \nabla \Psi_I + \sum_{|\beta| \leq n} \xi_{\beta I} \nabla \hat{\Psi}_I^\beta \right) v_I. \tag{61b}$$

Under this framework, the Galerkin formulation of the Poisson equation seeks  $(u^h, \lambda^h) \in U^h \times \Lambda^h$  such that for all  $(v^h, \gamma^h) \in V^h \times \Gamma^h$  the following equation holds:

$$\int_{\Omega} \tilde{\nabla} v^h \cdot \nabla u^h \, d\Omega = \int_{\Omega} v^h s \, d\Omega + \int_{\partial\Omega_h} v^h h \, d\Gamma + \int_{\partial\Omega_g} v^h \lambda^h \, d\Gamma + \int_{\partial\Omega_g} \gamma^h (u^h - g) \, d\Gamma, \tag{62}$$

where  $\tilde{\nabla}$  is the assumed gradient operator defined by (61b).

Remarks 4.2

Likewise, the Galerkin formulation for elasticity seeks  $(u^h, \lambda^h) \in U^h \times \Lambda^h$  such that for all  $(v^h, \gamma^h) \in V^h \times \Gamma^h$  the following equation holds:

$$\begin{aligned} \int_{\Omega} \tilde{\nabla}^s v^h : \mathbb{C} : \nabla^s u^h \, d\Omega &= \int_{\Omega} v^h \cdot b \, d\Omega + \int_{\partial\Omega_h} v^h \cdot h \, d\Gamma + \int_{\partial\Omega_g} v^h \cdot \lambda^h \, d\Gamma \\ &+ \int_{\partial\Omega_g} \gamma^h \cdot (u^h - g) \, d\Gamma, \end{aligned} \tag{63}$$

where  $\tilde{\nabla}^s u^h = 1/2 (\tilde{\nabla} \otimes u^h + u^h \otimes \tilde{\nabla})$ .

By using the assumed strain method for the Petrov–Galerkin formulation, it is possible to uncouple the equations in (58). Consider an assumed strain correction for (37) and (51), in two dimensions:

$$\tilde{\nabla} v^h = \sum_{I=1}^{NP} \left( \nabla \Psi_I + R_I \begin{Bmatrix} \xi_{1I} \\ \xi_{2I} \end{Bmatrix} \right) v_I. \tag{64}$$

Here,  $R_I$  is taken in its simplest form as

$$R_I(x) = \begin{cases} 1 & \text{if } x \in \text{supp}(\Psi_I(x)) \\ 0 & \text{if } x \notin \text{supp}(\Psi_I(x)) \end{cases}. \tag{65}$$

Note that different forms for  $R_I$  with higher-order continuity can also be considered.

The coefficients are then solved for directly by

$$\xi_{1I} = -(\langle \Psi_{I,1} \rangle_{\Omega} - \langle \Psi_I n_1 \rangle_{\partial\Omega}) / \langle R_I \rangle \quad (66a)$$

$$\xi_{2I} = -(\langle \Psi_{I,2} \rangle_{\Omega} - \langle \Psi_I n_2 \rangle_{\partial\Omega}) / \langle R_I \rangle. \quad (66b)$$

To satisfy the linear constraints (37) and (51), and quadratic constraints (38) and (54), consider the correction

$$\tilde{\nabla} v^h = \sum_{I=1}^{NP} \left( \nabla \Psi_I + R_I \begin{Bmatrix} \xi_{1I} \\ \xi_{2I} \end{Bmatrix} + S_I \begin{Bmatrix} \xi_{3I} \\ \xi_{4I} \end{Bmatrix} + T_I \begin{Bmatrix} \xi_{5I} \\ \xi_{6I} \end{Bmatrix} \right) v_I, \quad (67)$$

where

$$S_I = R_I \cdot (x - x_I) \quad (68a)$$

$$T_I = R_I \cdot (y - y_I). \quad (68b)$$

The use of (67) uncouples the constraints into two systems of equations

$$A_I \xi_I^1 = r_I^1 \quad (69a)$$

$$A_I \xi_I^2 = r_I^2, \quad (69b)$$

where

$$A_I = \langle P(x - x_I) P^T (x - x_I) R_I \rangle_{\Omega} \quad (70a)$$

$$P(x) = \{1 \ x \ y\}^T \quad (70b)$$

$$\xi_I^1 = \{\xi_{1I} \ \xi_{3I} \ \xi_{5I}\}^T \quad (70c)$$

$$\xi_I^2 = \{\xi_{2I} \ \xi_{4I} \ \xi_{6I}\}^T \quad (70d)$$

$$r_I^1 = \{r_{1I} \ r_{3I} \ r_{5I}\}^T \quad (70e)$$

$$r_I^2 = \{r_{2I} \ r_{4I} \ r_{6I}\}^T, \quad (70f)$$

and

$$r_{1I} = \langle \Psi_I n_1 \rangle_{\partial\Omega} - \langle \Psi_{I,1} \rangle_{\Omega} \quad (71a)$$

$$r_{2I} = \langle \Psi_I n_2 \rangle_{\partial\Omega} - \langle \Psi_{I,2} \rangle_{\Omega} \quad (71b)$$

$$r_{3I} = \langle \Psi_I n_1 (x - x_I) \rangle_{\partial\Omega} - \langle \Psi_I \rangle_{\Omega} - \langle \Psi_{I,1} (x - x_I) \rangle_{\Omega} \quad (71c)$$

$$r_{4I} = \langle \Psi_I n_2 (x - x_I) \rangle_{\partial\Omega} - \langle \Psi_{I,2} (x - x_I) \rangle_{\Omega} \quad (71d)$$

$$r_{5I} = \langle \Psi_I n_1 (y - y_I) \rangle_{\partial\Omega} - \langle \Psi_{I,1} (y - y_I) \rangle_{\Omega} \quad (71e)$$

$$r_{6I} = \langle \Psi_I n_2 (y - y_I) \rangle_{\partial\Omega} - \langle \Psi_I \rangle_{\Omega} - \langle \Psi_{I,2} (y - y_I) \rangle_{\Omega}. \quad (71f)$$

#### Remarks 4.3

- (1) Shifted polynomials  $x - x_I$  and  $y - y_I$  have been used in the construction of the assumed strain field to yield a symmetric matrix  $A_I$ . This assumed strain field in (61) along with the form of residual ensures the invertibility of  $A_I$ , so long as sufficient nodes are under the cover of the kernel function (65) for linear independency.
- (2) The form of the assumed strain fields in (61), (64), and (67) allows decoupling of the integration constraint correction equations. Further, the form chosen appears stable according to Section 5.2. Numerical observation demonstrates remarkable stability of the assumed strain method over a direct gradient approach.
- (3) The additional computational cost of using (61) is roughly the cost of integration of a body force and a total boundary term. It has been observed in large scale computations that the expense for linear VCI correction is negligible and therefore it is much more effective than using higher-order quadrature rules.

## 5. STABILITY ANALYSIS

Whenever a Petrov–Galerkin method such as the assumed strain VCI method presented in Section 4.2 is used, stability may become an issue. In this section, abstract stability estimates are presented for both Bubnov–Galerkin and Petrov–Galerkin methods. It is noted that for the assumed strain VCI method, the stability analysis of the Petrov–Galerkin method can be simplified and stability can be shown in terms of coercivity rather than an inf-sup condition.

## 5.1. Stability estimates for Bubnov–Galerkin and Petrov–Galerkin methods

Here, for clarity and simplicity, it is assumed that the test and trial functions are kinematically admissible so that the Lagrange multipliers in (29) are not taken into account. Consider the following weak form statement: find  $u^h \in V^h$  such that

$$a(v^h, u^h)_{\Omega} = F(v^h) \quad \forall v^h \in V^h. \quad (72)$$

For Bubnov–Galerkin methods, the existence of a unique solution  $u^h \in V^h$  to the abstract discrete problem is a direct consequence of the Lax–Milgram theorem, provided that the linear form  $F$  is continuous and that the bilinear form  $a$  is continuous and coercive. Note that in the Bubnov–Galerkin method,  $a$  is defined on  $V^h \times V^h$ . The stability of the approximate solution  $u^h$  can be easily verified by means of the coercivity of the bilinear form  $a$ , that is,

$$a(u^h, u^h)_{\Omega} \geq \rho \|u^h\|_V^2 \quad \forall u^h \in V^h, \quad (73)$$

with appropriate norm  $\|\cdot\|_V$  on  $V$ , holds for  $\rho > 0$ , because, by the continuity of  $F$  and the variational equation (72), one obtains

$$\|u^h\|_V \leq \frac{1}{\rho} \|F\|_{V'} \quad (74)$$

where  $\|\cdot\|_{V'}$  denotes the dual norm of  $\|\cdot\|_V$ .

In the case of Petrov–Galerkin methods, the bilinear form  $a$  is defined on  $V^h \times U^h$ . Existence and uniqueness of the discrete solution  $u^h \in U^h$  now mainly relies on an inf-sup condition, which can be equivalently expressed as

$$\sup_{v^h \in V^h} \frac{a(v^h, u^h)_{\Omega}}{\|v^h\|_V} \geq \kappa \|u^h\|_U \quad \forall u^h \in U^h, \quad (75)$$

with  $\kappa > 0$  and appropriate norm  $\|\cdot\|_U$  on  $U$ . By using the variational equation (72), stability can be shown in the same way as the Bubnov–Galerkin method and yields the estimate

$$\|u^h\|_U \leq \frac{1}{\kappa} \|F\|_{V'}. \quad (76)$$

Summarizing, both Bubnov–Galerkin and Petrov–Galerkin methods lead to a similar stability estimate. However, in the case of Bubnov–Galerkin methods, the stability estimate relies on the coercivity condition (73). In this case, the coercivity of  $a$  in the discrete setting is inherited from the coercivity of its continuous counterpart and therefore, in general, is easy to show. In the case of Petrov–Galerkin methods, the stability estimate relies on the inf-sup condition (75) and it requires well-balanced spaces  $U^h$  and  $V^h$ .

## 5.2. Stability analysis

Next, stability analysis is presented for the assumed strain VCI method. Because of the form of the proposed correction (61), the stability analysis of this Petrov–Galerkin method can be carried out by means of the coercivity of the bilinear form as shown in (73) rather than fulfilling an inf-sup

condition of the form (75). Without loss of generality, considerations are restricted to the case of a Poisson problem.

With the concept of assumed strains in the Petrov–Galerkin framework, and with quadratures considered in the linear products, the bilinear form takes the form

$$\tilde{a}(v^h, u^h)_\Omega = \langle \tilde{\nabla} v^h, \nabla u^h \rangle_\Omega. \quad (77)$$

Inserting the ansatz (64) into the above, and setting  $v^h = u^h$  (because  $V^h = U^h$ ) we arrive at

$$\tilde{a}(u^h, u^h)_\Omega = \sum_{I=1}^{NP} \sum_{J=1}^{NP} u_I \{ \langle \nabla \Psi_I, \nabla \Psi_J \rangle_\Omega + \langle R_I \xi_I, \nabla \Psi_J \rangle_\Omega \} u_J. \quad (78)$$

Performing integration by parts on this term, we obtain

$$\tilde{a}(u^h, u^h)_\Omega = \sum_{I=1}^{NP} \sum_{J=1}^{NP} u_I \{ \langle \nabla \Psi_I, \nabla \Psi_J \rangle_\Omega - \langle \nabla R_I \cdot \xi_I + \nabla \cdot \xi_I R_I, \Psi_J \rangle_\Omega + \langle \xi_I \cdot \mathbf{n} R_I, \Psi_J \rangle_{\partial\Omega} \} u_J. \quad (79)$$

Note that the second term vanishes if (65) is employed, and we have

$$\tilde{a}(u^h, u^h)_\Omega = \sum_{I=1}^{NP} \sum_{J=1}^{NP} u_I \{ \langle \nabla \Psi_I, \nabla \Psi_J \rangle_\Omega - \langle \nabla \cdot \xi_I R_I, \Psi_J \rangle_\Omega + \langle \xi_I \cdot \mathbf{n} R_I, \Psi_J \rangle_{\partial\Omega} \} u_J. \quad (80)$$

As can be seen, the stability of our proposed Petrov–Galerkin methods depends solely on the correction coefficients  $\xi_I$ , and is therefore stable for sufficiently ‘small’ correction coefficients  $\xi_I$  and their gradients. This also becomes clear, because in this case the quadrature versions of the integrals approach the exact integrals. In other words, the coefficients are dependent on the magnitude of the residual of the associated integration constraint to be satisfied. Therefore, increasing the accuracy of domain integration should yield an increasingly stable correction method for the technique proposed herein. Furthermore, increasing the support in (65) gives an even more stable result because of the coefficients in (66) being smaller on a whole.

Note that in the special cases of small corrections and pure homogeneous essential boundary conditions or for  $\xi_1 = \xi_2 = 0$  on the boundary  $\partial\Omega$  we obtain

$$\tilde{a}(u^h, u^h)_\Omega = \sum_{I=1}^{NP} \sum_{J=1}^{NP} u_I \{ \langle \nabla \Psi_I, \nabla \Psi_J \rangle_\Omega \} u_J. \quad (81)$$

The stability of such a discrete bilinear form can be analyzed by the coercivity condition with standard procedures.

## 6. NUMERICAL EXAMPLES

Because the boundary condition enforcement should attest to the strong form as described in Section 3, Nitsche’s method is used with a penalty parameter of  $10^3/h$  for the Poisson equation and  $10^3 E/h$  for elasticity, where  $E$  is Young’s modulus. Unless otherwise stated, quartic B-spline kernels are used in all examples with normalized supports for linear, quadratic, and cubic bases equal to 2.0, 3.0, and 4.0, respectively. The form of VCI used in all examples is the method described in Section 4.2.

### 6.1. Patch tests in one dimension

Consider the following one-dimensional model problem on the domain  $\Omega = (0, 1)$ :

$$u_{,xx}(x) + s(x) = 0 \quad \text{in } \Omega, \quad (82)$$

with boundary conditions

$$u(0) = 0, \quad u(1) = g. \quad (83)$$

The following cases for the source term  $s(x)$  are examined that correspond to the linear, quadratic, and cubic patch tests for case 1, 2, and 3, respectively, and a high order solution is considered for case 4:

$$\text{Case 1: } s(x) = 0, \quad g = 1 \quad (84a)$$

$$\text{Case 2: } s(x) = 8x, \quad g = 1 \quad (84b)$$

$$\text{Case 3: } s(x) = 8 + 16x, \quad g = 1 \quad (84c)$$

$$\text{Case 4: } s(x) = 4\pi^2 \sin(2\pi x), \quad g = 0. \quad (84d)$$

For these cases, consider the nonuniform node distribution of 26 nodes shown in Figure 8.

Here, single point GI, DNI, and their VCI counterparts are employed, herein denoted VC-GI and VC-DNI, respectively. The orders of completeness in the approximation are chosen to be 1, 2, and 3 for linear, quadratic, and cubic patch tests, respectively, for all the integration methods tested. The kernel supports in this example are normalized by the larger distance between the nodal neighbors.



Figure 8. Irregular node distribution in one dimension.

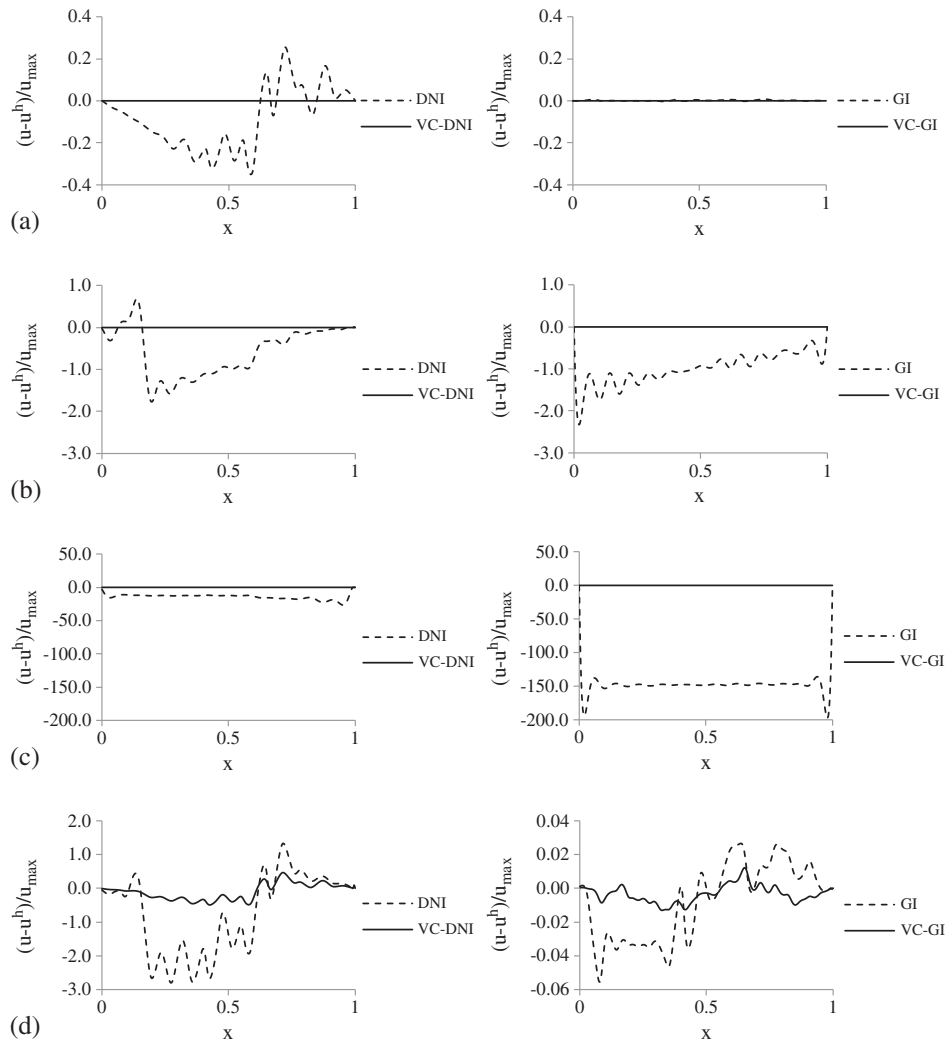


Figure 9. Errors in one-dimensional patch tests: (a) case 1, linear variationally consistent integration (VCI); (b) case 2, quadratic VCI; (c) case 3, cubic VCI; and (d) case 4, linear VCI.

For the assumed strain method, (60) and (61) is used with the following functions chosen for the assumed gradient for increasing orders of  $n$  for VCI:

$$\hat{\Psi}_{I,x}^n(x) = R_I(x)(x - x_I)^{n-1}. \tag{85}$$

First, case 1 is examined with linear VCI. Next, for cases 2 and 3, quadratic VCI, and cubic VCI are employed, respectively. Lastly, case 4 is examined with linear basis and linear VCI. The errors for the four analyses are shown in Figure 9. Variationally consistent integration is seen to pass arbitrarily high order patch tests as well as decrease the error for high order problems.

6.2. Patch tests for the 2D Poisson equation

Consider the Poisson problem (8) with the domain taken as  $\Omega : (-1, 1) \times (-1, 1)$  with the boundary decomposition  $\partial\Omega_h : 0 \leq x \leq 1, y = 1$ , and  $\partial\Omega_g = \partial\Omega \setminus \partial\Omega_h$ .

Let the prescribed body force and boundary conditions for (8) be consistent with a linear solution

$$u = x + 2y. \tag{86}$$

The domain discretization and integration schemes are depicted in Figure 10. SNNI smoothing zones are chosen to extend over the boundary so that completeness is maintained (see Remarks 2.1) for the quadratic patch tests. Nodes are also moved into the numerical centroid (21) of the Voronoi cells so that the gradient consistency of the smoothed strain is maintained for SCNI (see Remarks 2.1).

Linear bases are introduced with the standard methods along with linear VCI employed as correction of variationally inconsistent integration methods. The error for GI, DNI, and SNNI is shown in Table III, along with their VCI counterparts (denoted herein VC-SNNI for SNNI with VCI) and SCNI. It is seen that the proposed VCI enables arbitrary types of integration to pass the linear patch test.

Now consider the Poisson equation (8), again on  $(-1, 1) \times (-1, 1)$ , with the same boundary decomposition but with source term and boundary conditions consistent with the quadratic solution

$$u = 0.1x + 0.3y + 0.8x^2 + 1.2xy + 0.6y^2. \tag{87}$$

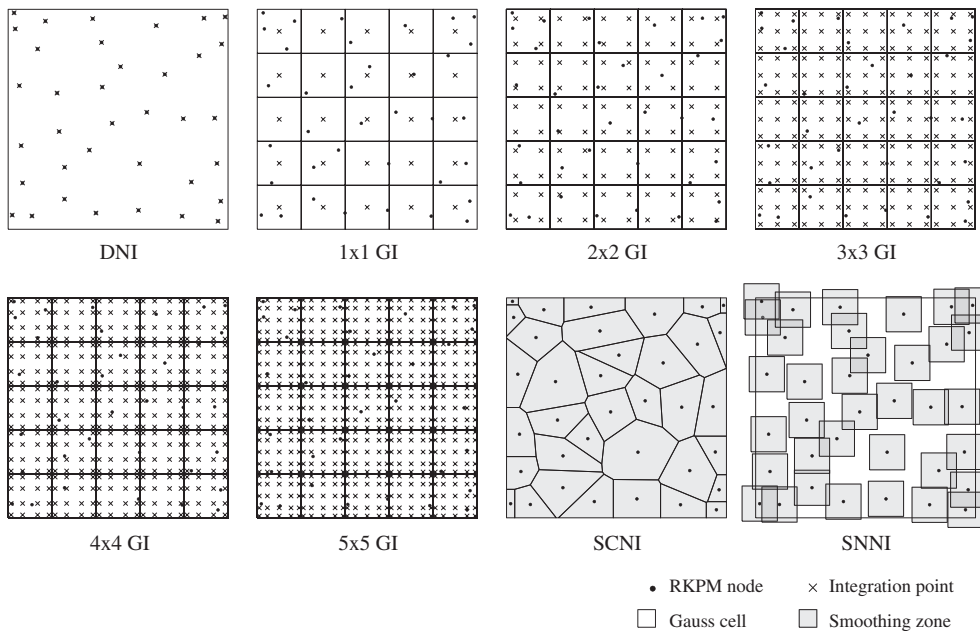


Figure 10. Domain discretization and integration schemes for patch tests.

Table III.  $L^2$  norm of error for various integration methods in linear patch test of Poisson equation.

Method	Standard	VCI
SCNI	1.20E-13	—
SNNI	0.0903225	5.28E-14
DNI	0.1200994	1.24E-13
1 × 1 GI	0.1249480	1.03E-13
2 × 2 GI	0.0233911	4.11E-14
3 × 3 GI	0.0060938	4.42E-14
4 × 4 GI	0.0020703	6.39E-14
5 × 5 GI	0.0007464	3.81E-14

SCNI, stabilized conforming nodal integration; SNNI, stabilized nonconforming nodal integration; DNI, direct nodal integration; GI, Gauss integration.

Table IV.  $L^2$  norm of error for various integration methods in quadratic patch test of Poisson equation.

Method	Standard	VCI
SCNI	0.1319736	1.69E-13
SNNI	0.1702456	1.88E-13
DNI	0.2183826	8.80E-14
1 × 1 GI	0.2298442	3.60E-13
2 × 2 GI	0.0088438	1.69E-13
3 × 3 GI	0.0017520	1.31E-13
4 × 4 GI	0.0003855	1.80E-13
5 × 5 GI	0.0000731	1.25E-13

VCI, variationally consistent integration; SCNI, stabilized conforming nodal integration; SNNI, stabilized nonconforming nodal integration; DNI, direct nodal integration; GI, Gauss integration.

As required to pass the quadratic patch test, a quadratic basis is used to construct the RKPM shape functions. The discretization and integration schemes depicted in Figure 10 are again employed with standard methods and their quadratic VCI counterparts, and the error is shown in Table IV. Note that SCNI passes only the linear patch test, and it requires VCI to pass the quadratic patch test (SCNI with quadratic VCI denoted herein as VC-SCNI).

### 6.3. Patch tests for elasticity

For the linear patch test, let the prescribed body force and boundary conditions for (40) be consistent with a linear solution as follows:

$$\mathbf{u} = \begin{Bmatrix} 0.1x + 0.3y \\ 0.2x + 0.4y \end{Bmatrix}. \quad (88)$$

For this problem and all elasticity patch tests, the plane strain formulation is used with Young's modulus  $E$  equal to 100 kN/m<sup>2</sup> and Poisson's ratio  $\nu$  equal to 0.3, and a domain  $\Omega = (-1m, 1m) \times (-1m, 1m)$  is discretized by 25 RKPM nodes. The decomposition of boundary condition is the same as that of Section 6.2. The four integration methods considered previously are employed and are depicted in Figure 10.

Linear bases are introduced along with linear VCI; the error is presented in Table V. It can be seen that the standard methods violate the integration constraint, and VCI precludes the situation for every integration scheme. The qualitative behavior of the solutions is shown in Figure 11, and spurious deformations are seen to take place for methods without VCI.

Linear exactness also means exactness in the constant stresses. For illustration, the shear stresses are plotted in Figure 12 for the standard methods and for VCI. It is seen that the variationally consistent methods can exactly represent this constant stress state in the domain. Note the performance of SNNI over DNI and 1 × 1 GI, which gives far less spurious stress in the domain.

Table V.  $L^2$  norm of error for various integration methods in linear patch test of elasticity problem.

Method	Standard	VCI
SCNI	8.66E-14	—
SNNI	0.0531788	3.21E-14
DNI	0.0648288	3.42E-14
1 × 1 GI	0.0810321	2.63E-14
2 × 2 GI	0.0118552	2.32E-14
3 × 3 GI	0.0023590	3.38E-14
4 × 4 GI	0.0008091	2.56E-14
5 × 5 GI	0.0003097	2.71E-14

VCI, variationally consistent integration; SCNI, stabilized conforming nodal integration; SNNI, stabilized nonconforming nodal integration; DNI, direct nodal integration; GI, Gauss integration.

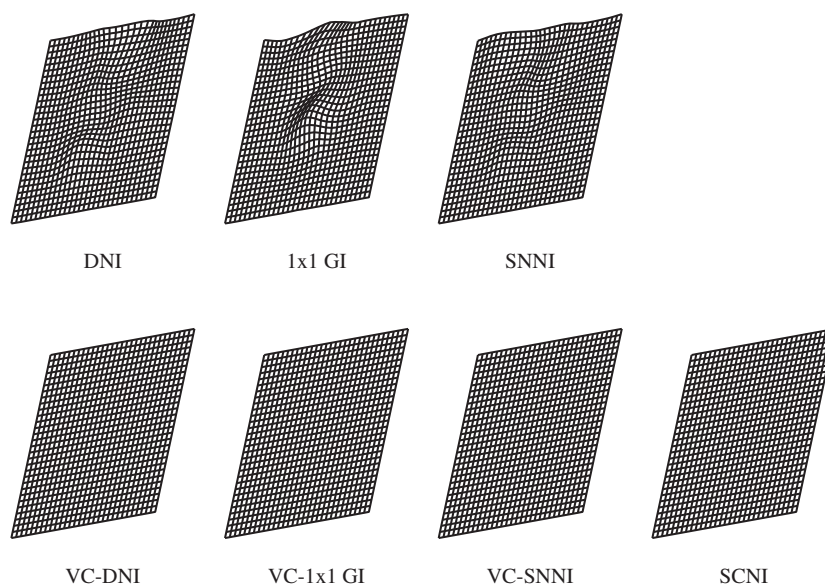


Figure 11. Solutions for elastic linear patch test.

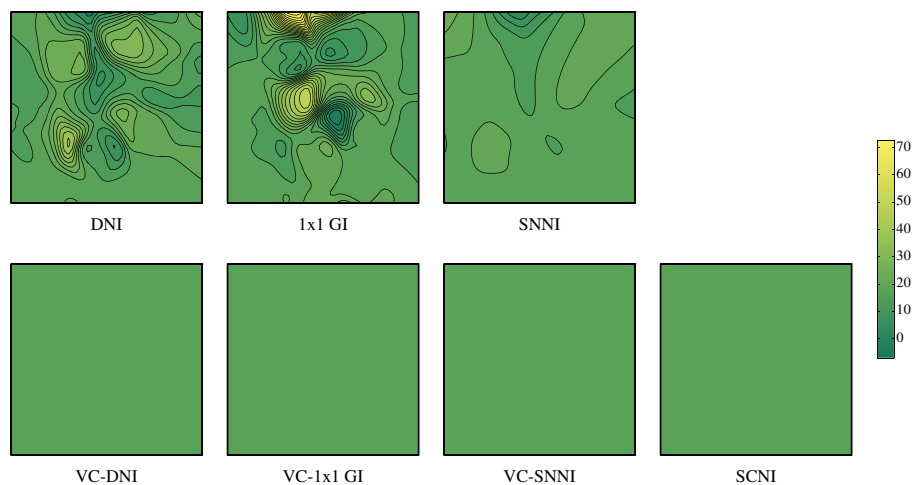
Figure 12. Stress distributions in elasticity linear patch test, units in  $\text{kN/m}^2$ .

Table VI.  $L^2$  norm of error for various integration methods in quadratic patch test of elasticity problem.

Method	Standard	VCI
SCNI	0.0622307	1.09E-13
SNNI	0.1081434	1.02E-13
DNI	0.1168936	1.46E-13
1 × 1 GI	0.1660389	1.44E-13
2 × 2 GI	0.0064088	5.73E-14
3 × 3 GI	0.0011188	9.68E-14
4 × 4 GI	0.0002739	5.68E-14
5 × 5 GI	0.0000572	4.28E-14

VCI, variationally consistent integration; SCNI, stabilized conforming nodal integration; SNNI, stabilized nonconforming nodal integration; DNI, direct nodal integration; GI, Gauss integration.

For the quadratic patch test, consider the prescribed conditions (44) for the elasticity BVP (40) with solution

$$\mathbf{u} = \begin{Bmatrix} 0.12x + 0.14y + 0.16x^2 + 0.18xy + 0.20y^2 \\ 0.11x + 0.13y + 0.15x^2 + 0.10xy + 0.21y^2 \end{Bmatrix}. \tag{89}$$

Here quadratic bases are introduced; the errors for the various methods are given in Table VI, and again it is seen that the variationally consistent methods are able to pass the patch test. In the case of methods that do not pass the patch test, oscillations are even more severe than in the linear patch test as seen in Figure 13, and the corresponding spurious stresses are shown in Figure 14. It can be observed that stresses obtained by the standard methods can have error on the same order of the exact stress itself. Gauss integration performs particularly poor, whereas DNI provides better results here. Note SCNI and SNNI generate far less error in the stress compared with the other variationally inconsistent methods.

#### 6.4. Convergence in the Poisson equation

Consider the Poisson equation (8) with the source term and homogeneous boundary conditions given as in (10). Here GI, DNI, and SNNI are employed with their VCI counterparts along with SCNI, and VC-SCNI if applicable. The domain discretization and subsequent uniform refinements are depicted in Figure 3. Normalized supports for all convergence studies are taken as 1.75 and 2.75 for linear and quadratic basis, respectively.

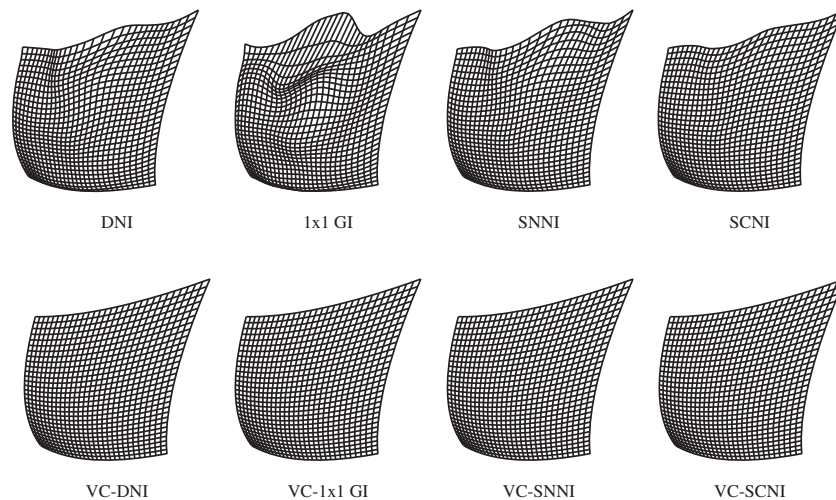


Figure 13. Solutions for quadratic elastic patch test in quadratic patch test of elasticity problem.

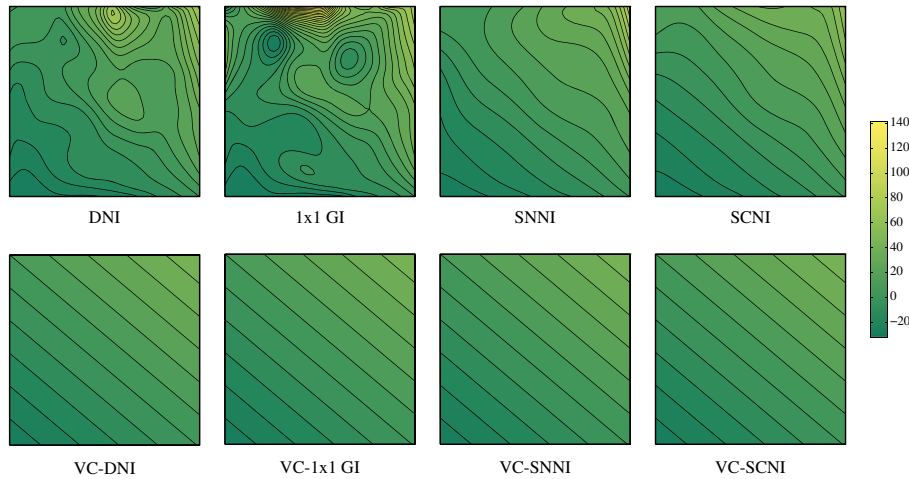


Figure 14. Shear stress distributions for quadratic elastic patch test of elasticity problem, units in  $\text{kN/m}^2$ .

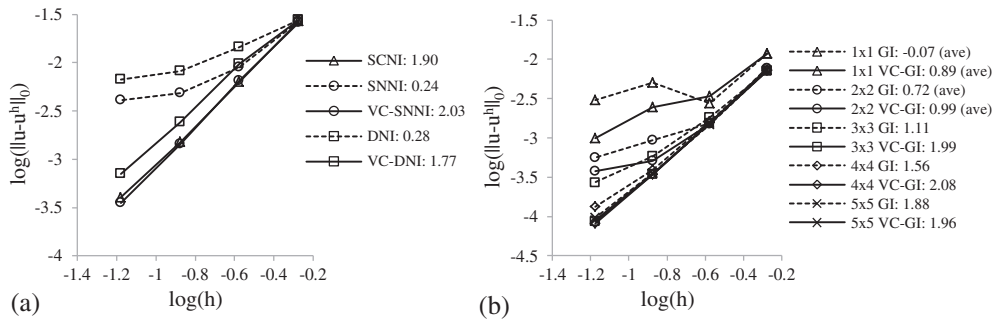


Figure 15. Convergence of error in the  $L^2$  norm for standard methods with first-order completeness and linear variationally consistent integration (VCI) methods for Poisson problem by using (a) nodal methods and (b) Gauss integration (GI).

The  $L^2$  norm of the error for nodal methods with first-order bases in the trial functions is plotted against the length  $h$  in Figure 15(a), and it is seen that VCI improves the rate of convergence and accuracy for all methods shown. Note the strikingly similar behavior of VC-DNI, VC-SNNI, and SCNI with respect to error and convergence in the  $L^2$  norm. The rates are nearly restored and fully restored for VC-DNI and VC-SNNI, respectively. Figure 15(b) shows the convergence plots for increasing orders of GI with their VCI counterparts. It is seen that convergence and error are superior for all cases by using the variationally consistent counterparts. Increasing orders GI achieves optimal rate with  $3 \times 3$  VC-GI, whereas  $5 \times 5$  GI is necessary for optimal convergence.

Variationally consistent integration also performs well regarding solution derivatives; the convergence of the nodal methods with first-order bases in the trial functions in the  $H^1$  semi-norm is shown in Figure 16(a). In the case of DNI and SNNI, the error is seen to have poor rates, whereas VC-DNI and VC-SNNI maintain near optimal and optimal convergence, respectively.

Figure 16(b) shows the convergence in the  $H^1$  semi-norm for increasing orders of GI. It is seen that VCI is able to reduce the severity of the error in the diverging result of  $1 \times 1$  GI, and that  $2 \times 2$  VC-GI can achieve optimum convergence, whereas  $5 \times 5$  GI can only partially restore optimum convergence.

A study is performed with quadratic VCI with the refinements shown in Figure 3. Figure 17(a) shows the convergence of the error in the  $L^2$  norm for nodal methods with second-order bases in the trial functions with their quadratic VCI counterparts. Here one can see again the similarity of VCI nodal methods with respect to error and convergence. VC-SCNI, VC-SNNI, and VC-DNI have enhanced convergence although the rate is not fully recovered.

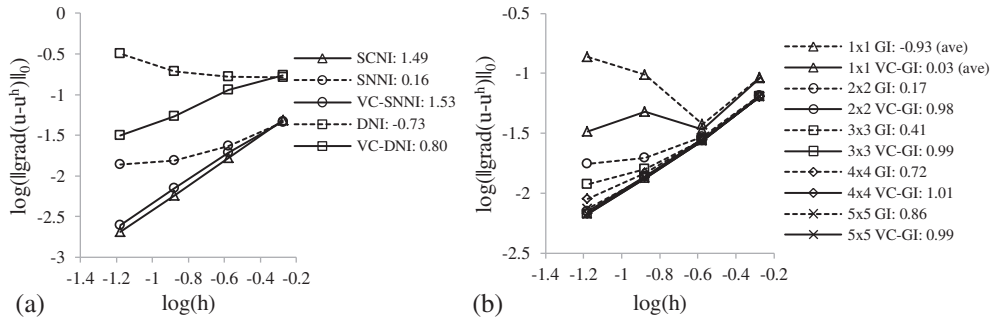


Figure 16. Convergence of error in the  $H^1$  semi-norm for standard methods with first-order completeness and linear variationally consistent integration (VCI) methods for Poisson problem by using (a) nodal methods and (b) Gauss integration (GI).

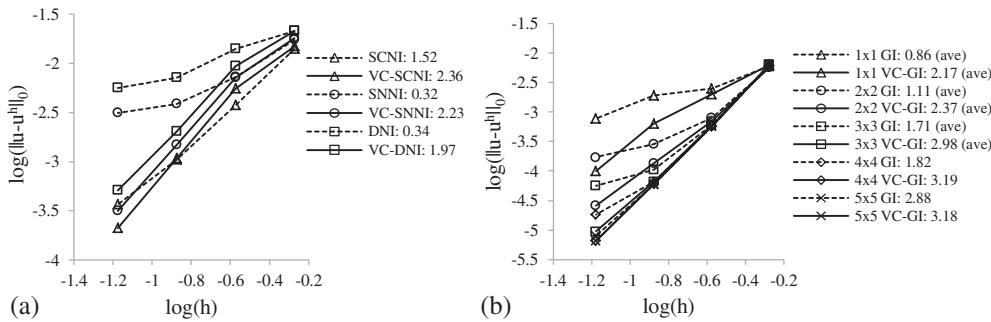


Figure 17. Convergence of error in the  $L^2$  norm for standard methods with second-order completeness and quadratic variationally consistent integration (VCI) methods for Poisson problem by using (a) nodal methods and (b) Gauss integration (GI).

Figure 17(b) shows the convergence of the error in the  $L^2$  norm for increasing orders of Gauss integration, and again the error and convergence is superior in all cases of variationally consistent integration. The rate is fully restored to the theoretical rate with  $3 \times 3$  VC-GI, and further improved with higher-order integration. In contrast,  $5 \times 5$  GI is necessary to nearly restore cubic convergence.

Figure 18(a) shows the convergence plots for the  $H^1$  semi-norm for quadratic standard and quadratic VCI nodal methods, where the VCI nodal methods again are superior to their counterparts. Convergence is nearly restored in the case of the smoothed nodal methods with VCI corrections, and partially restored for VC-DNI. The convergence in the  $H^1$  semi-norm for increasing orders of GI is

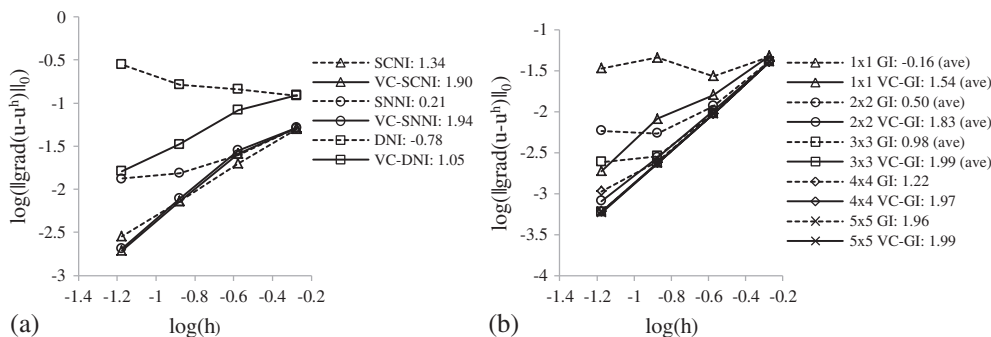


Figure 18. Convergence of error in the  $H^1$  semi-norm for standard methods with second order completeness and quadratic variationally consistent integration (VCI) methods for Poisson problem by using (a) nodal methods and (b) Gauss integration (GI).

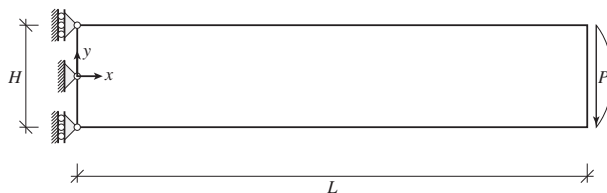


Figure 19. Cantilever beam with shear load.

shown in Figure 18(b). Here it is seen that the optimal rate is obtained with  $3 \times 3$  VC-GI, whereas for standard GI,  $5 \times 5$  GI is necessary to restore optimal rates.

### 6.5. Cantilever beam

A cantilever beam is considered with a parabolic shear load at one end, and the problem statement is shown in Figure 19. The plane stress assumption is made, and the exact solution to the problem is

$$u_x = \frac{Py}{6EI} \left[ (6L - 3x)x + (2 + \nu) \left( y^2 - \frac{H^2}{4} \right) \right] \quad (90a)$$

$$u_y = -\frac{P}{6EI} \left[ (L - x)3\nu y^2 + (4 + 5\nu) \frac{H^2}{4} x + (3L - x)x^2 \right], \quad (90b)$$

where  $I = H^3/12$  is the moment of inertia of the beam and  $P$  is the resultant of the shear stress applied. The load  $P$  was chosen to be  $10^3$  kN, and was applied according to the traction resulting from (90).

The domain is taken to be  $\Omega = (0\text{m}, 10\text{m}) \times (-1\text{m}, 1\text{m})$  with material constants  $E = 30 \cdot 10^6$  kN/m<sup>2</sup> and  $\nu = 0.3$ . The domain is discretized with two steps of refinement with nonuniform node distributions, shown in Figure 20. Linear basis is introduced with  $1 \times 1$  GI, DNI, and SNNI, and the linear assumed strain correction is used for each method, denoted as  $1 \times 1$  VC1-GI, VC1-DNI, and VC1-SNNI, respectively. Quadratic VCI is also employed for each integration method with linear bases, denoted as  $1 \times 1$  VC2-GI, VC2-DNI, and VC2-SNNI, respectively. SCNI is again employed for comparison. The reason for using linear bases with quadratic correction is to examine how higher-order corrections can improve solution accuracy without increasing the order of bases.

Tip displacement accuracy for various VCI methods is shown in Table VII. Although VC1 clearly enhances accuracy over the standard counterparts, VC2 improves the accuracy even further. Note that tip displacement in  $1 \times 1$  GI actually diverges with refinement, whereas the two  $1 \times 1$  VC-GI methods converge. We also see that VC2-SNNI provides the best results aside from SCNI.

The shear stress of the fine model along  $x = L/2$  for SCNI, standard integrations and their variationally consistent counterparts are shown in Figures 21–24. Looking over the figures we see that SCNI and VC2-SNNI give the most accurate stress results compared with all other methods,

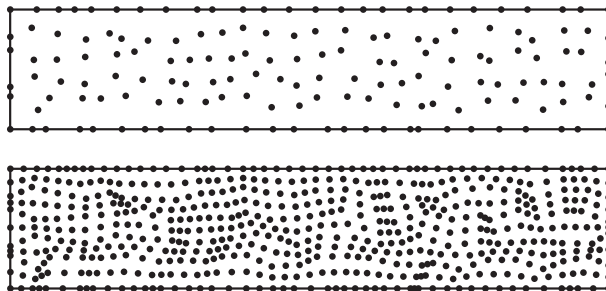


Figure 20. Discretizations for beam problem.

Table VII. Tip displacement accuracy for various integration methods.

Nodes	1 × 1 GI	1 × 1 VC1-GI	1 × 1 VC2-GI	SNNI	VC1-SNNI	VC2-SNNI	DNI	VC1-DNI	VC2-DNI	SCNI
156	142.3	115.0	105.3	132.7	118.6	101.9	171.0	118.1	96.3	99.4
561	147.5	108.0	105.1	106.5	102.0	99.3	107.1	97.4	98.7	100.0

VCI, variationally consistent integration; SCNI, stabilized conforming nodal integration; SNNI, stabilized nonconforming nodal integration; DNI, direct nodal integration; GI, Gauss integration.

although the VC1-SNNI and VC2-DNI results are also satisfactory. It is seen that all VCI methods have significantly improved accuracy compared with their standard counterparts, which are particularly inaccurate in the case of 1 × 1 GI and DNI. Although VCI-1 can provide improved results for all methods, the stress field is further enhanced using VCI-2, particularly for SNNI and DNI.

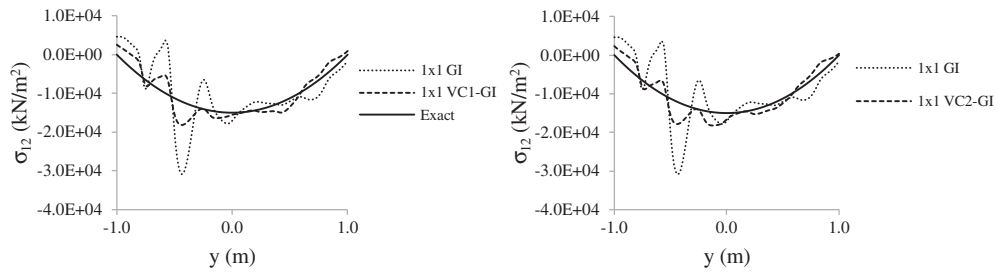


Figure 21. Shear stress along  $x = L/2$  for 1 × 1 Gaussian integration (GI), 1 × 1 variationally consistent Gaussian integration VC1-GI, and 1 × 1 VC2-GI.

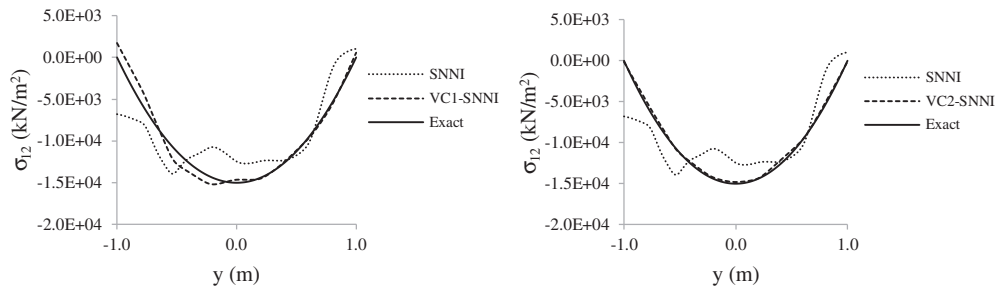


Figure 22. Shear stress along  $x = L/2$  for stabilized nonconforming nodal integration (SNNI), variationally consistent stabilized nonconforming nodal integration VC1-SNNI, and VC2-SNNI.

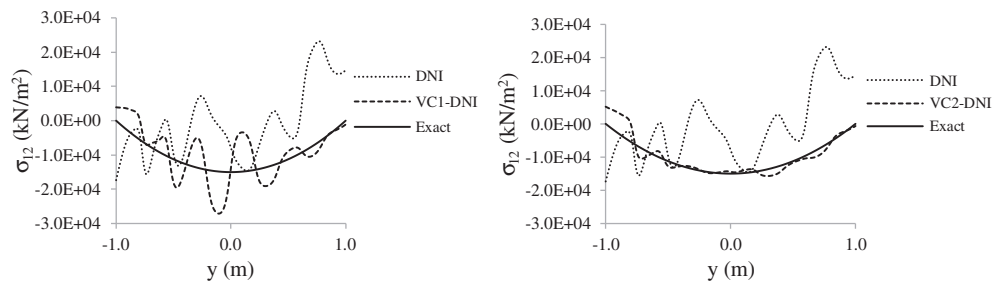


Figure 23. Shear stress along  $x = L/2$  for direct nodal integration (DNI), variationally consistent direct nodal integration VC1-DNI, and VC2-DNI.

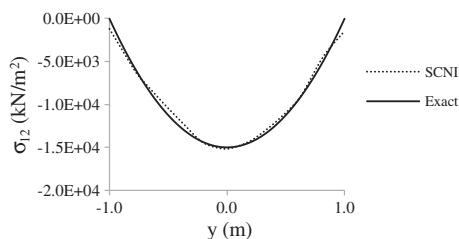


Figure 24. Shear stress along  $x = L/2$  for stabilized conforming nodal integration method (SCNI).

## 7. CONCLUSIONS

The approximation functions commonly employed in the Galerkin meshfree methods, such as MLS and RK, are capable of reproducing monomials of arbitrary order in arbitrary discretizations. This completeness property, however, does not guarantee optimal rate of convergence in the Galerkin solution of PDEs if the domain integration is not sufficiently accurate. Because the MLS/RK approximation functions are of rational type with overlapping supports, achieving high accuracy in the domain integration of Galerkin meshfree methods often requires considerably fine integration cells or very high quadrature order. This paper proposes an alternative approach to achieve optimal convergence consistent with the order of completeness in the approximation by introducing a variationally consistent integration formulation. This method uses integration constraints constructed from the discrete version of the weak equation as the basis for development, and it can be used as the correction for several commonly used domain integration methods to achieve optimal convergence.

This work begins with deriving the condition for  $n^{th}$  order exactness in the Galerkin approximation of PDEs. This condition is a generalization of the linear integration constraint [16], and the numerical methods that meet this condition are called VCI methods. The resulting  $n^{th}$  order variational consistency condition of a given PDE states that the numerical integration by parts conditions should hold for the inner product between the test functions and the differential operator acting on the  $n^{th}$  order monomials. If the domain and boundary integration methods of the Galerkin weak equation are consistent with the test function, the differential operator, and the boundary operator following the integration constraint, then the optimal convergence rates can be achieved.

The  $n^{th}$  order integration constraint has been applied to several PDEs to arrive at constraints specific to the problem and the desired order of exactness in the Galerkin approximation. A method has been proposed to correct integration methods that violate the integration constraints, such as DNI, GI, and SNNI. It is shown that improved accuracy and convergence is attained for variationally consistent integration, particularly in the derivatives of the solution. Several important observations are summarized as follows:

- (1) Variationally consistent nodal integration methods show promise with performance similar to SCNI, particularly VC-SNNI.
- (2) VC-SNNI is in general more accurate than VC-DNI, although similar convergence rates have been achieved between the two methods.
- (3) VCI for GI has been shown to supplement the convergence rates for lower order GI so that optimal convergence rates can be restored with far fewer quadrature points than would otherwise be required.
- (4) Integration methods that are far from being variationally consistent, such as using one point Gauss quadrature for achieving quadrature exactness, could violate the stability condition and result in suboptimal convergence even with the proposed correction.
- (5) SCNI that was developed for linear exactness can be corrected to achieve higher-order exactness by using VC-SCNI.
- (6) Corrected SNNI, namely VC-SNNI, possesses similar convergence and accuracy performance as that of SCNI, but offers a considerable simplicity over SCNI without the need of Voronoi cells in the strain smoothing.

- (7) Without increasing the order of bases, the second-order correction (VC2) further enhances the solution accuracy over the variationally inconsistent method with first-order correction (VC1).

The extension of this work to nonlinear mechanics, and plate and shell problems is under investigation, and the results will be published in forthcoming papers.

#### APPENDIX A: CUBIC CONSTRAINT FOR ELASTICITY

Similar to the procedures given in Section 3, arbitrarily high order constraints can be obtained for any PDE. Here the cubic constraint is derived for elasticity.

For cubic exactness in elasticity, consider the additional cubic components of the displacement field

$$u_1 = a_{16}x^3 + a_{17}x^2y + a_{18}xy^2 + a_{19}y^3 \quad (\text{A.1a})$$

$$u_2 = a_{26}x^3 + a_{27}x^2y + a_{28}xy^2 + a_{29}y^3, \quad (\text{A.1b})$$

which gives quadratic stresses

$$\begin{aligned} \sigma_{ij} = & \mathbb{C}_{ij11}(3a_{16}x^2 + 2a_{17}xy + a_{18}y^2) \\ & + \frac{1}{2}\mathbb{C}_{ij12}(a_{17}x^2 + 2a_{18}xy + 3a_{19}y^2 + 3a_{26}x^2 + 2a_{27}xy + a_{28}y^2) \\ & + \frac{1}{2}\mathbb{C}_{ij21}(a_{17}x^2 + 2a_{18}xy + 3a_{19}y^2 + 3a_{26}x^2 + 2a_{27}xy + a_{28}y^2) \\ & + \mathbb{C}_{ij22}(a_{27}x^2 + 2a_{28}xy + 3a_{29}y^2). \end{aligned} \quad (\text{A.2})$$

Substitution of (A.2) into the constraint (48) results in the following conditions:

$$\langle \hat{\Psi}_{I,1}x^2 \rangle_{\Omega} = -\langle 2\hat{\Psi}_I x \rangle_{\Omega} + \langle \hat{\Psi}_I x^2 n_1 \rangle_{\partial\Omega} \quad \forall I \quad (\text{A.3a})$$

$$\langle \hat{\Psi}_{I,2}x^2 \rangle_{\Omega} = \langle \hat{\Psi}_I x^2 n_2 \rangle_{\partial\Omega} \quad \forall I \quad (\text{A.3b})$$

$$\langle \hat{\Psi}_{I,1}xy \rangle_{\Omega} = -\langle \hat{\Psi}_I y \rangle_{\Omega} + \langle \hat{\Psi}_I xy n_1 \rangle_{\partial\Omega} \quad \forall I \quad (\text{A.3c})$$

$$\langle \hat{\Psi}_{I,2}xy \rangle_{\Omega} = -\langle \hat{\Psi}_I x \rangle_{\Omega} + \langle \hat{\Psi}_I xy n_2 \rangle_{\partial\Omega} \quad \forall I \quad (\text{A.3d})$$

$$\langle \hat{\Psi}_{I,1}y^2 \rangle_{\Omega} = \langle \hat{\Psi}_I y^2 n_1 \rangle_{\partial\Omega} \quad \forall I \quad (\text{A.3e})$$

$$\langle \hat{\Psi}_{I,2}y^2 \rangle_{\Omega} = -\langle 2\hat{\Psi}_I y \rangle_{\Omega} + \langle \hat{\Psi}_I y^2 n_2 \rangle_{\partial\Omega} \quad \forall I. \quad (\text{A.3f})$$

#### ACKNOWLEDGEMENTS

The support of this work by US Army Engineer Research and Development Center under contract W912HZ-07-C-0019 to the first and second authors and by German Research Foundation under grant number RU1213/2-1 to the third author are greatly acknowledged.

#### REFERENCES

1. Chen JS, Pan C, Roque CMOL, Wang HP. A Lagrangian reproducing kernel particle method for metal forming analysis. *Computational Mechanics* 1998; **22**:289–307.
2. Belytschko T, Tabbara M. Dynamic fracture using element-free Galerkin methods. *International Journal for Numerical Methods in Engineering* 1996; **39**:923–938.
3. Moës N, Dolbow J, Belytschko T. A finite element method for crack growth without remeshing. *International Journal for Numerical Methods in Engineering* 1999; **46**:131–150.
4. Guan PC, Chi SW, Chen JS, Slawson TR, Roth MJ. Semi-Lagrangian reproducing kernel particle method for fragment-impact problems. *International Journal of Impact Engineering* 2011; **38**:1033–1047.
5. Guan PC, Chen JS, Wu Y, Teng H, Gaidos J, Hofstetter K, Alsaleh M. Semi-Lagrangian reproducing kernel formulation and application to modeling earth moving operations. *Mechanics of Materials* 2009; **41**:670–683.
6. Nayroles B, Touzot G, Villon P. Generalizing the finite element method: diffuse approximation and diffuse elements. *Computational Mechanics* 1992; **10**:307–318.

7. Belytschko T, Lu YY, Gu L. Element-free Galerkin methods. *International Journal for Numerical Methods in Engineering* 1994; **37**:229–256.
8. Dolbow J, Belytschko T. Numerical integration of the Galerkin weak form in meshfree methods. *Computational Mechanics* 1999; **23**:219–230.
9. Atluri SN, Zhu T. A new meshless local Petrov–Galerkin (MLPG) approach in computational mechanics. *Computational Mechanics* 1998; **22**:117–127.
10. De S, Bathe KJ. The method of finite spheres. *Computational Mechanics* 2000; **25**:329–345.
11. De S, Bathe KJ. The method of finite spheres with improved numerical integration. *Computers and Structures* 2001; **79**:2183–2196.
12. Liu Y, Belytschko T. A new support integration scheme for the weakform in mesh-free methods. *International Journal for Numerical Methods in Engineering* 2010; **82**:699–715.
13. Carpinteri A, Ferro G, Ventura G. The partition of unity quadrature in meshless methods. *International Journal for Numerical Methods in Engineering* 2002; **54**:987–1006.
14. Duflot M, Nguyen-Dang H. A truly meshless Galerkin method based on a moving least squares quadrature. *Communications in Numerical Methods in Engineering* 2002; **18**:441–449.
15. Beissel S, Belytschko T. Nodal integration of the element-free Galerkin method. *Communications in Numerical Methods in Engineering* 1996; **139**:49–74.
16. Chen JS, Wu CT, Yoon S, You Y. A stabilized conforming nodal integration for Galerkin mesh-free methods. *International Journal for Numerical Methods in Engineering* 2001; **50**:435–466.
17. Puso MA, Chen JS, Zywicz E, Elmer W. Meshfree and finite element nodal integration methods. *International Journal for Numerical Methods in Engineering* 2008; **74**:416–446.
18. Chen JS, Hu W, Puso MA, Wu Y, Zhang X. Strain smoothing for stabilization and regularization of Galerkin meshfree methods. In *Meshfree Methods for Partial Differential Equations III*, Griebel M, Schweitzer MA (eds). Springer: Berlin, 2007; 57–75.
19. Liu GR, Dai KY, Nguyen TT. A smoothed finite element method for mechanics problems. *Computational Mechanics* 2007; **39**:859–877.
20. Dyka CT, Randles PW, Ingel RP. Stress points for tension instability in SPH. *International Journal for Numerical Methods in Engineering* 1997; **40**:2325–2341.
21. Krongauz Y, Belytschko T. Consistent pseudo-derivatives in meshless methods. *Computer Methods in Applied Mechanics and Engineering* 1997; **146**:371–386.
22. Bonet J, Kulasegaram S. Correction and stabilization of smooth particle hydrodynamics methods with applications in metal forming simulations. *International Journal for Numerical Methods in Engineering* 2000; **47**:1189–1214.
23. Wang D, Chen JS. Locking-free stabilized conforming nodal integration for meshfree Mindlin-Reissner plate formulation. *Computer Methods in Applied Mechanics and Engineering* 2004; **193**:1065–1083.
24. Chen JS, Wang D. A constrained reproducing kernel particle formulation for shear deformable shell in Cartesian coordinates. *International Journal for Numerical Methods in Engineering* 2006; **68**:151–172.
25. Wang D, Chen JS. A Hermite reproducing kernel approximation for thin-plate analysis with sub-domain stabilized conforming integration. *International Journal for Numerical Methods in Engineering* 2008; **74**:368–390.
26. Duan Q, Li X, Zhang H, Belytschko T. Second-order accurate derivatives and integration schemes for meshfree methods. *International Journal for Numerical Methods in Engineering* 2012; **92**:399–424.
27. Babuška I, Banerjee U, Osborn JE, Li Q. Quadrature for meshless methods. *International Journal for Numerical Methods in Engineering* 2008; **76**:1434–1470.
28. Babuška I, Banerjee U, Osborn JE, Zhang Q. Effect of numerical integration on meshless methods. *Computer Methods in Applied Mechanics and Engineering* 2009; **198**:2886–2897.
29. Liu WK, Jun S, Zhang YF. Reproducing kernel particle methods. *International Journal for Numerical Methods in Fluids* 1995; **20**:1081–1106.
30. Chen JS, Pan C, Wu CT, Liu WK. Reproducing kernel particle methods for large deformation analysis of non-linear structures. *Computer Methods in Applied Mechanics and Engineering* 1996; **139**:195–227.
31. Chen JS, Yoon S, Wu CT. Non-linear version of stabilized conforming nodal integration for Galerkin mesh-free methods. *International Journal for Numerical Methods in Engineering* 2002; **53**:2587–2615.
32. Yoo JW, Moran B, Chen JS. Stabilized conforming nodal integration in the natural-element method. *International Journal for Numerical Methods in Engineering* 2004; **60**:861–890.
33. Lu YY, Belytschko T, Gu L. A new implementation of the element free Galerkin method. *Computer Methods in Applied Mechanics and Engineering* 1994; **113**:397–414.